



**HAL**  
open science

# Measurement of the $\psi(2S)$ production in presence of a Quark-Gluon Plasma

Victor Feuillard

► **To cite this version:**

Victor Feuillard. Measurement of the  $\psi(2S)$  production in presence of a Quark-Gluon Plasma. Nuclear Experiment [nucl-ex]. Université Clermont Auvergne [2017-2020], 2017. English. NNT : 2017CLFAC079 . tel-01682850v2

**HAL Id: tel-01682850**

**<https://cea.hal.science/tel-01682850v2>**

Submitted on 18 Jul 2018

**HAL** is a multi-disciplinary open access archive for the deposit and dissemination of scientific research documents, whether they are published or not. The documents may come from teaching and research institutions in France or abroad, or from public or private research centers.

L'archive ouverte pluridisciplinaire **HAL**, est destinée au dépôt et à la diffusion de documents scientifiques de niveau recherche, publiés ou non, émanant des établissements d'enseignement et de recherche français ou étrangers, des laboratoires publics ou privés.

N° d'ordre : 925

**UNIVERSITÉ CLERMONT AUVERGNE**  
U.F.R. Sciences et Technologies

**ECOLE DOCTORALE DES SCIENCES FONDAMENTALES**

# **THESE**

Spécialité : Physique Nucléaire

présentée par

**Victor Feuillard**

## **Measurement of the $\psi(2S)$ production in presence of a Quark-Gluon Plasma**

soutenue le 16 novembre 2017, devant la commission d'examen :

Mme Roberta ARNALDI  
Mme Nathalie BESSON  
M. Frédéric FLEURET (Rapporteur)  
Mme Elena GONZALEZ FERREIRO (Rapporteur)  
M. Xavier LOPEZ (co-directeur de thèse)  
M. Hugo PEREIRA DA COSTA (co-directeur de thèse)  
M. Philippe ROSNET



# Contents

<b>Abstract</b>	<b>vii</b>
<b>Résumé</b>	<b>ix</b>
<b>Acknowledgments</b>	<b>xi</b>
<b>Introduction</b>	<b>1</b>
<b>1 Introduction to the Quark-Gluon Plasma</b>	<b>3</b>
1.1 The Standard Model . . . . .	4
1.1.1 An historical overview of particles discovery . . . . .	4
1.1.2 Elementary particles and fundamental interactions . . . . .	5
1.1.3 Basis of Quantum Chromo-Dynamics . . . . .	7
1.2 The QGP and the QCD phase diagram . . . . .	11
1.3 Heavy Ion Collisions . . . . .	12
1.3.1 Evolution of a collision . . . . .	14
1.4 Probes of the QGP . . . . .	16
1.4.1 Global Observables . . . . .	17
1.4.2 Soft Probes . . . . .	17
1.4.3 Hard probes . . . . .	18
1.5 The charmonium family . . . . .	19
1.5.1 Production Mechanism . . . . .	21
1.5.2 Cold Nuclear Matter Effects . . . . .	25
1.5.3 Charmonium production in presence of a QGP . . . . .	30
1.5.4 Theoretical Models . . . . .	34
1.6 Experimental Results from SPS to LHC . . . . .	38
1.6.1 Super Proton Synchrotron . . . . .	38
1.6.2 Relativistic Heavy Ion Collider . . . . .	39
1.6.3 Large Hadron Collider . . . . .	40

<b>2</b>	<b>The ALICE Detector</b>	<b>51</b>
2.1	ALICE at the LHC . . . . .	52
2.1.1	General description of the LHC . . . . .	52
2.1.2	Description of the ALICE detector . . . . .	55
2.2	Detectors from the Central Barrel . . . . .	57
2.2.1	The Inner Tracking System (ITS) . . . . .	57
2.2.2	The Time-Projection Chamber (TPC) . . . . .	58
2.2.3	The Transition Radiation Detector (TRD) . . . . .	59
2.2.4	The Time-Of-Flight detector (TOF) . . . . .	60
2.2.5	The High-Momentum Particle Identification Detector (HMPID) . . . . .	60
2.2.6	Photon Spectrometer (PHOS) . . . . .	61
2.2.7	ElectroMagnetic Calorimeter (EMCal) . . . . .	61
2.2.8	ALICE Cosmic Ray Detector (ACORDE) . . . . .	61
2.3	Forward Detectors . . . . .	62
2.3.1	Zero Degree Calorimeter (ZDC) . . . . .	62
2.3.2	Photon Multiplicity Detector (PMD) . . . . .	63
2.3.3	Forward Multiplicity Detector (FMD) . . . . .	63
2.3.4	V0 detector . . . . .	64
2.3.5	T0 detector . . . . .	64
2.4	The Muon Spectrometer . . . . .	65
2.4.1	General Layout . . . . .	65
2.4.2	Tracking Chambers . . . . .	66
2.4.3	Trigger Chambers . . . . .	67
2.4.4	Track reconstruction in the Muon Spectrometer . . . . .	71
2.5	Trigger and data acquisition systems . . . . .	72
2.5.1	The Central Trigger Processor and High Level Trigger . . . . .	72
2.5.2	Data Acquisition system . . . . .	73
<b>3</b>	<b>Measurement of <math>\psi(2S)</math> production</b>	<b>75</b>
3.1	Centrality Determination and Nuclear Overlap Function . . . . .	78
3.2	Data and Event selection . . . . .	80
3.2.1	Quality Assurance . . . . .	80
3.2.2	Physics selection . . . . .	81
3.3	Signal extraction . . . . .	82
3.3.1	Fit Functions used for the signal . . . . .	84
3.3.2	Fit Functions used for the background . . . . .	86
3.3.3	Direct Fit . . . . .	87
3.3.4	Fit after event-mixing . . . . .	89
3.3.5	Systematic uncertainty . . . . .	94

3.3.6	Results	95
3.4	Acceptance times Efficiency determination	98
3.4.1	Calculation of the $A\varepsilon$	98
3.4.2	Systematics uncertainties on the $A\varepsilon$	101
3.5	Number of equivalent minimum bias events	103
3.5.1	The $F_{norm}$ calculation methods	103
3.5.2	Pile-Up factor	105
3.5.3	Results	106
3.6	$\psi(2S)$ cross-section in pp collisions	107
3.6.1	Signal extraction	108
3.6.2	Acceptance and efficiency correction	109
3.6.3	Result	111
3.6.4	Energy-extrapolated Cross Section	111
3.7	Summary of the systematics uncertainties	113
3.8	Evaluation of Confidence limits with the CLs method	115
3.8.1	Test Statistic	116
3.8.2	Application to a simple example	117
3.8.3	Inclusion of the systematic uncertainties	119
3.8.4	Application to the $\psi(2S)$ signal extraction	120
3.8.5	Application to the $R_{AA}$	122
3.9	Measurement of the $\psi(2S)$ Nuclear Modification factor	123
3.9.1	Nuclear Modification Factor	124
3.9.2	Single Ratio	126
3.9.3	Double Ratio	130
3.9.4	Comparison to models	134
<b>4</b>	<b>Upgrades of the ALICE detector : the Muon Identifier (MID) - Estimation of the data flow</b>	<b>141</b>
4.1	Physics motivations	142
4.2	ALICE Upgrades	145
4.3	The Muon Identifier (MID)	150
4.4	Estimation of the Data Flow	153
4.4.1	Event Format	154
4.4.2	Data flow from scalers	155
	<b>Conclusion</b>	<b>167</b>
	<b>A Confidence Limit on the <math>J/\psi</math> signal</b>	<b>169</b>

<b>B</b>	<b>Comparison of the model prediction</b>	<b>173</b>
B.1	CoMover Interaction Model and Transport Model comparison	173
B.2	CoMover Interaction Model . . . . .	175
B.3	Transport Model . . . . .	177

# Abstract

## Measurement of the $\psi(2S)$ production in presence of a Quark-Gluon Plasma

The nuclear matter, which constitutes the atomic nuclei, is composed of quarks and gluons and interactions between them are described by quantum chromo-dynamics (QCD). Under ordinary conditions, quarks and gluons cannot be observed isolated and are confined inside hadrons such as protons and neutrons. The Quark-Gluon Plasma (QGP) is a state of nuclear matter predicted by QCD where quarks and gluons are deconfined. Experimentally, a QGP can be created in ultra-relativistic heavy ion collisions such as the lead-lead collisions delivered at the LHC, corresponding to speeds close to the speed of light. It is possible to obtain information on the characteristics of the QGP by measuring a large number of observables. In particular, the production of charmonium states such as the  $J/\psi$  and the  $\psi(2S)$ , heavy particles composed of a charm and anti-charm pair ( $c\bar{c}$ ), is studied to investigate the plasma. Indeed, the presence of QGP is expected to modify the charmonium production yields, due to a balance between the mechanism of color screening of the charm quark potential and a mechanism called recombination. This balance depends on the collision energy, the temperature of the plasma and nature on the considered particle, in particular one expects the  $\psi(2S)$  to be more suppressed than the  $J/\psi$ .

In this thesis the inclusive production of  $\psi(2S)$  in Pb – Pb collisions at an energy per nucleon-nucleon collision in the center of mass frame of  $\sqrt{s_{NN}} = 5.02$  TeV is measured in the dimuon-decay channel, using the ALICE Muon Spectrometer. The analysis is based on the data collected in ALICE (A Large Ion Collider Experiment) at the LHC in 2015 with an integrated luminosity of  $225 \mu\text{b}^{-1}$ . The nuclear modification factor  $R_{AA}$  is studied as a function of centrality. The ratio of the  $\psi(2S)$  and  $J/\psi$   $R_{AA}$  is also evaluated and shows that the  $\psi(2S)$  is more suppressed than the  $J/\psi$  for mid-central and central events. Compared with theoretical predictions, the

measurements are, within uncertainty, in agreement with theoretical model.

The upgrade of the Muon Trigger, the MID (Muon Identifier), is also studied, in particular the expected data flow at a collisions rate of 100 kHz. Based on the Pb – Pb data at a collision energy of  $\sqrt{s_{NN}} = 5.02$  TeV, the estimations predict that the technology that will be implemented in the MID provides a sufficient bandwidth to sustain the data flow.

**Keywords:** Quark Gluon Plasma, heavy ions, quarkonium,  $\psi(2S)$ , ALICE, LHC.

# Résumé

## Mesure de la production de $\psi(2S)$ en présence d'un Plasma de Quark et de Gluons

La matière nucléaire, constituant le noyau des atomes, est formée de quarks et de gluons, dont l'interaction est décrite par la théorie de la chromodynamique quantique (QCD). Dans des conditions normales, quarks et gluons ne peuvent être observés de façon isolée et sont confinés dans des hadrons tels que les protons et les neutrons. Le Plasma de Quarks et de Gluons (PQG) est un état de la matière nucléaire prédit par la QCD pour lequel ces quarks et gluons sont déconfinés. Expérimentalement, le PQG peut être créé dans des collisions d'ions lourds ultra-relativistes, telles que les collisions d'ions lourds effectuées au LHC, correspondant à des vitesses proche de celle de la lumière. Il est possible d'obtenir des informations sur le PQG en mesurant un large nombre d'observables. En particulier, la production de charmonium tels que le  $J/\psi$  et le  $\psi(2S)$ , particules lourdes constituées d'une paire de quarks charme et anti-charme ( $c\bar{c}$ ) est mesurée pour étudier le plasma. En effet, la présence d'un PQG est censée modifier les taux de production des charmonia, à cause d'un équilibre entre un mécanisme d'écrantage de couleur du potentiel des quarks charme et un mécanisme dit de recombinaison. La position de cet équilibre dépend de l'énergie de collision, la température du plasma, et la nature de la particule considérée, et plus spécifiquement, il est attendu que le  $\psi(2S)$  soit plus supprimé que le  $J/\psi$ .

Dans cette thèse, la production inclusive de  $\psi(2S)$  en collisions Pb – Pb à une énergie par collision nucléon-nucléon dans le référentiel du centre de masse de  $\sqrt{s_{NN}} = 5.02$  TeV est mesurée dans le canal de décroissance de dimuon avec le Spectromètre à Muons d'ALICE. L'analyse est basée sur les données collectées dans ALICE (A Large Ion Collider Experiment) au LHC en 2015 correspondant à une luminosité intégrée de  $225 \mu\text{b}^{-1}$ . Le facteur de modification nucléaire  $R_{AA}$  est étudié en fonction de la centralité des

collisions, correspondant à la distance transverse entre les centres des noyaux de plomb. Le rapport des  $R_{AA}$  du  $\psi(2S)$  et du  $J/\psi$  est également mesuré et montre que le  $\psi(2S)$  est plus supprimé que le  $J/\psi$  pour des collisions mi-centrales et centrales. Comparées aux prédictions théoriques, les mesures sont compatibles avec les modèles dans la limite des incertitudes.

L'amélioration du Muon Trigger, le MID, est également étudié, en particulier le débit de données attendu pour des fréquences de collision de 100 kHz. Basée sur les données en collisions Pb – Pb à une énergie de  $\sqrt{s_{NN}} = 5.02$  TeV, les estimations prédisent que la technologie qui sera implémentée sur le MID possède une bande passante suffisante.

**Mots-clés:** Plasma de Quarks et Gluons, ions lourds, quarkonium,  $\psi(2S)$ , ALICE, LHC.

# Acknowledgments

First of all I would like to thank my thesis supervisor, Hugo Pereira da Costa. It has been a privilege to have you help and guide me for the last three years. I would also like to thank my co-supervisor, Xavier Lopez, who has always been very helpful. Thank you for showing me the Muon Trigger and the facilities around ALICE.

Thank you to my referees, Elena Gonzalez Ferreiro and Frédéric Fleuret for reviewing my thesis. Thank you to Roberta Araldi, Philippe Rosnet, and Nathalie Besson for agreeing to be part of my jury.

I would like to extend those thanks to the ALICE group of the CEA Saclay, Javier Castillo, Hervé Borel, Stefano Panebianco, Andry Rakotozafindrabe, Alberto Baldisseri, and those who left during my thesis, Antoine Lardeux and Jean-Luc Charvet. You have made the life at the laboratory pleasant, fun, interesting, and you always have been here to lend me a helpful hand. Thank you also to the people from the administration, Danielle Coret, Isabelle Richard and Valérie Poyeton. I enjoyed our coffee breaks.

I also thank the people from Clermont Ferrand who I had the pleasure to meet during my times there, Philippe Crochet, Pascal Dupieux, Sarah Porteboeuf, and all the others I forget. In particular I would like to thank the IT department for saving my computer in a critical time.

I would like to thank all the other people from ALICE that I have met or talked to during the meetings and at CERN, Gines Martinez, Philippe Pilot, Ionut Arsene, Martino Gagliardi, Massimiliano Marchisone, Benjamin Audurier, Mohamad Tarhini... It has been a pleasure to work with all of you.

I would like to renew my thanks Alberto Baldisseri and Philippe Crochet for allowing me to perform my thesis in their laboratory and for accepting the strange situation regarding the financing. I would also like to thank the SPhN and the LPC at Clermont-Ferrand with the region Auvergne for financing the thesis.

Thank you to Pierre, Paul, Jérémy and Vincent, my friends from Cen-

trale Lyon, for keeping touch and sharing your experiences and going with my shenanigans. And thank you to my family, my mother Maria-Angeles, my father Jean, my cousin/roommate Eva, my big sister Patricia, her partner Joël and stepdaughter Loïse, and my little brother Raúl. Your support has meant and still means a lot.

Finally thank you to everybody I have not mentioned but has been part of this journey.

# Résumé détaillé : Mesure de la production de $\psi(2S)$ en présence d'un Plasma de Quark et de Gluons

## 1. Introduction au Plasma de Quarks et de Gluons

Développé dans les années 1970, le Modèle Standard (MS) décrit les particules fondamentales et les interactions entre elles. Les particules fondamentales sont les quarks, les leptons, et les bosons, ainsi que leurs antiparticules. Dans le MS les interactions fondamentales sont l'interaction électromagnétique, l'interaction nucléaire faible et l'interaction nucléaire forte. En particulier, les quarks sont sujets à l'interaction forte et interagissent par échange de gluons. Les quarks et les gluons portent des charges de couleurs, qui peuvent être interprétées comme l'équivalent de la charge électrique pour l'interaction électro-magnétique. La théorie décrivant les interactions entre quarks et gluons est la Chromo-Dynamique Quantique (QCD). Du fait que les gluons portent également une charge de couleur, ils peuvent interagir entre eux. Une conséquence de cette propriété est que la constante de couplage de l'interaction forte,  $\alpha_S$ , qui décrit l'intensité de l'interaction, est fonction de l'énergie. A basse énergie, la constante de couplage diverge, ce qui a pour conséquence que les quarks sont confinés au sein de particules neutres de couleur appelés hadrons (e.g. le proton ou le neutron). En revanche, à haute énergie la constante de couplage tend vers 0, et dans ces conditions, les quarks et gluons peuvent être considérés comme libres. C'est ce que l'on appelle la liberté asymptotique [1, 2]. Par ailleurs, la symétrie chirale, spontanément brisée à basse énergie, se restaure à haute énergie [3],

impliquant une transition de phase de la matière hadronique.

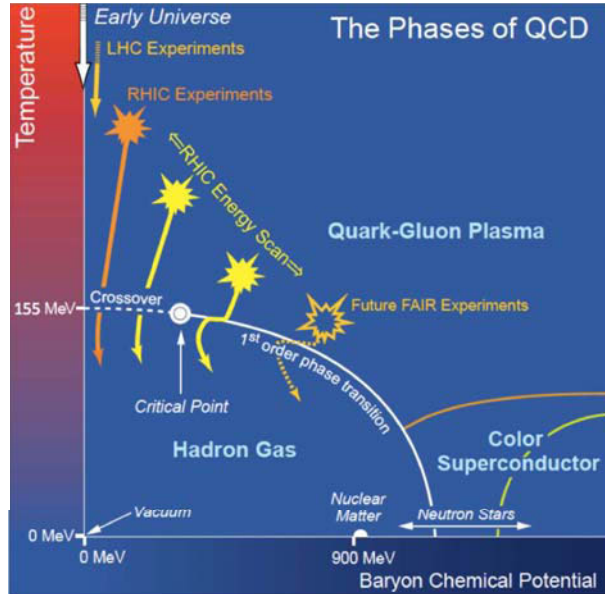


FIGURE 1: Schéma du diagramme de phase de la matière QCD en fonction de la température et du potentiel baryonique [4].

Les états de la matière hadronique peuvent être représentés dans un diagramme de phase de la matière, avec la densité baryonique en abscisse et la température en ordonnée, comme montré sur la Figure 1. À densité baryonique  $\mu_B = 939$  MeV et faible température, la matière se trouve dans son état ordinaire. Si la température augmente, la matière passe par une transition de phase et devient un Plasma de Quarks et de Gluons (QGP), où les quarks et les gluons sont déconfinés. Les modèles prédisent que la température de transition pour une densité baryonique nulle vaut environ  $T_c \approx 155$  MeV [5]. Cette transition correspond également à celle de la restauration de la symétrie chirale. Il est possible d'explorer le diagramme des phases à l'aide de collisions d'ions lourds ultra-relativistes, comme cela est fait au Relativistic Heavy Ion Collider (RHIC) [6] ou au Large Hadron Collider (LHC) [7].

Les collisions d'ions lourds peuvent être décrites par le scénario de Bjorken [8]. Quand des ions sont accélérés à des énergies ultra-relativistes, ils sont pratiquement transparents les uns pour les autres et lorsqu'ils se croisent, les

nucléons des ions se collisionnant laissent une gigantesque quantité d'énergie dans un très petit volume. Si la densité d'énergie est suffisamment élevée, un QGP se forme. Une collision se déroule en plusieurs étapes. Au moment de la collision, les quarks et les gluons des nucléons subissent de nombreuses interactions, provoquant une rapide augmentation de la température. Puis lorsque la température est suffisamment élevée, le plasma se forme, commence à se dilater, et il refroidit. Alors que le refroidissement continue, les quarks et les gluons sont finalement confinés dans des hadrons, c'est le gel chimique. Enfin, lorsque la température diminue suffisamment, les hadrons cessent d'interagir entre eux et les distributions cinématiques des particules sont gelées : c'est le gel thermique. Le QGP a une durée de vie extrêmement courte, il est par conséquent impossible de l'observer directement. Des informations peuvent en revanche être récupérées en détectant les particules émises lors de la collision qui vont permettre de sonder le plasma. On distingue différents types de sondes. Les observables globales fournissent des informations sur les caractéristiques de la collision, telles que la centralité, qui est liée à la distance entre les centres des noyaux. Les sondes molles, produites dans le plasma, sont par exemple les mésons de basse masse, les pions, les kaons, ou les hadrons étranges. Les sondes dures sont produites au tout début de la collision, avant la formation du plasma, et sont par conséquent affectées par l'évolution du milieu. On y trouve en particulier les quarkonia, qui sont des états liés quark-antiquark lourds.

Les quarkonia sont séparés en deux familles, les charmonia, qui sont des particules constituées d'une paire de quarks charme-anticharme  $c\bar{c}$  et les bottononia, qui sont des états beauté-antibéauté  $b\bar{b}$ . Parmi les charmonia on trouve le  $J/\psi$ , qui est l'état fondamental, et le  $\psi(2S)$  qui est le sujet de cette thèse. Ces différents états sont caractérisés par leur masse, mais également par l'énergie de liaison entre le quark  $c$  et le quark  $\bar{c}$ . Le  $\psi(2S)$ , légèrement plus lourd que le  $J/\psi$ , a une énergie de liaison dix fois plus faible. Les états plus lourds peuvent décroître vers l'état  $J/\psi$ , c'est ce que l'on appelle le *feed-down*. Dans des collisions hadroniques, on distingue deux types de production de charmonia. La production dite "prompte" inclut les charmonia produits directement et les charmonia issus de décroissances d'états plus lourds. Pour le  $J/\psi$ , cela représente environ 60% issus de la production directe, 30% issus de la décroissance de l'état  $\eta_c$  et 10% issus de la décroissance de  $\psi(2S)$ . La production dite "non-prompte" est issue de la décroissance des mésons B. Dans des collisions pp à une énergie de  $\sqrt{s} = 7$  TeV, l'expérience LHCb a mesuré que 10% de la production totale de  $J/\psi$  et 14% de la production

totale de  $\psi(2S)$  était non-prompte [9, 10].

Les hadrons sont nécessairement blancs, par conséquent les modèles de formation des charmonia doivent décrire la neutralisation de la couleur. Il en existe plusieurs mais tous ont en commun de considérer séparément les processus de haute énergie et courte distance, permettant un développement perturbatif de QCD en puissances de  $\alpha_S$ , et les processus de basse énergie et longue distance, qui par contre ne peuvent pas être traités de façon perturbative.

Le modèle du singulet de couleur (CSM) [11] suppose que les paires de quarks qui évoluent en un charmonium possèdent déjà le même spin et moment angulaire que le charmonium et sont produites dans un état de singulet de couleur. Le modèle de l'évaporation de couleur (CEM) [12] suppose que toutes les paires de quarks évoluent en un charmonium si leur masse invariante est supérieure à la masse nécessaire pour former un charmonium et inférieure à deux fois la masse du méson D. La neutralisation de la couleur dans le cas où la paire ne serait pas déjà dans un état de singulet se fait par interaction avec le champ de couleur induit par la collision. Enfin le modèle basé sur la QCD non-relativiste (NRQCD) [13] décrit la probabilité pour qu'une paire de quarks évolue en un charmonium à l'aide d'éléments de matrice longue distance (LDME). Ces termes ont une dépendance en impulsion transverse, rapidité et énergie qui est évaluée à l'aide d'ajustements sur les données. Par ailleurs le modèle NRQCD prédit que lors de collisions pp, les  $J/\psi$  à haute impulsion transverse possèdent une polarisation transverse. Cependant les mesures actuelles indiquent que le  $J/\psi$  n'est pas polarisé. En plus de la production hadronique, les charmonia peuvent aussi être produits par photo-production, c'est à dire par interaction entre un photon et un gluon, mais ceux-ci sont beaucoup moins nombreux que ceux produits lors de processus hadroniques.

La production de charmonium peut être affectée par la présence de matière nucléaire, même en l'absence de plasma. C'est ce que l'on appelle les effets nucléaires froids.

La fonction de distribution partonique (PDF)  $f(x, Q^2)$ , qui décrit la probabilité de trouver un gluon avec une fraction  $x$  de l'impulsion du nucléon à une énergie  $Q^2$ , est modifiée lorsque les nucléons sont à l'intérieur d'un noyau. Plusieurs effets sont observables en fonction de la valeur de  $x$  [14] : à petit  $x$ , la PDF est plus petite en présence de matière nucléaire, c'est ce que l'on appelle le *shadowing* ; quand  $x$  augmente, on observe l'effet inverse, l'*anti-shadowing*, où la PDF est plus grande en présence de matière

nucléaire ; puis alors que  $x$  devient plus grand on entre dans la région EMC (European Muon Collaboration) puis dans la région de mouvement de Fermi. Aux énergies du LHC, la région à petit  $x$  est accessible, on attend donc un shadowing important, ce qui pourrait impliquer une suppression des charmonia.

Un autre effet attendu est la saturation de gluons. Lorsque l'énergie augmente, la densité de gluons dans les nucléons augmente jusqu'à atteindre un point de saturation, où le nucleon peut alors être décrit comme un condensat de verre de couleur [15]. Ce condensat peut expliquer le shadowing à petit  $x$ .

L'absorption nucléaire, qui est due à l'interaction entre les charmonia avec les nucleons, peut dissocier les charmonia [16]. Cependant aux énergies du LHC, l'absorption nucléaire est négligeable. On observe également des effets de perte d'énergie partonique cohérente, due à l'interaction des partons avec les charges de couleurs du milieu.

D'autres effets se manifestent en présence d'un plasma de quark et de gluons.

Le premier effet attendu est l'écrantage de couleur, qui peut causer une suppression des charmonia [17]. La présence de charges de couleurs libres dans le milieu modifie le potentiel d'interaction entre les quarks et peut empêcher la paire  $c\bar{c}$  de se lier comme elle aurait pu le faire dans le vide. La portée de la liaison entre les quarks est caractérisée par le rayon de Debye  $r_D$ , qui décroît avec la densité de charges de couleurs et avec la température. Par conséquent, les différents états liés seront dissociés à différentes températures en fonction de leur énergie de liaison : le  $\psi(2S)$  étant moins lié que le  $J/\psi$ , il est dissocié à plus basse température.

Un autre mécanisme, appelé recombinaison peut également se produire dans des collisions d'ions lourd et donnerait au contraire lieu à une augmentation du nombre de charmonia. Lors de la collision des noyaux, de nombreux quarks charme sont produits, et s'ils sont produits en nombre suffisant, ils peuvent se recombinaison au moment de la transition de phase "inverse", lorsque le plasma retourne à l'état de matière nucléaire "normale", pour former des charmonia. C'est la régénération [18]. Aux énergies du LHC, cet effet est suffisamment important pour être du même ordre de grandeur que la suppression. Par ailleurs, la probabilité de régénération est différente en fonction de l'état de charmonium : la régénération du  $\psi(2S)$  arrive plus tard dans l'évolution du système que celle du  $J/\psi$ .

Il existe différents modèles pour décrire la production de charmonium dans des collisions d'ions lourds.

Le modèle d'interaction avec les co-movers (CIM) [19] décrit la suppression des charmonia par l'interaction avec un milieu dense de co-movers, et la régénération est ajoutée grâce à un terme de gain à l'équation décrivant la dissociation par interaction avec les co-movers. L'interaction avec les co-movers est décrite avec un section efficace d'interaction  $\sigma_{co}$ , mesurée lors des collisions au SPS à basse énergie. Cette section efficace est 10 fois plus grande pour le  $\psi(2S)$  que pour les  $J/\psi$ .

Le modèle de transport (TM) [20] considère une dissociation et une régénération constante des charmonia dans le plasma. L'évolution de la quantité de charmonium est décrite par une équation différentielle dépendant d'un coefficient de dissociation. Ce coefficient est fonction de la température et de l'état de charmonium considéré. La régénération est prise en compte par un paramètre de gain.

Le modèle de hadronisation statistique (SHM) [21] suppose que les charmonia sont complètement dissociés dans le plasma et ne se forment que par hadronisation des quarks charmés à la limite de la transition de phase. Ce modèle prend en compte la différence de densité de nucléons entre le coeur des noyaux, qui participent à la formation du plasma, et la périphérie des noyaux, dont les nucléons ne participent pas à la formation du plasma.

Historiquement, le QGP a d'abord été étudié dans des collisions d'ions lourds (Pb – Pb) sur le SPS, au CERN, où la formation du plasma a été observée pour la première fois. Une première suppression des  $J/\psi$  a été observée dans des collisions Pb – Pb centrales [22]. Au RHIC, dans des collisions d – Au, les effets nucléaires froids comme le shadowing furent mis en évidence. dans des collisions Au – Au à une énergie au centre de masse  $\sqrt{s_{NN}} = 0.2$  TeV, la suppression du  $J/\psi$  a été également mise en évidence, avec une augmentation de la suppression avec la centralité [23].

Au LHC, dans des collisions pp, les sections efficaces de production du  $J/\psi$  et du  $\psi(2S)$  ont été mesurées dans ALICE à plusieurs énergies de collision, et comparées aux modèles théoriques de production. Les calculs NRQCD [24] pour la composante prompt de la production, additionnés à des prédictions pour la production non-prompte, permettent de décrire les données avec précision.

Les mesures dans des collisions p – Pb à une énergie de collision  $\sqrt{s_{NN}} = 5.02$  TeV ont permis de mettre en évidence les effets nucléaires froids, en particulier une suppression plus importante du  $\psi(2S)$  par rapport au  $J/\psi$  à rapidité vers l'arrière [25]. Les mesures récentes du  $J/\psi$  à  $\sqrt{s_{NN}} = 8.16$  TeV sont compatibles avec les précédentes mesures, ainsi qu'avec les différents

modèles théoriques.

Dans des collisions Pb – Pb, ALICE a mesuré le flot elliptique  $v_2$ , qui caractérise l'asymétrie azimutale de production de particules mesurées par rapport au plan de réaction, pour le  $J/\psi$  aux énergies de collision de  $\sqrt{s_{NN}} = 2.76$  TeV et  $\sqrt{s_{NN}} = 5.02$  TeV, mettant en évidence un  $v_2$  positif, indiquant qu'une part importante des  $J/\psi$  mesurés sont issus de la recombinaison des quarks charmés.

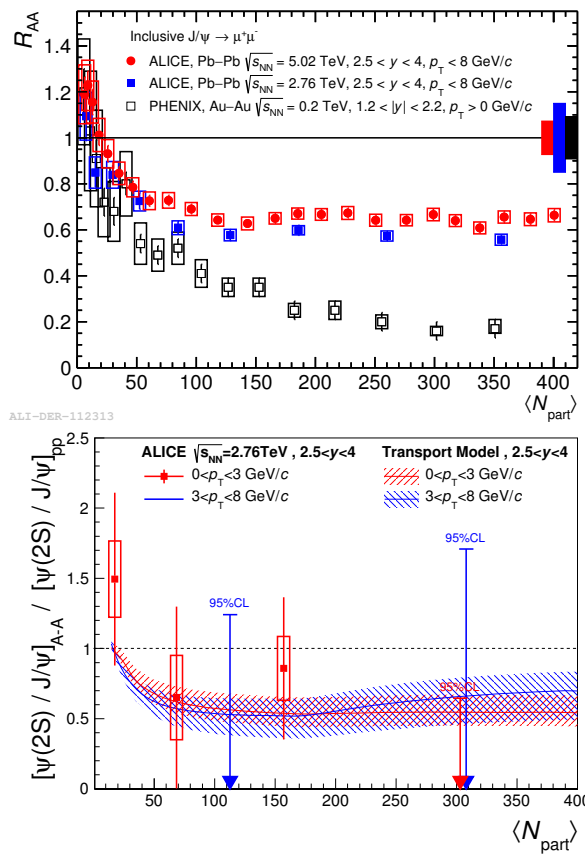


FIGURE 2: Haut : Facteur de modification nucléaire inclusif du  $J/\psi$  en fonction du  $N_{part}$  mesuré dans des collisions Pb – Pb à  $\sqrt{s_{NN}} = 2.76$  TeV et  $\sqrt{s_{NN}} = 5.02$  TeV comparé aux mesures de PHENIX dans des collisions Au – Au à  $\sqrt{s_{NN}} = 0.2$  TeV [26, 27]. Bas : Double rapport en fonction de  $N_{part}$  mesuré dans des collisions Pb – Pb à  $\sqrt{s_{NN}} = 2.76$  TeV [26].

Le facteur de modification nucléaire, qui est le rapport du taux de production dans des collisions Pb – Pb et du taux de production dans des collisions pp normalisé par le nombre de collisions binaires, a également été mesuré pour le  $J/\psi$  à  $\sqrt{s_{NN}} = 2.76$  TeV et  $\sqrt{s_{NN}} = 5.02$  TeV en fonction de la centralité. Il est montré sur la Figure 2, haut. Une suppression du  $J/\psi$  est clairement observée, cependant elle est beaucoup moins importante que celle observée au RHIC, indiquant que la régénération des  $J/\psi$  est bien plus importante aux énergies du LHC qu'à celles du RHIC. Entre les mesures à une énergie de collision de  $\sqrt{s_{NN}} = 2.76$  TeV et  $\sqrt{s_{NN}} = 5.02$  TeV, aucune différence significative n'est observée. Ces mesures sont compatibles avec les prédictions des modèles théoriques précédemment décrits, dans la limite des incertitudes.

A une énergie de collision de  $\sqrt{s_{NN}} = 2.76$  TeV, le rapport de production entre le  $\psi(2S)$  et le  $J/\psi$  a été mesuré en fonction de la centralité, comme montré sur la Figure 2. Cependant du fait des erreurs statistiques, il a été impossible de déterminer si l'une des particules était plus supprimée que l'autre.

## 2. Le détecteur ALICE

Le LHC est le plus grand accélérateur de particules au monde et peut effectuer des collisions pp jusqu'à  $\sqrt{s} = 14$  TeV et Pb – Pb jusqu'à  $\sqrt{s_{NN}} = 5.5$  TeV. Il utilise les accélérateurs PS et SPS pour accélérer les protons ou les noyaux avant de les insérer par paquets dans le LHC. Les faisceaux se croisent en quatre points où sont installés les quatre principales expériences du LHC : ATLAS, qui est dédiée à la recherche du Boson de Higgs et à la recherche de physique au delà du Modèle Standard, CMS, qui a les mêmes objectifs qu'ATLAS mais utilise des solutions techniques différentes, LHCb, qui est dédiée à l'étude de la violation CP ainsi qu'à l'étude de phénomènes rares lors de la décroissance de hadrons avec un quark b, et ALICE qui est la seule expérience spécifiquement dédiée à l'étude du QGP.

ALICE est composée de deux parties principales [28, 29], le tonneau central et le spectromètre à muons - ce dernier ayant été utilisé pour les données de cette analyse - ainsi que de détecteurs placés à petits angles. Le spectromètre à muons est situé dans la partie qui est définie comme "avant" du détecteur, la direction opposée est la direction "arrière". Un schéma du détecteur est montré sur la Figure 3.

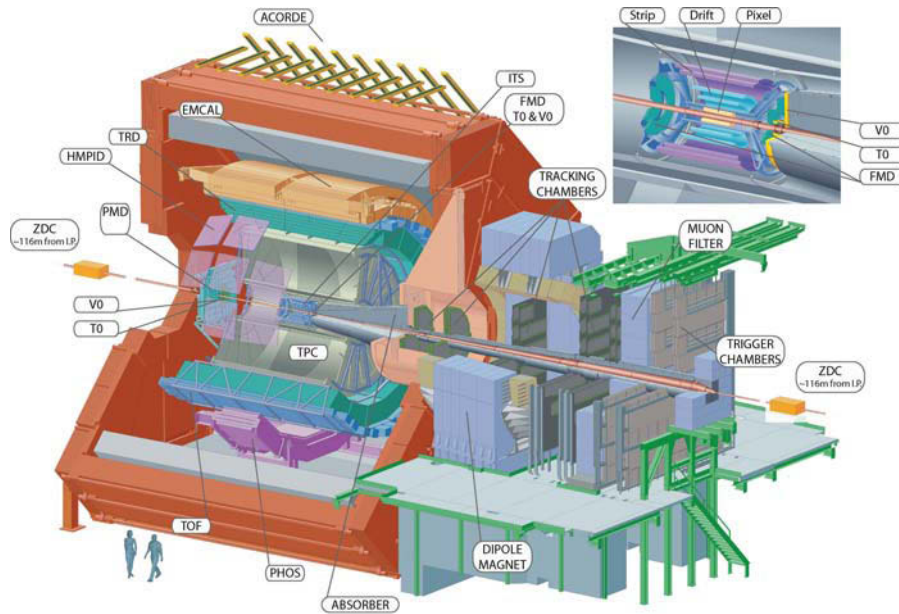


FIGURE 3: Schéma du détecteur ALICE.

Dans le tonneau central, en partant de l'intérieur vers l'extérieur, on trouve en premier l'Inner Tracking System (ITS), utilisé pour déterminer la position du vertex, correspondant au point d'interaction et la position des vertex secondaires, ainsi que pour mesurer la trajectoire de particules chargées. Il est composé de six couches concentriques de détecteurs en silicium. Ensuite se trouve la Time Projection Chamber (TPC). Elle mesure les traces des particules chargées de bas  $p_T$ , et permet d'identifier les particules via leur perte d'énergie dans la chambre. Elle est composée d'un cylindre rempli de gaz où un fort champ électrique est appliqué. Aux extrémités du cylindre est placée l'électronique de lecture. Autour de la TPC est placé le Transition Radiation Detector (TRD), qui permet d'identifier les électrons de  $p_T$  intermédiaire. Le TRD identifie les particules en mesurant le rayonnement de transition causé par les particules traversant le détecteur. Le detector de temps de vol (TOF) est utilisé pour détecter les particules chargées d'impulsion moyenne. L'identification se fait en mesurant le temps que mettent les particules à voyager depuis le point d'interaction jusqu'au détecteur. Le High Momentum Particle Identifier (HMPID) est utilisé pour détecter les particules chargées de haut  $p_T$ . Il est composé de détecteurs

Cherenkov et n'occupe qu'une partie du tonneau central en termes de couverture azimutale. Enfin, il y a deux calorimètres électromagnétiques, le PHOS, qui est utilisé pour détecter les photons, et l'EMCal, composé de deux sous-détecteurs, l'EMCal et le DCAL, utilisés pour détecter les photons, les électrons et les pions neutres.

Les détecteurs à petits angles sont utilisés pour caractériser les collisions. Le Zero Degree Calorimeter (ZDC), composé de deux sous-stations situées de part et d'autre du point d'interaction, est utilisé pour déterminer le nombre de nucléons participants lors d'une collision et pour rejeter les collisions satellites lors de collisions pp et Pb – Pb. Le Photon Multiplicity Detector (PMD) est placé dans la direction arrière et est utilisé pour mesurer la distribution des photons afin de déterminer le plan de réaction. Le Forward Multiplicity Detector (FMD) est utilisé pour déterminer la multiplicité des particules chargées. Il est composé de trois stations, deux placées dans la direction avant et une placée dans la direction arrière. Le V0 est composé de deux sous-stations, V0A et V0C, placées de part et d'autre du point d'interaction. Le V0 est utilisé comme système de déclenchement (trigger) de biais minimum, sert pour mesurer la centralité d'une collision et est utilisé pour rejeter les interactions faisceau-gaz. Enfin, le T0 est également composé de deux sous-stations placées de part et d'autre du point d'interaction. Il sert pour fournir un temps de départ au TOF pour mesurer le temps de vol des particules et pour mesurer la position du vertex.

Le spectromètre à muons est utilisé pour identifier les muons dans la région en pseudo-rapacité  $-4.0 < \eta < -2.5$ . Il est composé d'un absorbeur frontal qui sert à rejeter les hadrons, cinq stations de tracking utilisées pour reconstruire la trajectoire des particules, un aimant pour mesurer l'impulsion des particules, d'un autre absorbeur servant de filtre à muons puis de deux stations de trigger. De plus, un autre absorbeur est situé autour du tube faisceau afin de protéger les chambres.

Les stations de tracking sont composées de chambres à fils : chaque chambre contient un plan d'anode et deux plans cathode, de part et d'autre du plan d'anode. Les chambres sont remplies de gaz et utilisent le principe d'avalanche pour détecter le passage des particules. Les deux plans cathode sont segmentés avec des pistes de lectures afin de fournir un signal de sortie en deux dimensions. Les stations de tracking utilisent différentes configurations : les deux premières stations, situées avant l'aimant, utilisent une configuration en quadrants, à cause de la grande multiplicité des particules près de l'absorbeur. La troisième station, située dans l'aimant, ainsi que les stations quatre et cinq, situées après l'aimant, utilisent des chambres rectangulaires disposées en damier.

Les stations de trigger utilisent des *Resistive Plate Chambers* (RPC), qui sont composées d'électrodes en bakélite séparées par un gaz, avec un important champ électrique appliqué entre les électrodes. Le passage d'une particule dans le gaz déclenche un phénomène d'avalanche qui permet de générer un signal. Le trigger permet d'effectuer une sélection sur l'impulsion transverse des muons. En effet, la déviation des particules par l'aimant est fonction de leur impulsion transverse  $p_T$ , par conséquent en comparant la trajectoire des particules dans le trigger par rapport à leur trajectoire supposée si elles avaient une impulsion infinie (trajectoire droite), il est possible de déterminer leur  $p_T$ , et par conséquent de sélectionner les muons avec une impulsion suffisante afin de rejeter un maximum de bruit de fond tout en conservant le maximum de muons issus des résonances d'intérêt.

Afin de reconstruire les particules dans le spectromètre à muons, on identifie en premier lieu les pistes adjacentes sur lesquelles une charge a été déposée et correspondant au passage de la même particule (clusters). La reconstruction commence par les chambres 4 et 5 du tracking, plus éloignées de l'absorbeur et moins affectées par le bruit de fond. Les clusters obtenus dans les différentes chambres sont ensuite associés afin de déterminer des trajectoires possibles, puis celles-ci sont extrapolées vers la station 3 et les traces ne correspondant à aucun cluster dans la troisième station, ou sortant de l'acceptance géométrique du spectromètre, sont rejetées. Le procédé est reproduit pour la station 2 puis la station 1. De plus, la correspondance entre les traces reconstruites dans le tracking et dans le trigger est effectuée, afin de rejeter le maximum de bruit de fond.

La gestion des triggers dans ALICE est assurée par le *Central Trigger Processor* (CTP). Il reçoit les informations de la part des détecteurs participant à la sélection des événements, et si ceux-ci passent les critères requis par au moins un des triggers, il envoie un signal afin qu'ils soient enregistrés. La CTP possède trois niveaux de trigger, L0, L1 et L2, en fonction de la vitesse de réponse de détecteurs. Les signaux de sortie sont ensuite organisés en classe de trigger, qui se composent d'un niveau de trigger ainsi que d'un ou plusieurs détecteurs utilisés comme sortie. Par exemple, le trigger de biais minimum CINT est défini comme une coïncidence temporelle entre des signaux reçus dans chacune des deux stations du V0.

L'enregistrement des événements choisis par le CTP est effectué par le système d'acquisition de données (DAQ) qui doit gérer la bande passante accordée aux différents détecteurs, en essayant d'enregistrer le maximum d'événements dont les triggers sont très fréquents tout en ménageant un espace suffisant pour les triggers d'événements rares. Lorsque le CTP donne

le signal, les détecteurs envoient leurs données à la DAQ, qui collecte les données lues par les détecteurs de ALICE, avant de les transférer vers un système de stockage permanent.

### 3. Mesure du facteur de modification nucléaire du $\psi(2S)$

Avec les données collectées par le spectromètre à muons, l'objectif est de mesurer la production de  $\psi(2S)$ . Les données utilisées proviennent des collisions Pb – Pb enregistrées par ALICE en décembre 2015 à une énergie par collisions nucléon-nucléon dans le référentiel du centre de masse de  $\sqrt{s_{NN}} = 5.02$  TeV. Afin de quantifier les effets du QGP sur la production de  $\psi(2S)$  on mesure le facteur de modification nucléaire  $R_{AA}$ , qui est défini comme le rapport entre la production de  $\psi(2S)$  dans des collisions Pb – Pb et la production de  $\psi(2S)$  dans des collisions pp, normalisée par le nombre de collisions binaires. Si les collisions Pb – Pb étaient une simple superposition de collisions pp, sans effet du plasma, alors on observerait  $R_{AA} = 1$ . De la même façon, l'observation d'une valeur de  $R_{AA} \neq 1$  permet de mettre en évidence la présence d'effets nucléaires. Explicitement, le facteur de modification nucléaire s'exprime :

$$R_{AA}^{\psi(2S)} = \frac{N_{\psi(2S)}}{\text{BR}_{\psi(2S) \rightarrow \mu^+ \mu^-} \times (A\varepsilon) \times N_{\text{MB}} \times T_{AA} \times \sigma_{\psi(2S)}^{pp}}$$

où  $N_{\psi(2S)}$  est le nombre de particules mesurées pas le détecteur,  $\text{BR}_{\psi(2S) \rightarrow \mu^+ \mu^-}$  est le rapport d'embranchement du canal de décroissance dimuon,  $A\varepsilon$  est le coefficient prenant en compte l'acceptance et l'efficacité du détecteur,  $N_{\text{MB}}$  est le nombre d'évènements de biais minium équivalent au nombre d'évènements dimuons passant la condition de trigger,  $T_{AA}$  est la fonction de recouvrement nucléaire et  $\sigma_{\psi(2S)}^{pp}$  est la section efficace de production dans des collisions pp.

La fonction de recouvrement nucléaire  $T_{AA}$  est un paramètre relié à la centralité de la collision. La centralité d'un évènement est définie comme le pourcentage d'évènements avec une multiplicité supérieure à celle de l'évènement considéré. Cette multiplicité est mesurée avec le V0, et est définie comme la somme de l'amplitude mesurée dans les deux stations du V0. Cette amplitude est ensuite ajustée avec une distribution binomiale négative d'après le modèle de Glauber [30]. Cela permet de définir dans le

cadre de ce modèle la distance entre le centre des noyaux  $b$ , le nombre de nucléons participants  $N_{\text{part}}$ , le nombre de collisions binaires  $N_{\text{coll}}$ , ainsi que la fonction de recouvrement nucléaire  $T_{AA}$ , qui définit la surface pour laquelle un nucléon d'un des noyaux participant à la collision est susceptible d'interagir avec un nucléon du second noyau. Pour un évènement central (petites valeurs de centralité), la distance  $b$  est petite, et  $N_{\text{part}}$ ,  $N_{\text{coll}}$  et  $T_{AA}$  sont grands. A l'inverse pour un évènement périphérique (grandes valeurs de centralité),  $b$  est grand et  $N_{\text{part}}$ ,  $N_{\text{coll}}$  et  $T_{AA}$  sont petits.

Le nombre de  $\psi(2S)$ ,  $N_{\psi(2S)}$ , est mesuré à partir des muons ayant passé la condition trigger du spectromètre à muons. Avant de procéder à la mesure, il est nécessaire de sélectionner les traces afin de retirer le plus de bruit de fond possible. Pour cela les différents runs sont soumis à une procédure de *Quality Assurance* (QA) afin de vérifier que les conditions de prise de données étaient bonnes. Sont ensuite appliqués plusieurs critères permettant de sélectionner les évènements correspondant à une collision entre noyaux des paquets principaux, et à éliminer les interactions entre le faisceau et le gaz dans le tube. Cette sélection est effectuée en regardant les temps pour lesquels des évènements sont mesurés dans les deux stations du V0 : les interactions faisceau-gaz n'ayant généralement pas lieu près du point d'interaction, les temps mesurés pour ces évènements sont décalés par rapport à ce qui est attendu pour une collision noyau-noyau. De la même façon, le ZDC est utilisé pour rejeter les interactions entre le paquet de noyaux principal et les paquets satellites.

Une fois les évènements sélectionnés, des critères supplémentaires sont appliqués aux trajectoires des muons candidats. La pseudo-rapacité des muons doit être contenue dans l'acceptance du détecteur,  $-4.0 < \eta < -2.5$ . La rapidité de la paire de muons doit être dans l'intervalle  $2.5 < y < 4.0$ . Les traces trop proches du centre de l'absorbeur sont rejetées car elles ont subi trop d'interactions dans l'absorbeur. Les traces dans le tracker doivent avoir une correspondance dans le trigger. Enfin ne sont considérées que les paires de muons de signe opposé, car ce sont les seules qui peuvent éventuellement correspondre à la décroissance d'un quarkonia.

Avec les paires de muons choisies, on forme le spectre de masse invariante, qui donne le nombre de dimuons en fonction de leur masse. Dans ce spectre il est possible d'identifier un pic autour de  $3.1 \text{ GeV}/c$ , correspondant au  $J/\psi$ . Un continuum décroissant avec la masse est également visible. Il correspond principalement au bruit de fond combinatoire. Le pic correspondant au  $\psi(2S)$  est complètement invisible à l'oeil nu dans des collisions centrales, et à peine visible dans des collisions périphériques.

Afin de déterminer le nombre de  $J/\psi$  et de  $\psi(2S)$ , le nombre de particules dans les pics est "compté". Pour cela, on ajuste plusieurs fonctions décrivant le signal et le bruit de fond au spectre de masse invariante mesuré. Il existe deux méthodes différentes pour effectuer cet ajustement. La première consiste à faire l'ajustement directement sur le spectre de masse invariante. Le signal est ajusté avec une fonction pseudo-gaussienne, la même étant utilisé pour le  $J/\psi$  et le  $\psi(2S)$ . Le bruit de fond est décrit avec une fonction *ad hoc*. La deuxième méthode consiste à soustraire le bruit de fond combinatoire avant d'effectuer l'ajustement, en utilisant les données plutôt qu'une fonction d'ajustement pour décrire le bruit de fond combinatoire. Un bruit de fond artificiel est formé en "mélangeant" des muons provenant d'événements différents afin de former des paires décorréelées : c'est la méthode du "mélange d'événements". L'avantage est que l'on peut mélanger autant de paires de muons que souhaité afin de rendre l'erreur statistique de ce bruit de fond artificiel négligeable devant l'erreur statistique des données. Une fois le bruit de fond mélangé normalisé aux données, il est soustrait au spectre de masse invariante mesuré. Le spectre restant est ensuite ajusté avec des pseudo-gaussiennes pour le signal, et une fonction décrivant le bruit de fond restant.

Les fonctions utilisées pour le signal sont la fonction CB2 et la fonction NA60, qui sont des fonctions avec un coeur gaussien et des queues dont la décroissance est plus lente que celles d'une fonction Gaussienne. Ces queues permettent de prendre en compte les effets dus à la résolution des détecteurs, la possible dépendance en impulsion et en rapidité de la résolution en masse invariante, les éventuelles erreurs dues à l'alignement des détecteurs, et dans le cas de la queue à basse masse, la perte d'énergie dans l'absorbeur et la décroissance radiative des charmonia. Afin de faciliter la convergence de l'ajustement, les paramètres des queues sont fixés. Le signal du  $\psi(2S)$  étant du même ordre de grandeur que la fluctuation statistique du bruit de fond, la masse et la largeur de la fonction d'ajustement du  $\psi(2S)$  fixées à celles utilisées pour la fonction du  $J/\psi$ , et les paramètres des queues sont les mêmes que ceux utilisés pour le  $J/\psi$ . Cela laisse comme paramètres libres : l'amplitude, la masse et la largeur du  $J/\psi$ , et l'amplitude du  $\psi(2S)$ . Pour la fonction de bruit de fond, tous les paramètres sont laissés libres. Des exemples d'ajustements sont montrés sur la Figure 4.

Afin de déterminer l'incertitude systématique liée à l'extraction du signal, différents tests sont réalisés en variant les conditions de l'ajustement. Chaque test est une combinaison entre une fonction décrivant le signal, une fonction décrivant le bruit de fond, un jeu de paramètres de queues, un domaine en masse pour l'ajustement, et une valeur du rapport entre la largeur

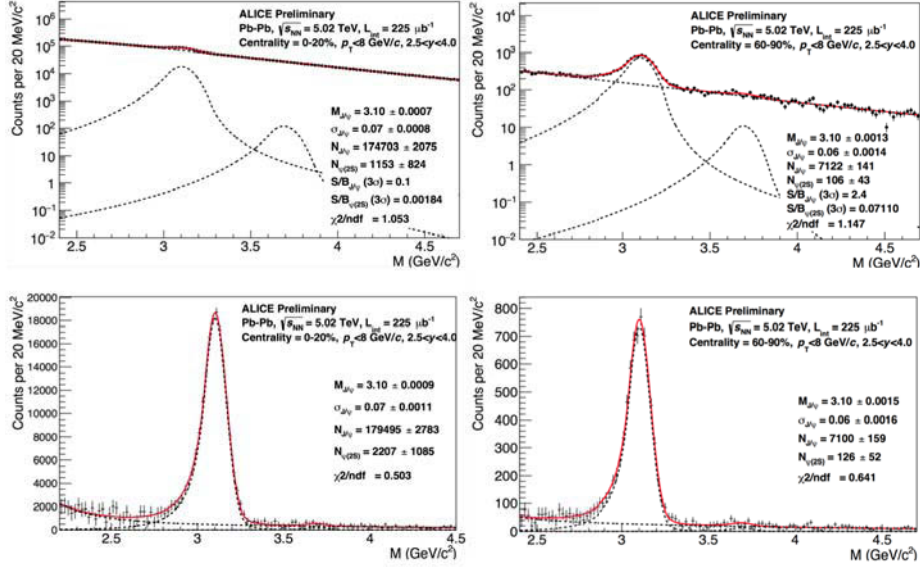


FIGURE 4: Exemple d’ajustements directs (haut) et après soustraction du bruit de fond (bas). La colonne de gauche correspond à l’intervalle en centralité 0-20%, celle de droite à l’intervalle 60-90%.

pour la fonction du  $J/\psi$  et celle du  $\psi(2S)$ . La fonction signal peut être la CB2 ou la NA60. La fonction de bruit de fond est une fonction ”pseudo-gaussienne”, pour laquelle la largeur varie avec la masse invariante, ou un rapport de polynômes pour l’ajustement direct, et une somme d’exponentielles pour l’ajustement après soustraction du bruit de fond. Les paramètres des queues sont soit déterminés à partir de simulations Monte Carlo, soit à partir d’un ajustement sur les données obtenues pour des collisions pp à une énergie de  $\sqrt{s} = 13$  TeV [31]. Au total 56 tests sont effectués. Le nombre de  $\psi(2S)$  extrait est la moyenne des résultats des différents tests, l’incertitude statistique est la moyenne des incertitudes statistiques des différents tests, et l’incertitude systématique est l’écart-type entre les valeurs des différents tests.

Dans l’intervalle en centralité 0-90%, le nombre de  $\psi(2S)$  extrait est  $N_{\psi(2S)} = 2024 \pm 1043$  (stat)  $\pm 740$  (syst). Le rapport entre le nombre de  $\psi(2S)$  et le nombre de  $J/\psi$  produits est :  $0.007 \pm 0.004$  (stat)  $\pm 0.0002$  (syst). A cause du faible nombre de  $\psi(2S)$  produits, si l’on considère le nombre de  $\psi(2S)$  extrait en fonction de la centralité, seulement quatre intervalles

peuvent être considérés : 0-20%, 20-40%, 40-60%, et 60-90%. Pour les intervalles 20-40% et 40-60%, le nombre extrait est compatible avec zéro dans la limite de l'incertitude statistique, par conséquent pour ces intervalles, un intervalle de confiance à 95% sera utilisé au lieu de la valeur directe.

Le produit de l'acceptance et de l'efficacité du détecteur  $A\varepsilon$  est un coefficient prenant en compte le fait qu'il ne couvre qu'une partie du domaine angulaire (acceptance) et que le détecteur n'est pas parfaitement efficace dans la détection de muons. Ce coefficient est déterminé à l'aide de simulations Monte-Carlo. Les particules sont générées en utilisant des distributions en  $p_T$  et en rapidité basées sur les données. On les force ensuite à décroître en deux muons, et la trajectoire de ces muons dans les détecteurs de ALICE est simulée à l'aide d'un modèle GEANT3 [32], qui décrit les interactions entre les particules et la matière dans les détecteurs et qui reproduit de façon réaliste les performances de ces détecteur. Les trajectoires sont ensuite reconstruites et le signal est extrait des simulations en appliquant les mêmes conditions que sur les données. L'acceptance×efficacité est ensuite définie comme le rapport entre le nombre de particules reconstruites et le nombre de particules simulées. Dans des collisions Pb – Pb, une particularité est que les particules simulées sont insérées dans un événement de biais minimum, afin de reproduire de façon plus réaliste le grand nombre de particules produites en même temps que celle à laquelle on s'intéresse, et dont la présence est susceptible de dégrader la qualité de la reconstruction des trajectoires. L'acceptance×efficacité est calculée pour chaque run, et pour obtenir l' $A\varepsilon$  totale, une moyenne est faite en prenant en compte des poids correspondant au nombre de  $J/\psi$  extrait run par run, puis au nombre de  $J/\psi$  extrait par intervalle en centralité, ainsi qu'un poids prenant en compte les différences entre les distributions en fonction de la centralité. Les poids utilisés pour le  $J/\psi$  sont également utilisés pour le calcul de l' $A\varepsilon$  du  $\psi(2S)$  car le nombre de  $\psi(2S)$  extrait est trop faible pour pouvoir définir ces poids directement. L'acceptance×efficacité du  $\psi(2S)$  dans l'intervalle en centralité 0-90% est  $0.1738 \pm 0.0003$ .

Les incertitudes systématiques sur l'acceptance×efficacité proviennent des incertitudes sur les distributions en  $p_T$  et rapidité utilisées pour les simulations Monte-Carlo, des incertitudes sur l'efficacité de reconstruction, des incertitudes sur l'efficacité de trigger et des incertitudes sur la correspondance entre les traces dans le tracker et les traces dans le trigger. Les incertitudes sur le tracking sont évaluées en comparant des simulations réalistes aux données, elles valent environ 3% dans l'intervalle 0-90%. Les incertitudes sur le trigger proviennent de deux sources différentes : l'incertitude sur la

réponse du trigger en  $p_T$ , qui est évaluée en changeant la forme de la réponse dans les simulations, et l'efficacité intrinsèque du trigger évaluée avec des simulations. L'incertitude sur le trigger est de 3.6% dans l'intervalle 0-90%. L'incertitude sur les distributions en  $p_T$  et rapidité est évaluée en changeant la forme des distributions dans les simulations. La valeur évaluée en 2011 lors des collisions Pb – Pb à une énergie de  $\sqrt{s_{NN}} = 2.76$  TeV est réutilisée ici, et correspond à 3% dans l'intervalle 0-90%.

Le nombre  $N_{MB}$ , qui est le nombre d'évènements de biais minimum équivalent au nombre d'évènements dimuons passant le trigger  $N_{MUL}$ , est calculé à l'aide d'un facteur de normalisation,  $N_{MB} = F_{norm} \cdot N_{MUL}$ . Le facteur  $F_{norm}$ , qui est la probabilité inverse d'avoir un évènement dimuon parmi un évènement de biais minimum, est calculé avec différentes méthodes. Chaque méthode implique le calcul du facteur d'empilement (pile-up), qui prend en compte les cas où plusieurs collisions sont enregistrées dans le même évènement.

La première méthode utilisée consiste à regarder la fraction d'évènements passant la condition du trigger dimuon parmi les évènements de biais minimum. La seconde méthode est similaire à la première mais utilise un trigger intermédiaire : il s'agit de calculer la fraction d'évènements satisfaisant la condition de trigger dimuon parmi les évènements satisfaisant la condition de trigger muon seul, multiplié par la fraction d'évènements satisfaisant la condition de trigger muon seul parmi les évènements de biais minimum. Cette méthode est utilisée quand le nombre d'évènements de biais minimum est faible, du fait que seule une partie de ces évènements est enregistrée, pour des raisons de bande passante limitée. La troisième méthode consiste à calculer le taux de comptage relatif entre le trigger de biais minimum et le trigger dimuon. Dans l'intervalle en centralité 0-90%, la valeur du facteur de normalisation est  $F_{norm} = 11.84 \pm 0.06$ , où l'erreur est principalement dominée par l'incertitude systématique, qui prend en compte les différences entre les méthodes. En fonction de la centralité, le facteur de normalisation est  $F_{norm}^i = F_{norm} \cdot \Delta Cent^i$ , où  $\Delta Cent^i$  est la fraction de la section efficace d'interaction inélastique d'un intervalle en centralité donné par rapport à l'intervalle 0-90%.

La section efficace de production de  $\psi(2S)$  dans des collisions pp à  $\sqrt{s} = 5$  TeV,  $\sigma_{pp}$ , est évaluée à l'aide de données enregistrées dans ces conditions pendant quelques jours avant les collisions Pb – Pb. Cette section efficace s'exprime :

$$\sigma_{pp}^{\psi(2S)} = \frac{1}{L_{int}} \frac{N_{\psi(2S)}}{\text{BR}_{\psi(2S) \rightarrow \mu^+ \mu^-} \cdot A\varepsilon}$$

où  $N_{\psi(2S)}$  est le nombre de  $\psi(2S)$  extrait,  $L_{int}$  est la luminosité intégrée,  $\text{BR}_{\psi(2S) \rightarrow \mu^+ \mu^-}$  est le rapport d'embranchement pour la décroissance du  $\psi(2S)$  en deux muons et  $A\varepsilon$  est l'acceptance  $\times$  efficacité du détecteur dans des collisions pp.

La luminosité intégrée est évaluée grâce à la technique de van der Meer [33], et vaut  $L_{int}^{pp} = 106.3 \pm 2.2 \text{ nb}^{-1}$ . Le nombre de  $\psi(2S)$  est extrait en utilisant les mêmes sélections pour les traces que pour les collisions Pb – Pb et les mêmes techniques pour les ajustements, ainsi que les mêmes tests pour l'évaluation de l'incertitude systématique, hormis ceux avec soustraction du bruit de fond. Le mélange d'évènements n'est pas utilisé dans des collisions pp, car le rapport signal sur bruit est beaucoup plus grand que dans des collisions Pb – Pb. Le nombre total de  $\psi(2S)$  extrait est  $N_{\psi(2S)} = 158 \pm 34 \pm 15$ . Le produit de l'acceptance et de l'efficacité dans des collisions pp est évaluée de façon similaire à ce qui est fait dans des collisions Pb – Pb, mais les évènements ne sont pas insérés dans des collisions de biais minimum, car l'occupation du détecteur est plus faible et n'affecte que de façon négligeable l'efficacité de reconstruction des trajectoires. L'acceptance  $\times$  efficacité moyenne pour le  $\psi(2S)$  est  $A\varepsilon = 0.2579 \pm 0.0003$ .

La section efficace de production est  $\sigma_{pp}^{\psi(2S)} = 0.72 \pm 0.16 \pm 0.06 \text{ } \mu\text{b}$ . Cependant, du fait que la prise de données dans des collisions pp à une énergie de collision de  $\sqrt{s} = 5 \text{ TeV}$  fut très brève, le nombre de  $\psi(2S)$  extrait est petit, ce qui a pour conséquence que l'incertitude sur la section efficace de production est grande, autour de 24%. Dans ces conditions, il peut être préférable d'utiliser une valeur extrapolée à partir des mesures à des énergies de collision plus élevées, où la quantité de données disponible est bien plus importante, ce qui permet de diminuer les incertitudes statistiques. En se basant sur les mesures dans des collisions pp à des énergies de  $\sqrt{s} = 5, 7, 8$  et  $13 \text{ TeV}$ , le rapport entre les sections efficaces de production du  $\psi(2S)$  et  $J/\psi$  apparaît constant en fonction de l'énergie dans la limite des incertitudes. Il est donc possible d'extrapoler la valeur de ce rapport à  $\sqrt{s} = 5 \text{ TeV}$  en faisant la moyenne des mesures du rapport aux différentes énergies pondérée par leurs incertitudes respectives. En utilisant la section efficace de production du  $J/\psi$  dans des collisions pp à  $\sqrt{s} = 5 \text{ TeV}$ , on peut alors calculer la valeur extrapolée de la section efficace du  $\psi(2S)$  à  $\sqrt{s} = 5 \text{ TeV}$ , qui vaut  $\sigma_{pp}^{\psi(2S)} = 0.84 \pm 0.07$  et possède donc une incertitude nettement inférieure à celle de la mesure directe. Cependant, l'utilisation d'une valeur extrapolée introduit de nouvelles corrélations entre les mesures du  $J/\psi$  et du  $\psi(2S)$ , par conséquent, la valeur utilisée dans cette analyse est celle mesurée dans

des collisions pp à  $\sqrt{s} = 5$  TeV.

Le facteur de modification nucléaire dans l'intervalle en centralité 0-90% est  $R_{AA} = 0.2187 \pm 0.1123$  (stat)  $\pm 0.0963$  (syst). Pour considérer l'évolution du  $R_{AA}$  en fonction de la centralité, il faut calculer les intervalles de confiance à 95% pour les intervalles où le signal est compatible avec zéro.

La méthode utilisée pour déterminer ces intervalles de confiance est la méthode CLs [34, 35]. Dans cette méthode, il est supposé que le bruit de fond est parfaitement connu et l'hypothèse porte sur le signal. Etant donné une mesure expérimentale, une hypothèse est faite sur le signal, puis une série de pseudo-expériences est effectuée sous cette hypothèse *signal+bruit de fond*. Ces pseudo-expériences sont triées en fonction de leur probabilité de correspondre à la mesure expérimentale à l'aide d'un test statistique, ce qui définit une fonction de distribution de probabilité (pdf) pour l'hypothèse *signal+bruit de fond*. L'intervalle de confiance  $CL_{s+b}$  sur l'hypothèse *signal+bruit de fond* est définie comme la probabilité étant donné l'hypothèse *signal+bruit de fond* pour le test statistique d'être inférieur ou égal à la valeur correspondant à la mesure expérimentale :  $CL_{s+b} = P_{s+b}(X \leq X_{obs})$ . L'hypothèse sur le signal est exclue à 95% si  $CL_{s+b} \leq 0.05$ .

Il est également possible de définir un intervalle de confiance  $CL_b = P_b(X \leq X_{obs})$  pour l'hypothèse *bruit de fond seul*, où l'on suppose qu'il n'y a pas de signal. Le CLs est ensuite défini comme le rapport de ces deux intervalles de confiance, et on dira qu'une hypothèse sur le signal est exclue à 95% si  $CLs = CL_{s+b}/CL_b \leq 0.05$ . Cette normalisation par l'hypothèse *bruit de fond seul* permet d'être conservatif sur les valeurs exclues, et protège des cas où le bruit de fond mesuré expérimentalement est inférieur au bruit de fond attendu, ce qui pourrait provoquer une exclusion à tort de certaines valeurs du signal.

Le choix du test statistique qui trie les pseudo-expériences est donc important dans la méthode CLs. D'après le lemme de Neyman-Pearson [36], le test du rapport de vraisemblance  $Q = L(data|s+b)/L(data|b)$  est le meilleur choix possible. En supposant que les probabilités pour le signal et le bruit de fond suivent une loi de Poisson, on peut exprimer le logarithme du rapport de vraisemblance comme  $q = -2 \ln(Q) = 2(s - n \cdot \ln(1 + \frac{s}{b}))$  où  $s$  est l'hypothèse faite sur le signal,  $b$  est le bruit de fond, supposé connu, et  $n$  est le résultat de l'expérience, qu'il s'agisse des données mesurées ou des pseudo-expériences simulées. Il est alors possible de définir une distribution  $q_{s+b}$ , correspondant à l'hypothèse *signal+bruit de fond*, et une distribution  $q_b$ , correspondant à l'hypothèse *bruit de fond seul*. Ces distributions sont

comparées à la valeur  $q_{obs}$  correspondant à la mesure expérimentale, afin de calculer la valeur de CLs correspondant à l'hypothèse de signal testée. Ce procédé est appliqué pour les hypothèses sur le signal allant de 0 jusqu'à trouver la valeur pour laquelle  $CL_s \leq 0.05$ , qui donne la limite de l'intervalle de confiance à 95%. Un exemple de recherche de valeur de la limite de l'intervalle de confiance à 95% est montré sur la Figure 5.

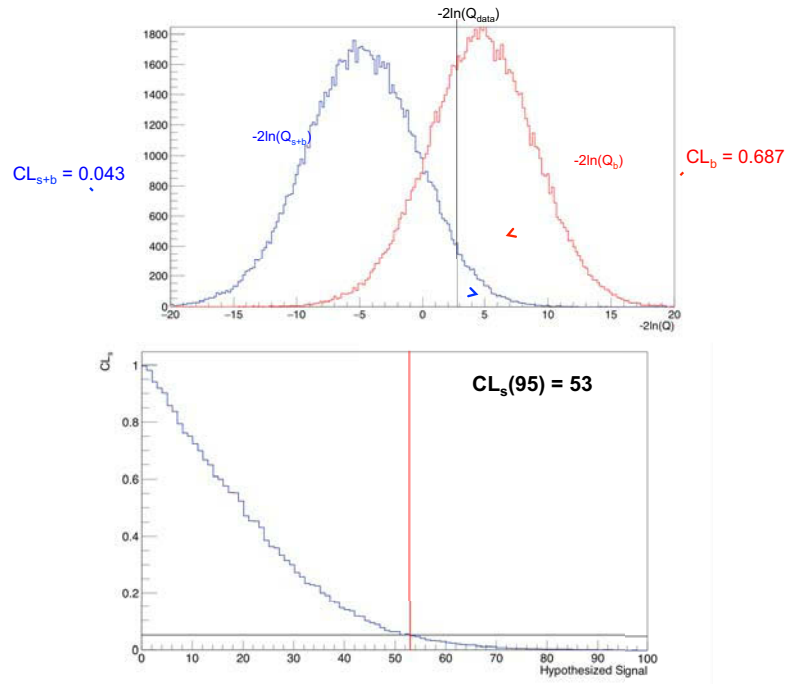


FIGURE 5: Haut : Exemple de distributions du logarithme du rapport de vraisemblance. Dans cet exemple  $s = 50$ ,  $b = 500$  et le nombre d'évènements observés est  $n_{data} = 510$ . La valeur correspondante est  $CL_s = 0.063$ , ce qui signifie que le signal  $s = 50$  n'est pas exclus avec 95% de confiance. Base : Recherche de la valeur limite pour laquelle  $CL_s = 0.05$ .

L'intervalle de confiance étant en soi un expression de l'incertitude sur la mesure, on ne peut citer une incertitude systématique pour le CLs. Afin de prendre en compte les incertitudes systématiques dans l'évaluation du CLs, on utilise la méthode hybride appelée bayésienne-fréquentiste [37]. Le principe de cette méthode est d'introduire un paramètre de nuisance  $\theta$ , dont les valeurs du signal  $s$  et  $b$  vont être fonction :  $s(\theta) = \bar{s} + \sigma_s \cdot \theta$  et  $b(\theta) =$

$\bar{b} + \sigma_b \cdot \theta$ , où  $\bar{s}$  et  $\bar{b}$  sont les valeurs moyennes du signal et du bruit de fond et  $\sigma_s$  et  $\sigma_b$  sont les incertitudes systématiques considérées pour le signal et le bruit de fond respectivement. Pour prendre en compte ces incertitudes, on définit le test statistique  $q$  avec les valeurs  $\sigma_s$  et  $\sigma_b$ , et avant chaque pseudo-expérience, une valeur aléatoire de  $\theta$  est tirée afin de déterminer  $s$  et  $b$ , et donc le nombre observé  $n$ .

Pour appliquer cette méthode à l'extraction du signal du  $\psi(2S)$ , le test statistique  $q$  est étendu à tous les intervalles en masse considérés, et s'écrit comme la somme des  $q_i$  dans chaque intervalle :  $q = \sum_{i=0}^{n_{intervalles}} q_i = \sum_{i=0}^{n_{intervalles}} 2(s_i - n_i \cdot \ln(1 + \frac{s_i}{b_i}))$ . Le signal  $s_i$  dans chaque intervalle est défini comme le nombre total de  $\psi(2S)$ , qui est l'hypothèse, multiplié par la valeur de la fonction signal du  $\psi(2S)$  normalisée en cet intervalle. Le bruit de fond  $b_i$ , supposé parfaitement connu grâce aux fonctions d'ajustement, est défini comme la valeur de bruit de fond "normal" additionné à la valeur de la fonction de signal du  $J/\psi$  en cet intervalle. Pour prendre en compte l'incertitude systématique sur le signal, la valeur moyenne des fonctions de signal du  $\psi(2S)$  et celle du bruit de fond sont définies comme la moyenne des fonctions obtenues lors de tous les différents tests pour l'extraction du signal afin de calculer  $s_i$  et  $b_i$ , et avant chaque pseudo-expérience, une des combinaisons de fonctions signal, de fonction de bruit de fond, d'intervalle en masse, et de jeu de paramètres de queues sont tirés aléatoirement pour définir valeurs de  $s(\theta)$  et  $b(\theta)$ .

Cependant, on ne souhaite pas un intervalle de confiance sur le signal du  $\psi(2S)$ , mais sur le facteur de modification nucléaire. Pour ce faire, le signal est écrit en fonction du facteur de modification nucléaire :

$$N_{\psi(2S)} = BR_{\psi(2S) \rightarrow \mu^+ \mu^-} \times (A\varepsilon) \times N_{MB} \times T_{AA} \times \sigma_{\psi(2S)}^{pp} \times R_{AA}^{hyp}$$

L'hypothèse est alors faite sur la valeur du  $R_{AA}$ , ce qui se traduit en une valeur sur le nombre de  $\psi(2S)$ , utilisée pour déterminer les CLs. L'inclusion des systématiques correspondant aux membres de l'expression précédente se fait en tirant une valeur aléatoire pour ces termes avant chaque pseudo-expérience comme décrit précédemment.

Une fois les intervalles de confiance pour le  $R_{AA}$  calculés pour les intervalles en centralité où le signal est compatible avec zéro, il est possible de voir l'évolution du  $R_{AA}$  du  $\psi(2S)$  en fonction de la centralité. Les résultats sont présentés sur la Figure 6. Il apparaît que le  $\psi(2S)$  est supprimé en présence d'un QGP, pour  $N_{part} > 70$ . Comparé au  $R_{AA}$  du  $J/\psi$ , il apparaît également que le  $\psi(2S)$  est plus supprimé que le  $J/\psi$  pour des valeurs de  $N_{part} > 70$ . La valeur correspondant à l'intervalle 60-90% est compatible avec celle du  $J/\psi$  et avec l'unité. Les effets de la production non-prompte sont évalués en

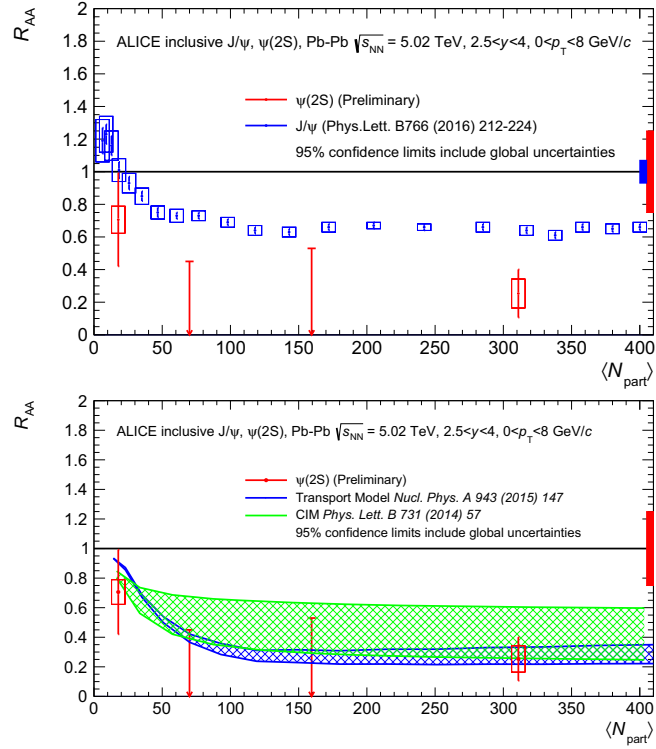


FIGURE 6: Haut : Facteur de modification nucléaire du  $\psi(2S)$  (rouge) comparé à celui du  $J/\psi$  (bleu). Bas : Facteur de modification nucléaire du  $\psi(2S)$  comparé à des modèles théoriques en fonction de  $N_{part}$ . Pour les intervalles où le signal ne peut pas être extrait, la limite à 95% de confiance est montrée. L'incertitude systématique globale est dessinée autour de l'unité. L'incertitude globale est incluse dans le calcul des intervalles de confiance.

faisant des suppositions extrêmes sur les  $\psi(2S)$  non-prompts. Si le  $R_{AA}$  des  $\psi(2S)$  non-prompt était égal à zéro, ce qui signifie que les  $\psi(2S)$  non-prompt sont complètement supprimés, alors le  $R_{AA}$  prompt serait 16% plus grand que le  $R_{AA}$  inclusif. Si le  $R_{AA}$  des  $\psi(2S)$  non-prompt était égal à un, alors le  $R_{AA}$  prompt serait entre 7% plus petit que le  $R_{AA}$  inclusif dans l'intervalle le plus périphérique et 47% plus petit dans l'intervalle le plus central.

Afin de quantifier la suppression du  $\psi(2S)$  relativement à celle du  $J/\psi$ , on s'intéresse au rapport simple, qui est le rapport des taux de production  $Y_{\psi(2S)}/Y_{J/\psi}$ , et le double rapport, qui est le rapport des facteurs de modifica-

tion nucléaire,  $R_{AA}^{\psi(2S)}/R_{AA}^{J/\psi}$ . Lorsqu'ils sont nécessaires, les intervalles de confiance sont calculés de la même manière que pour le  $R_{AA}$ , en écrivant le signal du  $\psi(2S)$  en fonction du rapport simple ou du rapport double.

Le rapport simple dans l'intervalle en centralité 0-90% est  $Y_{\psi(2S)}/Y_{J/\psi} = 0.0057 \pm 0.0029 \pm 0.0021$ . En fonction de la centralité, les résultats à une énergie de collision de  $\sqrt{s_{NN}} = 5.02$  TeV sont compatibles avec ceux à une énergie de collision de  $\sqrt{s_{NN}} = 2.76$  TeV.

Le double rapport est  $R_{AA}^{\psi(2S)}/R_{AA}^{J/\psi} = 0.335 \pm 0.172 \pm 0.122$  dans l'intervalle en centralité 0-90%, ce qui confirme que le  $\psi(2S)$  est plus supprimé que le  $J/\psi$ . En fonction de la centralité, les résultats sont compatibles avec les mesures du double rapport à une énergie de collision de  $\sqrt{s_{NN}} = 2.76$  TeV. De plus les résultats sont comparés avec les mesures de CMS à une énergie de collision de  $\sqrt{s_{NN}} = 5.02$  TeV. Les mesures de CMS ne sont que pour les charmonia prompts, et dans un domaine en rapidité adjacent. Cependant les résultats d'ALICE de CMS sont compatible dans la limite des incertitudes. Les résultats sont montrés sur la Figure 7.

Les résultats sont également comparés aux modèles théoriques décrits précédemment. Le modèle d'interaction avec les co-mover et le modèle de transport fournissent une prédiction théorique pour le  $R_{AA}$ , et le résultat est montré en Figure 6 bas. Dans les deux cas les données sont compatibles avec les modèles, mais les grandes incertitudes sur les mesures empêchent de tirer des conclusions plus contraignantes sur les modèles. Le modèle de hadronisation statistique fournit une prédiction pour le rapport simple. De même que pour les autres modèles, les données sont compatibles avec le calcul correspondant à ce modèle mais les grandes incertitudes empêchent de tirer de plus fortes conclusions.

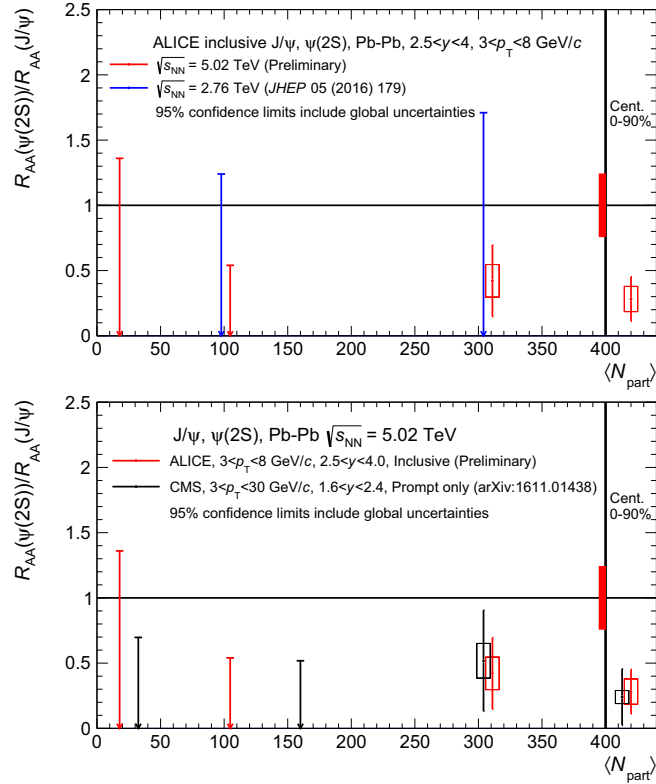


FIGURE 7: Double-rapport  $R_{AA}^{\psi(2S)}/R_{AA}^{J/\psi}$  en fonction de  $N_{part}$  comparé aux valeurs à  $\sqrt{s_{NN}} = 2.76$  TeV (Haut) et aux valeurs de CMS à  $\sqrt{s_{NN}} = 5.02$  TeV. Pour les intervalles où le signal ne peut pas être extrait, la limite à 95% de confiance est montrée. L'incertitude systématique globale est dessinée autour de l'unité. L'incertitude globale est incluse dans le calcul des intervalles de confiance. La valeur à  $N_{part} > 400$  correspond à la valeur intégrée en centralité (0-90%).

#### 4. Améliorations d'ALICE : estimation du volume de données du MID

Afin d'accroître la précisions des mesures et de permettre de nouvelles mesures jusqu'alors impossibles, ALICE prévoit une amélioration de ses détecteurs lors de l'arrêt du LHC en 2019-2020 [38]. L'objectif est de pouvoir enregistrer des données à un taux d'interaction de 50 kHz dans des collisions Pb – Pb lors de la reprise des collisions, ce qui est 5 fois plus que le taux maximum actuel. Avec l'augmentation du taux de collision et l'amélioration des détecteurs, il sera entre autres possible de mesurer les taux de production du  $J/\psi$  et du  $\psi(2S)$  plus précisément, de distinguer les particules promptes des non-promptes, de détecter des  $\psi(2S)$  photo-produits et d'affiner les mesures du flot elliptique du  $J/\psi$ .

Ces améliorations vont consister à remplacer, modifier les détecteurs existants ainsi que le système d'acquisition ou encore d'ajouter de nouveaux détecteurs. Le CTP sera amélioré pour pouvoir traiter les données enregistrées à ce nouveau taux d'interaction. Une nouvelle version de l'ITS sera installée à la place de l'actuelle. Un nouveau détecteur, le Muon Forward Tracker, sera ajouté devant le spectromètre à muons afin notamment de distinguer les particules promptes des non-promptes et améliorer le rapport signal sur bruit de fond pour le  $\psi(2S)$ . La TPC sera modifiée pour pouvoir soutenir des taux d'interaction plus élevés. Les chambres de tracking seront modifiées pour pouvoir fonctionner sans trigger. Le trigger du spectromètre à muons sera utilisé comme "muon identifier". Le T0, V0 et FMD seront remplacés par un nouveau détecteur, le Forward Interaction Trigger (FIT). Le TRD, TOF, et ZDC seront modifiés pour pourvoir supporter les taux d'interaction plus élevés.

Le Muon Trigger ne sera plus utilisé comme déclencheur, puisque tous les événements seront enregistrés. En revanche, il sera utilisé pour identifier les muons, et sera renommé Muon Identifier (MID). En outre, l'électronique de lecture sera modifiée pour prendre en compte les taux d'interaction plus élevés. Dans la nouvelle architecture, les cartes locales reçoivent le signal des pistes de lecture. Ce signal est ensuite transmis à l'une des cartes régionales, qui le transmettra ensuite à la *Common Read-out Unit* (CRU).

De plus, le mode de fonctionnement des RPC du trigger sera modifié pour pouvoir supporter le nombre de coups plus élevé et pour les protéger du vieillissement. Le nouveau mode de fonctionnement requiert un amplificateur. L'électronique frontale des RPC sera modifiée pour ajouter cet amplificateur.

L'une des questions soulevées par le changement d'architecture est de savoir si les câbles seront capables supporter le flux de données passant d'une carte locale à une carte régionale, et des cartes régionales à la CRU. Le volume de données qui transitera dans les câbles est évalué en se basant sur les collisions Pb – Pb à  $\sqrt{s_{NN}} = 5.02$  TeV. Les *scalers*, qui fournissent un comptage des événements dans les chambres de chaque plan du Muon Trigger toutes les 600 secondes, sont utilisés pour cette estimation. Pour le MID, la taille d'un événement varie entre 72 et 168 bits, selon le nombre de plans du MID touchés par la particule. Comme les *scalers* ne fournissent pas d'information sur la corrélation entre les coups, l'hypothèse conservatrice considérant que chaque coup est une trace indépendante est effectuée. Cela correspond à ne considérer que du bruit de fond et que chaque coup enregistré par les scalers correspond à 72 bits.

En considérant pour tous les runs des données dans des collisions Pb – Pb la carte locale avec le plus grand nombre de coups, il est possible d'estimer le volume de données maximum en fonction du taux d'interaction. On observe une tendance linéaire, et en extrapolant ces valeurs à 100 kHz (un facteur 2 de sécurité est appliqué), on obtient une valeur estimée du volume de donnée transitant d'une carte locale à une carte régionale de 20.3 Mbits/s. Les résultats sont montrés en Figure 8. Les câbles prévus ont une bande passante de 320 Mbits/s, ce qui est largement suffisante étant donné les hypothèses conservatrices qui sont faites.

La même opération est effectuée ensuite pour mesurer le volume de données entre une carte régionale et la CRU. On obtient une valeur extrapolée à 100 kHz de 3.6 Gbits/s. Les câbles prévus peuvent supporter 100 Gbits/s, ce qui est là encore amplement suffisant.

La même prédiction est faite en se basant sur les données pp à  $\sqrt{s} = 13$  TeV, mais les volumes de données sont 10 fois plus petits que ceux estimés pour les collisions Pb – Pb à  $\sqrt{s_{NN}} = 5.02$  TeV. Par conséquent, les technologies prévues ont une bande passante suffisante pour pouvoir transmettre les données des cartes locales aux cartes régionales et des cartes régionales à la CRU.

En conclusion, l'augmentation de l'énergie de collision jusqu'à  $\sqrt{s_{NN}} = 5.02$  TeV a permis de mesurer pour la première fois le  $R_{AA}$  du  $\psi(2S)$  jusqu'à  $p_T = 0$ . Les résultats sont en accord avec ceux de CMS pour des charmonia prompts et dans un domaine en rapidité différent. Les modèles théoriques sont compatibles avec les données, mais aucune conclusion plus forte ne

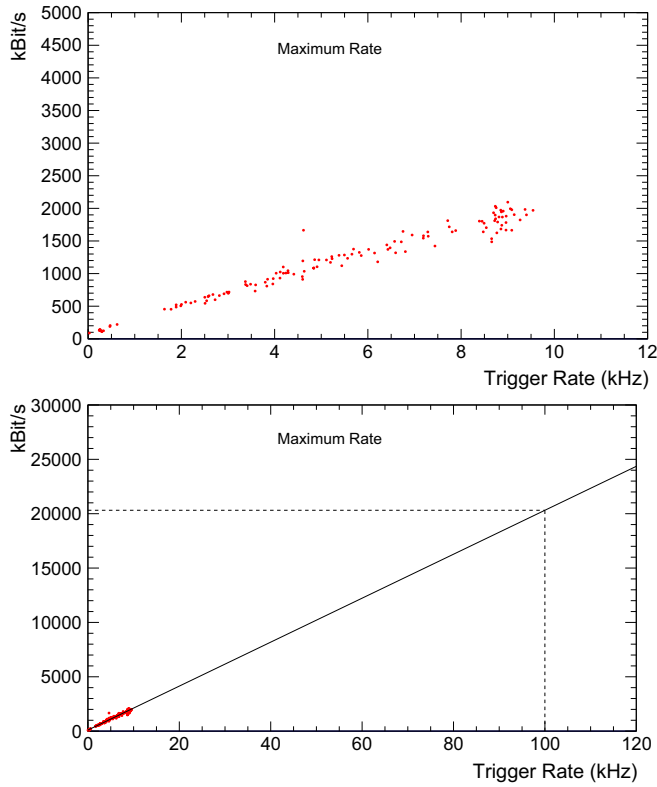


FIGURE 8: Volume de données en fonction de la fréquence de trigger pour tous les runs Pb – Pb. Les valeurs sont extrapolées à 100 kHz avec une fonction linéaire (bas).

peut être tirée à cause des grandes incertitudes. Afin de diminuer ces incertitudes, des améliorations de ALICE sont prévues, en particulier pour le Muon Trigger, qui deviendra un Muon Identifier. Afin de s'assurer que les technologies implémentées pourront supporter le volume de données prévu à un taux d'interaction de 50 kHz, une estimation du volume de données transitant dans le MID est effectuée. Les résultats montrent que même avec des grands facteurs de sécurité, la bande passante des connecteurs prévus est suffisamment grande.



# Bibliographie

- [1] David J. Gross and Frank Wilczek. **Ultraviolet Behavior of Non-Abelian Gauge Theories.** *Phys. Rev. Lett.*, 30 :1343–1346, Jun 1973. (Cited on page 1.)
- [2] H. David Politzer. **Reliable Perturbative Results for Strong Interactions?** *Phys. Rev. Lett.*, 30 :1346–1349, Jun 1973. (Cited on page 1.)
- [3] Berndt Müller. **Hadronic signals of deconfinement at RHIC.** *Nuclear Physics A*, 750(1) :84 – 97, 2005. Quark-Gluon Plasma. New Discoveries at RHIC : Case for the Strongly Interacting Quark-Gluon Plasma. Contributions from the RBRC Workshop held May 14-15, 2004. (Cited on page 1.)
- [4] Ulrich Heinz et al. **Exploring the properties of the phases of QCD matter - research opportunities and priorities for the next decade.** 2015. (Cited on page 2.)
- [5] A. Bazavov et al. **The chiral and deconfinement aspects of the QCD transition.** *Phys. Rev.*, D85 :054503, 2012. (Cited on page 2.)
- [6] T. Roser. **RHIC performance.** *Nuclear Physics A*, 698(1) :23 – 28, 2002. 15th Int. Conf. on Ultra-Relativistic Nucleus-Nucleus Collisions (Quark Matter 2001). (Cited on page 2.)
- [7] Lyndon Evans and Philip Bryant. **LHC Machine.** *JINST*, 3 :S08001, 2008. (Cited on page 2.)
- [8] J. D. Bjorken. **Highly relativistic nucleus-nucleus collisions : The central rapidity region.** *Phys. Rev. D*, 27 :140–151, Jan 1983. (Cited on page 2.)
- [9] R. Aaij et al. **Measurement of  $J/\psi$  production in pp collisions at  $\sqrt{s} = 7$  TeV.** *Eur. Phys. J.*, C71 :1645, 2011. (Cited on page 4.)

- [10] R Aaij et al. **Measurement of  $\psi(2S)$  meson production in pp collisions at  $\sqrt{s}=7$  TeV.** *Eur. Phys. J.*, C72 :2100, 2012. (Cited on page 4.)
- [11] Edmond L. Berger and D. Jones. **Inelastic photoproduction of  $J/\psi$  and  $\Upsilon$  by gluons.** *Phys. Rev. D*, 23 :1521–1530, Apr 1981. (Cited on page 4.)
- [12] Harald Fritzsche. **Producing heavy quark flavors in hadronic collisions - A test of quantum chromodynamics.** *Physics Letters B*, 67(2) :217 – 221, 1977. (Cited on page 4.)
- [13] G. Peter Lepage, Lorenzo Magnea, Charles Nakhleh, Ulrika Magnea, and Kent Hornbostel. **Improved nonrelativistic QCD for heavy-quark physics.** *Phys. Rev. D*, 46 :4052–4067, Nov 1992. (Cited on page 4.)
- [14] K. J. Eskola, H. Paukkunen, and C. A. Salgado. **EPS09 : A New Generation of NLO and LO Nuclear Parton Distribution Functions.** *JHEP*, 04 :065, 2009. (Cited on page 4.)
- [15] Edmond Iancu and Raju Venugopalan. **The Color glass condensate and high-energy scattering in QCD.** In *In \*Hwa, R.C. (ed.) et al. : Quark gluon plasma\* 249-3363*. 2003. (Cited on page 5.)
- [16] C. Gerschel and J. Hüfner. **A contribution to the suppression of the  $J/\psi$  meson produced in high-energy nucleus-nucleus collisions.** *Physics Letters B*, 207(3) :253 – 256, 1988. (Cited on page 5.)
- [17] T. Matsui and H. Satz.  **$J/\psi$  suppression by quark-gluon plasma formation.** *Physics Letters B*, 178(4) :416 – 422, 1986. (Cited on page 5.)
- [18] P. Braun-Munzinger and J. Stachel. **(Non)thermal aspects of charmonium production and a new look at  $J/\psi$  suppression.** *Phys. Lett.*, B490 :196–202, 2000. (Cited on page 5.)
- [19] E. G. Ferreira. **Charmonium dissociation and recombination at LHC : Revisiting comovers.** *Phys. Lett.*, B731 :57–63, 2014. (Cited on page 6.)
- [20] Xiaojian Du and Ralf Rapp. **Sequential Regeneration of Charmonia in Heavy-Ion Collisions.** *Nucl. Phys.*, A943 :147–158, 2015. (Cited on page 6.)
- [21] A. Andronic, P. Braun-Munzinger, and J. Stachel. **The Horn, the hadron mass spectrum and the QCD phase diagram : The Statistical model of hadron production in central nucleus-nucleus collisions.** *Nucl. Phys.*, A834 :237C–240C, 2010. (Cited on page 6.)

- [22] Roberta Araldi. **J/ $\psi$  production in p-A and A-A collisions at fixed target experiments.** *Nuclear Physics A*, 830(1) :345c – 352c, 2009. Quark Matter 2009. (Cited on page 6.)
- [23] A. Adare and others. **J/ $\psi$  suppression at forward rapidity in Au-Au collisions at  $\sqrt{s_{\text{NN}}} = 200$  GeV .** *Phys. Rev. C*, 84 :054912, Nov 2011. (Cited on page 6.)
- [24] Yan-Qing Ma, Kai Wang, and Kuang-Ta Chao. **J/ $\psi$ ( $\psi'$ ) production at the Tevatron and LHC at  $\mathcal{O}(\alpha_s^4 v^4)$  in nonrelativistic QCD.** *Phys. Rev. Lett.*, 106 :042002, 2011. (Cited on page 6.)
- [25] Jaroslav Adam et al. **Centrality dependence of  $\psi$ (2S) suppression in p-Pb collisions at  $\sqrt{s_{\text{NN}}} = 5.02$  TeV.** *JHEP*, 06 :050, 2016. (Cited on page 6.)
- [26] Jaroslav Adam et al. **Differential studies of inclusive J/ $\psi$  and  $\psi$ (2S) production at forward rapidity in Pb-Pb collisions at  $\sqrt{s_{\text{NN}}} = 2.76$  TeV.** *JHEP*, 05 :179, 2016. (Cited on page 7.)
- [27] Jaroslav Adam et al. **J/ $\psi$  suppression at forward rapidity in Pb-Pb collisions at  $\sqrt{s_{\text{NN}}} = 5.02$  TeV.** *Phys. Lett.*, B766 :212–224, 2017. (Cited on page 7.)
- [28] K. Aamodt et al. **The ALICE experiment at the CERN LHC.** *JINST*, 3 :S08002, 2008. (Cited on page 8.)
- [29] B. Abelev et al. **Performance of the ALICE Experiment at the CERN LHC.** *Int. J. Mod. Phys.*, A29 :1430044, 2014. (Cited on page 8.)
- [30] J. Adam et al. **Centrality dependence of the charged-particle multiplicity density at midrapidity in Pb-Pb collisions at  $\sqrt{s_{\text{NN}}} = 5.02$  TeV.** *Phys. Rev. Lett.*, 116(22) :222302, 2016. (Cited on page 12.)
- [31] Shreyasi Acharya et al. **Energy dependence of forward-rapidity J/ $\psi$  and  $\psi$ (2S) production in pp collisions at the LHC.** 2017. (Cited on page 15.)
- [32] R. Brun et al. *CERN Program Library Long Write-up W5013*, 1994. <http://wwwasd.web.cern.ch/wwwasd/geant/>. (Cited on page 16.)
- [33] S. van der Meer. **Calibration of the effective beam height in the ISR.** Technical Report CERN-ISR-PO-68-31. ISR-PO-68-31, CERN, Geneva, 1968. (Cited on page 18.)
- [34] A L Read. **Modified frequentist analysis of search results (the CL<sub>s</sub> method).** (CERN-OPEN-2000-205), 2000. (Cited on page 19.)

- [35] Thomas Junk. **Confidence level computation for combining searches with small statistics.** *Nucl. Instrum. Meth.*, A434 :435–443, 1999. (Cited on page 19.)
- [36] J. Neyman and E. S. Pearson. **On the Problem of the Most Efficient Tests of Statistical Hypotheses.** *Philosophical Transactions of the Royal Society of London A : Mathematical, Physical and Engineering Sciences*, 231(694-706) :289–337, 1933. (Cited on page 19.)
- [37] Robert D. Cousins and Virgil L. Highland. **Incorporating systematic uncertainties into an upper limit.** *Nucl. Instrum. Meth.*, A320 :331–335, 1992. (Cited on page 20.)
- [38] B Abelev and al. **Upgrade of the ALICE Experiment : Letter of Intent.** Technical Report CERN-LHCC-2012-012. LHCC-I-022. ALICE-UG-002, CERN, Geneva, Aug 2012. (Cited on page 25.)

# Introduction

The Quantum Chromo-Dynamics (QCD) is the theory that describes the strong interaction, which is the interaction between quarks and gluons. At normal temperature and pressure, quarks and gluons are confined in protons and neutrons and cannot be observed isolated. However models predict that under extreme conditions of temperature and matter density, the intensity of the strong interaction tends towards zero. This implies a phase transition between hadronized matter and a state of matter where the quarks and gluons are deconfined, called the Quark-Gluon Plasma (QGP).

Models predict that in the early stages of the Universe, a few microseconds after the Big Bang, quarks and gluons were in this deconfined state. With the expansion and cooling of the Universe, they hadronized. Understanding the properties of the QGP will be helpful in the comprehension of the formation of matter in the Universe. In the laboratory, it is possible to recreate the conditions of energy density necessary to the formation of the QGP by doing ultra relativistic heavy ions collisions in particle accelerators such as the Super Proton Synchrotron (SPS) at CERN, the Relativistic Heavy Ion Collider (RHIC) at the Brookhaven National Laboratory (BNL) and the Large Hadron Collider (LHC) at CERN.

The ALICE (A Large Ion Collider Experiment) collaboration at the LHC is dedicated to the study of the QGP by means of heavy ion collisions. The different types of detectors installed on the experiment allow to measure a large number of observables as a function of variables such as the centrality of the collision, the transverse momentum and the rapidity of the particles. These measurements give access to informations on the QGP and allow to test different models.

In particular the ALICE Muon Spectrometer is used to detect charmonia via their decay into two muons in the forward rapidity region. Charmonia,

such as the  $J/\psi$  and the  $\psi(2S)$ , are mesons composed of a charm quark and an anti-charm quark that are particularly interesting since they are produced at the very beginning of the collision and therefore go through the entire evolution of the medium. Models predict that the charmonium production is affected by the presence of a QGP, as the presence of free quarks and gluons prevents the charm quarks from binding because of the color screening effect.

In this thesis, the study of the  $\psi(2S)$  production in Pb – Pb collisions at center of mass energy per nucleon-nucleon collision  $\sqrt{s_{NN}} = 5.02$  TeV with the ALICE Muon Spectrometer will be presented.

In the first chapter, elements of the theoretical context are presented. An introduction to QCD and the phase diagram of the nuclear matter are presented, as well as the formation of a QGP by heavy ion collisions and the main observables used to characterize the QGP. The charmonium family is then discussed, including the charmonium production mechanisms and the effects expected in presence of a QGP, as well as the theoretical models describing the charmonium production in presence of a QGP.

In the second chapter, the ALICE detector is presented, with a description of all the sub-detectors, focusing on the elements composing the Muon Spectrometer.

In the third chapter, the analysis of  $\psi(2S)$  production is presented. In Pb – Pb collisions, this production is evaluated thanks to the nuclear modification factor, which is defined as the ratio of the  $\psi(2S)$  cross-section in Pb – Pb collision with respect to the cross-section in pp collision, normalized by the number of nucleon-nucleon collisions equivalent to one Pb – Pb collision. The first sections explain how the different terms entering the  $R_{AA}$  determination are evaluated. Then the method used to calculate confidence limits when the  $\psi(2S)$  signal is too small is described. Finally the results of the  $\psi(2S)$   $R_{AA}$  is presented, compared to the  $J/\psi$   $R_{AA}$  and to theoretical predictions.

In the fourth and final chapter, the future of the ALICE detector is discussed, presenting the upgrades that are planned for the next run of data taking. In particular the Muon Trigger will be repurposed into a Muon Identifier (MID) and the data flow that will be generated in the MID under the expected conditions of the next data taking run is evaluated.

## Chapter 1

# Introduction to the Quark-Gluon Plasma

The Quark-Gluon Plasma is a state of matter where quarks and gluons are deconfined. In the 1980s, this state was predicted by Quantum Chromo-Dynamics (QCD) [1], which is the theory describing the interactions involving quarks and gluons. It is expected to have been the state of the Universe in the early stages of its evolution, a few micro-seconds after the Big Bang [2, 3]. The first report of a QGP created experimentally was made at the Super Proton Synchrotron (SPS) at CERN in 2000 [4]. Since then, the QGP is also studied at the Brookhaven National Laboratory, on the Relativistic Heavy Ion Collider (RHIC) [5] and starting in 2009, at the Large Hadron Collider (LHC) at CERN [6].

In this chapter are presented some notions on the Standard Model of particle physics, focusing on QCD and the QGP formation through heavy ion collisions, as well as the probes to study it. Then the charmonium family and the theoretical models describing the production in the QGP are introduced. In the end an overview of the different main results obtained at the SPS, RHIC and LHC will be presented.

## 1.1 The Standard Model

### 1.1.1 An historical overview of particles discovery

The understanding of the elementary components of matter has progressed over time. The idea of atoms as elementary components of matter gained weight in the 19<sup>th</sup> century with the periodic table of elements, proposed in 1869. However in 1897, Joseph J. Thompson discovered the electron [7], identifying it as one of the components of the atoms. In 1911, Ernest Rutherford identified the atomic nuclei as the element where all the positive charge of the atom was concentrated [8]. In 1919, Rutherford identified the nuclei of hydrogen atoms and called it proton [9]. He proved that heavier nuclei were composed of protons. It is in 1932 that Chadwick discovered the neutron [10]. At that moment, the fundamental components of matter were believed to be the proton and neutron, composing the atomic nuclei and the electron.

However the discovery of the muon in 1937 [11], that appeared to have similar properties to the electron but a much larger mass, and the discovery of pions [12] and kaons [13] in 1947 through the study of cosmic rays entering the atmosphere put an end to that model. An important number of new particles were discovered in the following years, causing discussion about

which were the fundamental ones.

A first step in the solving of this question was achieved in 1961, when Murray Gell-Mann proposed a classification of these particles, called the Eightfold Model [14], that arranged the particles into geometrical forms according to their charge and strangeness (a property that Gell-Mann attributed to the particles, conserved by strong interaction but not by weak interaction). This classification allowed to predict the existence of the  $\Omega^-$  particle, which was confirmed in 1964 [15]. That same year Gell-Mann [16] and George Zweig [17] proposed a new model explaining this classification, hypothesizing that baryons and mesons were composed of more elementary particles, that were called quarks. These quarks are confined inside the baryons and mesons and are subject to the strong interaction.

It is in the end of the 1970s that a model formalizing the interactions between all the elementary particles was developed, called the Standard Model (SM). This model is still considered successful today, as it has been able to provide very accurate predictions, such as the mass of the  $Z$  and  $W^\pm$  bosons [18, 19].

However this model is still incomplete and some questions still remain unanswered by the Standard Model. The Standard Model does not include the Gravitational Force. Moreover the neutrinos are considered massless by the SM but have been proven to have a non-zero mass [20, 21]. The Standard Model provides no particle or mechanism that could explain neither the dark matter<sup>1</sup> [22] nor the dark energy, which is the invisible energy responsible for the accelerated expansion of the universe [23].

### 1.1.2 Elementary particles and fundamental interactions

The particles that are considered elementary in the framework of the Standard Model are summarized in Figure 1.1. They are classified into two main categories. The fermions have a spin of  $1/2$  and are the component of the matter. The bosons have a spin integer; the gauge bosons serve as vectors for the interactions between fermions whereas the scalar Higgs boson  $H$  is responsible for the mass generation [24, 25]. The discovery of the Higgs boson was one of the main reasons for the construction of the LHC and its existence was confirmed in 2012 by the ATLAS [26] and CMS [27] experiments. This discovery resulted in the attribution of the Nobel Prize to Peter Higgs and François Englert in 2013.

---

<sup>1</sup>Observations of galaxies movements indicate that there might be more matter than the visible matter and this missing matter is called dark matter.

	mass →	charge →	spin →					
	<math>\approx 2.3 \text{ MeV}/c^2</math>	$2/3$	$1/2$	<b>u</b> up	$\approx 1.275 \text{ GeV}/c^2$	$2/3$	$1/2$	<b>c</b> charm
					$\approx 173.07 \text{ GeV}/c^2$	$2/3$	$1/2$	<b>t</b> top
					0	0	1	<b>g</b> gluon
								<b>H</b> Higgs boson
<b>QUARKS</b>								
	$\approx 4.8 \text{ MeV}/c^2$	$-1/3$	$1/2$	<b>d</b> down	$\approx 95 \text{ MeV}/c^2$	$-1/3$	$1/2$	<b>s</b> strange
					$\approx 4.18 \text{ GeV}/c^2$	$-1/3$	$1/2$	<b>b</b> bottom
					0	0	1	<b><math>\gamma</math></b> photon
	$0.511 \text{ MeV}/c^2$	-1	$1/2$	<b>e</b> electron	$105.7 \text{ MeV}/c^2$	-1	$1/2$	<b><math>\mu</math></b> muon
					$1.777 \text{ GeV}/c^2$	-1	$1/2$	<b><math>\tau</math></b> tau
								<b>Z</b> Z boson
<b>LEPTONS</b>								
	<math>\approx 2.2 \text{ eV}/c^2</math>	0	$1/2$	<b><math>\nu_e</math></b> electron neutrino	<math>\approx 0.17 \text{ MeV}/c^2</math>	0	$1/2$	<b><math>\nu_\mu</math></b> muon neutrino
					<math>\approx 1.5 \text{ MeV}/c^2</math>	0	$1/2$	<b><math>\nu_\tau</math></b> tau neutrino
								<b>W</b> W boson
								<b>GAUGE BOSONS</b>

Figure 1.1: Table of the different elementary particles of the Standard Model.

The fermions are divided between quarks and leptons. Quarks are composed of six flavors regrouped by pairs in three generations: up and down, charm and strange, top and bottom. Leptons are also separated in three generations: the electron, the muon and the tau, and their respective neutrinos  $\nu_e$ ,  $\nu_\mu$  and  $\nu_\tau$ . The generations are sorted in order of increasing mass. The ordinary matter is composed of the fermions of lower mass, namely the up and down quarks and the electron. The heavier generations decay into the next most stable level. To each fermion there is an equivalent anti-particle, with the same properties of mass and spin, but with a charge of opposite sign (but same absolute value).

In the Standard Model, three fundamental interactions are considered:

- The electromagnetic interaction, which affects electrically charged particles, can be described by Quantum Electro-Dynamics [28] and has the photon  $\gamma$  as a boson vector. Because of the null mass of the photon, this interaction has an infinite range.
- The Weak Interaction, which is responsible for  $\beta$  nuclear decays, is carried by the electroweak bosons  $W^\pm$  and  $Z$  and is measurable at the subatomic level. The particularity of the weak interaction is that its bosons have a non-zero mass, which can be explained by the Higgs mechanism and the involvement of the Higgs Boson  $H$ .

- The Strong Interaction, that is responsible for the cohesion of the nucleus and can be described by Quantum Chromo-Dynamics (QCD). The bosons of the strong interaction are the gluons.

In addition to these three fundamental interactions, the gravitational interaction has been identified as a fundamental interaction, but is separated from the three other interaction since it doesn't enter in the SM. So far, no boson for the gravitational interaction has been discovered.

Composite particles such as protons and neutrons can be regrouped under a larger classification. Here is a summary of the different particle categories:

- the *quarks* are the fundamental particles of semi-integer spin that are sensitive to the strong interaction.
- the *leptons* are the fundamental particles of semi-integer spin that are not sensitive to the strong interaction. It is composed of the charged leptons  $e$ ,  $\mu$  and  $\tau$  that have an electric charge  $-e$  and of the neutrinos  $\nu_e$ ,  $\nu_\mu$  and  $\nu_\tau$ , that are not charged.
- the *bosons* are the fundamental particles of integer spin. We can distinguish the gauge bosons  $\gamma$ ,  $g$ ,  $W^\pm$  and  $Z^0$  and the scalar boson  $H$ .
- the *mesons* are composed of a quark and an anti-quark. We can give for example the pion  $\pi^+$  composed of  $u\bar{d}$ , the Kaon  $K^-$  composed of  $\bar{u}s$  and the  $J/\psi$  and  $\psi(2S)$  composed of  $c\bar{c}$ .
- the *baryons* are composed of three quarks and for instance the proton  $uud$  and the neutron  $udd$  are baryons. The other baryons are regrouped into the  $\Delta$ ,  $\Lambda$ ,  $\Sigma$ ,  $\Xi$  and  $\Omega$  families. For instance the  $\Sigma^0$  is composed of  $uds$ .
- the *hadrons* regroup both the baryons and the mesons.

In addition to this structures, evidences of the existence of a structure in pentaquark, composed of four quarks and one anti-quark were recently found [29].

### 1.1.3 Basis of Quantum Chromo-Dynamics

The Quantum Chromo-Dynamics is the theory that describes the strong interaction, that only affects quarks and gluons [30, 31]. During the elaboration of the quark model, the existence of the  $\Delta^{++}$  and  $\Omega^-$  baryons, which

are composed of three quarks up and three quarks strange respectively, was an indication of a missing component in the particles properties. Indeed, since these particles are composed of three identical quarks, they necessary violated the Pauli exclusion principle by having at least two quarks with the same spin orientation, unless a new quantum number is added, that can have three different values for quarks of the same type. This new characteristic property of the particles was called the color charge and can be seen as an equivalent for the strong interaction of the electric charge for the electromagnetic interaction. This in turn led to the development of QCD.

Quarks can be in one of the three color (red, green and blue) and three anti-color states. One of the particularities of QCD is that the gluons  $g$  also carry a color charge, which means that gluons can interact with each other. Gluons are bicolored particles and can be in 8 different color states, which are independent combinations of the three color and three anti-color states presented before<sup>2</sup>.

The fact that gluons can interact with themselves introduces non-linear effects in the equations of QCD.

### Confinement and asymptotic freedom

The quantum fluctuations of the vacuum in QCD lead to the creation and annihilation of  $q\bar{q}$  pairs. Therefore, as a quark propagates in the vacuum, it can emit gluons and is surrounded by a cloud of color charges caused by the creation-annihilation of  $q\bar{q}$  pairs. These color charges interact with the quark, causing the vacuum to be polarized with respect to the quark. This will tend to "screen" the quark charge. This is a phenomenon similar to what is observed in QED with  $e^+e^-$  creation-annihilation. However, since contrary to the photons, gluons can interact with each other, the creation and annihilation of gluons pairs will also cause a vacuum polarization. But since gluons color charge is different than the quarks one, the polarization of gluons does not screen the color field, but rather augments it. This is called anti-screening. Because of the number of quark flavors and color charges, the anti-screening has a more important effect than the screening [32, 33]. Both phenomenon are represented by their Feynman diagrams in Figure 1.2.

The intensity of the strong interaction is given by the strong coupling

---

<sup>2</sup>For the gluons 9 combination are possible :  $R\bar{R}$ ,  $R\bar{B}$ ,  $R\bar{G}$ ,  $B\bar{R}$ ,  $B\bar{B}$ ,  $B\bar{G}$ ,  $G\bar{R}$ ,  $G\bar{B}$  and  $G\bar{G}$ . However  $(R\bar{R} + B\bar{B} + G\bar{G})/3$  is the color singlet (white), so only 8 combinations are independent.

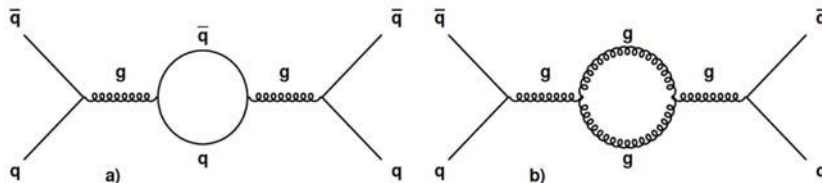


Figure 1.2: Feynman Diagram of the QCD vacuum polarization, with a) the screening phenomenon on the left and b) the anti-screening phenomenon on the right.

constant,  $\alpha_s$ . Its dependence as a function of the energy scale is given by:

$$\alpha_s(Q^2) = \frac{12\pi}{(11n - 2f) \ln(\frac{Q^2}{\Lambda_{QCD}^2})} \quad (1.1)$$

where  $n$  is the number of colors,  $f$  the number of quark flavors and  $\Lambda_{QCD}$  is a constant that corresponds to the limit below which the perturbation theory is not applicable anymore to QCD calculation, meaning that using only a finite number of Feynman diagrams is not sufficient to obtain a good description of the phenomena.

The evolution of  $\alpha_s$  as a function of the momentum is presented in Figure 1.3. What can be seen in the figure is that for a small  $Q^2$ , which corresponds to large distances, the coupling constant diverges. The consequence is that colored particles cannot exist in a free state and are necessarily bound into hadrons, which are colorless. This is called confinement. In this regime, the perturbation theory of QCD cannot be applied, this is the non-perturbative regime of QCD.

On the contrary, when  $Q^2$  is very large, which corresponds to small distances,  $\alpha_s$  tends to zero. The quarks are then considered free. This is called asymptotic freedom. It was described by David Gross and Franz Wilczek [32], and independently by David Politzer [33] in 1973. In this regime, the perturbation theory of QCD is applicable, this is the perturbative QCD (pQCD) regime.

### Chiral symmetry

If only three quark flavors ( $u$ ,  $d$ ,  $s$ ) are considered and they have a zero mass, one of the properties of the corresponding QCD Lagrangian is the chiral symmetry. It corresponds to the symmetry under helicity transformation

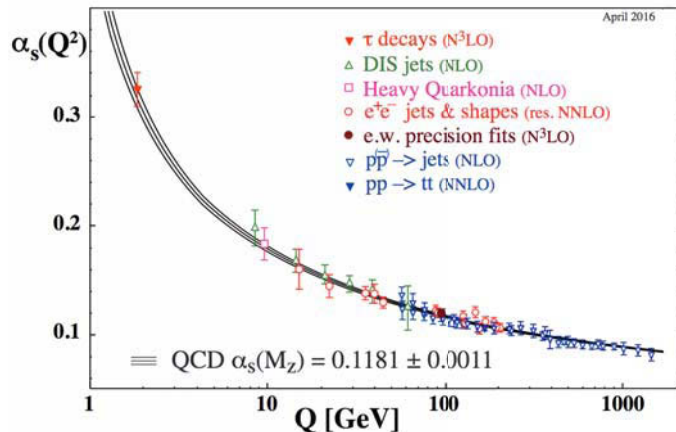


Figure 1.3: Summary of the measurements of  $\alpha_s$  as function of the energy scale  $Q$ . Lines correspond to QCD prediction [34].

(the helicity is the projection of the spin along the propagation direction) and implies that there is no interaction between particle of different helicities. The symmetry can be characterized with the chiral condensate  $\langle \bar{\psi}\psi \rangle$ :

$$\langle \bar{\psi}\psi \rangle = \langle \bar{\psi}_L\psi_R + \bar{\psi}_R\psi_L \rangle = 0 \quad (1.2)$$

where  $\psi_L$  and  $\psi_R$  are the left-hand (of helicity  $h = -1/2$ ) and right-handed (of helicity  $h = +1/2$ ) quark fields respectively.

However, if chiral symmetry was realized in nature, one would expect that hadron spectra exhibit parity doublets, meaning that each hadron should have a chiral partner of opposite parity and same mass, but this is not the case [35]. This is due to the fact that the mass of the quarks is non-zero at low energies, due to the mass generation through the Higgs mechanism and as a consequence the values of the chiral condensates for  $\langle \bar{u}u \rangle$  and  $\langle \bar{d}d \rangle$  are non-zero. Therefore the chiral symmetry is spontaneously broken. This breaking of the chiral symmetry has for consequence the existence of the following Goldstone bosons : pions, kaons, et  $\eta$  mesons [36]. Most of the observed mass of light quarks is generated by the spontaneous breaking of chiral symmetry [37].

At higher energy a restoration of the chiral symmetry is expected. Indeed at high energy modifications in the properties of the Higgs field cause the mass of the light quarks to be close to zero and therefore  $\langle \bar{\psi}\psi \rangle = 0$  is

observed [37]. The restoration of the chiral symmetry implies a phase transition of hadronic matter.

## 1.2 The QGP and the QCD phase diagram

After the discovery of the asymptotic freedom, the existence of a deconfined state of matter at high temperature was predicted [1, 38, 39], where the strong interaction becomes weak enough for the quarks and gluons to be free. This new state of matter is called Quark-Gluon Plasma (QGP). The transition from hadronic matter to the QGP can be studied with Lattice QCD (lQCD) calculations [40], which is a technique exploring the non-perturbative domain of QCD by formulating QCD on a discrete Euclidian space-time lattice. Other models such the MIT bag model [41] or the NJL models [42, 43] also attempt to describe the hadronic matter. It can be noted that the transition to a deconfinement state is accompanied by a chiral symmetry restoration.

Using these different models, it is possible to create a sketch of the hadronic phase diagram, as illustrated in Figure 1.4, as a function of temperature on the  $y$  axis and net baryon chemical potential<sup>3</sup>  $\mu_B$  on the  $x$  axis. At low temperature and baryonic density, matter can be described as a hadron gas, quarks and gluons are confined. The point  $\mu_B = 939$  MeV and  $T \approx 0$  corresponds to the nucleon mass and represents ordinary hadronic matter, in the form of atomic nuclei.

For higher temperatures, the quarks and gluons are deconfined and there is a QGP. The nature of the transition depends on  $\mu_B$ . When  $\mu_B$  is close to zero, lQCD calculations predict a transition of type cross-over [44, 45, 46], which is a rapid transition without divergences or discontinuities. The value of the transition temperature for  $\mu_B = 0$  has been evaluated to  $T_c \approx 155$  MeV [47]. The cross-over transition corresponds to values of  $\mu_B$  below the one of the critical point. At the critical point, the transition is of the second order type. The position of the critical point on the  $(T, \mu_B)$  plane is not well known yet [48, 49]. For larger values of  $\mu_B$  the transition is believed to be of the first order type [50].

---

<sup>3</sup>The baryon chemical potential  $\mu_B$  illustrates the balance between matter and antimatter. When  $\mu_B = 0$ , the equilibrium is perfect. The baryon chemical potential is therefore an indication of the density of matter: the higher is  $\mu_B$ , the more dense is the matter.

For very large values of  $\mu_B$  and low values of the temperature, it is assumed that matter would reach a property of color superconductivity that could be found inside neutron stars [51]. And if both the temperature and  $\mu_B$  are large, there could be another state called the "quark matter phase" [52].

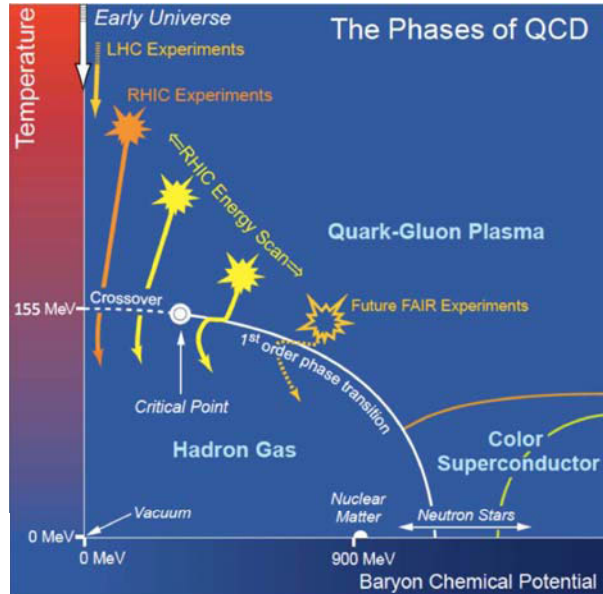


Figure 1.4: Sketch of the QCD phase diagram as a function of temperature and the Baryon Chemical Potential [53].

The QGP is studied in heavy ion colliders such as the RHIC and the LHC. The region of the phase diagram that are accessible by these heavy-ion experiments, as well as future experiments at the FAIR facility, are also shown in Figure 1.4.

### 1.3 Heavy Ion Collisions

Experimentally, the QGP can be produced in colliders by accelerating and colliding heavy nuclei. Experiments at SPS were fixed target experiments, meaning that a heavy ion beam is collided on a heavy fixed target, whereas at RHIC and LHC, collider experiments are conducted, meaning

that two relativistic heavy ion beams are collided.

When ions are accelerated at relativistic speed, the colliding nuclei are almost transparent to each other and the nucleons participating to the collisions leave a huge quantity of energy in a very small volume. For this to happen the nuclei crossing time has to be much smaller than the characteristic time of the strong interaction:  $\tau_{crossing} \ll \tau_{strong}$ . If the energy density of the system is larger than the critical energy density ( $\approx 0.7 \text{ GeV}/\text{fm}^3$  [54]), it might lead to the formation of a QGP.

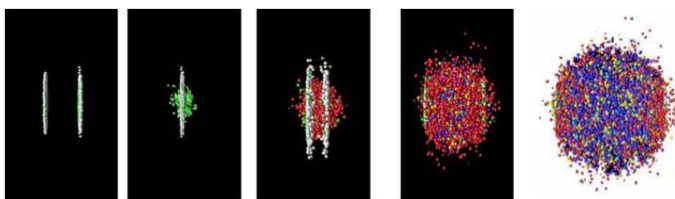


Figure 1.5: Representation of a nucleus-nucleus collision using URQMD.

A representation of a collision is shown in Figure 1.5. This figure was produced using Ultra Relativistic Quantum Molecular Dynamics, a model used to simulate heavy ion collisions [55, 56]. The nuclei appear flat because they are subject to the Lorentz contraction due to their ultra-relativistic speed.

Before describing in more details the collision, it is useful to remind the definitions of some important terms:

- The transverse momentum  $p_T$  is the component of the particle momentum perpendicular to the direction of the colliding nuclei, in the center of mass frame, whereas  $p_z$  is the component along the direction of the colliding nuclei.
- The rapidity  $y$  is defined as  $y = \frac{1}{2} \ln \left( \frac{E+p_z}{E-p_z} \right)$ , using natural units ( $c = 1$ ).
- The pseudo-rapidity  $\eta$  is a geometrical value linked to the angle  $\theta$  of the emitted particle with respect to the beam axis and is defined as  $\eta = -\ln[\tan(\theta/2)] = \frac{1}{2} \ln \left( \frac{|p|+p_z}{|p|-p_z} \right)$ . For massless particles or when the mass is negligible with respect to energy, rapidity and pseudo-rapidity are equivalent. In these cases, the rapidity is used preferably, as it is additive under Lorentz boosts. In particular the rapidity of a particle is equal to the sum of the rapidities of its decay particles.

- The transverse distance between the center of the colliding nuclei is called the impact parameter  $b$ . Smaller the impact parameter is, larger the overlapping area between the nuclei is, leading to a higher number of nucleons participating to the collision, and therefore to more energy left in the system.
- The number of participant nucleons is written  $N_{\text{part}}$  and corresponds to the number of nucleons suffering at least one inelastic collision.
- The number of binary nucleon-nucleon collisions among participants is written  $N_{\text{coll}}$ .

The parameters  $N_{\text{part}}$ ,  $N_{\text{coll}}$  and  $b$  are correlated. A collision with a small impact parameter is said to be central, and a collision with a large impact parameter is said to be peripheral (see Section 3.1). For central collisions,  $N_{\text{part}}$  and  $N_{\text{coll}}$  are large whereas for peripheral collisions  $N_{\text{part}}$  and  $N_{\text{coll}}$  are small.

### 1.3.1 Evolution of a collision

The dynamical evolution of a collision of heavy ions can be modeled with the Bjorken scenario [57]. It provides a picture of the space-time evolution of the system using the Landau hydrodynamical model [58]. The hypothesis assumed in the Bjorken scenario are:

- The nuclei crossing time is smaller than the characteristic time of the strong interaction. This ensures that the quark and gluons are created after the nuclei have crossed. The crossing time can be estimated as  $\tau_{\text{cross}} = 2R/\gamma$ , where  $R$  is the nuclei radius and  $\gamma$  is the Lorentz factor. Since  $\tau_{\text{strong}} \approx 1/\Lambda_{\text{QCD}} \approx 1 \text{ fm}/c$ , the condition  $\tau_{\text{cross}} \ll \tau_{\text{strong}}$  is reached for  $\gamma > 12$ , which corresponds to a center of mass energy per nucleon larger than 25 GeV.
- The particle production distribution presents a plateau at mid-rapidity, implying that there is an invariance of the system along rapidity that leads to a simplification of the solutions of the hydrodynamic equations. This has been verified experimentally at RHIC [59].

There are different stages in the evolution of a heavy ion collision, represented in Figure 1.6. The evolution is presented as a function of the time and the  $z$  axis, which is the direction of the colliding nuclei. The hyperbolic

lines represent the constant proper time  $\tau$  defined in the center of mass of the collision as  $\tau = \sqrt{c^2 t^2 - z^2}$ . The initial energy density generated can be estimated using the Bjorken formula measuring the particle density at  $y = 0$ :

$$\epsilon = \frac{\langle m_T \rangle}{\tau_f A} \frac{dN}{dy} \Big|_{y=0} \quad (1.3)$$

where  $\tau_f$  is the formation time of the particles,  $A$  is the overlapping section of the nuclei and  $\langle m_T \rangle = \langle \sqrt{p_T^2 + m^2} \rangle$  is the average transverse mass.

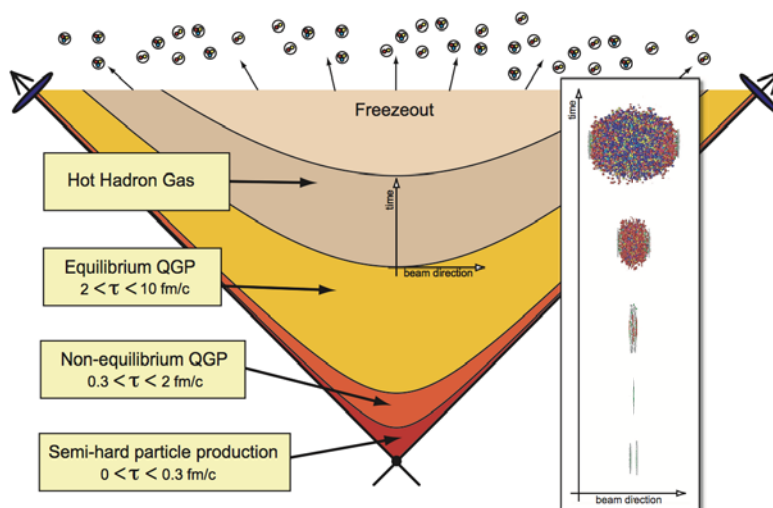


Figure 1.6: Illustration of the space-time evolution of the QGP as generated in a heavy ion collision at LHC energies. The overlay on the right shows the lab-frame evolution [60].

The successive stages are explained below :

- Pre-equilibrium ( $0 < \tau < 2 \text{ fm}/c$ ): the collision occurs at  $\tau = 0$ . Immediately after the collision, the multiple interactions between quarks and gluons lead to a rapid increase in the temperature of the system and the creation of a pre-equilibrium phase. In particular it is during this phase that heavy quarks, quarkonia, direct photons are produced through the interactions of the quarks and gluons of the colliding nuclei.
- QGP formation and hydrodynamic expansion ( $2 < \tau < 10 \text{ fm}/c$ ):

If the energy of the system reaches the critical value to transition toward a deconfined phase, there is a formation of a QGP, out of equilibrium. Due to the high pressure gradient between the medium which has a very high density and the vacuum surrounding it, the QGP starts to quickly expand. If the QGP exists long enough, it reaches a thermodynamical equilibrium. The process by which the QGP reaches this equilibrium is called thermalization.

- Mixed State ( $10 < \tau < 20 \text{ fm}/c$ ): the cooling down of the medium, combined with its expansion, leads to the confinement of the quark and gluons in the hadrons. This process is called the hadronization<sup>4</sup>.
- Hadronic gas phase: Once the hadronization is complete and the quarks are all confined, the medium can be described as an expanding hadronic gas.
- Freeze-out: As the cooling down and expansion continue, the medium reaches the freeze-out phase which is composed in two separate phases: first, the hadrons cease to have inelastic interactions with each other, it is the chemical freeze-out (the chemical composition of the medium doesn't change anymore). Then when the system continues its cooling, the hadrons have no more elastic interaction with each other: this is the thermal freeze-out (the kinetic distributions of the particles are frozen). Finally, as the system continues to expand, particles stream freely to the detectors.

The lifetime of the QGP is extremely short, as seen in the description above, which is why it cannot be observed directly, but rather through the detection of different probes. These probes can be distinguished between hard probes, that are produced before the formation of the QGP and travel through it, and soft probes that are produced in or by the QGP.

## 1.4 Probes of the QGP

In order to study the QGP, an experiment will try to measure the kinetic properties of all the particles that are emitted, either directly or by detecting their decay products. These probes will then provide informations on the

---

<sup>4</sup>The hadronization is possible even without QGP.

different phases of the collision [61]. The experimental probes can be sorted in different categories depending on the information that they provide, as described in the following.

### 1.4.1 Global Observables

These probes are used to determine the characteristics of the collisions, such as the impact parameter, reaction plane and initial energy density.

The measurement of charged particle multiplicity and transverse energy is used to evaluate the centrality of the collision, number of participating nucleons, and number of binary nucleon-nucleon collisions, but also information on the initial energy density of the collision using the Bjorken formula (see Equation 1.3).

The measurement of particle momentum allows to determine the reaction plane of the collision, which is defined by the beam axis and the impact parameter vector of the colliding nuclei.

### 1.4.2 Soft Probes

These probes come from the quarks and gluons from the QGP, and involve processes of low energy transfer, typically up to 1-2 GeV. They allow to study signals from the late stage of the collision (hadronic phase). Among this probes we can find:

- Measurement of pions, kaons, protons, and anti-protons.
- The strange hadrons such as  $\Lambda$ ,  $\Sigma^\pm$ ,  $\Xi^\pm$  and  $\Omega^-$ . The restoration of the chiral symmetry in a QGP should decrease the energy needed for the creation of  $s\bar{s}$  pairs in nucleus-nucleus collision with respect to pp collisions. Therefore an augmentation of the production of these strange hadrons is expected [62, 63].
- The elliptic flow, which is defined as the second coefficient of the Fourier expansion describing the final state particle azimuthal distribution with respect to the reaction plane, and is named  $v_2$ . There is a geometrical asymmetry in the overlapping area between the two colliding nuclei, with respect to the reaction plane. It results in asymmetry of the pressure gradients in the medium, which disappears as the system expands. A  $v_2$  different from 0 for the measured hadrons would

mean that the asymmetry still exists at the moment of the thermalization. This would provide information on the hydrodynamic properties of the medium during the thermalization [64, 65].

- The correlation between hadrons pairs, which provides information on the expansion rate of the medium.
- The low mass vector mesons, such as the  $\rho$ ,  $\omega$ , and  $\phi$ . A modification in the mass and width of these mesons would be an indication of a restoration of the chiral symmetry.
- The production of thermal photons emitted by the QGP, that do not interact strongly, and may provide information on the initial temperature of the medium. These photons have a low transverse momentum:  $p_T \lesssim 4 \text{ GeV}/c$  [66].

As opposed to the hard probes, the soft probes can be produced and destroyed in all the phases of the expansion.

### 1.4.3 Hard probes

Hard probes are produced by processes involving high energy transfers, for instance around 3 GeV for the  $J/\psi$  and around 10 GeV for the  $\Upsilon$ , given by the particle mass. They are created at the early stages of the collision, therefore they are involved in all the stages of the evolution of the plasma. These probes provide informations on the first stages such as the thermodynamical equilibration of the QGP and its transition. Some examples of this type of probes are:

- The measurement of direct photons produced in hard scatterings provide information on parton<sup>5</sup> distributions in nuclei. These photons have a higher transverse momentum than thermal photons:  $p_T \gtrsim 5 \text{ GeV}/c$  [66]. They can be used to study the parton distribution functions (PDF), which are the probability to find a parton with a momentum fraction  $x$  of the total nucleon momentum at a given energy scale.
- The measurement of electro-weak bosons  $W^\pm$  and  $Z$ , that do not interact strongly and the production of which is not affected by the

---

<sup>5</sup>*parton* is a general denomination for the components of the nucleons, it regroups both quarks and gluons.

presence of a quark and gluon plasma. Like for direct photons they can be used to study PDFs.

- The production of high transverse momentum particles ( $p_T \gtrsim 7 \text{ GeV}/c$ ), which is modified in presence of a QGP [67]. The high energy partons from which these particles originate go through a dense medium of quark and gluons and lose energy through radiation and collision processes. This provides information on the hot and dense region of the collision, such as the density of gluons in the QGP and the mean free path of high energy partons in the QGP [68].
- The production of quarkonia, which are bound states of heavy quarks  $Q\bar{Q}$ , is used to measure the potential screening effects due to the presence of free color charges in the plasma. These heavy quarks pairs, because of their large mass, are produced in the very first moments of the collision, before the formation of the plasma and therefore can be used to probe the QGP formation.

For all the probes mentioned above, a study in pp collisions, where no QGP is formed, but also in pA collisions is necessary in addition to the AA study, in order to put in evidence the phenomenon that are linked to the presence of the plasma.

## 1.5 The charmonium family

Quarkonia are separated in two families, the charmonia which are bound states of a charm  $c$  and an anti-charm  $\bar{c}$  quarks and the bottomonia which are bound states of a bottom  $b$  and an anti-bottom quark  $\bar{b}$ . The charmonium family includes the  $J/\psi$  and the  $\psi(2S)$  which is the focus of this thesis; the bottomonium family includes mesons such as the  $\Upsilon(1S)$ .

The fundamental state of the charmonium family was discovered in two separate experiments [69, 70] in 1974 and was baptized  $J/\psi$ . The different states of the charmonium are summarized in the Figure 1.7. The higher masses can decay into the  $J/\psi$ , which is called the feed-down effect.

In hadronic collisions, the charmonium production can be separated between the "prompt" charmonium and the "non-prompt" charmonium. The "prompt" charmonia come from the direct production and in the case of the  $J/\psi$  also from decay from higher states. Measurements at the Fermilab E705 experiment [71, 72] and at the HERA-B [73, 74] in pA collisions at

$\sqrt{s_{NN}} = 300$  GeV and  $\sqrt{s_{NN}} = 920$  GeV, respectively, allowed to determine that the prompt  $J/\psi$  production comes from about 60% from the direct production, about 30% from the  $\chi_c$  decay and about 10% from the  $\psi(2S)$  decay.

The "non-prompt"  $J/\psi$  and  $\psi(2S)$  come from the decay of B mesons. The fraction of  $J/\psi$  decaying from B has been measured in the LHCb experiment and is about 10% in pp collisions at  $\sqrt{s} = 7$  TeV [75] and 7% in pp collisions at  $\sqrt{s} = 2.76$  TeV [76]. For the  $\psi(2S)$  the fraction of particles decaying from B-mesons is about 14% in pp collisions at  $\sqrt{s} = 7$  TeV [77].

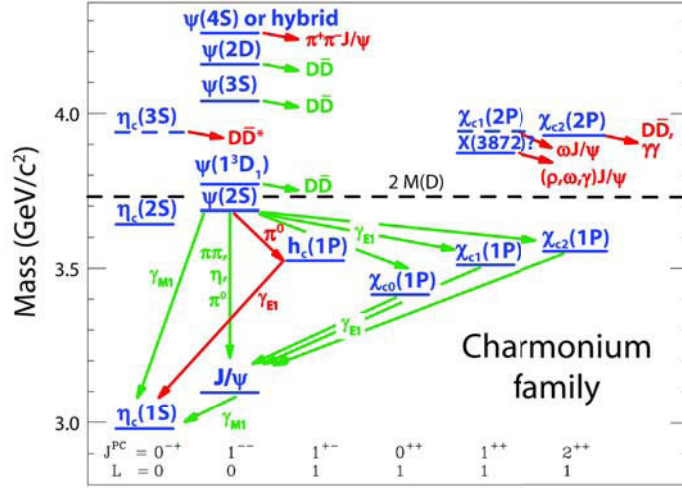


Figure 1.7: Spectroscopic diagram of the Charmonium family. The bottom rows show the spin, parity and charge conjugation quantum numbers associated with the particles above [78].

Given that the mass of the charm quark is large,  $m_c = 1.3$  GeV, the spectroscopy of the charmonia can be studied in non-relativistic potential theory. The Cornell potential is used to describe the interaction between de two quarks [79, 80]:

$$V(r) = \sigma \cdot r - \frac{\alpha}{r} \quad (1.4)$$

where  $\sigma$  is the string tension between the quarks, and  $\alpha$  is the gauge coupling of a Coulomb-like potential for the color interaction ( $\alpha = \frac{4}{3}\alpha_s$ ). The solutions of the Schrödinger equation using this potential correspond to the different charmonium bound states presented in the Figure 1.7.

The observed stable charmonium states are summarized in Table 1.1. The binding energies  $\Delta E$  listed there are the differences between the quarkonium masses and the open charm threshold [81]. As it will be discussed in

State	$\eta_c$	$J/\psi$	$\chi_{c0}$	$\chi_{c1}$	$\chi_{c2}$	$\psi(2S)$
Mass (GeV/ $c^2$ )	2.98	3.10	3.42	3.51	3.56	3.69
$\Delta E$ (GeV)	0.75	0.64	0.32	3.22	0.18	0.05

Table 1.1: Charmonium states and binding energies.

the following sections, the difference in the  $J/\psi$  and  $\psi(2S)$  binding energy results in different behaviors of the two particles in presence of nuclear matter and in presence of the QGP.

### 1.5.1 Production Mechanism

The production of  $Q\bar{Q}$  pairs in heavy ion collisions results mostly of high energy parton interactions. The leading order processes of the  $Q\bar{Q}$  pair formation are presented in Figure 1.8.

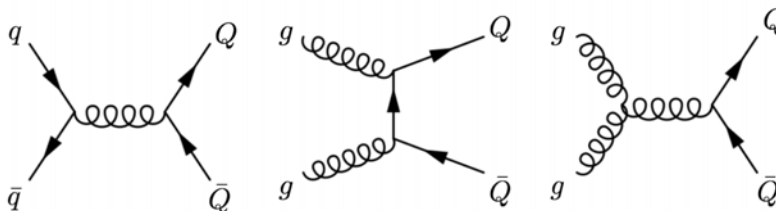


Figure 1.8: Heavy Quark pair production Feynman diagrams at leading order. The left diagram corresponds to quark antiquark annihilation, and the middle and right one correspond to gluon fusion, and are the dominant processes at LHC energies [82].

The formation of a quarkonium from a  $Q\bar{Q}$  pair is possible only if this pair is in a colorless state (the color singlet state). But as we have seen from the diagrams, the production of  $Q\bar{Q}$  pairs involves gluons, which have a color charge. In order to have a quarkonium state, it is necessary to neutralize

the color charge of the pair. The mechanism of the color neutralization is not fully understood from a theoretical point of view.

The theoretical study of quarkonium production processes involves both perturbative and non-perturbative aspects of QCD. The production of the  $Q\bar{Q}$  pair involves momentum transfers  $p$  at least as large as the mass of the heavy quarks. This short distance processes (the distance scale is  $1/p$ ) involve perturbative QCD since  $p \geq 2m_Q \geq \Lambda_{QCD}$ . The subsequent evolution of the  $Q\bar{Q}$  pair, however, involves smaller dynamical scales such as the momentum of the heavy quarks in the bound-state rest frame  $m_Q v$ , and their binding energy  $m_Q v^2$  where  $v$  is the typical velocity of the heavy quark or antiquark in the quarkonium rest frame,  $v^2 = 0.3$  for the  $J/\psi$  [83]. This long-distance processes involve non-perturbative physics. In the models, the short-distance, perturbative effects are separated from the long-distance, non-perturbative effects. The different models mainly differ in their description of the hadronization of the quarks. In the following, three models describing the production of charmonium are summarized: the Color Singlet Model, the Color Evaporation Model, and the NRQCD model. Extensive reviews of the quarkonium physics can be found in [83, 84, 85].

### Color-Singlet Model

The Color-Singlet Model (CSM) was the first model proposed for the charmonium production after the  $J/\psi$  discovery [86, 87]. In this model, the  $Q\bar{Q}$  pair that evolves into a quarkonium has the same spin and angular-momentum quantum numbers as the quarkonium and is produced in a color singlet state. The quantum state of the pair does not evolve between its production and its hadronization. The non-perturbative factor of the quarkonium cross section is then proportional to the bound state's wave function. These quantities can be extracted by comparing theoretical expressions for quarkonium decay rates in the CSM with experimental measurements [88]. Once this extraction has been carried out, the CSM has no free parameters.

The CSM model at Leading Order was successful to reproduce the total  $J/\psi$  cross section as a function of the collision center of mass energy [89], however, it underestimated the  $\psi(2S)$  cross-section and failed to reproduce the  $p_T$  dependence of the different charmonium states [90, 91, 92]. The hypothesis of the color neutralization at the formation of the  $Q\bar{Q}$  pair does not reproduce the data correctly, and it is necessary to consider coalescence mechanism in a larger time scale. It has been found that, at high energies, very large corrections to the CSM appear at next-to-leading order (NLO) and next-to-next-to-leading order (NNLO) [93, 94].

### Color Evaporation Model

The Color Evaporation Model (CEM) was proposed in the late 1970s and describes the quarkonium production based on a statistical description of the quarkonium formation probability [95]. In this model, the hadronization is uncorrelated from the  $Q\bar{Q}$  pair. It is assumed that every produced  $Q\bar{Q}$  pair evolves into a quarkonium if it has an invariant mass that is less than the threshold for producing a pair of open-flavor heavy mesons. The color neutralization occurs through the absorption or emission of a gluon by the pair with color fields induced by the collision, which gives the name "color evaporation" to the model. Then, the cross-section  $\sigma_{quarkonium}$  of a quarkonium state is proportional to the integrated production cross-section of the  $Q\bar{Q}$  pair  $\sigma_{Q\bar{Q}}$ , in the invariant mass range  $2m_Q < m_{Q\bar{Q}} < 2m_M$ , where  $m_M$  is the lightest meson that can be created with the  $Q\bar{Q}$  pair:

$$\sigma_{quarkonium} = F_{quarkonium} \cdot \int_{2m_Q}^{2m_M} \frac{d\sigma_{Q\bar{Q}}}{dm_{Q\bar{Q}}} dm_{Q\bar{Q}} \quad (1.5)$$

where  $F_{quarkonium}$  is related to the probability that the  $Q\bar{Q}$  pair hadronizes into the considered quarkonium state.  $F_{quarkonium}$  is energy-momentum and process independent and can be determined experimentally.

What derives from this model is that since the production cross section of a charmonium state is directly linked to the production cross section of a  $c\bar{c}$  pair, the ratio of the production cross-section of the different charmonium states has to be constant with respect to the energy. In particular, we have  $\sigma_{\psi(2S)}/\sigma_{J/\psi} = F_{\psi(2S)}/F_{J/\psi} = cst.$

This model is able to give correct prediction for the energy dependence and  $p_T$  dependence of the observed quarkonium cross-section. However, it is unable to give predictions on the quarkonium polarization, and some discrepancies were found in the description of the  $p_T$  spectra. Moreover, the CEM model does not describe the space-time evolution of the color neutralization.

### NRQCD Model

This model is based on Non Relativistic QCD (NRQCD) [96, 97, 98]. It allows to express in a more rigorous way the hadronization probability of a heavy quark pair into a quarkonium via long-distance matrix elements (LDME). These LDME are constants appearing in front of terms of well defined  $p_T$  and  $y$  dependence, calculable via NRQCD. Their magnitude is determined from fits to measured cross sections. In addition to the usual

expansion in terms of  $\alpha_s$ , NRQCD introduces an expansion in terms of the relative velocity between the two quarks  $v$ . If one only considers the first order in  $v$  of the development in the NRQCD model, then one obtains the CSM.

### Charmonium Polarization

The distribution of the charmonium decay products can be expressed as [99]:

$$W(\theta, \phi) \propto \frac{1}{3 + \lambda_\theta} (1 + \lambda_\theta \cos^2 \theta + \lambda_\phi \sin^2 \theta \cdot \cos 2\phi + \lambda_{\theta\phi} \sin 2\theta \cdot \cos \phi) \quad (1.6)$$

where  $\theta$  and  $\phi$  are the polar and azimuthal angles respectively in a given reference frame, whereas  $\lambda_\theta$ ,  $\lambda_\phi$ , and  $\lambda_{\theta\phi}$  quantify the degrees of polarization. In particular  $\lambda_\theta > 0$  indicates a transverse polarization and  $\lambda_\phi < 0$  indicates a longitudinal polarization.

Examples of reference frames are the Collins-Soper (CS) frame, where the  $z$ -axis is defined as the bisector of the angle between the direction of one beam and the opposite of the direction of the other one, in the rest frame of the decaying particle, and helicity (HE) frame where the  $z$ -axis is given by the direction of the decaying particle in the center of mass frame of the collision. The  $\phi = 0$  plane is the one containing the two beams, in the charmonium rest frame.

In pp collisions, a transverse polarization is expected at high- $p_T$  according to NLO-NRQCD calculations [100], but it was not observed in the data (see Section 1.6.3). In presence of a QGP, a polarization is predicted at low  $p_T$  [101] but hasn't been observed yet.

### Photo-production

Charmonia can also be produced by photo-production [102, 103]. When a nucleus is accelerated at ultra-relativistic energies, all the electric charges can become a source of quasi-real photons. The production of photo-produced  $J/\psi$  occurs when a quasi-real photon from a nucleus interacts with the gluons of another nucleus, as illustrated in Figure 1.9. This production is enhanced in AA collision, because of the stronger electric field, but remains in most cases negligible in front of the hadronic production. However in ultra-peripheral collisions, which are collisions where the nuclei are separated by impact parameters larger than the sum of their radii  $b > 2R$ , hadronic interactions are strongly suppressed. The cross sections for photon induced

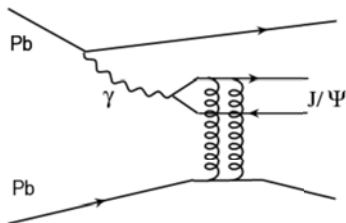


Figure 1.9: Feynman diagram of the  $J/\psi$  photo-production.

reactions remain large because the strong electromagnetic field of the nucleus enhances the intensity of the virtual photon flux. At the LHC energies in ultra-peripheral collisions with Pb nuclei, the two contributions are of the same order of magnitude [104, 105]. Moreover, non-negligible production of photo-produced  $J/\psi$  has been observed in peripheral collisions (where  $b < 2R$ ) at the LHC energies [106].

### 1.5.2 Cold Nuclear Matter Effects

The production mechanism presented in the previous section are affected in heavy ion collision even in the absence of a plasma, due to the presence of nuclear matter. These effects are referred to as Cold Nuclear Matter (CNM) effects. In order to disentangle them from the ones related to the presence of a QGP, the charmonium production is studied in pA collisions, where the energy is not sufficient to expect the formation of a QGP, but where there is nuclear matter. Some of those CNM effects are presented in the following.

#### Modification of the Parton Distribution Functions

The Parton Distribution Functions (PDF) represent the probability to find a parton (e.g. a quark or a gluon) in a nucleon with a fraction  $x$  of the longitudinal momentum of the nucleon at an energy scale  $Q^2$  and is written  $f(x, Q^2)$ . These PDFs enter in a factorization of the cross-section of any hadronic process, therefore their knowledge is essential in order to make any theoretical prediction for hadronic processes. An example of the PDFs is shown in Figure 1.10.

In a nuclear environment, the partonic structure of the nucleons may be modified and consequently the PDFs may be modified. The modification can

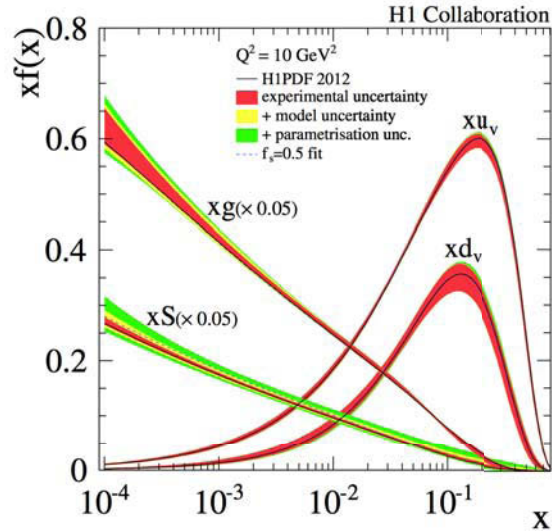


Figure 1.10: Parton distribution functions for the gluons ( $xg$ ), the valence quarks ( $xu$  and  $xd$ ) and the sea quarks ( $xS$ ) as a function of  $x$  measured by H1 experiment. The gluon and sea quark distributions are scaled by a factor 0.05 [107].

be parametrized through the PDF nuclear modification factor  $R_i^A(x, Q^2)$ :

$$R_i^A(x, Q^2) = \frac{f_i^A(x, Q^2)}{A \cdot f_i(x, Q^2)} \quad (1.7)$$

where  $f_i^A(x, Q^2)$  is the nuclear parton distribution function in a nucleus  $A$  for the parton  $i$ ,  $f_i(x, Q^2)$  is the PDF in a nucleon, and  $A$  is the number of nucleons in the nucleus.

If there are no nuclear effects and the nucleus is a simple superposition of nucleons without interference, then  $R_i^A(x, Q^2) = 1$ . An illustration of the parametrization of the nuclear effects is given in Figure 1.11. Several effects are observable: at small  $x$ , the parton probability density in the nucleon is smaller within the nuclear matter than for a free nucleon, it is the shadowing effect leading to the suppression of the charmonium production; at higher  $x$  the opposite effect is observable, it is the anti-shadowing, and at even higher  $x$  there is the EMC region (European Muon Collaboration) [108], where  $R_i^A(x, Q^2) < 1$  is observed again, and then there is the region of the Fermi motion where the  $R_i^A(x, Q^2)$  diverges.

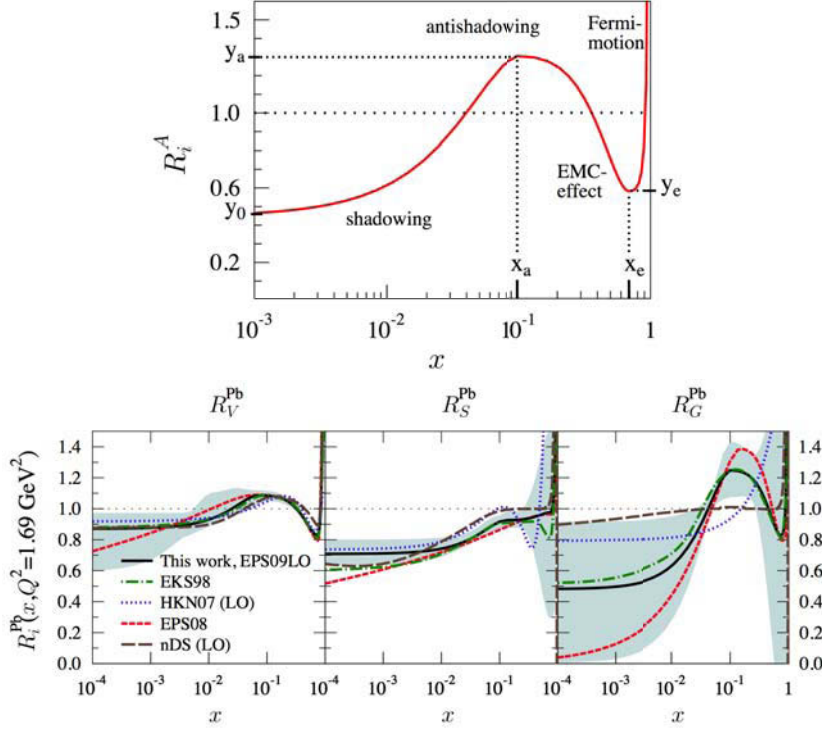


Figure 1.11: The different regions of  $R_i^A(x, Q^2)$  for a gluon (top) and comparison of the average valence quark, sea quark and gluon modifications at  $Q^2 = 1.69 \text{ GeV}^2$  for Pb nucleus, with EKS98 [109], EKPS [110], nDS [111], HKN07 [112] and EPS09 parametrizations (bottom). The uncertainty band corresponds to the EPS09 calculations [113].

As can be seen from the bottom panel of Figure 1.11, there are many parametrizations of these nPDFs. These parametrizations are fitted to the data, and the uncertainties on the parametrizations originate from the uncertainties on the data. The difference between the different parametrizations lies in different theoretical models and different choices in the fit function for the gluon distribution function [114].

At the energies of the LHC, the region of the very small  $x$  is accessible where an important shadowing is expected [115], which implies a suppression of the quarkonium such as the  $J/\psi$  and  $\psi(2S)$ .

### Gluon Saturation

As seen in Figure 1.10, the gluon density increases at low  $x$ . Moreover, at low  $x$  the gluon density increase with the energy  $Q^2$ . However the gluon density eventually reaches a saturation, which is characterized by the saturation scale  $Q_s(x)$ .

The Color Glass Condensate (CGC) is an effective theory that has been developed in order to describe this saturation [116, 117]. At large  $x$ , a nucleon is described in a conventional manner and is composed of three valence quarks. But as  $x$  decreases and/or  $Q^2$  increases, gluons are emitted and the gluon density increases, until the typical separation of the gluons is small enough that the gluons can recombine via gluon fusion processes. When the maximum occupation is reached, the system can be seen as a color condensate.

The CGC is thus able to explain the shadowing effect that occurs at small  $x$ : when the gluon density is close to saturation, some of the gluons of two nucleons from a nucleus can recombine through gluon fusion. As a consequence, the gluon density in the nucleus is smaller than the sum of the gluon density in the nucleons.

### Nuclear Absorption

The interactions between the pre-resonant or bound state  $c\bar{c}$  with the other interacting nuclei can lead to the dissociation of the state, which leads to a suppression of the charmonium production. This is referred to as "normal" nuclear absorption [118]. The nuclear absorption depends on the amount of nuclear matter that the  $c\bar{c}$  crosses and the probability  $S$  for the pair to survive when going through a nucleus.  $S$  is written:

$$S = \exp(-\rho_A \sigma_{abs} L) \quad (1.8)$$

where  $\rho_A$  is the nuclear density,  $\sigma_{abs}$  is the absorption cross section and  $L$  the average length of the nuclear matter crossed. The value of  $\sigma_{abs}$  can be determined in pA collision, and then extrapolated to AA collisions thanks to the Glauber Model [119] (see Section 3.1). The values of  $\sigma_{abs}$  for the  $J/\psi$  measured at the SPS and RHIC are shown in Figure 1.12 and exhibit a decrease with increasing collision energy. The value of  $\sigma_{abs}$  has been found to be higher for the  $\psi(2S)$  than for the  $J/\psi$  [120]. However, for both particles, the extrapolation to LHC energies indicates that nuclear absorption should become negligible.

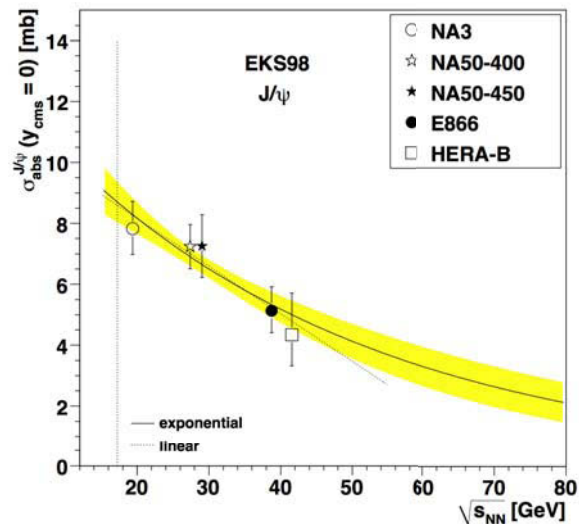


Figure 1.12:  $J/\psi$  nuclear absorption dependence with energy. The lines represent the fits to the different nuclear absorption parametrizations [119].

### Coherent Parton Energy Loss

A parton traveling through a medium can interact with the color charges it contains. The parton will lose energy through multiple elastic scatterings and gluon radiation. For a medium of density  $\rho$ , the mean free path of a parton is  $\lambda = 1/(\rho\sigma)$ , where  $\sigma$  is the scattering cross section. The medium can then be characterized by its transport coefficient  $\hat{q} = \mu^2/\lambda$ , where  $\mu$  is the momentum transfer in a scattering. This results in an energy loss per unit of length in the form of [121]:

$$\frac{dE}{dz} \approx \alpha_S C_R \sqrt{\hat{q}E} \quad (1.9)$$

where  $E$  is the parton energy,  $C_R$  is the QCD color factor,  $C_R = 4/3$  for quarks and  $C_R = 3$  for gluons.

In Cold Nuclear Matter, the transport coefficient is  $\hat{q}_{CNM} \approx 0.01 \text{ GeV}^3$  [121, 122]. For a QGP, calculations result in  $\hat{q}_{QGP} \approx 20\hat{q}_{CNM}$  [123].

### 1.5.3 Charmonium production in presence of a QGP

Charmonia are produced in the early stages of the collision, and interact with the Quark-Gluon Plasma when going through it. Therefore the study of charmonium is particularly interesting to probe the QGP. There are two main effects that affect charmonium production and are directly linked to the presence of a hot medium: the color screening that would prevent the binding of the  $c\bar{c}$  pairs, and the regeneration mechanism, which is based on the possibility of charmonium formation by uncorrelated  $c\bar{c}$  pairs and competes with the color screening effect. In this section we will present these two mechanisms and how they may affect differently the  $J/\psi$  and  $\psi(2S)$  in a QGP at equilibrium.

#### Color Screening

The suppression of the charmonium in presence of a QGP was proposed in 1986 by Matsui and Satz [124]. In a Quark-Gluon Plasma, the binding potential of the strong interaction between the  $c$  quark and the  $\bar{c}$  quark is attenuated by the presence of the surrounding color charges, carried by the quarks and gluons of the plasma. The binding potential can be derived by adding Debye screening effects to the Cornell potential introduced in Equation 1.4. This potential then becomes:

$$V(r) \approx \sigma \cdot r \cdot \left( \frac{1 - \exp(-\frac{r}{r_D})}{\frac{r}{r_D}} \right) - \frac{\alpha}{r} \cdot \exp\left(-\frac{r}{r_D}\right) \quad (1.10)$$

The Debye radius  $r_D$ , that characterizes the average range of the binding potential of the  $c\bar{c}$  pair, decreases with the density of the color charges. Therefore when the temperature  $T$  of the plasma increases,  $r_D$  decreases. With the increase of the temperature in the plasma, at some point the Debye radius becomes smaller than the radius of a considered charmonium state, then this state cannot bind anymore and is suppressed [81]. The corresponding temperature is called the dissociation temperature  $T_d$ . The  $c$  and  $\bar{c}$  quarks resulting from this process will then travel through the medium, and during the hadronization will be more likely to bind with light quarks and to form open charm hadrons, essentially D mesons. As a consequence, the color screening causes a diminution of the number of produced charmonia.

The dissociation temperature depends on the considered charmonium state: the larger the binding energy of the particle is, the smaller its binding radius and the larger its dissociation temperature. Measuring the suppression of different charmonium states therefore provides a way to measure the

plasma temperature. This phenomenon is illustrated in Figure 1.13, where the  $J/\psi$  production probability is shown as a function of the medium energy density. The  $\psi(2S)$ , which is the least bound particle, is suppressed first and does not contribute anymore to the  $J/\psi$  production through the feed-down processes (see Section 1.5), leading to a 10% decrease of the  $J/\psi$  production probability. Then the  $\chi_c$  dissociation temperature is reached leading to another decrease of about 20% of the production probability, until the  $J/\psi$  dissociation temperature is reached, and the particle is completely suppressed. This is called the sequential suppression: different charmonium states are suppressed one after the other, from the least to the more bound. However, this suppression picture is a rather naive and to date it has in fact never been observed in the data.

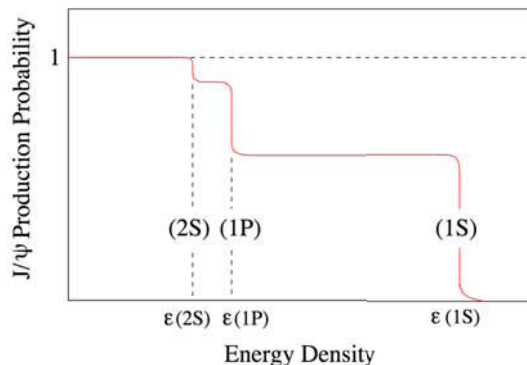


Figure 1.13: Illustration of the sequential suppression of different charmonium states by the color screening [81].

The quarkonium dissociation temperatures can be calculated with phenomenological binding potential models or with lattice QCD. The different melting temperatures calculated with different models for the different quarkonium states are presented in Figure 1.14.

### Regeneration

In competition with the quarkonium suppression caused by the color screening, another phenomenon takes place in presence of a QGP. This mechanism is called recombination: if the charm density in the system is large enough and if the charm quarks are thermalized via interaction with the surrounding color charges, the charmonium could be statistically formed at the

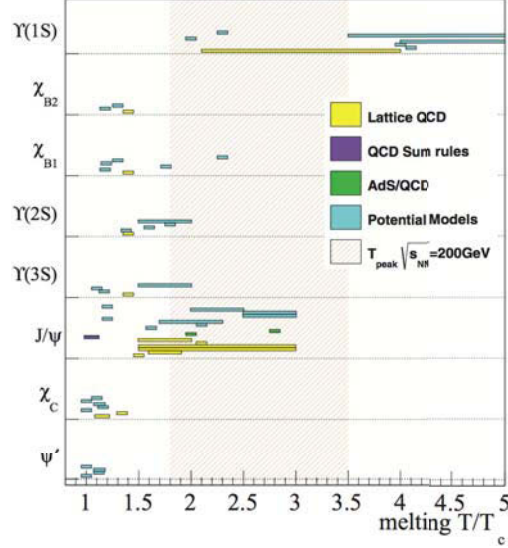


Figure 1.14: Compilation of medium dissociation temperatures relative to the critical temperature  $T_c$  for different quarkonium states. These estimations were performed assuming different  $T_c$  values. Each horizontal bar corresponds to one estimation and its temperature extension (when applied) represents the range where the quarkonia state undergoes a mass/size modification until it completely melts. The shaded band from  $1.8T/T_c$  to  $3.5T/T_c$  represents the hydrodynamic estimation for the peak temperature reached in Au - Au collisions at  $\sqrt{s_{NN}} = 200$  GeV [125].

phase boundary from uncorrelated  $c\bar{c}$  pairs created in different initial hard collisions [126, 127]. In AA collisions, the number of produced charm pairs  $N_{c\bar{c}}$  grows with the number of binary nucleon-nucleon collisions  $N_{\text{coll}}$ . For a given charm quark, a simple view of the probability to form a charmonium state is to expect it to be proportional to the number of available anti-charm quarks  $N_{\bar{c}}$  relative to the number of light antiquarks  $N_{\bar{u},\bar{d},\bar{s}}$ . The number of light antiquarks is normalized by the number of light hadron produced  $N_{ch}$ , which is proportional to the number of participant nucleons  $N_{\text{part}}$ :

$$P(\text{charmonium}) \propto \frac{N_{\bar{c}}}{N_{\bar{u},\bar{d},\bar{s}}} \approx \frac{N_{c\bar{c}}}{N_{ch}} \quad (1.11)$$

The number of recombined charmonium can be obtained by multiplying this probability by the number of available charm quarks  $N_c$  to obtain the

number of expected charmonium in a given event [128]:

$$N_{\text{charmonium}} = \frac{N_{c\bar{c}}^2}{N_{ch}} \quad (1.12)$$

The number of recombined charmonium is therefore dependent on the energy of the system, and increases with the energy. This recombined charm pair provides a new charmonium production mechanism in which the  $c$  and  $\bar{c}$  quarks have different parents, in contrast to the direct production, in pp collisions, for which both charm quarks originate from the same hard process. This contribution could be dominant at very high energy, as illustrated in Figure 1.15. When the energy density starts to increase, the suppression by color screening starts, then as the energy continues to increase, the regeneration starts to contribute in a significant manner, and even an enhancement of the charmonium can be observed. This throws a blur on the use of the charmonium suppression as a thermometer of the plasma. Moreover, this regeneration can have different probabilities with the different charmonium states: the  $\psi(2S)$  being less bound than the  $J/\psi$ , its recombination may occur later in time, when the system is more diluted [129]. A study of different charmonium states can be a good test for the different models.

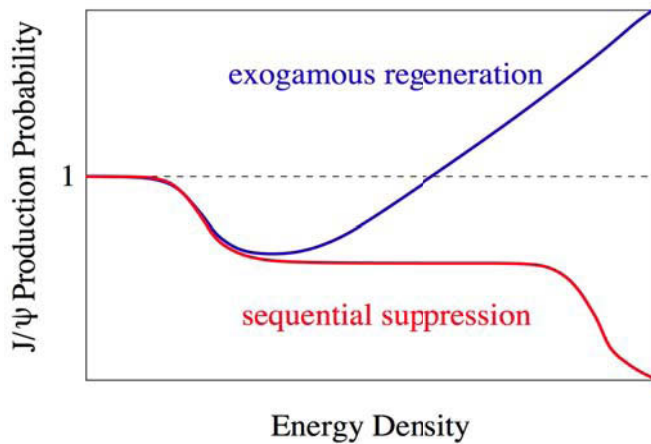


Figure 1.15: Illustration of the regeneration phenomenon [81].

### Interaction with comover medium

In a dense system, the charmonium can interact with the constituents of the medium, called comovers [130]. In a hadronic medium, this mechanism leads to the production of open charm through collisions with hadrons in processes such as  $c\bar{c} + h \rightarrow D + \bar{D} + X$ . In a QGP the high density of gluons leads to even more important effects. The higher the comover density is, the higher the suppression of the considered charmonium state is.

### 1.5.4 Theoretical Models

There are several models that describe the quarkonium production in ultra-relativistic heavy ion collisions and account for the phenomena described in the previous section. Among the different existing ones, three different models predicting charmonium production yields at LHC energies are presented.

#### Co-Mover interaction Model

The Co-Mover interaction (CIM) model [131, 132] does not assume thermal equilibrium and, thus, does not use thermodynamical concepts. The model takes into account the gluon shadowing and the nuclear absorption. The specific characteristics of the model is that dissociation effect is described through the interaction with a co-moving medium: in a hadronic medium the charmonium can interact with the component of the medium called the co-movers. In a deconfined medium as the QGP, the interactions with the co-movers are more important due to the high density of gluons. These interactions cause a dissociation of the  $c\bar{c}$  bound states, and the effect increases with the density of co-movers. Therefore this mechanism occurs mainly at the early stages of the collision when the partonic medium is very dense.

The suppression of charmonium is usually described with the nuclear modification factor  $R_{AB}$  (see Section 3 page 76). In the CIM, the  $R_{AB}$  for a charmonium state  $\psi$  is expressed as:

$$R_{AB}^{\psi}(b) = \frac{dN_{AB}^{\psi}/dy}{N_{\text{coll}}(b)dN_{pp}^{\psi}/dy} \quad (1.13)$$

$$R_{AB}^{\psi}(b) = \frac{\int \sigma_{AB}(b)N_{\text{coll}}(b, s)S^{abs}(b, s)S_{\psi}^{sh}(b, s)S^{co}(b, s)d^2s}{\int \sigma_{AB}(b)N_{\text{coll}}(b, s)d^2s} \quad (1.14)$$

where:

- $N_{\text{coll}}(b)$  is the number of binary nucleon-nucleon collisions at a given impact parameter  $b$ :

$$N_{\text{coll}}(b) = \int N_{\text{coll}}(b, s) d^2s = \int \sigma_{pp} AB T_A(s) T_B(b-s) / \sigma_{AB}(s) d^2s \quad (1.15)$$

where  $A$  and  $B$  are the number of nucleons,  $\sigma_{pp}$  is the interaction cross-section in pp collisions,  $T_A(b)$  and  $T_B(b)$  are the nuclear profile functions, defined with the Wood-Saxon nuclear density (see Section 3.1) and  $s$  is the transverse coordinate, measured with respect to the center of one of the nuclei.

- $\sigma_{AB}(s) = 1 - \exp[-\sigma_{pp} AB T_{AB}(b)]$ , and  $T_{AB}(b) = \int T_A(s) T_B(b-s) d^2s$  is the nuclear overlap function.
- $S^{abs}$ ,  $S_{\psi}^{sh}$  and  $S^{co}$  denote the effects of the nuclear absorption, shadowing and interaction with the comoving matter respectively.

The number of charmonia in the final state  $N_{\psi}$  is described by a rate equation describing the suppression by interaction with the comover medium, but also the recombination by adding to the rate equation a term proportional to the squared density of the open charm production. For a given transverse coordinate  $s$ , impact parameter  $b$  and rapidity  $y$ , the rate equation describing the time evolution of  $N_{\psi}$  is:

$$\tau \frac{dN_{\psi}}{d\tau}(b, s, y) = -\sigma_{co} [N^{co}(b, s, y) N_{\psi}(b, s, y) - N_c(b, s, y) N_{\bar{c}}(b, s, y)] \quad (1.16)$$

where  $\sigma_{co}$  is the cross section of charmonium dissociation due to interaction with the co-moving medium of density  $N^{co}$ . The value of  $\sigma_{co}$  is fixed from fits to SPS data and assumed to be energy-independent. It has been found that  $\sigma_{co} = 0.65$  mb for the  $J/\psi$  and  $\sigma_{co} = 6$  mb for the  $\psi(2S)$  [133].

In this equation, the effective recombination cross-section is equal to the dissociation cross-section. This choice was made to not involve additional parameters with the inclusion of the recombination to the model. An approximate solution of Equation 1.16 is given by:

$$S^{co}(b, s, y) = \exp \left[ -\sigma_{co} \left( N^{co}(b, s, y) - \frac{N_c(b, s, y) N_{\bar{c}}(b, s, y)}{N_{\psi}(b, s, y)} \right) \ln \left( \frac{N^{co}(b, s, y)}{N_{pp}(0)} \right) \right] \quad (1.17)$$

where  $N_{pp}$  is the density of comovers in pp collisions.

The first term of the exponential corresponds to the solution of the rate equation with suppression only and is the survival probability of a charmonium interacting with comovers. It is proportional to the number of nucleon-nucleon collisions, corrected by a term of shadowing for light particles:  $N^{co} = N_{pp}N_{\text{coll}}(b, s)S_{ch}^{sh}$ .

The second term accounts for the recombination. The densities  $N_c$ ,  $N_{\bar{c}}$  and  $N_\psi$  are computed from their densities in pp collisions, with a correction factor due to the shadowing for heavy quark production:  $N_c(b, s) = N_c^{pp}N_{\text{coll}}(b, s)S_{HQ}^{sh}$ . A similar expression is found for  $N_{\bar{c}}$  and  $N_\psi$ .

The solution to the rate equation then becomes:

$$S^{co}(b, s, y) = \exp \left[ -\sigma_{co} \left( N^{co}(b, s, y) - \frac{(d\sigma_{pp}^{c\bar{c}}/dy)^2}{\sigma_{pp}d\sigma_{pp}^\psi/dy} N_{\text{coll}}(b, s)S_{HQ}^{sh} \right) \ln \left( \frac{N^{co}(b, s, y)}{N_{pp}(0)} \right) \right] \quad (1.18)$$

The value of  $\sigma_{pp}^\psi$  can be extracted from the experimental pp data or a model using extrapolation of experimental results. The value of the production cross-section of  $c\bar{c}$  pairs  $\sigma_{pp}^{c\bar{c}}$  is estimated from experimental measurements, but is not known precisely. The choice of  $\sigma_{pp}^{c\bar{c}}$  is one of the major uncertainties in the model.

### Transport Model

The Transport Model (TM) [129, 134, 135] describes the evolution of the system dynamically. The charmonium production is caused by constant dissociation and recombination of the  $c\bar{c}$  induced by light partons  $p$ :  $p + \psi \longleftrightarrow c + \bar{c} + p$ .

It is assumed that the medium can be described by an isentropically expanding fireball, which includes an initial QGP phase followed by a hadronic phase, connected via a mixed-phase. Charmonia are considered as an external heavy probe, whose evolution through the expanding medium can be described by a Boltzmann equation. From that equation, the time evolution of the number of charmonium can be described by a simplified rate equation:

$$\frac{dN_\psi}{d\tau} = -\Gamma_\psi(T)[N_\psi - N_\psi^{eq}(T)] \quad (1.19)$$

where  $\Gamma_\psi(T)$  is the dissociation (and formation) rate for the process described before. This rate is dependent on the temperature  $T$ , induced by the density of the light partons, but also dependent on the charmonium binding energy. The stronger the binding energy is, the smaller the corresponding dissociation rate is.

The equilibrium limit  $N_{\psi}^{eq}(T)$  controls the gain term. This term is switched off when the temperature of the medium is above the dissociation temperature of the charmonium  $T_{diss}^{\psi}$ , meaning that the  $\psi$  formation is prohibited if the bound state cannot be supported by the medium. This term is dependent on the number of charm quark pairs in the fireball, and therefore depends on the production cross-section  $\sigma_{c\bar{c}}$ . Cold nuclear matter effect such as the shadowing are taken into account in the determination of  $\sigma_{c\bar{c}}$ . This value of  $\sigma_{c\bar{c}}$  and its shadowing is the main uncertainty in the model.

### Statistical Hadronization Model

In the Statistical Hadronization Models (SHM) [136, 137], charmonium states are completely dissociated in the QGP and quarkonium production only occurs through statistical hadronization of the charm quarks at the phase boundary (meaning the transition between the plasma and the hadronic gas).

The only free parameters within the model are the number of initial produced charm quarks  $N_c$ , the chemical freeze-out temperature  $T$ , the baryonic chemical potential  $\mu_B$  and the volume of the fireball  $V$ . It is assumed that all the charm quarks are produced at the primary hard collisions and their number stays constant until hadronization. It is also assumed that there is thermal equilibration in the QGP, at least near the critical temperature  $T_c$ .

The total number of charm quarks is determined by using the charm production cross section  $\sigma_{c\bar{c}}$  measured in pp collisions and extrapolated to nucleus-nucleus collisions assuming scaling with the number of hard scatterings and inclusion of gluon shadowing.

The temperature and baryonic chemical potential are obtained from fits and can be parametrized as a function of  $\sqrt{s_{NN}}$  with the expressions:  $T = T_{lim}/[1 + \exp(2.60 - \ln(\sqrt{s_{NN}}(GeV)/0.45)]$  and  $\mu_B[MeV] = 1303/[1 + 0.286\sqrt{s_{NN}}(GeV)]$ , with the limiting temperature  $T_{lim} = 164$  MeV [138].

When looking at the centrality dependence of the charmonium production in nucleus-nucleus collisions, it is important to properly account for the so-called "corona effect". In a nucleus, the nucleon density can be described with the Woods-Saxon models (see Section 3.1). In this model, the density is the highest in the center of the nuclei and decreases with the distance from the center. Therefore, only the nucleons from the core of the colliding nuclei participate in the formation of the hot fireball, where QGP is produced, whereas nucleons from the surface of the nuclei cannot form a plasma. To account for this effect, the core is treated as QGP using the SHM and the

corona as a superposition of nucleon-nucleon collisions, corresponding to a local nuclear modification factor equal to unity. Since the SHM applies only to the QGP zone, and since charmonium production in nucleon-nucleon collisions is, in general, very different from that predicted in the SHM, it is relevant to distinguish between core and corona: for peripheral collisions, the majority of nucleons involved are corona nucleons and in central collisions, the majority of nucleons involved are core nucleons.

## 1.6 Experimental Results from SPS to LHC

Ultra-Relativistic Heavy ion collisions have been first studied at the Super Proton Synchrotron (SPS), then at the Relativistic Heavy Ion Collider (RHIC), in particular with the PHENIX and STAR experiments and now at the Large Hadron Collider (LHC), in particular with ALICE. The phenomena described in the previous sections have been studied in these different experiments, and in this section we will present the most important results regarding charmonium production.

### 1.6.1 Super Proton Synchrotron

At SPS, the formation of the QGP was expected with a low temperature, close to the critical temperature  $T_c$ . The charmonium production was studied in fixed target collisions with the muon spectrometers of the experiments NA38, NA50 and NA60, with collisions of type pp, pA, Pb – Pb and In – In, with a center of mass energy of  $\sqrt{s_{NN}} = 17.3$  GeV. The cold nuclear matter effects were attested, in particular the gluon shadowing, the nuclear absorption and the anti-shadowing [139].

In February 2000, the CERN released a press document announcing that the different experiments found evidences of the formation of a deconfined medium in Pb – Pb collisions. Several observables were measured, such as enhancement of the strange quarks production and the correlation between hadron pairs. In particular, a decrease of the  $J/\psi$  production was measured and more pronounced than what was expected with only CNM effects.

This is illustrated in Figure 1.16, where the ratio between observed and expected  $J/\psi$  is presented as a function of  $N_{\text{part}}$ . The data in In – In from NA60 and in Pb – Pb from NA50 at a beam energy of 158 GeV per nucleon are compared. The analysis is performed in the rapidity domain  $0 < y < 1$ . It is observed that for the most central collisions, a decrease of 25% is visible

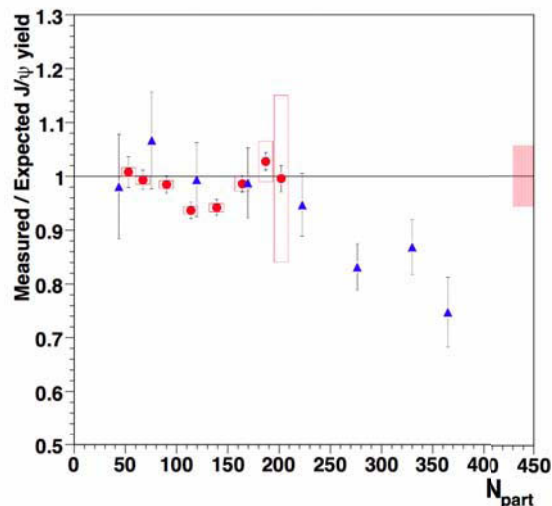


Figure 1.16: Measurement of  $J/\psi$  normalized to only Drell-Yann production and CNM performed by NA60 (circles) and NA50 (triangles) in In-In and Pb-Pb collisions, respectively [140].

in the  $J/\psi$  production with respect of what is expected with only the Cold Nuclear Matter effects. This is referred to as the anomalous  $J/\psi$  suppression.

### 1.6.2 Relativistic Heavy Ion Collider

The RHIC is located at the Brookhaven National Laboratory, on Long Island in the state of New York, USA. It can perform collisions in pp, d-Au, Cu-Cu, Au-Au, U-U, and Cu-Au, with a center of mass energy up to  $\sqrt{s_{NN}} = 200$  GeV in Au-Au collisions.

At RHIC, a clear suppression of the  $J/\psi$  was observed in Au-Au collisions. Figure 1.17 (left) shows the  $J/\psi$  nuclear modification factor (see Section 3 page 76) measured by the PHENIX experiment [141] at mid-rapidity ( $|y| < 0.35$ ) in the dielectron decay channel and at forward rapidity ( $1.2 < |y| < 2.2$ ) in the dimuon decay channel. A suppression of the  $J/\psi$  is observed in both rapidity ranges for the most central collisions, with an increase of the suppression with the centrality. In the most peripheral events, the  $R_{AA}$  is equal to unity.

The PHENIX results are also compared to the SPS results in Figure 1.17

(right), where the measured  $J/\psi$   $R_{AA}$  corrected by the CNM effects is plotted as a function of the charged particles multiplicity per unit of rapidity, measured at mid-rapidity. Both experiments exhibit the same trend for the  $J/\psi$  suppression, even if the center of mass energy differs by more than one order of magnitude.

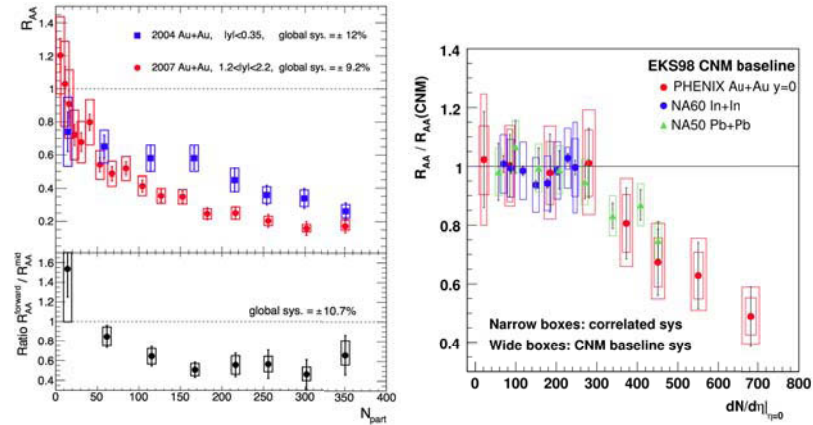


Figure 1.17: Left panel: Measured  $J/\psi$  nuclear modification factors  $R_{AA}$  vs  $N_{part}$ . The lower panel shows the ratio of forward rapidity (circles, red) to mid-rapidity (squares, blue) for the points in the upper panel [142]. Right panel:  $R_{AA}$  corrected by the CNM effects as a function of the charged particle multiplicity for NA50, NA60 and PHENIX [143].

Figure 1.18 presents the  $J/\psi$  nuclear modification factor as a function of rapidity measured by the PHENIX experiment in d Au collisions. The comparison with the EPS09 parametrization points towards evidences of gluon shadowing effects [144].

### 1.6.3 Large Hadron Collider

The LHC collides Pb nuclei with a center of mass energy per nucleon-nucleon collision up to  $\sqrt{s_{NN}} = 5.02$  TeV. At this energy scale, the QGP is expected to have a lifetime of several fm/c [146], and the temperature of the plasma is expected to be above  $2T_c$ , which is enough to completely suppress the  $J/\psi$ .

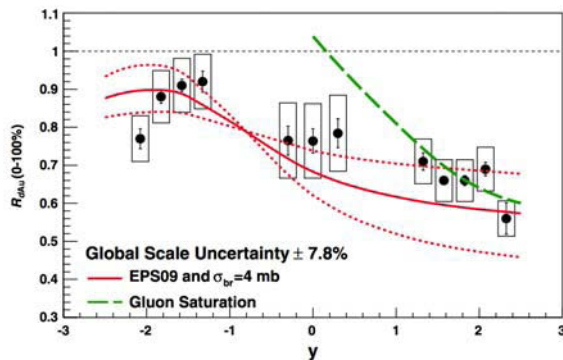


Figure 1.18:  $J/\psi$  nuclear modification factor in the centrality range 0-100% as a function of rapidity in d Au collisions measured by PHENIX [144]. Results are compared to EPS09 calculations [113] and calculations incorporating gluon saturation effects [145].

### Results in pp collisions

Measurements of the  $J/\psi$  and  $\psi(2S)$  production cross-sections in pp collisions have been performed at the LHC in a wide range of energies, as illustrated in Figure 1.19. This figure presents the production cross-section for  $J/\psi$  (left) and  $\psi(2S)$  (right) as a function of  $p_T$  for different energies. The increase in the collision energy and luminosity allows to reach higher  $p_T$  values. A hardening of the  $p_T$  spectra with increasing collision energy is observed. Moreover, for the  $J/\psi$  cross-section at  $\sqrt{s} \geq 7$  TeV, a change in the slope at high  $p_T$  is observed, which is attributed to the contribution from non-prompt  $J/\psi$ . For the  $\psi(2S)$ , because of the smaller cross-section with respect to the  $J/\psi$ , the statistical uncertainties are larger and the  $p_T$  reach is smaller.

Comparison to models have been done at all energies, and the results for the collision energy of  $\sqrt{s} = 13$  TeV are presented in Figure 1.20. At low  $p_T$ , the results are compared to a sum of a prompt charmonium leading order NRQCD calculation coupled to a CGC description of the low- $x$  gluons in the proton [148] and a non-prompt Fixed-Order Next-To-Leading Logarithm (FONLL) calculation [149]. At high- $p_T$ , the results are compared to a prompt charmonium Next-to-Leading-Order NRQCD calculation [150] summed with a FONLL calculation to account for the non-prompt contribution, which increases at high  $p_T$ . A good description of the data for both

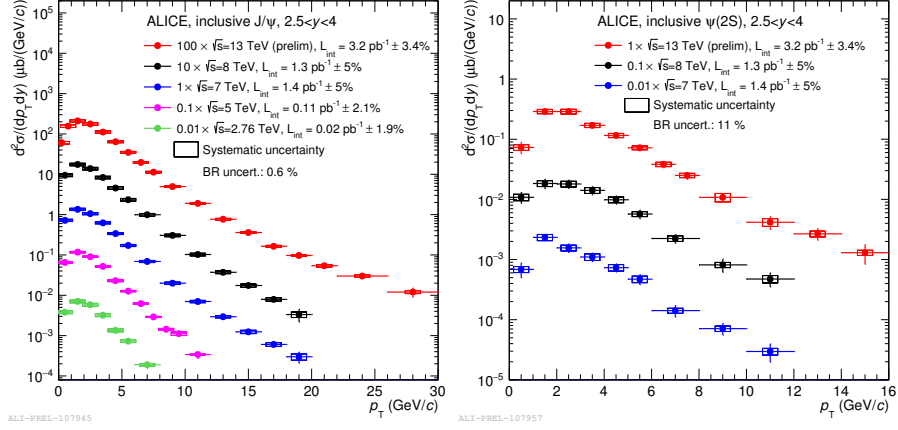


Figure 1.19:  $J/\psi$  production cross-section in pp collisions at  $\sqrt{s}=2.76, 5, 7, 8,$  and  $13$  TeV (left) and  $\psi(2S)$  production cross-section in pp collisions at  $\sqrt{s}=7, 8,$  and  $13$  TeV (right) as a function of  $p_T$  [147].

$J/\psi$  and  $\psi(2S)$  is obtained in the full  $p_T$  range.

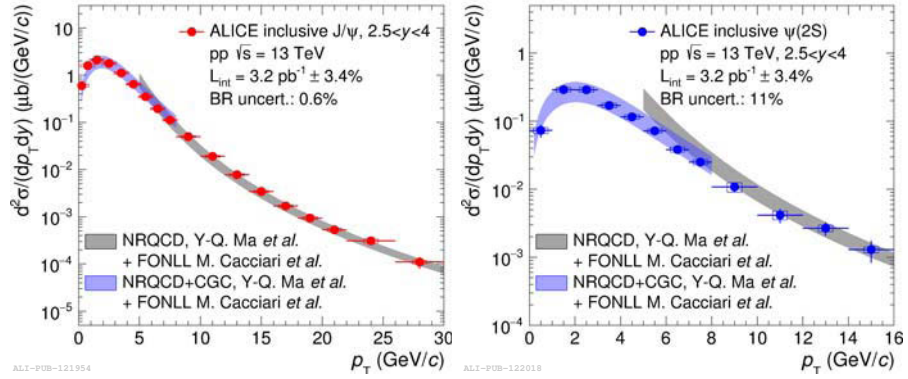


Figure 1.20:  $J/\psi$  (left) and  $\psi(2S)$  (right) production cross-sections in pp collisions at  $\sqrt{s} = 13$  TeV compared to NLO NRQCD summed with FONLL calculations (grey) and LO NRQCD summed with FONLL calculation and CGC (blue) [147].

Measurement of the  $J/\psi$  polarization were also performed at  $\sqrt{s} = 7$  TeV and are shown in Figure 1.21. The study was performed in the kinematic

region  $2.5 < y < 4$  and  $2 < p_T < 8$  GeV/ $c$ , in the Helicity and Collins-Soper reference frames. In both frames, the polarization parameters are compatible with zero, within uncertainties.

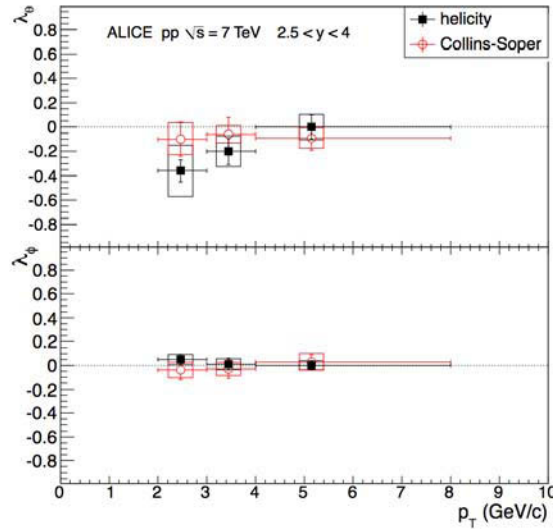


Figure 1.21:  $\lambda_\theta$  and  $\lambda_\phi$  parameters of the inclusive  $J/\psi$  polarization as a function of  $p_T$ , measured in the Helicity (closed squares) and Collins-Soper (open circles) reference frames [151].

### Results in p-Pb collisions

Measurements in p-Pb collisions have been performed in ALICE at a collision energy of  $\sqrt{s_{NN}} = 5.02$  TeV in order to study CNM effects. The nuclear modification factor  $R_{pA}$  for  $J/\psi$  and  $\psi(2S)$  are presented in Figure 1.22, both in the forward and in the backward rapidity regions, as a function of  $N_{coll}$ . Results are compared to theoretical models with only shadowing effects [133, 152], only coherent parton energy loss effects [153], and final states interactions [129, 133].

At backward rapidity, values show that the  $J/\psi$   $R_{pA}$  is compatible with unity within uncertainty, indicating that the  $J/\psi$  production would scale with  $N_{coll}$  between pp and pA. On the contrary the  $\psi(2S)$  exhibits a significant suppression. At forward rapidity, both  $J/\psi$  and  $\psi(2S)$  are suppressed for all the considered centrality classes, with a stronger suppression for the

$\psi(2S)$ . While the  $J/\psi$  results are reproduced by shadowing or energy loss calculations, additional final state effects have to be included to describe the  $\psi(2S)$  results.

A recent measurement of the  $R_{pA}$  at an energy of  $\sqrt{s_{NN}} = 8.16$  TeV was performed, and the corresponding values as a function of rapidity are presented in Figure 1.23. Results show a good agreement with models, and are compatible with the previous measurement at  $\sqrt{s_{NN}} = 5.02$  TeV.

### Elliptic flow

Measurements of the  $J/\psi$  elliptic flow (see Section 1.4.2) were performed at  $\sqrt{s_{NN}} = 2.76$  and  $\sqrt{s_{NN}} = 5.02$  TeV. This measurements were highly anticipated as a contribution of the  $J/\psi$  from recombination could lead to a positive value of the  $v_2$ . Results at both energies are presented in Figure 1.24, where the  $v_2$  for the centrality range 20-40% is presented as a function of  $p_T$ . Results at both energy are compatible within uncertainties and a significantly positive  $v_2$  is observed at the collision energy of  $\sqrt{s_{NN}} = 5.02$  TeV. This indicates that a large fraction of the  $J/\psi$  production comes from regeneration, as it shows that  $J/\psi$  thermalize in the QGP.

### Nuclear Modification Factor

Measurements of the  $J/\psi$  nuclear modification factor have been performed in Pb – Pb collisions at  $\sqrt{s_{NN}} = 2.76$  TeV and  $\sqrt{s_{NN}} = 5.02$  TeV. Results as a function of centrality are presented in Figure 1.25 (top), compared to the results from PHENIX in Au – Au at  $\sqrt{s_{NN}} = 0.2$  TeV. A suppression of the  $J/\psi$  for central and mid-central collisions is observed both in PHENIX and ALICE data, however the suppression is less important in ALICE despite the much higher collisions energy. This is explained by the fact that at the LHC energies, the recombination becomes sufficiently important to have a visible effect, whereas at the RHIC energies, only the suppression of the  $J/\psi$  is observable. In ALICE, results between the  $\sqrt{s_{NN}} = 2.76$  TeV collision energy and  $\sqrt{s_{NN}} = 5.02$  TeV are compatible within uncertainties.

Figure 1.25 (bottom) presents the comparison between the results at  $\sqrt{s_{NN}} = 5.02$  TeV and several theoretical models. A  $p_T$  cut  $p_T > 0.3$  GeV/ $c$  is applied in order to remove the contribution from the photo-produced  $J/\psi$ , which is not included in the models. Models and data are compatible within uncertainties, however for the Transport Models and the Co-mover Interaction Model, a better agreement is found with the upper limit of the models, which corresponds for the Transport Model to an absence of gluon shadow-

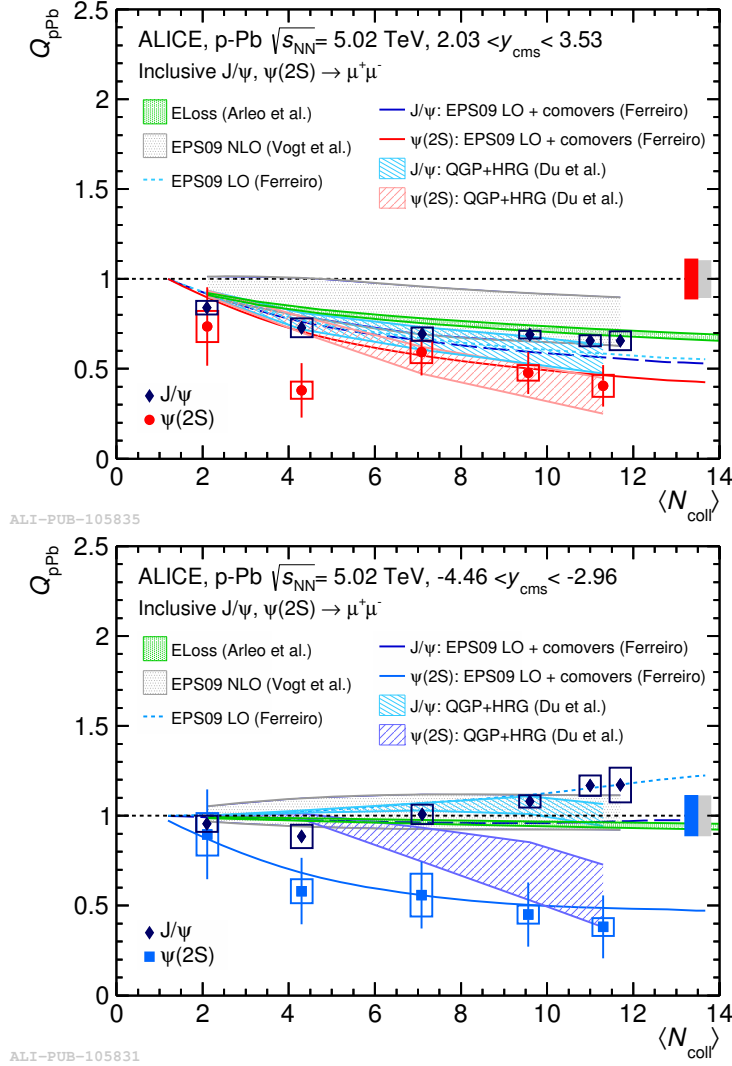


Figure 1.22:  $J/\psi$  and  $\psi(2S)$   $R_{pA}$  at  $\sqrt{s_{NN}} = 5.02$  TeV as a function of  $N_{\text{coll}}$  at forward (top) and backward (bottom) rapidities compared to models [129, 133, 152, 153]. The boxes around unity correspond to the global  $\psi(2S)$  systematic uncertainties at forward (red box) and backward (blue box) rapidities. The grey box is a global systematic uncertainty common to both  $J/\psi$  and  $\psi(2S)$  [154].

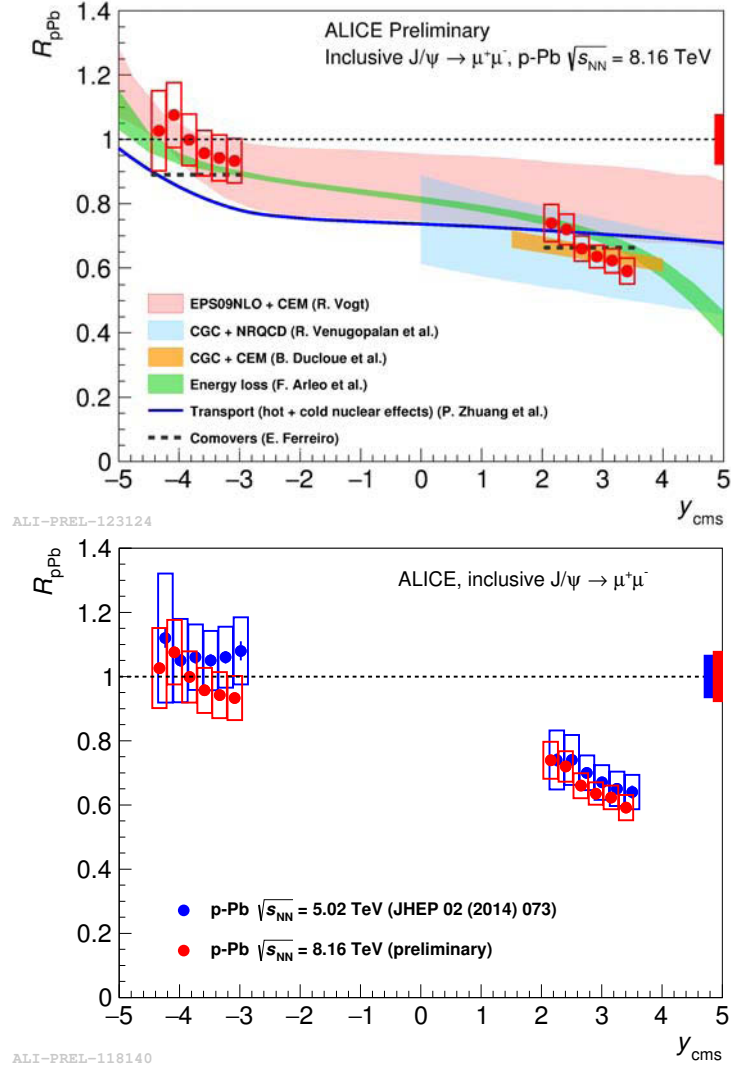


Figure 1.23:  $J/\psi$   $R_{pA}$  at  $\sqrt{s_{\text{NN}}} = 8.16$  TeV as a function of  $y$  compared to models (top) and with results at  $\sqrt{s_{\text{NN}}} = 5.02$  TeV (bottom) [155].

ing. This is a surprising result considering that the gluon shadowing has been attested in several experiments, including ALICE as shown previously.

Figure 1.26 presents the  $p_T$  dependence of the  $J/\psi$   $R_{AA}$  in three different centrality bins, compared to transport model calculations. A stronger sup-

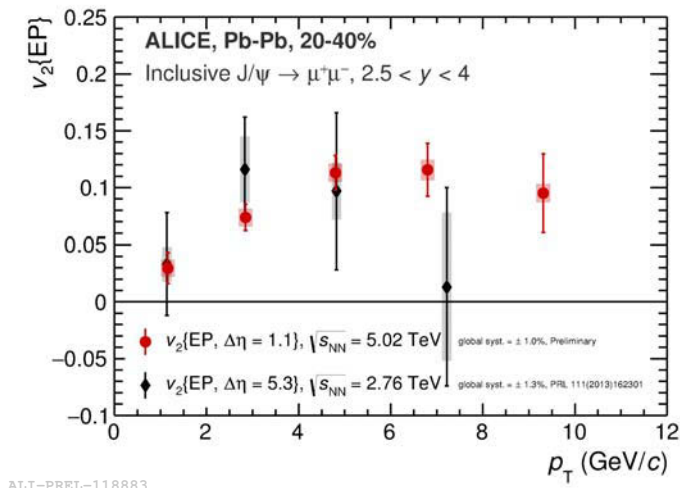


Figure 1.24:  $J/\psi$  elliptic flow in the centrality range 20-40% as a function of rapidity at  $\sqrt{s_{NN}} = 2.76$  TeV (black) and  $\sqrt{s_{NN}} = 5.02$  TeV (red) [155].

pression is observed at high  $p_T$  and in central collisions, as expected from models including a strong regeneration component and one can conclude that the regenerated  $J/\psi$  are at low  $p_T$ . When comparing the results with the measurements at  $\sqrt{s_{NN}} = 2.76$  TeV, both measurements are compatible within uncertainties.

#### $\psi(2S)$ -to- $J/\psi$ ratio

Measurements of the  $\psi(2S)$ -to- $J/\psi$  ratio in Pb – Pb collisions were performed in ALICE at  $\sqrt{s_{NN}} = 2.76$  TeV. Figure 1.27 presents the results in two different  $p_T$  bins. When the signal could not be extracted, a 95% confidence limit is quoted.

The Single Ratio (Figure 1.27 left), meaning the  $\psi(2S)$ -to- $J/\psi$  production cross-section ratio, is compared to the NA50 measurement and SHM predictions. Results are in agreement within uncertainties with the model prediction, and with the NA50 data. Therefore, no evidence of energy dependence or rapidity dependence of the single ratio could be found.

The Double Ratio (Figure 1.27 right), which is the ratio of nuclear modification factors, is compared to Transport Model calculations. Results and model are compatible within uncertainties. In the most central bin for

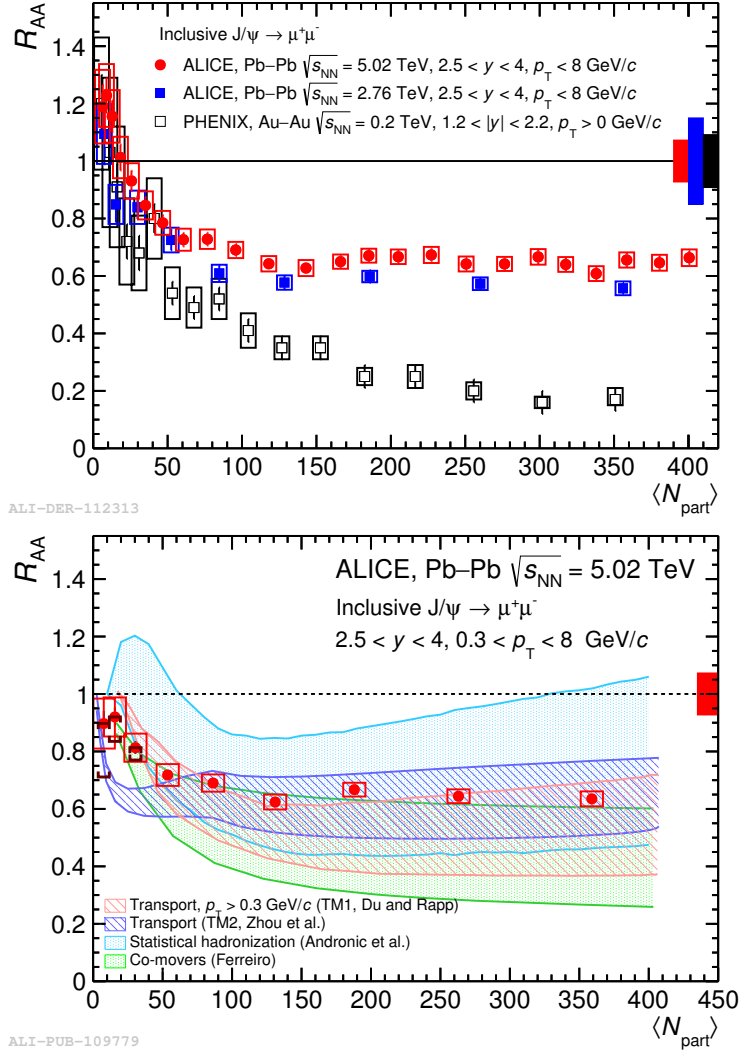


Figure 1.25: Top: Inclusive  $J/\psi$   $R_{AA}$  as of function of  $N_{part}$  measured in Pb – Pb collisions at  $\sqrt{s_{NN}} = 2.76$  TeV and  $\sqrt{s_{NN}} = 5.02$  TeV compared to PHENIX measurement in Au – Au collisions at  $\sqrt{s_{NN}} = 0.2$  TeV [156, 157]. Bottom: Inclusive  $J/\psi$   $R_{AA}$  as of function of  $N_{part}$  with a cut  $p_T > 0.3$  GeV measured in Pb – Pb collisions at  $\sqrt{s_{NN}} = 5.02$  TeV compared to models [157].

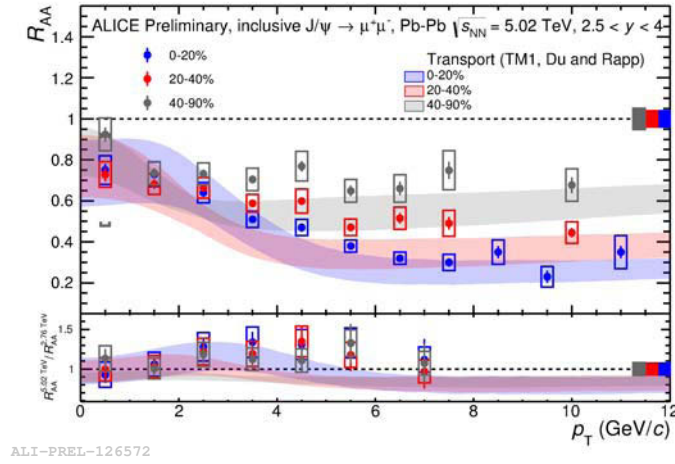


Figure 1.26: Inclusive  $J/\psi$   $R_{AA}$  at  $\sqrt{s_{NN}} = 5.02$  TeV as a function of  $p_T$  measured in three different centrality bins, compared to Transport Model Calculations. The lower panel presents the ratio of this  $R_{AA}$  with respect to the  $\sqrt{s_{NN}} = 2.76$  TeV [158].

$0 < p_T < 3$  GeV/ $c$ , there is an indication of a stronger suppression for the  $\psi(2S)$  than the  $J/\psi$ . In all the other bins, the results do not allow a firm conclusion since statistical fluctuations allow the data points to range between very low double ratios (stronger  $\psi(2S)$  suppression with respect to  $J/\psi$ ) to values higher than unity (less  $\psi(2S)$  suppression with respect to  $J/\psi$ ).

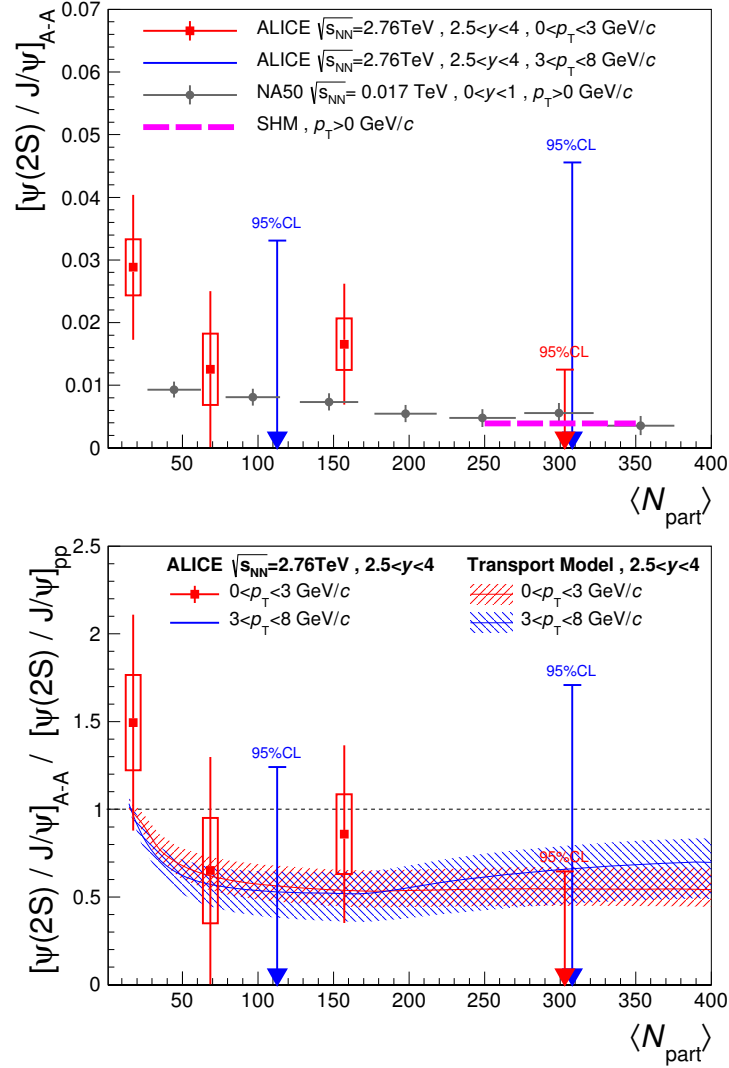


Figure 1.27: Inclusive  $\psi(2S)$ -to- $J/\psi$  ratio measured as a function of centrality in Pb – Pb collisions at  $\sqrt{s_{NN}} = 2.76$  TeV for two  $p_T$  intervals, compared to NA50 results [159] and to a theoretical calculation [160] (left). Double ratio as a function of centrality, between the  $\psi(2S)$  and  $J/\psi$  measured in Pb – Pb collisions at  $\sqrt{s_{NN}} = 2.76$  TeV and pp collisions at  $\sqrt{s} = 7$  TeV, compared to theoretical calculations [161] (right) [156].

## Chapter 2

# The ALICE Detector

The Large Hadron Collider (LHC) at CERN is the largest particle accelerator in the world. There are four major experiments at the LHC and in particular, the ALICE experiment is dedicated to the study of the Quark-Gluon Plasma (QGP) through the collisions of lead nuclei.

In this chapter, the LHC and the main experiments installed on the accelerator will be presented. Then the detectors of the ALICE experiment will be described, focusing on the Muon Spectrometer, which provides the data for the analysis presented in this thesis.

## 2.1 ALICE at the LHC

### 2.1.1 General description of the LHC

The LHC is located across the border between France and Switzerland and is part of the European Organization for Nuclear Research (CERN) complex. With a circumference of 27 km, it is composed of two beam pipes in which protons or nuclei can be accelerated [6, 162, 163, 164, 165]. These beam pipes intersect in four points where the major LHC experiments are placed. The LHC is designed to produce a beam energy of  $7Z/A$  TeV, with  $Z$  being the number of protons and  $A$  the total number of nucleons in the nuclei. In pp collisions it corresponds to an energy in the center of mass frame of 14 TeV per collisions, and in Pb – Pb collisions ( $Z = 82$  and  $A = 208$ ) to a center of mass energy of 5.5 TeV per nucleon-nucleon collision.

In order to achieve the nominal energy for the particle bunches, several accelerators are involved, as presented in Figure 2.1. For pp collisions, protons are taken from a bottle containing hydrogen atoms that are stripped from their electrons. The protons are then accelerated by a linear accelerator called LINAC 2, next they are injected in the Proton Synchrotron (PS) before going in the SPS. After being accelerated at an energy of 450 GeV, protons are injected in bunches in the LHC, where they reach the desired energy.

For Pb – Pb collisions, the acceleration process is quite similar. Lead ions are produced from a highly purified lead sample that is heated to a temperature of about 1073 K. The lead vapor is ionized by an electric current. The LINAC 3 accelerator first accelerates the Pb nuclei, then they go through a carbon foil which strips the nuclei from most of their electrons (reaching a charge as high as  $Pb^{54+}$ ). Then they go in the Low-Energy Injection Ring (LEIR) before being injected in the PS, and then the SPS after

Year	Collision Type	Energy at the center of mass
2009	pp	0.9 TeV
2010-2011	pp	7 TeV
2011	Pb – Pb & pp	2.76 TeV
2012	pp	8 TeV
2013	p – Pb	5.02 TeV
2015	pp	13 TeV
2015	Pb – Pb & pp	5.02 TeV
2016	pp	13 TeV
2016	p – Pb	8.16 TeV

Table 2.1: Summary of the collisions performed at the LHC.

first passing it through a second foil where it is fully stripped to  $Pb^{82+}$ . Finally, beam are sent in the LHC where the intended collision energy is reached.

The different types of collisions that have been carried at the LHC are summarized in Table 2.1. The LHC has progressively increased the collision energy until reaching 13 TeV in pp collisions, and 5.02 TeV in Pb – Pb collisions.

Besides the energy of the collision, another important parameter to consider is the collision rate. The number of events per second generated in the collisions is given by  $N_{events} = \sigma_{event} \cdot \mathcal{L}$ , where  $\sigma_{event}$  is the cross-section of the event and  $\mathcal{L}$  the instantaneous luminosity. This instantaneous luminosity is defined as:

$$\mathcal{L} = \frac{N_1 \cdot N_2 \cdot f}{A_{eff}} \quad (2.1)$$

where  $N_1$  and  $N_2$  are the two beam intensities,  $f$  is the accelerator revolution frequency and  $A_{eff}$  is the effective beam crossing area. The luminosity is not constant over a physics run, and decreases due to the degradation of the intensity and emittance of the circulating beams, mainly due to the beam loss from collisions. The integrated luminosity  $L_{int}$ , which is the instantaneous luminosity integrated over the run period, is used to describe the quantity of events collected by an experiment and is expressed as the inverse of a cross section.

To determine the integrated luminosity, the van der Meer technique [166]

is used. The value of  $A_{eff}$  is determined by doing the van der Meer scan, that consists in independently moving the two beams along the vertical and horizontal direction. During a van der Meer Scan, one can also measure the cross section of any reference process (or trigger) using:  $\sigma_{ref} = R_{ref}/\mathcal{L}$ , where  $R_{ref}$  is the trigger rate of the process in question and  $\mathcal{L}$  is the luminosity given by Equation 2.1. The values of  $N_1$  and  $N_2$  are given by the LHC instrumentation. The same  $\sigma_{ref}$  is then used during the data taking to calculate back the integrated luminosity corresponding to a given data sample by dividing the integrated number of triggers for the reference process by the corresponding cross-section  $\sigma_{ref}$ . A more detailed description of the luminosity determination can be found in [167] and in [168] for the pp runs at 13 TeV of 2016.

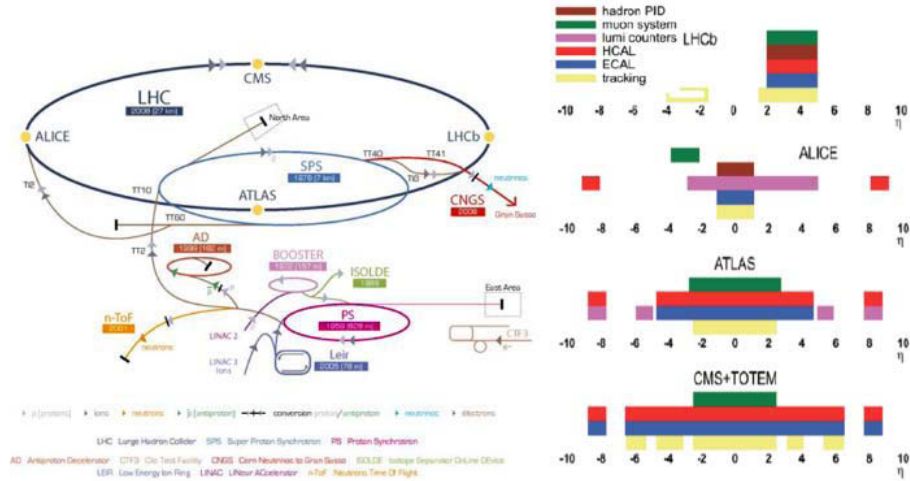


Figure 2.1: Schematic of the CERN accelerator complex (left) and angular coverage of the different detectors for the four main LHC experiments (right) [169].

The four largest experiments at the LHC are built around the points where the LHC beams intercept and are:

- ATLAS (A Toroidal LHC Apparatus) [170] is a detector mainly dedicated to the search of the Higgs boson, but also to beyond Standard Model physics (super-symmetric particles and dark matter candidates). It is the largest detector ever built for a collider.

- CMS (Compact Muon Solenoid) [171] is, as ATLAS, dedicated to the study of the Higgs boson, but uses different technical solutions and designs for its detectors. CMS is also involved in the search of beyond SM particles.
- LHCb (Large Hadron Collider beauty) [172] is dedicated to the study of the violation of the CP symmetry and to the rare phenomena in the heavy flavor decay, mainly through the decay of beauty hadrons.
- ALICE (A Large Ion Collider Experiment) [173] is the only experiment dedicated to the study of heavy ion collisions and in particular the formation of the Quark Gluon Plasma (QGP). It is described in more detail in Section 2.1.2.

Even if ALICE is the only experiment specifically designed for the study of heavy ions, all four experiments have a heavy ion program and are complementary in terms of transverse momentum and pseudo-rapidity coverage, thanks to different detector designs. Figure 2.1 (right) illustrates the angular coverage of the different sub-detectors for these four experiments. For instance, ALICE can measure charmonia at mid-rapidity in the dielectron decay channel and at forward rapidity  $2.5 < y < 4.0$  in the dimuon decay channel, whereas ATLAS and CMS are equipped of muons detectors in the mid-rapidity region. Because of its weaker magnetic field, ALICE can study the charmonium down to  $p_T = 0$  GeV/ $c$ , where ATLAS and CMS cannot go down to  $p_T = 0$  GeV/ $c$  but can reach a much higher resolution for muon detection at high  $p_T$ .

### 2.1.2 Description of the ALICE detector

ALICE is a heavy ion experiment designed to study the Quark-Gluon Plasma produced in ultra-relativistic heavy ion collisions [173, 174, 175]. It allows a comprehensive study of hadrons, electrons, muons, and photons produced during the collisions.

ALICE is optimized for a charged particle multiplicity of  $dN/d\eta = 4000$ . During the Pb – Pb collisions at  $\sqrt{s_{NN}} = 5.02$  TeV, the charged particle multiplicity reaches  $dN/d\eta \approx 2000$  [176].

In order to systematically study all the products of the collisions, ALICE employs all the known particle identification techniques: energy loss, time of flight, transition and Cherenkov radiation, electromagnetic calorimetry, muon filters and topological decay reconstruction. ALICE uses high-

granularity but slow detectors, which limits the maximum interaction rate that can be supported by the detector.

A scheme of the ALICE experiment is shown in Figure 2.2. The first concepts for heavy-ion detectors at the LHC were proposed in 1990 and the ALICE experiment was approved in 1997. Today, ALICE is a collaboration of over 1800 members, 174 institutes over 42 countries. The detector has an overall dimension of  $16 \times 16 \times 26 \text{ m}^3$  with a total weight of approximately 10 000 tons. ALICE has a total of 18 sub-detectors and consists in a central barrel, embedded in a large solenoid magnet L3 and a muon spectrometer. The side of the Muon Spectrometer is the forward direction, the opposite side is the backward direction.

The central barrel covers the pseudo-rapidity range  $|\eta| < 0.9$  and measures hadrons, electrons and photons. It contains from the inside out: the Inner Tracking System (ITS), the Time Projection Chamber (TPC) the Time-Of-Flight detector (TOF), the Transition Radiation Detector (TRD), the High Multiplicity Particle Identifier (HMPID) and two Electromagnetic Calorimeters, PHOS and EMCal. On top of the L3 magnet, a cosmic ray detector is located. A more complete description of these detectors can be found in Section 2.2. Several smaller detectors for global event characterization are located at small angles and are described in Section 2.3.

The Muon Spectrometer is located in the forward direction, covering the pseudo-rapidity range  $-4.0 < \eta < -2.5$ . It is composed of several absorbers, a dipole magnet, five stations of Tracking Chambers and two stations of Trigger Chambers. It measures essentially muons, as its names indicates. Since the main detectors used in this analysis compose the Muon Spectrometer, a more detailed description of the apparatus can be found in Section 2.4.

The detectors and their performances are described in the following section, but a more complete description can be found in [173, 175, 177, 178].

ALICE uses a system of cartesian coordinates, where the z-axis is along the beam line and towards the opposite side of the Muon Spectrometer and the y-axis is vertical.

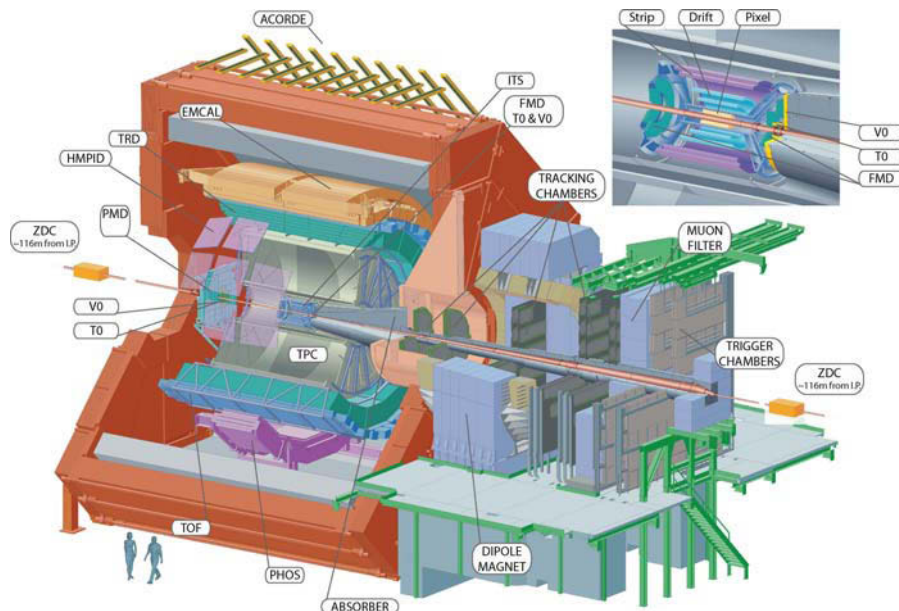


Figure 2.2: Schematic of the ALICE detector.

## 2.2 Detectors from the Central Barrel

### 2.2.1 The Inner Tracking System (ITS)

The main purposes of the Inner Tracking System [179] are to localize the primary vertex, to reconstruct the secondary vertices from the decays of hyperons<sup>1</sup>, D and B mesons, to track and identify charged particles with low momentum ( $< 100 \text{ MeV}/c$ ), to improve the momentum and angle resolution for particles reconstructed by the Time-Projection Chamber and to reconstruct particles going through dead regions of the TPC. Because of these many purposes, the ITS detector participates in almost every physics analysis of ALICE.

The ITS surrounds the beam pipe and is composed of six cylindrical layers of silicon detectors, which covers the rapidity range  $|\eta| < 0.9$ . The two innermost layers are composed of Silicon Pixel Detectors (SPD), the two middle layers are composed of Silicon Drift Detectors (SDD) and the two outer layers are equipped with Silicon micro-Strip Detectors (SSD). For

<sup>1</sup>Hyperons are baryons containing at least one strange quark.

muon analyses, only the SPD layers are used.

The SPD is fundamental in the determination of the position of the primary vertex corresponding to the interaction point, which is the point where the primary particles are produced. Its position is determined by finding the space point where the maximum number of tracks converge. The four outer layers are used for particle identification by measuring the energy-loss  $dE/dx$  as they pass through the silicon detectors.

Once the primary vertex and the tracks of the particles are reconstructed using the ITS, TPC and TOF, the ITS is used to determine the secondary vertices by selecting the tracks in the ITS for which the point of closest approach to the primary vertex exceeds a certain distance.

The ITS is optimized to work in an environment with a very high density of particles and can detect simultaneously more than 15 000 particles.

## 2.2.2 The Time-Projection Chamber (TPC)

The Time-Projection Chamber (TPC) [180, 181] is the main tracking detector of the central barrel and provides charged particle momentum measurement, particle identification and vertex determination together with the SPD. The TPC is described in Figure 2.3. It is made of a cylindrical field cage of 5 m length, 85 cm of inner radius and 2.5 m of outer radius for a volume of 90 m<sup>3</sup>, filled with mixture of a Ne/CO<sub>2</sub>/N<sub>2</sub> gas. The detector covers the pseudo-rapidity range  $|\eta| < 0.9$  and is divided in two regions by a thin high voltage surface. The two endplates are covered with the readout chambers. The gas is ionized when a particle goes through it. The free electrons drift towards the end plates for a distance up to 2.5 m, where a set of 18 trapezoidal sectors of readout pads are installed to collect the signal.

The TPC is the largest detector of this kind ever built. Because of its dimension, it can take up to 94  $\mu$ s for the signal to reach the readout pads, making the TPC the slowest detector in ALICE. The TPC reaches a spatial resolution of 1.1 mm along the  $x$  and  $y$  axis and 1.25 mm along the  $z$  axis near the inner cylinder and 0.8 mm along the  $x$  and  $y$  axis and 1.1 mm along the  $z$  axis near the outer cylinder.

The particle identification is performed by measuring its charge over momentum ratio and specific energy loss  $dE/dx$ , which is the kinetic energy loss in the matter and is described by the Bethe-Bloch formula [182].

The TPC is also the starting point to the track reconstruction in the Central Barrel: following an inward-outward-inward scheme [183, 184], the tracks reconstructed in the TPC are propagated to the ITS and used as

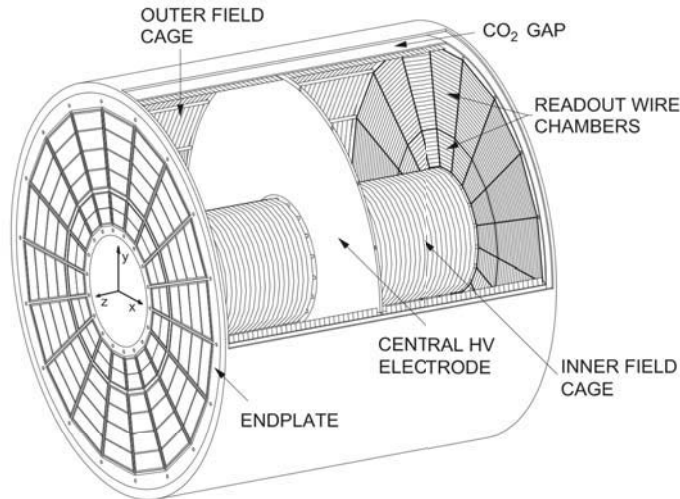


Figure 2.3: 3D view of the TPC. The high voltage electrode is located at the center of the drift volume. The endplates with 18 sectors and 36 readout chambers on each end are shown [180].

a starting point for track reconstruction in the ITS. The track momentum, charge and position are determined using a fit to its constituting points. The fit is performed two times, first propagating the tracks from the interaction vertex going outwards and second from the outermost side of the TPC going inwards.

### 2.2.3 The Transition Radiation Detector (TRD)

The Transition Radiation Detector (TRD) [185] is used to provide electron identification in the central barrel for particles with a momentum above  $1 \text{ GeV}/c$ . The TRD is composed of 540 individual read-out modules organized in 18 super-modules containing each 30 modules arranged in 6 layers. Each module consists of a radiator, which is a composite structure of fiber and foam, followed by a drift chamber. The modules are arranged in a cylindrical manner and are surrounded by the TPC on the inner side and the Time-Of-Flight (TOF) detector on the outer side.

The particle identification is obtained by measuring the specific energy loss and transition radiation in the detector. When a relativistic charged

particle crosses the interfaces of two media with different dielectric constants that compose the radiator, it produces a transition radiation photon that will be absorbed and converted in the gas mixture (85% Xe, 15% CO<sub>2</sub>) of the detector. Only the electrons with a high enough Lorentz factor will create a transition radiation that can be detected. This allows to reject, for instance, charged pions. The drift chamber is also used to measure the  $dE/dx$  of the particle.

#### 2.2.4 The Time-Of-Flight detector (TOF)

The Time-Of-Flight detector (TOF) [186] is used for charged particle identification in the intermediate momentum range ( $< 2.5$  GeV/ $c$  for pions and kaons,  $< 4$  GeV/ $c$  for protons). It is a large array of Multi-gap Resistive Plate Chambers (MRPC) covering the full azimuthal range and the pseudo-rapidity range  $|\eta| < 0.9$ . The MRPC are composed of double-stack of resistive plates, separated by a gas mixture (90% C<sub>2</sub>H<sub>2</sub>F<sub>4</sub>, 5% SF<sub>6</sub> and 5% C<sub>4</sub>H<sub>10</sub>). When a charged particle traverses the gas, it causes an avalanche process which generates the observed signal. The TOF measures the time for a particle to travel from the interaction point to the TOF with a resolution of less than 50 ps. The start time is given by the T0 detector (see Section 2.3.5).

Coupled with the ITS and the TPC, the TOF provides event by event identification of pions, kaons and protons, with a very good K/p and K/ $\pi$  separation.

#### 2.2.5 The High-Momentum Particle Identification Detector (HMPID)

The High-Momentum Particle Identification Detector (HMPID) [187] provides measurements of identified charged hadrons for a transverse momentum  $p_T > 1$  GeV/ $c$ . It enhances the capability of identifying charged hadrons beyond the momentum attainable through the energy-loss technique (as it the case in the ITS and the TPC) and time-of-flight measurements (in the TOF detector). The HMPID is composed of 7 Ring Imaging Cherenkov (RICH) counters of about  $1.5 \times 1.5$  m<sup>2</sup> each. The detector covers the azimuthal range  $1.2^\circ < \phi < 58.8^\circ$  and the pseudo-rapidity range  $|\eta| < 0.6$ . Each RICH is composed of a liquid radiator, a gas chamber filled with CH<sub>4</sub> and a multi-wire proportional chamber (MWPC). The principle is the same as the TRD.

When a fast charged particle crosses the detector, Cherenkov photons are emitted in a light cone with a specific angle. These photons are detected by a photon counter made of a Cesium Iodine (CsI) photo-cathode, that can measure the angle with a precision of a few mRad. This allows the particle identification as well as K/p and K/ $\pi$  separation up to 5 GeV/ $c$  and 3 GeV/ $c$ , respectively.

### 2.2.6 Photon Spectrometer (PHOS)

The Photon Spectrometer (PHOS) [188] is a high-resolution calorimeter used to detect photons and electrons. It is composed of 5 PHOS modules, consisting of a Charged-Particle Veto (CPV) detector associated to an electromagnetic calorimeter. Each PHOS module is composed of 3584 detection cells of lead-tungsten crystals coupled with Avalanche Photo-Diodes (APD). The CPV detector is a multi-wire proportional chamber placed on top of the PHOS modules. It covers  $220^\circ < \phi < 320^\circ$  azimuthally and  $|\eta| < 0.12$  in pseudo-rapidity.

### 2.2.7 ElectroMagnetic Calorimeter (EMCal)

The Electromagnetic Calorimeter of ALICE is also used to detect photons and electrons [189]. It is a large cylindrical Pb-scintillator calorimeter covering  $|\eta| < 0.7$  and positioned approximatively in the azimuthal range opposite to the PHOS calorimeter, covering  $\Delta\phi = 107^\circ$ . It is made of twelve super-module units, composed of unitary modules of four towers, made of 77 layers of lead alternating with 76 layers of polystyrene base. In addition, an extension of the calorimeter was added in 2010, covering  $\Delta\phi = 60^\circ$ , named DCal to separate from the EMCal part [190]. A transverse view of EMCal and DCal is presented in Figure 2.4.

The EMCal is used complementary to the PHOS detector for photon detection. As for the PHOS, the principle of detection is based on the electromagnetic showers produced by photons and electrons going through the scintillator.

### 2.2.8 ALICE Cosmic Ray Detector (ACORDE)

The ALICE cosmic ray detector, ACORDE, is used to provide a fast L0 trigger signal on cosmic muons traveling through the detector from top to

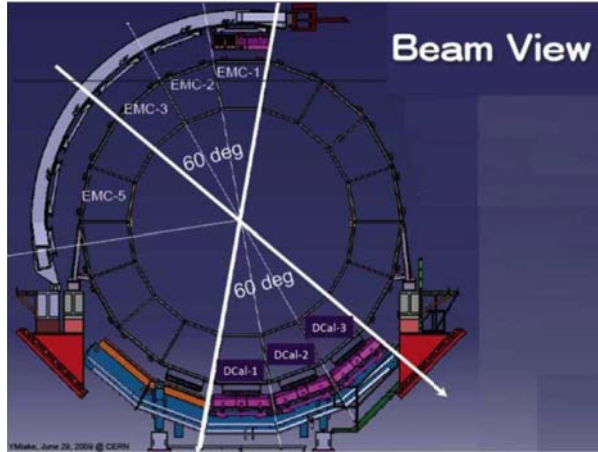


Figure 2.4: Transverse view of EMCAL (above mid-plane) and DCal (below mid-plane) [190].

bottom (see Section 2.5). In combination with the TPC, TRD and TOF, it is used to detect single atmospheric muons and multi-muons events, in order to study high-energy cosmic ray. The detector is composed of 60 modules, each one composed of two scintillator counters, covering the pseudo-rapidity range  $|\eta| < 1.3$  and the azimuthal range  $-60^\circ < \phi < 60^\circ$ .

When atmospheric muons hit the ALICE detector, the signal delivered by ACORDE is used for the calibration and alignment of several detectors, such as the TPC, TOF, HMPID and ITS.

## 2.3 Forward Detectors

### 2.3.1 Zero Degree Calorimeter (ZDC)

The Zero Degree Calorimeter [191] is composed of two stations located at 116 meters on the both sides of the interaction point and is used to determine the number of participants nucleons (see Section 1.3): this number can be estimated by measuring the energy carried in the forward direction by spectator nucleons and is related to the centrality of the collision. Each ZDC set is composed of two detectors, one for the spectators neutrons and one for the spectator protons. They are made of calorimeters producing a

Cherenkov radiation when crossed by a particle.

In addition two small electromagnetic calorimeters (ZEM) are placed at 7 meters from the interaction point on both sides, to disentangle the most central events, which have few spectator nucleons and the most peripheral, where the spectator nucleons are bound in nuclear fragments and cannot be detected by the ZDCs.

The ZDC is also used to reject satellite collisions in pp and Pb – Pb collisions, which are the interactions between the bunches not located in the main interaction area. Finally, the ZDC is also used to determine the centrality in p – Pb collisions.

### 2.3.2 Photon Multiplicity Detector (PMD)

The Photon Multiplicity Detector (PMD) [192] is used to measure the distribution of photons in the pseudo-rapidity region  $2.3 < \eta < 3.7$  in order to provide estimations of the reaction plane angle and the transverse electromagnetic energy. Because of the large particle density in the forward region, the PMD has to use the pre-shower method: a lead converter is sandwiched between two planes of gas counters. The first gas plane is used as the charged particle veto, to reject charged particles, the passage of particles through the converter produces the pre-shower and the pre-shower data from the second detector plane is used for the photon identification.

The PMD is composed of 24 modules, each module being an array of honeycomb cells, containing a gas mixture of Argon and CO<sub>2</sub> and is placed at 3.6 meters from the interaction point in the backward direction.

### 2.3.3 Forward Multiplicity Detector (FMD)

The Forward Multiplicity Detector (FMD) [193] main goal is to provide information on the charged particle multiplicity. The FMD consists of three stations, the first one is made of one ring placed at 320 cm of the interaction point in the forward direction, the second station is made of two rings, the inner ring and the outer ring placed respectively at 83.4 cm and 75.2 cm of the interaction point and the third station is placed in the backward direction, the inner and outer ring placed respectively at -62.8 cm and -75.2 cm of the interaction point. Each detector ring consists of silicon sensors, which detect particles via their energy loss. The detectors cover the pseudo-rapidity range  $-3.4 < \eta < -1.7$  and  $1.7 < \eta < 5.1$ , respectively.

### 2.3.4 V0 detector

The V0 detector [193] is a small angle detector consisting of two array of scintillating counters called V0A and V0C, installed on each side of the interaction point. The V0A detector is located 340 cm from the interaction point and covers the pseudo-rapidity range  $2.8 < \eta < 5.1$ . The V0C is placed 90 cm from the vertex in front of the muon spectrometer and covers  $3.7 < \eta < 1.7$ . Each V0 detector is segmented in 32 individual counters. A picture of the V0A and V0C can be found in Figure 2.5.

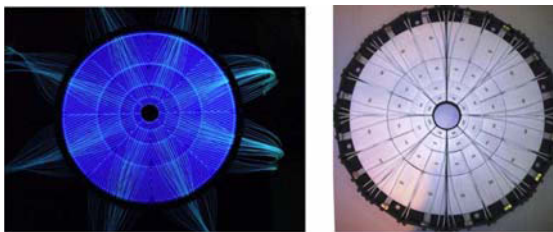


Figure 2.5: Front view of V0A (left) and V0C (right) arrays [174].

The V0 detectors serves several purposes: it provides a Minimum Bias trigger, measures the collision centrality via the charged-particle multiplicity distributions and is also used to reject beam-gas interaction via timing cuts (see Section 3.2.2).

Finally the V0 is also used in the measurement of the luminosity in pp collisions as a reference trigger for the van der Meer scan.

### 2.3.5 T0 detector

The T0 detector [193] serves three main objectives. First, it is used to generate the start time for the Time-Of-Flight detector (see Section 2.2.4). Second, the T0 is used to measure the vertex position with a precision of  $\pm 1.5$  cm for each interaction and provide a L0 trigger (see Section 2.5) when the vertex is within the preset value, that will discriminate against beam-gas interactions. Finally, the T0 provides an alternative Minimum Bias trigger. It can also be used as a reference trigger for luminosity determination, like the V0.

The detector consists of two arrays of Cherenkov counters, composed of a quartz radiator coupled with a photomultiplier tube, with twelve counters per array. The first array, T0-A, is placed 375 cm from the interaction point and covers the pseudo-rapidity range  $4.61 < \eta < 4.92$ . T0-A is grouped with the other forward detectors: FMD, PMD and V0A. The second array, called T0-C, is placed 72.7 cm from the interaction point on the opposite side and covers  $-3.28 < \eta < -2.97$ .

## 2.4 The Muon Spectrometer

### 2.4.1 General Layout

The Muon spectrometer is used for muon detection and covers the pseudo-rapidity region  $-4.0 < \eta < -2.5$  [194, 195]. A schematic representation of the spectrometer is presented in Figure 2.6. It is composed of the following elements: a passive front absorber of  $10\lambda_{int}$  (nuclear interaction length) to reject hadrons produced in the collision, a tracking system composed of five stations of 2 tracking planes each, which is used to reconstruct the particles trajectories, a large dipole magnet that allows to measure the momentum of the particles, a passive muon filter wall, followed by two stations of trigger chambers, with two trigger planes per station and a rear absorber of  $7\lambda_{int}$ . In addition, there is an additional absorber around the beam pipe in order to protect the chambers from particles produced at high rapidity.

The front absorber has a 4.13 m length and is made predominantly of carbon and concrete to limit small-angle scattering and energy loss by traversing particles. The muon filter is made of a 1.2 m thick iron wall which provides an additional protection to the muon trigger chambers, in order to reduce further the hadronic background and is placed between the last tracking chamber and the first trigger chamber. The combination of the front absorber and the muon filter stops muons with a total momentum smaller than 4 GeV/c. The beam shield is a tungsten, lead and stainless steel conical like tube surrounding the beam-pipe. The rear absorber is a 1 m thick iron wall installed in order to protect the trigger chambers from beam-gas interaction occurring in the LHC tunnel.

The dipole magnet is located 7 m from the interaction point. The magnet is composed of resistive coils and provides a horizontal field perpendicular to the beam axis of 3 T.m along the beam axis. Therefore it bends the trajectory of the particles in the vertical ( $z, y$ ) plane, which is referred as

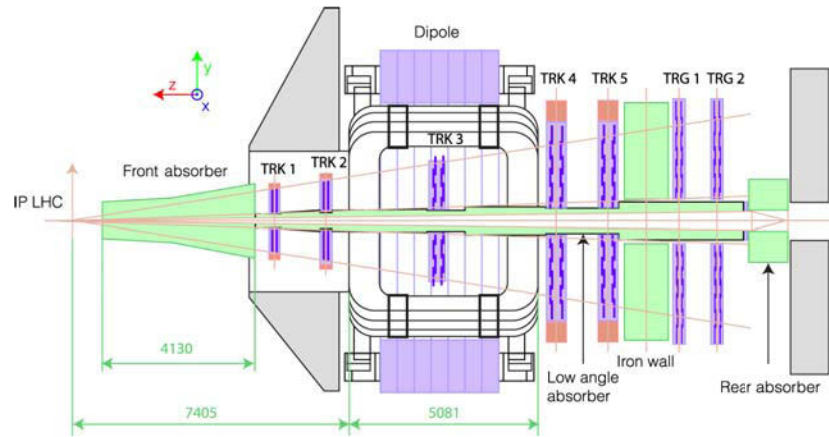


Figure 2.6: Muon Spectrometer longitudinal section [173].

the "bending plane". The "non-bending plane" is defined as the  $(z, x)$  plane.

### 2.4.2 Tracking Chambers

The tracking system is composed of 10 tracking chambers separated in 5 stations, placed on each side of the dipole magnet. The first two stations are placed before the magnet, the third one is inside the dipole magnet and the last two are placed after. The tracking system covers a total area of about  $100 \text{ m}^2$ . The detectors used are Cathode Pad Chambers (CPC): each chamber is composed of an anode wire plane with a segmented cathode plane on each side. The chamber is filled with a gas mixture of Argon (80%) and  $\text{CO}_2$  (20%). When a particle goes through the chamber, it ionizes the gas and because of the electric field applied, the free electrons will drift towards the anode plane. Near the anode, the electric field becomes intense, therefore the electrons are accelerated and can ionize again the gas, causing an avalanche phenomenon. The resulting ions will drift towards the cathode planes and induce a charge distribution on the cathode pads close to the avalanche position. Both cathode planes are read-out to provide a two dimensional hit information, therefore there are 4 measures per chamber. The position of the impact is then reconstructed thanks to the charge distribution on the cathode planes.

The first station is located right behind the front absorber to measure the exit points of the muons as precisely as possible. For this station, the

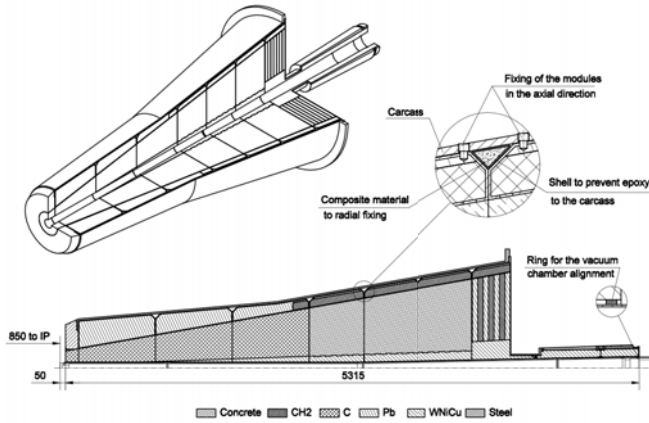


Figure 2.7: Layout of the front absorber [194].

region close to the beam pipe uses the smallest segmentation because this is where the multiplicity is the highest. The hit density decreases with the distance from the beam, therefore larger pads are used at larger radii. The size of the pads ranges from  $2.2 \times 6.3 \text{ mm}^2$  to  $5 \times 100 \text{ mm}^2$ , resulting in a total number of channels of 1.08 million. Because of the different sizes of the stations, two different designs were adopted: for the first two stations, a quadrant structure was chosen, with the readout electronics distributed on their surface and for the station 3, 4 and 5, a slat architecture was adopted, with the electronics implemented on the side of the slats. A picture of the two different designs is shown in Figure 2.9.

The Muon Tracker achieves a spatial resolution of about  $100 \mu\text{m}$ , which allows to have a resolution on the invariant mass distribution of muon pairs of the order of  $70 \text{ MeV}/c^2$  at the  $J/\psi$  mass ( $3.1 \text{ GeV}/c^2$ ) and around  $140 \text{ MeV}/c^2$  at the  $\Upsilon$  mass ( $9.6 \text{ GeV}/c^2$ ). For the Upsilon, this resolution allows to separate the  $\Upsilon(1S)$ ,  $\Upsilon(2S)$  and  $\Upsilon(3S)$  resonances.

### 2.4.3 Trigger Chambers

The Muon Trigger structure is illustrated in Fig 2.10. It is made of four Resistive Plate Chambers (RPC) planes arranged in two stations. Each plane consists in 18 RPC modules. A RPC module is made of two highly resistive bakelite electrodes separated by a gas gap, as described in Fig-

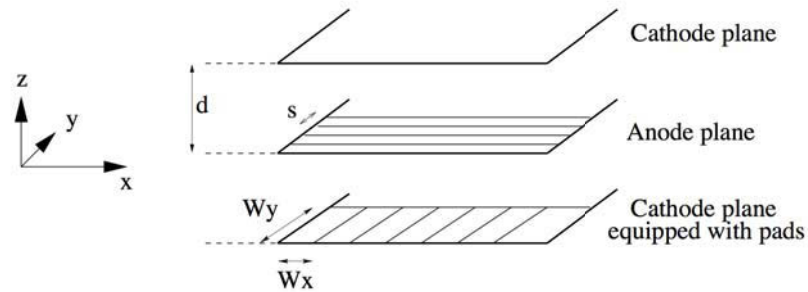


Figure 2.8: Schematic of the CPC [194].

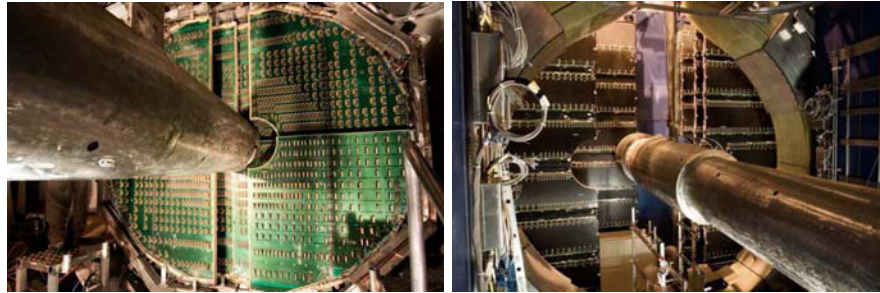


Figure 2.9: Pictures of the station 2 with a quadrant design (left) and of the stations 4 and 5 with a slat design (right) of the Tracking system [173].

ure 2.10. The high voltage applied between the two electrodes maintains a uniform electrical field in the gas volume. As for other detectors described previously, when a particles crosses a chamber, it ionizes the gas, creating a signal due to the free electrons, amplified by an avalanche phenomenon. The signal is then collected by the segmented read-out strips on the  $x$  and  $y$  direction, allowing the determination of the position of the hits. The  $X$  cathode is segmented with horizontal strips (parallel to the  $x$  direction), and therefore measures the position in the bending plane ( $y, z$ ). The  $Y$  cathode is segmented with vertical strips and measures the position in the non-bending plane ( $x, z$ ). The Muon Trigger has a time resolution of 2 ns and a space resolution of less than 1 cm.

The RPC can operate in two different modes, the "avalanche mode" and the "streamer mode". The avalanche mode works as described for other

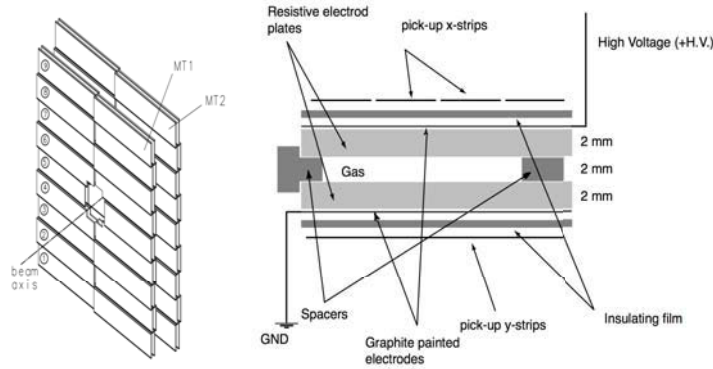


Figure 2.10: Structure of the Trigger Detector (left) and schematic view of the RPC (right) [194].

detectors: when a particle goes through the RPC, the gas is ionized and the free electrons drift towards the anode. Due to the intensity of the electric field, they can reach an energy large enough to ionize the gas, causing an avalanche phenomenon.

The streamer mode appears for an applied electric field more important than in the avalanche mode. When the number of charges is sufficient, they generate locally an electric field equivalent to the one applied in the RPCs. The inhomogeneity in the electric field leads to the appearance of a finger-like discharge that goes from the anode to the cathode. The signals induced in the streamer mode are much more important than in the avalanche mode.

The RPCs are presently operated in a "highly-saturated avalanche mode", meaning that the electric field is not important enough to cause the streamer mode, but the signal created by the saturated avalanches is important enough to not require an amplification in the electronics.

The two stations of trigger chambers are named MT1 and MT2. They allow to select single muons and dimuons events. In order to limit the trigger rates of low- $p_T$  muons from  $\pi$  and  $K$  decays, a  $p_T$  threshold on single muons is applied. This cut is chosen in order to reject most muons from  $\pi$  and  $K$  decays, while having little impact on muons from heavy flavor or charmonia decay. The principle of the trigger system is to measure the deviation  $\theta_d$ , which is the angle between the muon track bent by the dipole and the trajectory of the muon of infinite momentum (straight line). By considering that the deviation are at small angles, one can then use the approximate

relation:

$$p_T \approx BL \times \frac{Z_2 - Z_1}{Z_1} \times \frac{Z_F}{Z_1} \times \frac{Y_1}{\theta_d} \quad (2.2)$$

where:

- $B$  is the magnetic field
- $L$  is the length of the magnet
- $Z_1, Z_2$  and  $Z_F$  are the position along the beam axis of MT1, MT2 and the dipole middle plane
- $Y_1$  is the Y coordinate at the position where the muon crosses MT1

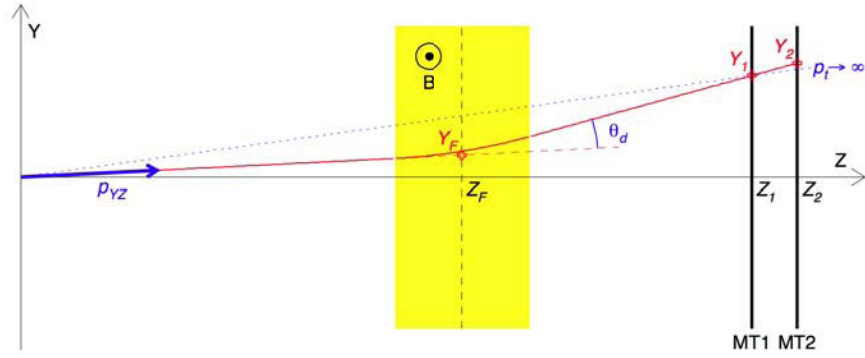


Figure 2.11: Principle of the Muon Trigger represented in the bending plane (Y,Z) [194].

This principle is illustrated in Figure 2.11: the measurement of the deviation  $\theta_d$  allows to perform a selection on the muon transverse momentum: since  $\theta_d$  is linked to the positions  $Y_1$  and  $Y_2$  by the formula:

$$\theta_d = \frac{1}{Z_F} \left( \frac{Y_1 Z_2}{Z_2} - \frac{Y_2 Z_1}{Z_1} \right) \quad (2.3)$$

by simply putting a cut on the value  $Y_2$  compared to the estimated straight track, it is possible to apply a cut on the transverse momentum.

Two  $p_T$  cuts are programmable, a high- $p_T$  and a low- $p_T$  cut, which are applied in parallel by the trigger electronics. The threshold for the low- $p_T$  and high- $p_T$  cuts are set to have a compromise between background rejection and signal efficiency in the  $J/\psi$  and  $\Upsilon$  invariant mass region respectively.

#### 2.4.4 Track reconstruction in the Muon Spectrometer

As explained in Section 2.4.2, the particles going through the tracking system leave a cluster of charges detected by the chamber pads. These clusters are identified using a Maximum Likelihood Expectation Maximization (MLEM) algorithm [196] and then their spatial position is determined by fitting them with a 2D Mathieson function [197].

Then the trajectory of the particles across the five tracking stations is reconstructed using a tracking algorithm based on the Kalman filter [198, 199]. The procedure begins using the clusters of the two most downstream stations (station 4 and 5), less subject to the background caused by hadrons going through the front absorber. Straight lines are formed between clusters on the two planes of each station, giving a first estimate of the position, slope and bending momentum. Then, the tracks candidates are extrapolated from one station to the other and paired with at least one cluster. If several clusters are found, the track is duplicated to consider all the possible combinations. At each step, the track parameters (charge to momentum ratio and position) are recomputed using the Kalman filter.

The process is then repeated by extrapolating the tracks to station 3, then station 2 and finally station 1 and at each extrapolation, the candidates for which no cluster is found or whose parameters indicate they don't match the acceptance of the detector are eliminated. Finally the remaining tracks are extrapolated to the vertex position measured by the SPD. A correction to the track momentum is then applied to account for the multiple scattering and energy loss in the front absorber.

In order to exclude a maximum of fake tracks, additional selections on the tracks are performed. It is required that the tracks in the Tracking chamber have a corresponding track in the Trigger Chambers. For a track to be selected by the Muon Trigger, it has to hit at least 3 out of 4 planes. This allows to apply the transverse momentum selection described in Section 2.4.3. For a track to be selected by the Muon Tracker, it has to have at least one chamber hit per station for stations 1, 2 and 3, and at least 3 out of 4 chambers hits in stations 4 and 5. Additional selections are applied in order to keep only the tracks matching the interaction point and remaining in the acceptance of the Muon Spectrometer, this is discussed in more detail in Section 3.3.

## 2.5 Trigger and data acquisition systems

### 2.5.1 The Central Trigger Processor and High Level Trigger

The Central Trigger Processor (CTP) [200] is designed to combine the trigger signals from the detectors participating in the event selection, such as the V0 and the Muon Trigger for each event, and to send a trigger signal to a cluster of detectors if the event presents the required characteristics. The CTP has three trigger levels depending on the time needed to build the trigger response:

- L0: it is the fastest trigger, with a response time of  $1.2 \mu\text{s}$ . The detectors participating in the L0 level trigger are the V0, the T0, the SPD, the EMCal (photon trigger signal), the PHOS and the Muon Trigger.
- L1: this trigger has a response time of  $6.5 \mu\text{s}$ , treats signals from the ZDC, EMCal (neutral jet trigger) and TRD and is in particular involved in the rejection of electromagnetic background.
- L2: The L2 level is the slowest trigger level and only the TPC participates to this level. Its response time is  $94 \mu\text{s}$ , corresponding to the drift time of electrons in the TPC.

The CTP evaluates the trigger inputs from the trigger detectors every machine clock cycle ( $= 25 \text{ ns}$ ).

All the physics observable measured by ALICE do not require the same event sample, therefore the CTP allows to select events according to several different conditions. The outputs of the CTP are organized in trigger classes. A trigger class consists of a trigger cluster, which is a group of detectors set as a read-out and a L0, L1 and/or L2 decision. For instance, the CINT trigger class that is used later for the analysis consists in a coincidence between the V0A and V0C. This trigger class is often used as the Minimum Bias trigger, meaning the trigger that selects the largest fraction of inelastic Pb – Pb collisions.

The trigger class can have additional information regarding the scaling factors of the trigger (some triggers are downscaled by a fixed factor, in order to reduce the bandwidth they occupy, and leave enough room to the other triggers) and the region of interest (for some applications it might not be necessary to record all the regions of the detector, but only some azimuthal sectors, which define the region of interest).

A High-Level Trigger (HLT) [201] has been developed in order to assist the CTP in the event selection and perform a more refined selection. It is implemented only for detectors generating a large volume of data, such as the TPC. The HLT operates during the pre-reconstruction of the events by the Local Data Concentrators (see Section 2.5.2). The HLT reduces the volume of the data without losing any physics information. For the TPC, the data volume is reduced by a factor 5 [175].

### 2.5.2 Data Acquisition system

The events selected by the CTP are recorded by the Data Acquisition (DAQ) system [200]. As explained before, a large number of trigger classes is used to characterize the events, but the bandwidth available for the data transfer is limited to  $1.25 \text{ Go.s}^{-1}$ . Triggers such as the Minimum Bias trigger are so frequent that the limitation on the number of events collected lies on the performance of the data acquisition system. The data from these triggers will use a large fraction of the bandwidth available for the data transfer. On the other hand, data from rare triggers such as the dimuon or dielectron triggers use less bandwidth and are limited by the luminosity. The DAQ system has to balance between the capability to record central collisions, which generate a large number of events, with the ability to acquire the largest possible fraction of rare events.

The DAQ proceeds as follows: when the trigger decision is sent by the CTP to the detectors, these detectors send their data to the DAQ. The data is then either transferred to Local Data Concentrators (LDC), which are in charge of the sub-events reconstruction for each sub-detector, or stored in a buffer in case the LDCs are busy with the processing of previous events. Thanks to the HLT algorithm, the volume of the data is reduced. The sub-events are then centralized in the Global Data Concentrator (GDC) and are reconstructed globally or partially. Then the data is sent in a Permanent Data Storage.

Because the size of data is very large (1.25 Go of data is produced every second) the storage and analysis of the data is performed through the LHC Computing Grid, which dispatches the processing load over several calculation center over the world. Moreover, all the information regarding the detectors performances and calibrations as well as the trigger definitions and trigger counts are stored in a distributed database, for future uses in the analysis.



## Chapter 3

# Measurement of $\psi(2S)$ production

In 2015, ALICE recorded Pb – Pb collisions at center-of-mass energy per nucleon-nucleon collision  $\sqrt{s_{NN}} = 5.02$  TeV, which is almost twice as large as the previous Pb – Pb collisions of 2011, at  $\sqrt{s_{NN}} = 2.76$  TeV. The resulting integrated luminosity went from  $L_{int}^{Pb-Pb} \approx 68.8 \mu\text{b}^{-1}$  in 2011 to  $L_{int}^{Pb-Pb} \approx 225 \mu\text{b}^{-1}$  in 2015. With this new data, the goal is to have a better understanding of the contribution of the different phenomenon affecting the charmonium production in the QGP, thanks to the increased statistics and to the higher charm cross-section at a higher energy. This also allows to measure the  $J/\psi$  and  $\psi(2S)$  independently and see how these particles are affected differently by the QGP.

In order to quantify the effects of the QGP on the charmonium production, the nuclear modification factor  $R_{AA}$  is measured. The  $R_{AA}$  is defined as:

$$R_{AA} = \frac{Y_{Pb-Pb}}{N_{\text{coll}} \cdot Y_{pp}} \quad (3.1)$$

where  $Y_{Pb-Pb}$  and  $Y_{pp}$  are the yield of charmonium in lead-lead collisions and proton-proton collisions respectively and  $N_{\text{coll}}$  is the average number of binary nucleon-nucleon collisions.

If the Pb – Pb collisions were an independent superposition of nucleon-nucleon collisions, with no effect of the QGP, then  $R_{AA} = 1$  would be observed. On the contrary, if  $R_{AA} \neq 1$  is observed, then there is evidence of nuclear effects influencing the quarkonium production.

Since this study is focused on the  $\psi(2S)$  measured in the dimuon decay channel, the expression of the  $R_{AA}$  described in the following corresponds to that particular case. But the expression can be easily changed for another particle and/or another decay channel.

The numerator  $Y_{Pb-Pb}^{\psi(2S)}$  is written as:

$$Y_{Pb-Pb}^{\psi(2S)} = \frac{N_{\psi(2S)}}{\text{BR}_{\psi(2S) \rightarrow \mu^+ \mu^-} \times N_{\text{MB}} \times (A\varepsilon)} \quad (3.2)$$

where:

- $N_{\psi(2S)}$  is the number of  $\psi(2S)$  measured with the Muon Spectrometer in the dimuon decay channel.
- $\text{BR}_{\psi(2S) \rightarrow \mu^+ \mu^-} = 0.79 \pm 0.09\%$  [34] is the branching ratio of the  $\psi(2S)$  decay into two muons, which gives the probability for the  $\psi(2S)$  to decay into two muons.
- $N_{\text{MB}}$  is the number of equivalent Minimum Bias events, which is the number of collisions that triggered the Minimum Bias trigger.

- $A\varepsilon$  is the acceptance  $\times$  efficiency of the Muon Spectrometer, which evaluates the percentage of the total number of produced  $\psi(2S)$  that the detector can measure, because of its finite geometry (acceptance) and its efficiency in particle detection, triggering and reconstruction.

By correcting the number of detected charmonium with the branching ratio of the measured decay channel and the  $A\varepsilon$  of the detector, we evaluate the number of produced charmonium. The number of produced charmonium per Minimum Bias event gives the production yield.

For the denominator of Equation 3.1, instead of using  $N_{\text{coll}} \cdot Y_{pp}^{\psi(2S)}$ , we use the following expression:

$$N_{\text{coll}} \cdot Y_{pp}^{\psi(2S)} = T_{AA} \cdot \sigma_{\psi(2S)}^{pp} \quad (3.3)$$

with :

- $\sigma_{\psi(2S)}^{pp}$  is the production cross section of the  $\psi(2S)$  in pp collisions:

$$\sigma_{\psi(2S)}^{pp} = \frac{Y_{pp}^{\psi(2S)}}{\text{BR}_{\psi(2S) \rightarrow \mu^+ \mu^-}} \cdot \sigma_{NN}^{inel} \quad (3.4)$$

- $T_{AA}$  is nuclear overlap function, which is related to the centrality of the collision and describes how the volumes of the nuclei overlap at the collision. It is defined as (see Section 3.1):

$$T_{AA} = \frac{N_{\text{coll}}}{\sigma_{NN}^{inel}} \quad (3.5)$$

- $\sigma_{NN}^{inel}$  is the nucleon-nucleon inelastic cross section.

The resulting expression for the  $\psi(2S)$  nuclear modification factor, measured in the dimuon decay channel, is then:

$$R_{AA}^{\psi(2S)} = \frac{N_{\psi(2S)}}{\text{BR}_{\psi(2S) \rightarrow \mu^+ \mu^-} \times (A\varepsilon) \times N_{\text{MB}} \times T_{AA} \times \sigma_{\psi(2S)}^{pp}} \quad (3.6)$$

In the following, we will describe how to evaluate the different elements used to measure the  $R_{AA}$ .

### 3.1 Centrality Determination and Nuclear Overlap Function

The centrality of the collision is related to the impact parameter, the distance between the center of the colliding nuclei. It is expressed in terms of percentage of the total hadronic interaction cross section. Experimentally, the cross section is replaced by the number of observed events and the centrality percentile  $c$  is defined as the fraction of events with the largest detected charged particle multiplicity:

$$c = \frac{1}{N_{ev}} \int_{N_{ch}}^{\infty} \frac{dn}{dN'_{ch}} dN'_{ch} \quad (3.7)$$

where  $N_{ev}$  is the total number of events. The centrality percentile of a given event, with a given charged particle multiplicity  $N_{ch}$ , corresponds to the fraction of events with a multiplicity higher than  $N_{ch}$ .

This multiplicity is evaluated using the V0 detector : the V0 multiplicity, which is the sum of the V0A and V0C amplitude, is recorded and the centrality bins are defined by integrating the charged particle multiplicity according to equation 3.7. The events corresponding to the higher amplitude are the most central events, whereas the events corresponding to the lower amplitude are the most peripheral events. The amplitude distribution is then fitted to a Negative Binomial Distribution (NBD) according to the Glauber model [176] as shown in Figure 3.1.

The fit to the distribution using the NBD-Glauber function is also used to estimate the number of participant nucleon, the number of binary collisions, the impact parameter  $b$  and the nuclear overlap function  $T_{AA}$  (see Section 1.3). In the Glauber model [202], the nucleon density in the nucleus is given by the Woods-Saxon profile:

$$\rho(r) = \rho_0 \frac{1}{1 + \exp\left(\frac{r-R}{a}\right)} \quad (3.8)$$

where  $\rho_0$  is the average nucleon density, which provides the overall normalization,  $R$  is the nucleus radius,  $R = 6.62 \pm 0.06$  fm for a Pb nuclei,  $a = 0.546 \pm 0.010$  fm is the skin thickness of the nucleus, which indicates how quickly the nuclear density falls off near the edge of the nucleus.

We can then define, for a nucleus accelerated along the  $z$  direction, the probability for a nucleon to be located in a target region at a displacement  $\mathbf{s}$  with respect to the the center of the nucleus as:

$$T_A(\mathbf{s}) = \int \rho(\mathbf{s}, z) dz \quad (3.9)$$

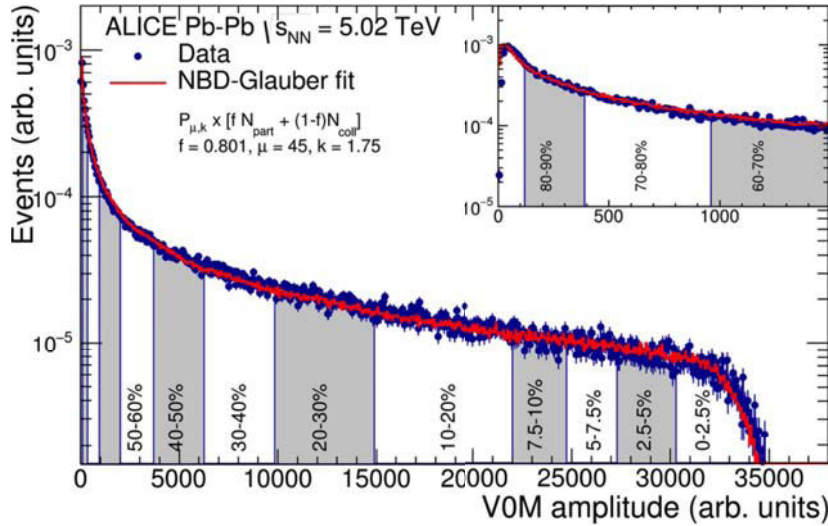


Figure 3.1: Centrality estimation based on a NBD-Glauber fit (red line) to the distribution of the V0 amplitudes. The insert shows a zoom on the most peripheral region [176].

where  $\rho(\mathbf{s}, z)dz$  is the probability per unit volume to find the nucleon at location  $(\mathbf{s}, z)$  evaluated with Equation 3.8.

Then for two nucleus separated by an impact parameter  $b$ , the nuclear overlap function is defined as:

$$T_{AA}(\mathbf{b}) = \int T_A(\mathbf{s})T_A(\mathbf{s} - \mathbf{b})d^2s \quad (3.10)$$

$T_{AA}$  can be interpreted as the effective overlap area for which a specific nucleon in the first nucleus can interact with a nucleon in the second nucleus.

Once  $T_{AA}$  is known, one can evaluate the number of collisions  $N_{\text{coll}}$  using Equation 3.5 as well as the number of participants  $N_{\text{part}}$  which is the number of nucleons that experience at least one collision. The value of  $\sigma_{NN}^{\text{inel}}$  is estimated by interpolation of pp data at different energies and from cosmic rays,  $\sigma_{NN}^{\text{inel}} = 70 \pm 5$  mb [176].

The centrality classes and the corresponding geometrical parameters used in this analysis are presented in Table 3.1. The choice is made to cut at 90% centrality, because for a higher centrality there are not enough tracks in the V0 to do an accurate fit (uncertainties on the parameters are of the same order than the parameters themselves).

Centrality (%)	$N_{\text{part}}$	$N_{\text{coll}}$	$b$ (fm)	$T_{AA}$ ( $\text{mb}^{-1}$ )
0-20%	$311 \pm 3.3$	$1320 \pm 133.5$	$0 \leq b < 7.01$	$18.85 \pm 0.62$
20-40%	$159.5 \pm 2.65$	$472.5 \pm 41.5$	$7.01 \leq b < 9.92$	$6.755 \pm 0.215$
40-60%	$69.95 \pm 1.45$	$136.4 \pm 10.0$	$9.92 \leq b < 12.1$	$1.945 \pm 0.0815$
60-90%	$17.86 \pm 0.46$	$20.82 \pm 1.20$	$12.1 \leq b < 15.0$	$0.298 \pm 0.018$

Table 3.1: Centrality classes considered in this analysis and corresponding values of  $N_{\text{part}}$ ,  $N_{\text{coll}}$ ,  $b$  and  $T_{AA}$ . The systematic uncertainties on the mean values are obtained by varying the parameters of the Glauber model independently within their estimated uncertainties.

## 3.2 Data and Event selection

This analysis is based on the data collected in Pb – Pb collisions during the month of December 2015 at a center of mass energy per nucleon-nucleon collision  $\sqrt{s_{\text{NN}}} = 5.02$  TeV. The data sample used in this analysis corresponds to an integrated luminosity of  $L_{\text{int}}^{\text{Pb-Pb}} \approx 225 \mu\text{b}^{-1}$ .

Only the dimuon triggered events are considered. The dimuon trigger, named CMUL, consists in a coincidence between the V0A and V0C and the Muon Trigger. The Muon Trigger condition consists in requiring two muons of opposite sign, with a transverse momentum larger than 1 GeV/ $c$ .

### 3.2.1 Quality Assurance

The runs selected had to go through a Quality Assurance (QA) task in order to make sure of the quality of the runs and to remove any set of collected data that may have been tainted by a bad behaviour of the detectors or the LHC conditions, such as the quality of the vacuum.

In order for a run to pass the QA, it has to respect a set of conditions. There are a number of flags attached to the runs to describe its characteristics and here are the ones that are required to consider the run to be a good run:

- The Run Type has to be PHYSICS, meaning that the LHC beam and the detectors are calibrated for the physics analysis (instead of, for instance, CALIBRATION used for calibrating the detectors or test beam).
- The duration has to be at least 10 min, because runs with a duration

of less than 10 min are likely to have something that went wrong (detector malfunctioning, beam unstable, etc...).

- The GDC (see Section 2.5.2) has to be recording the events.
- The beam mode has to be registered as stable, again to ensure the quality of the data, as opposed to the other modes like tuning, which indicate that the beam is reaching its optimum.
- The Muon Trigger has to be used as a trigger detector.
- At least the Muon Trigger and the Muon Tracker have to be used as read-out detectors.
- The quality of the data has to be tagged as "good" when considering all the detectors globally and tagged "not bad" for the read-out detectors, meaning that they are validated for reconstruction (see Section 2.5.2).

A total of 147 runs out of 322 match these criterion, which corresponds to 138 millions dimuon triggered events.

### 3.2.2 Physics selection

In addition to the QA, which ensures the quality of the data collected, an other selection is done to ensure that the selected events correspond to nucleus-nucleus collisions, as opposed, for instance, to interaction between the beam and the residual gas in the beam pipe: this is called the Physics Selection.

The V0 and ZDC detectors are used to reject the events that come from beam-gas interactions, meaning the interactions between the beam and the residual gas inside the beam pipe. These interaction usually do not happen at the interaction point, but rather upstream on the side from which the beam arrives. This will cause one of the V0 stations (see Section 2.3.4) to receive an early signal when compared to the one expected from a collision at the interaction point and the other V0 station to receive a delayed signal. Therefore by measuring the times when the V0A and V0C receive the signal, the background collisions can be rejected. From a practical standpoint, events are looked in the sum-difference plane ( $t_{V0A} + t_{V0C}$  ;  $t_{V0A} - t_{V0C}$ ), which allows to define the region of the plane corresponding to collision events.

In a similar fashion, the ZDC is used to reject the satellite collisions in Pb – Pb collisions [175]: since the Pb nuclei arrive in bunches, the main

bunches that collide at the interaction point can also interact with the other bunches, called satellites. All the runs are processed in order to select the events in the time window corresponding to main bunch nuclei-nuclei collisions.

Of the 147 QA approved runs, 10 were rejected because they missed the ZDC. In the end 137 runs passed the selections, which corresponds to 128 millions dimuon triggered events.

### 3.3 Signal extraction

Once the runs are properly selected, the next step is to extract the number of produced  $\psi(2S)$  from the selected data. In order to evaluate the charmonium production, we measure the raw number of charmonium detected. As previously stated, the data come from the muon spectrometer, which is designed to detect muons, including the ones coming from the decay of a charmonium, which are the ones that interest us. To count the number of charmonium measured in the muon spectrometer, we look at the invariant mass distribution of opposite sign dimuons. Among all the pairs formed out of the reconstructed tracks for a given collision, we look at the pairs that satisfy the following conditions:

- The pseudo-rapidity on each muon verifies  $-4.0 < \eta < -2.5$ , which corresponds to the acceptance of the detector.
- The radial position at the end of the front absorber of each muon verifies  $17.6 < R_{abs} < 89.5$  cm, which rejects the particles that went through the center of the absorber, which is the denser part. These particles are likely to have been subject to too much scattering inside the absorber. This allows to reject the tracks whose "pointing resolution" towards the collision point is likely to be poor due to the multiple scattering.
- The rapidity of the dimuon pair verifies  $2.5 < y < 4.0$ , which defines the rapidity in which the measurement is performed.
- Muons have to be of opposite signs, since we look at the  $\psi(2S) \rightarrow \mu^+\mu^-$  decay channel.
- The tracks reconstructed in the tracking chambers must match a track reconstructed in the trigger chambers and fulfill the single muon trigger

requirement ( $p_{\text{T}}^{\text{muon}} > 1 \text{ GeV}/c$ ) which ensures that the reconstructed tracks have fulfilled the trigger condition.

The values of the rapidity and pseudo-rapidity are measured at the interaction point, before the front absorber. This requires that the track momentum and position, measured in the first chamber of the Muon Tracker are extrapolated backwards, towards the interaction point. This extrapolation properly accounts for the additional uncertainty associated to the multiple scattering in the absorber, as well as the corresponding average energy loss.

Once the muon pair candidate is constructed, its invariant mass can be calculated, since the mass of the muons is known and the transverse momentum of the muons are measured by the detector. The following formula is used:

$$m_{\mu^+\mu^-} = \sqrt{2m_{\mu}^2 + 2\left(\frac{E_{\mu^+} E_{\mu^-}}{c^2} - \frac{p_{\mu^+} p_{\mu^-}}{c} \cos \theta_{\mu^+\mu^-}\right)} \quad (3.11)$$

where :

- $m_{\mu^+\mu^-}$  is the invariant mass of the dimuon pair.
- $m_{\mu}$  is the invariant mass of the muon.
- $p_{\mu^+}$  and  $p_{\mu^-}$  are the momentum of the muons of positive and negative charge respectively, measured at the interaction point.
- $E_{\mu^+}$  and  $E_{\mu^-}$  are the energy of the muons of positive and negative charge respectively,  $E_{\mu} = \sqrt{m_{\mu}^2 \cdot c^4 + p_{\mu}^2 \cdot c^2}$ .
- $\theta_{\mu^+\mu^-}$  is the angle between the trajectories of the two muons measured at the interaction point.

Figure 3.2 displays the number of dimuons pairs detected as a function of their invariant mass: this is the invariant mass distribution. On the figure, the range of the  $x$  axis is restricted to the mass region of the  $J/\psi$  and  $\psi(2S)$ . In this distribution, we can clearly identify a peak around the  $3.1 \text{ GeV}/c^2$  region. This corresponds to the muon pair coming from the decay of a  $J/\psi$ .

We can also observe a continuum, decreasing as the mass increases. It is composed of a combinatorial background and a *physical* background. The combinatorial background is the main part and consists of uncorrelated muons, mainly from pion decay. For low- $p_{\text{T}}$   $J/\psi$ , the *physical* background remains negligible in front of the combinatorial background and consists of muons coming from Drell-Yan process and open charm decay [203].

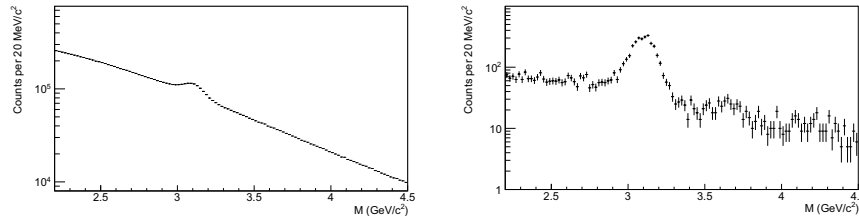


Figure 3.2: Dimuon invariant mass distributions in the centrality range 0-90% (left) and in the centrality range 70-90% (right). The peripheral centrality range is chosen in order to exhibit a distinguishable  $\psi(2S)$  peak at  $M \approx 3.6 \text{ GeV}/c^2$ .

Close to the  $J/\psi$  peak is the  $\psi(2S)$ , whose peak is only visible for the most peripheral collisions. In pp collisions, the magnitude of the  $\psi(2S)$  peak is expected to be around 2% of that of the  $J/\psi$ , which is why it is difficult to observe. In Pb – Pb collisions, the difficulty is even greater because the combinatorial background is much larger than in pp collisions, due to the larger number of interacting nucleons in a single collision, and the magnitude of the  $\psi(2S)$  peak is of the same order of magnitude as the statistical fluctuations of this background.

To evaluate the number of  $J/\psi$  and  $\psi(2S)$  we "count" the number of particles entering the peaks. In order to do so, the invariant mass spectrum is fitted with the sum of two signal functions, to describe the  $J/\psi$  and  $\psi(2S)$  peaks, and a background function describing the continuum. There are two different methods to fit the data: a direct fit to the data and a fit after subtraction of the combinatorial background with the event mixing technique.

In the next section, we will describe the fit functions used and then the two different approaches.

### 3.3.1 Fit Functions used for the signal

For the signal, the functions used are based on Monte Carlo (MC) simulations. They are composed of a gaussian core and two tails. The tails account for the effect due to the regions of the detectors where the resolution is poorer than on average, the possible dependence of the invariant mass resolution on the momentum and rapidity and the possible misalignments

of some parts of the detector with respect to the rest of the spectrometer. Additionally the left tail (towards lower masses) also accounts for the energy loss of the muons due to multiple scattering in the front absorber and to the possible emission of low energy photons by the radiative decay of charmonia:  $\psi \rightarrow \gamma\mu^+\mu^-$ .

The Crystal Ball function was proposed by the Stanford Linear Accelerator Center (SLAC) to reproduce the shape of the  $J/\psi$  and  $\psi(2S)$  signals [204]. The version presented here is an extended version of that function, called Extended Crystal Ball (CB2) and is defined as a function of the invariant mass of the muon pair  $m$  as [205]:

$$f(m) = N \cdot \begin{cases} \exp(-t^2/2) & \text{for } -\alpha < t < \alpha' \\ A.(B-t)^{-n} & \text{for } t \leq -\alpha \\ C.(D+t)^{-n'} & \text{for } t \geq \alpha' \end{cases} \quad (3.12)$$

with:

$$t = \frac{m - m_\psi}{\sigma}$$

$$A = \left(\frac{n}{\alpha}\right)^n \cdot \exp\left(-\frac{\alpha^2}{2}\right), \quad B = \frac{n}{\alpha} - \alpha$$

$$C = \left(\frac{n'}{\alpha'}\right)^{n'} \cdot \exp\left(-\frac{\alpha'^2}{2}\right), \quad D = \frac{n'}{\alpha'} - \alpha'$$

The expression of the parameters A, B, C and D as a function of  $\alpha$ ,  $n$ ,  $\alpha'$ ,  $n'$  is chosen such as the function and its derivative are continuous when  $t = -\alpha$  and  $t = \alpha'$ .

Another function used to describe the signal is the NA60 function, which is also a pseudo-gaussian function proposed by NA60 collaboration and is defined as:

$$f(m) = N \cdot \exp\left(-0.5 \left(\frac{t}{t_0}\right)^2\right) \quad (3.13)$$

with:

$$t = \frac{m - m_\psi}{\sigma}$$

and

$$\begin{cases} t_0 = 1 & \text{for } -\alpha < t < \alpha' \\ t_0 = 1 + p_1(-\alpha - t)^{(p_2 - p_3\sqrt{-\alpha - t})} & \text{for } t \leq -\alpha \\ t_0 = 1 + p'_1(t - \alpha')^{(p'_2 - p'_3\sqrt{t - \alpha'})} & \text{for } t \geq \alpha' \end{cases}$$

The expression of the function has been chosen to ensure the continuity and derivability at  $t = \alpha$  and  $t = \alpha'$ .

For the  $J/\psi$ , the free parameters are the mass  $m_\psi$ , the width  $\sigma$  and the amplitude  $N$ . The tail parameters are fixed, otherwise the fit is not reliable in the cases where the background is large, because it becomes impossible to distinguish the tails from the background. Consequently, the choice of the values for the tail parameters is important and will constitute one of the sources of systematic uncertainties. In order to determine the values of the tail parameters, a dimuon invariant mass distribution at the  $J/\psi$  mass is generated using MC simulations, and the signal function is fitted to it with all the parameters free. Another way to have a value for the tail parameters is to take the values obtained using pp data collected in 2015 at a collision energy of  $\sqrt{s} = 13$  TeV [147], where the data sample is much larger and for which the signal-to-background ratio more favorable than in Pb – Pb collisions, so that the tail parameters of the CB2 can be left free. However, this procedure is not applied to the NA60 function, because it has too many parameters and the fit is still unstable, even with the large pp data sample. Therefore for the NA60 function, only MC simulations are used to obtain the tail parameters values.

For the  $\psi(2S)$ , the signal function used is the same as for the  $J/\psi$ . Because the signal is much weaker than for the  $J/\psi$ , it is impossible to make the fit converge if the same parameters are left free. Therefore the mass and the width of the  $\psi(2S)$  are fixed to the ones of the  $J/\psi$  as follows:

- $m_{\psi(2S)} = m_{J/\psi} + \Delta m_{\text{PDG}}$ ,  $\Delta m_{\text{PDG}}$  being the mass difference between the values collected by the Particle Data Group (PDG) [34].
- $\sigma_{\psi(2S)} = \sigma_{J/\psi} \times R$ , where  $R$  is a fixed factor. The value of  $R$  can be estimated either with Monte Carlo simulations or with the  $\sqrt{s} = 13$  TeV pp data.

Tails parameters are the same for  $J/\psi$  and  $\psi(2S)$ , since the differences in the results from Monte Carlo simulations for  $J/\psi$  and  $\psi(2S)$  are negligible.

### 3.3.2 Fit Functions used for the background

For the background function, two functions are used in the case of the direct fit (section 3.3.3), and one in the case of the fit after Event Mixing (section 3.3.4). The first function for the direct fit is called the Variable Width Gaussian, which as its name indicates has the same expression as a Gaussian function, but with a width that varies with the mass. It is written:

$$f(m) = N \cdot \exp\left(\frac{-(m - \bar{m})^2}{2\sigma^2}\right), \quad (3.14)$$

with:

$$\sigma = \sigma_s + \beta \left(\frac{m - \bar{m}}{\bar{m}}\right) + \gamma \left(\frac{m - \bar{m}}{\bar{m}}\right)^2$$

The second function is a ratio of a second order polynomial form at the numerator and a third order polynomial form at the denominator:

$$f(m) = \frac{a_0 + a_1 m + a_2 m^2}{1 + b_1 m + b_2 m^2 + b_3 m^3} \quad (3.15)$$

For the background function, all the parameters are left free.

The background function used after removing the combinatorial background with the event mixing technique is a sum of two exponential functions, to reproduce the remaining correlated background:

$$f(m) = A_1 \cdot \exp\left(\frac{-m}{\sigma_1}\right) + A_2 \cdot \exp\left(\frac{-m}{\sigma_2}\right) \quad (3.16)$$

### 3.3.3 Direct Fit

With this method, the number of measured  $J/\psi$  and  $\psi(2S)$  are evaluated by doing a fit directly to the dimuon invariant mass distribution. The signal is extracted in several centrality bins. The large number of measured  $J/\psi$  allows to consider many bins in centrality, however for the  $\psi(2S)$ , since the number of measured particles as well as the signal-to-background ratio (S/B) are much smaller, we decided to consider only 4 bins: 0-20%, 20-40%, 40-60% and 60-90%. Examples of fits for two centrality bins are shown in Figure 3.3.

We can see from the values of the fit that the mass of the  $J/\psi$  is found very close to the value quoted by the PDG ( $m_{J/\psi}(\text{PDG}) = 3.097 \text{ GeV}/c^2$ ) with a resolution of  $\sigma_{J/\psi} = 70 \text{ MeV}/c^2$ . The number of  $J/\psi$  is almost 25 times larger in the centrality range 0-20% than in the range 60-90%, which is expected as there are more nucleon-nucleon collisions in central collisions and therefore more particles produced. However the other consequence is that the signal-to-background ratio is 25 times higher in the peripheral collisions.

For the  $\psi(2S)$  it can already be noted that the number extracted is close to a hundredth of the  $J/\psi$  one. In central collisions, the statistical

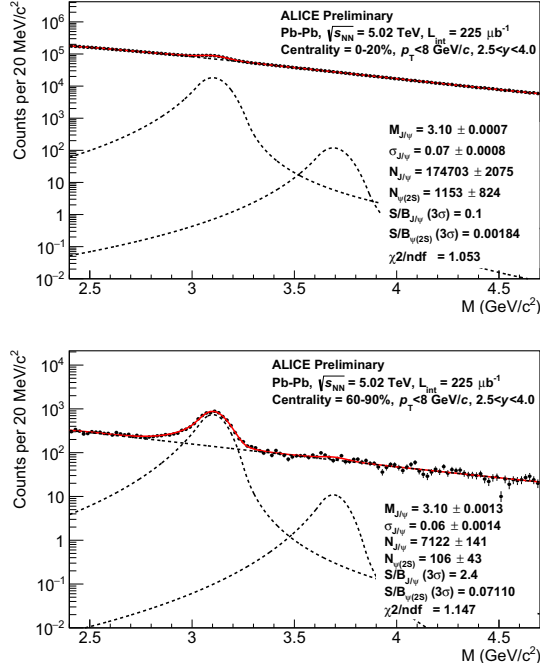


Figure 3.3: Direct Fit to the dimuon invariant mass distribution in the centrality range 0-20% (top) and 60-90% (bottom). The distributions are fitted with an extended Crystal-Ball function and a Variable Width Gaussian.

uncertainty on the number of  $\psi(2S)$  is of the same order of magnitude as the extracted number. In peripheral collisions, the relative uncertainty is smaller because of the higher  $\psi(2S)$  signal-to-background ratio. The value of the signal-to-background ratio for the  $\psi(2S)$ , which is very small, shows the difficulty there is to distinguish between the  $\psi(2S)$  peak and background fluctuations (particularly in the most central collisions). Finally the  $\chi^2/ndf$  value is an indicator of the quality of the fit, a value around 1 corresponding to a good fit.

This method for extracting the signal is common to all quarkonium analysis and is for instance used in the analysis of proton-proton data [147, 206, 207].

### 3.3.4 Fit after event-mixing

The second method to extract the signal from the data consists in first removing the combinatorial background using the Event Mixing technique, before fitting the data. The idea is to use the data themselves to obtain the distribution of the combinatorial background rather than relying on an empirical fit function. Of course, fit functions are still used, but only to describe the remaining background after the combinatorial background has been subtracted.

To remove this combinatorial background, an artificial background distribution is created and then subtracted to the data. Since the combinatorial background is by definition composed of pairs of uncorrelated muons, the process of creating the artificial background distribution, that we will call "event mixing distribution", consists in forming uncorrelated pairs by *mixing* muons from different events. To be more specific, the process goes as follows: a first muon track,  $T_1$ , is chosen in a given event. It is combined with a muon Track  $T'_1$  from a different event to form a first muon pair  $(T_1, T'_1)$ . The process is then repeated with a second track  $T'_2$  also from a different event, until  $T'_n$ , with  $n$  being arbitrarily large. Then the same procedure is applied with  $T_2$ , a second muon track from the same event as  $T_1$ , until all tracks from the first event have been used, as described in Figure 3.4.

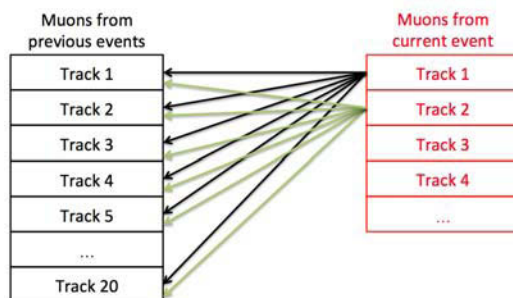


Figure 3.4: Illustration of the principle of the event mixing.

The only condition to form a muon pair is that the muons have to come from the same run, in order to have experienced the same detector conditions, and belong to events that lie in the same centrality range, because the shape of the background changes with the centrality.

The advantage of using this method is that the event mixing histogram can be created with as many muon pairs as desired and therefore the corre-

sponding statistical uncertainty can be made arbitrarily small. In practice, each muon is combined with 20 tracks from previous events and the relative statistical uncertainty on the event mixing distribution is negligible with respect to the one from the data.

Before it is subtracted from the data invariant mass distribution, the event mixing distribution is normalized with respect to the data. This normalization is performed using muon pairs of the same sign. Since there is no correlated background in the same sign distributions, they should be reproduced perfectly by the event mixing, at least starting from a high enough mass. The normalization factor is:

$$F = \frac{\int_{m_{min}}^{m_{max}} 2R \sqrt{N_{Raw}^{++} N_{Raw}^{--}} dm}{\int_{m_{min}}^{m_{max}} N_{Mix}^{+-} dm} \quad (3.17)$$

where the  $N_{Raw}^{++}$  and  $N_{Raw}^{--}$  are the number of positive muon pairs and negative muon pairs measured in the data,  $N_{Mix}^{+-}$  is the number of unlike-sign pairs obtained with mixed events and  $R$  is a detector-related factor given by  $R = \frac{N_{Mix}^{+-}}{2\sqrt{N_{Mix}^{++} N_{Mix}^{--}}}$ , which takes in account the slight differences in performance of the detector between the detection of positive and negative muons and is calculated bin by bin. The distribution of  $R$  as a function of the mass is shown in Figure 3.5. The range of the integral to normalize the event mixing

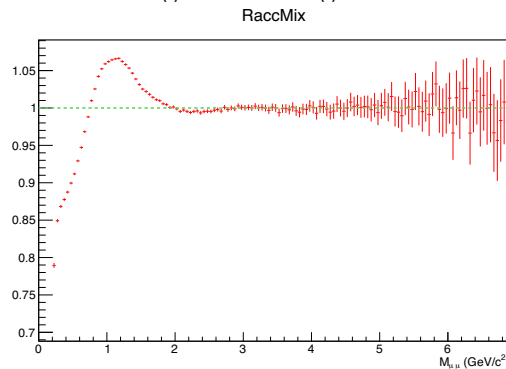


Figure 3.5: Normalization factor  $R$  as a function of the invariant mass obtained from events in the 0-10% centrality range.

distribution is chosen to be as large as possible, but in a mass region where the like sign event mixing shape reproduces the one of the like-sign from the data. In this analysis, the range chosen is 2-8  $\text{GeV}/c^2$ , which includes the

charmonium region but not the bottomonium region ( $m_{\Upsilon(1S)} = 9.6 \text{ GeV}/c^2$ ) and avoids the region below  $2 \text{ GeV}/c^2$  where the correlated background is more important. Moreover, in this region the factor  $R$  is very close to unity.

In order to control if the event mixing spectrum reproduces correctly the combinatorial background, some checks are done using the  $p_T$  and  $y$  distribution of the like-sign spectra, restrained to the  $2\text{-}8 \text{ GeV}/c^2$  region. Figure 3.6 show how the constructed event mixing spectrum compares to the data.

For the unlike sign distributions, we can see in the mass distribution the peak corresponding to the  $J/\psi$ , which is why naturally the mixed event distribution and the data don't match. However for the  $p_T$  and  $y$  distributions, the region  $2.5 - 4 \text{ GeV}/c^2$  is removed in order to verify that the  $p_T$  and  $y$  distributions match for the rest of the mass region. For the like-sign distributions, we expect the like-sign mixed-event spectrum to reproduce perfectly the  $p_T$ ,  $y$  and mass distribution, since the like-sign spectrum from the data are composed of only combinatorial background.

For the  $p_T$  distribution, the event mixing spectrum reproduces the data with a precision better than 2% at low  $p_T$  and at higher  $p_T$  the statistical fluctuations in the data makes the difference larger. For the  $y$  distribution, the event mixing like sign spectra reproduces the data with a precision better than 3% in the considered rapidity range. Finally for the mass distribution, the difference is again less than 3%. For the unlike sign distributions in mass and rapidity, we can see that the data points are systematically above the mixed event distribution points, which is expected because of the correlated background. This differences are then accounted for in the fit with the function describing the remaining background.

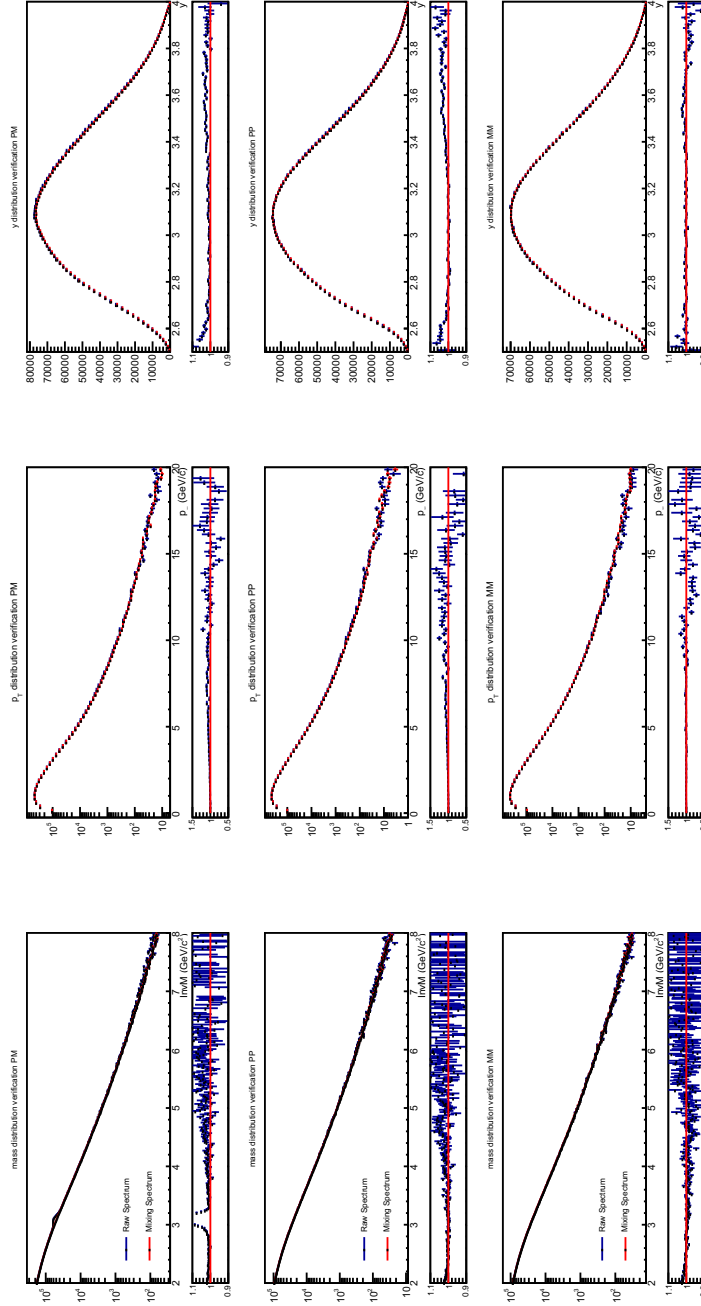


Figure 3.6: Comparison between the event mixing distribution and the data as a function of invariant mass (left),  $p_T$  (middle) and rapidity (right), for the  $\mu^+\mu^-$  distribution (top),  $\mu^+\mu^+$  distribution (middle) and  $\mu^-\mu^-$  distribution (bottom). For each figure the ratio between the data and the mixed event spectrum is also shown.

Examples of the fits with the event mixing technique are shown in Figure 3.7. As for the direct fit, the  $J/\psi$  mass is very close to the one measured by the PDG, and the resolution is similar. We can see that for the peripheral bin, the number of  $J/\psi$  and  $\psi(2S)$  are very close to the ones extracted with the direct fit. However for the more central bin, the number of  $\psi(2S)$  is larger, even though both results are compatible considering the statistical uncertainties. This difference is due to the large background in the central region, that causes large systematic uncertainties on the  $\psi(2S)$  signal. The statistical uncertainty however remains of the same order of magnitude.

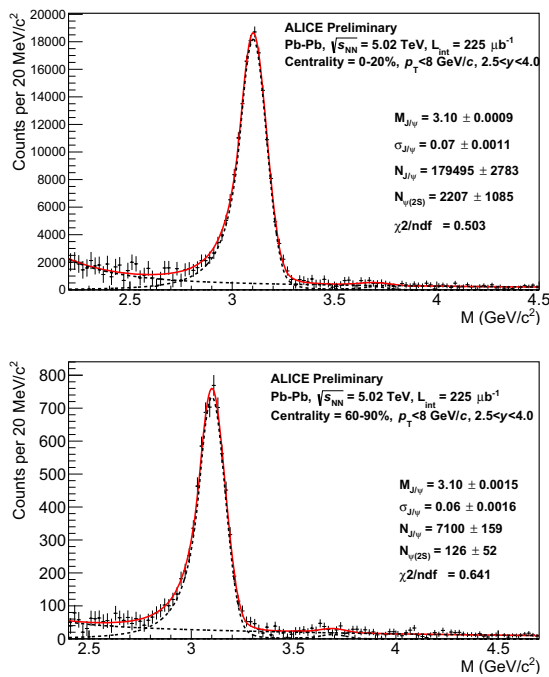


Figure 3.7: Fit to the dimuon invariant mass distribution after event mixing subtraction in the centrality range 0-20% (top) and 60-90% (bottom). The distributions are fitted with the sum of two extended crystal ball functions (one for the  $J/\psi$  and one for the  $\psi(2S)$ ) and a sum of exponential functions.

### 3.3.5 Systematic uncertainty

As mentioned before, the signal extraction is performed using different techniques and different assumptions for the fit on the data, such as the signal function and tail parameters values. Several tests are performed to evaluate the systematic uncertainty, chosen to be consistent between the  $J/\psi$  and the  $\psi(2S)$  signal extraction. For the direct fit (Section 3.3.3), this results in:

- 2 fit ranges:  $2.2 < m_{\mu\mu} < 4.5 \text{ GeV}/c^2$  and  $2.4 < m_{\mu\mu} < 4.7 \text{ GeV}/c^2$ .
- 2 signal functions: CB2 and NA60.
- 2 background functions: VWG and polynomial ratio.
- 2 sets of tail parameters for the CB2: one based on the Monte Carlo (MC) simulations and one based on a fit to the dimuon invariant mass distribution in pp collisions at  $\sqrt{s} = 13 \text{ TeV}$  [147]. For the NA60, only the MC simulations are used.
- 2  $\psi(2S)$ -to- $J/\psi$  resolution ratios: 1.01 based on MC simulations and 1.05, based on the same fit to the pp data at  $\sqrt{s} = 13 \text{ TeV}$ .

For the event mixing case (Section 3.3.4), the tests are:

- 3 fit ranges:  $2.2 < m_{\mu\mu} < 4.5 \text{ GeV}/c^2$ ,  $2.4 < m_{\mu\mu} < 4.7 \text{ GeV}/c^2$  and  $2 < m_{\mu\mu} < 5 \text{ GeV}/c^2$ .
- 2 signal functions.
- 2 sets of tail parameters for the CB2 and one for NA60.
- 2 resolution ratios.

In total, 56 tests<sup>1</sup> are performed. Each test gives a  $\psi(2S)$  yield and an associated statistical uncertainty. The final yield and statistical uncertainty are taken as the average of the results for each test. The systematic uncertainty on the signal extraction is given by the root mean square (RMS) of the different results provided by the tests.

---

<sup>1</sup>The tests with tail parameters from pp data are counted twice, in order to have the same amount of contributions from MC simulations and from data in the systematic uncertainty evaluation.

### 3.3.6 Results

#### Centrality integrated result

Figure 3.8 shows the distribution of the 56  $\psi(2S)$  yields and uncertainties obtained for the tests detailed above. The corresponding total number of measured  $\psi(2S)$  is  $N_{\psi(2S)} = 2024 \pm 1043$  (stat)  $\pm 740$  (syst). The different combinations are indicated in the abscissa axis. The mean value of the tests is indicated by the red full line and the dotted lines correspond to the systematic uncertainty at  $+1\sigma$  and  $-1\sigma$ . It can be noted that for 6 tests, the extracted value is compatible with 0.

Figure 3.9 shows the  $\psi(2S)$ -to- $J/\psi$  ratio integrated over centrality for all the different tests. The mean value of the ratio is:  $0.007 \pm 0.004$  (stat)  $\pm 0.002$  (syst). This value is obtained by doing the ratio of the extracted value of  $\psi(2S)$  and  $J/\psi$  for each of the test, then the average, mean statistical uncertainty and the RMS. Another way to evaluate the ratio is to set the  $\psi(2S)$ -to- $J/\psi$  ratio as a fit parameter rather than the  $\psi(2S)$  amplitude. This allows to properly account for possible correlations between the  $J/\psi$  and  $\psi(2S)$ . However it was verified that this correlation is negligible with respect to the statistical uncertainty of the  $\psi(2S)$ .

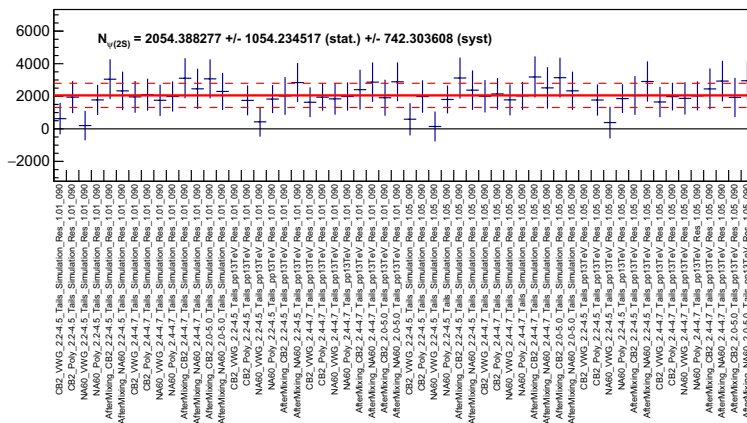


Figure 3.8: Different signal extraction tests, for the rapidity and  $p_T$ -integrated invariant mass distributions, in the centrality range 0-90%.

The value of the ratio integrated over centrality illustrates the difficulty of the measurement for the  $\psi(2S)$ , with a number of extracted particles less

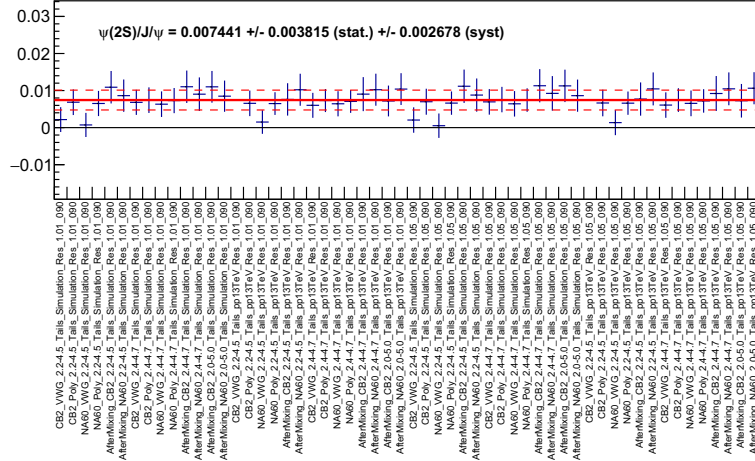


Figure 3.9: Distribution of the  $\psi(2S)/J/\psi$  ratio as a function of the different signal extraction tests, for the rapidity and  $p_T$ -integrated invariant mass distributions, in the centrality range 0-90%.

than 1% of the  $J/\psi$ .

### Centrality dependence

The next step is to look at the centrality dependence of the  $\psi(2S)$  signal. For the  $\psi(2S)$ , only 4 centrality intervals are considered: 0-20%, 20-40%, 40-60% and 60-90%. In addition, and in order to compare the results with the  $\sqrt{s_{NN}} = 2.76$  TeV, three different  $p_T$  ranges were considered:  $0 < p_T < 8$  GeV/c,  $0 < p_T < 3$  GeV/c and  $3 < p_T < 8$  GeV/c. For this last range, only three centrality intervals could be considered. Table 3.2 shows the resulting yields in each centrality bin with both statistical and systematic uncertainties. The average signal-to-noise for the  $\psi(2S)$  ranges from  $(S/B)_{\psi(2S)}^{40-60\%} = 0.0013$  in the bin 40-60% to  $(S/B)_{\psi(2S)}^{60-90\%} = 0.095$  in the bin 60-90%. For the  $J/\psi$ , the lowest signal-to-noise ratio is found in the most central bin and is  $(S/B)_{J/\psi}^{0-20\%} = 0.1$ . The highest value is in the bin 60-90% and is  $(S/B)_{J/\psi}^{60-90\%} = 2.4$

The values quoted in Table 3.2 show that the signal extraction for the  $\psi(2S)$  is difficult and in a lot of cases the number of measured  $\psi(2S)$  is compatible with zero. In those cases, a confidence limit (CL) must be calculated.

Centrality (%)	$N_{\psi(2S)} \pm (stat) \pm (sys)$
$0 < p_T < 8 \text{ GeV}/c$	
0-20	$1553 \pm 905 \pm 543$
20-40	$381 \pm 415 \pm 159$
40-60	$28 \pm 144 \pm 12$
60-90	$111 \pm 45 \pm 11$
$0 < p_T < 3 \text{ GeV}/c$	
0-20	$1184 \pm 815 \pm 731$
20-40	$275 \pm 372 \pm 72$
40-60	$8 \pm 128 \pm 6$
60-90	$86 \pm 38 \pm 10$
$3 < p_T < 8 \text{ GeV}/c$	
0-20	$542 \pm 353 \pm 160$
20-60	$103 \pm 165 \pm 37$
60-90	$27 \pm 76 \pm 4$

Table 3.2:  $\psi(2S)$  counts in four centrality bins and for three  $p_T$  intervals. First uncertainty is statistical, second is systematic.

The method for calculating the confidence limits is discussed in Section 3.8.

### 3.4 Acceptance times Efficiency determination

The number of  $J/\psi$  and  $\psi(2S)$  extracted in the previous section does not correspond to the total number of charmonium produced, because the detector doesn't cover the full phase space and doesn't have a perfect efficiency for detecting the dimuons. One must correct the extracted number of charmonium by a number called the acceptance $\times$ efficiency, noted  $A\varepsilon$ , which will take these factors into account.

#### 3.4.1 Calculation of the $A\varepsilon$

The  $\psi(2S)$   $A\varepsilon$  is obtained using MC simulations, by computing the ratio between the number of charmonia reconstructed in the muon spectrometer and the number of generated charmonia in the same  $p_T$  and  $y$  interval.

Charmonia are generated using input  $p_T$  and  $y$  distributions obtained from the data. The charmonia are then forced to decay into two muons using EVTGEN [208] and PHOTOS [209] to properly account for the possible emission of radiative photons.

The decay muons are tracked through a GEANT3 (GEometry ANd Tracking) [210] model of the ALICE detector. This model describes the particle-matter interaction inside the detector and includes a realistic description of the detectors as well as their performance during data taking. Track reconstruction and signal extraction are performed from the simulated hits generated in the detector using the same procedure and selection criteria as those used for the data.

In Pb – Pb collisions, the large number of produced particles causes the detector to have large occupancies<sup>2</sup>. This might deteriorate the reconstruction efficiency and the quality of the reconstructed tracks, because of the increased number of overlapping clusters in the detectors and the increased probability to select a hit belonging to another particle when reconstructing the tracks. In order to reproduce this effect, the acceptance $\times$ efficiency is estimated using the embedding technique. It consists in embedding the MC simulated charmonium in a Minimum Bias event from real data (see Section 2.5).

All efficiencies are calculated on a run by run basis. Since the embedding is done in Minimum Bias events but the analysis on dimuon triggered events, when evaluating the run-averaged efficiencies one must weight the

---

<sup>2</sup>The occupancy is the fraction of electronic channels to receive a hit for a given collision. In the most central collisions, the occupancy of the Muon Tracker is around 2%.

run by run efficiencies by the number of dimuon triggers in each run. To calculate the centrality integrated efficiencies, one must first calculate a per-centrality bin efficiency and take the average using weights proportional to the raw number of reconstructed charmonium in each centrality bin. For the  $\psi(2S)$ , since the signal is not large enough, the number of measured  $J/\psi$  is used as a weight. These weights are defined for 10% width centrality bins, therefore when considering the larger centrality bins in the case of the  $\psi(2S)$  these weights are also considered. Using the  $J/\psi$  numbers is only an approximation because it assumes that the centrality dependent suppression pattern for the  $\psi(2S)$  is the same as that of the  $J/\psi$ , which may not be the case. However, differences are expected to have a negligible impact with respect to other sources of systematic uncertainties, given the small dependence of the  $A\varepsilon$  as a function of centrality.

The  $J/\psi$  and  $\psi(2S)$  production is assumed to be unpolarized consistently to the values measured by ALICE [151] and LHCb [211, 212] in pp collisions. It is assumed that this result holds in Pb – Pb collisions. An assumption on the polarization of the charmonia affects the angular distribution of the decaying muons for a given set of  $p_T$  and  $y$  input distributions and as a consequence, the acceptance $\times$ efficiency.

The shapes of the  $p_T$  and  $y$  distribution of the charmonium used as inputs to the MC simulation are the same for both particles. The  $J/\psi$  distributions are used because the  $\psi(2S)$  measurements were not precise enough to determine these distributions directly. The  $J/\psi$  input distribution have been tuned directly on the data in the centrality range 0-90%, using an iterative procedure. The adopted input functions are, for the  $p_T$  distribution:

$$f(p_T) = p_0 \times p_T / (1 + (p_T/p_1)^{p_2})^{p_3} \quad (3.18)$$

with  $p_0=1.01 \cdot 10^6$ ,  $p_1=3.50$ ,  $p_2=1.93$ ,  $p_3=3.96$ .

For the rapidity distribution:

$$f(y) = p_0 \times \exp(-0.5 \times ((y - p_1)/p_2)^2) \quad (3.19)$$

with  $p_0=1.10 \cdot 10^6$ ,  $p_1=0$ ,  $p_2=2.13$

A third weight is applied to the  $A\varepsilon$ , to take into account the centrality dependence of the input shapes. In particular, given the high statistics collected in the 2015 Pb – Pb run, it has been possible to extract, directly from the acceptance corrected data, the  $J/\psi$   $p_T$  shapes,  $f_i = dN_{J/\psi}/dp_T$ , in several centrality bins and to use these distributions as weights for the

embedding. In a given centrality bin  $i$ , the  $A\varepsilon$  for a given  $p_T$  is:

$$(A\varepsilon)_i = \frac{\sum_{p_T} (A\varepsilon)_{i,p_T}^{0-90\%} \times f_i(p_T)}{\sum_{p_T} f_i(p_T)} \quad (3.20)$$

where  $(A\varepsilon)_{i,p_T}^{0-90\%}$  is the acceptance computed using as input the shapes tuned on data in 0-90%.

The  $J/\psi$   $p_T$  distribution has been evaluated in the centrality bins 0-10%, 10-20%, 20-30%, 30-40%, 40-50%, 50-60% and 60-90%. They are shown in Figure 3.10.

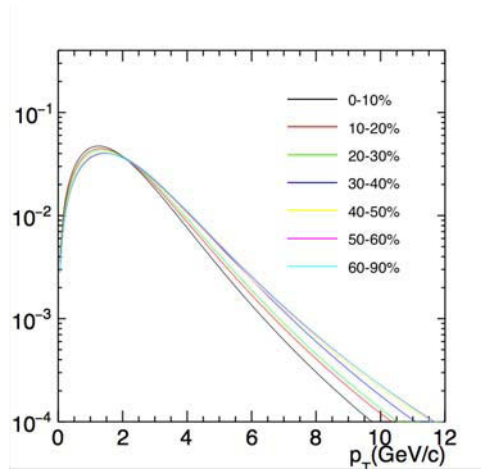


Figure 3.10: Simulated acceptance×efficiency corrected  $J/\psi$   $p_T$  distributions in seven centrality bins.

The influence of the centrality dependence of the  $y$  distributions on the  $A\varepsilon$  was also evaluated in a similar way as it was done for the  $p_T$  distribution: the  $y$  shapes have been tuned in the same seven centrality bins as for  $p_T$  and the impact of the differences between these distributions on the  $A\varepsilon$  was found to be negligible.

The acceptance×efficiency as a function of centrality is shown in Figure 3.11. The centrality bin 100-110% corresponds to the  $A\varepsilon$  in the centrality range 0-90%. We can note that  $A\varepsilon$  corrections for  $\psi(2S)$  are systematically larger than for  $J/\psi$ , especially at low  $p_T$ : because the  $\psi(2S)$  mass is larger than the one of the  $J/\psi$ , the resulting muons from the decay have in average a larger transverse momentum and therefore are less often cut by the dimuon trigger minimum  $p_T$  requirement.

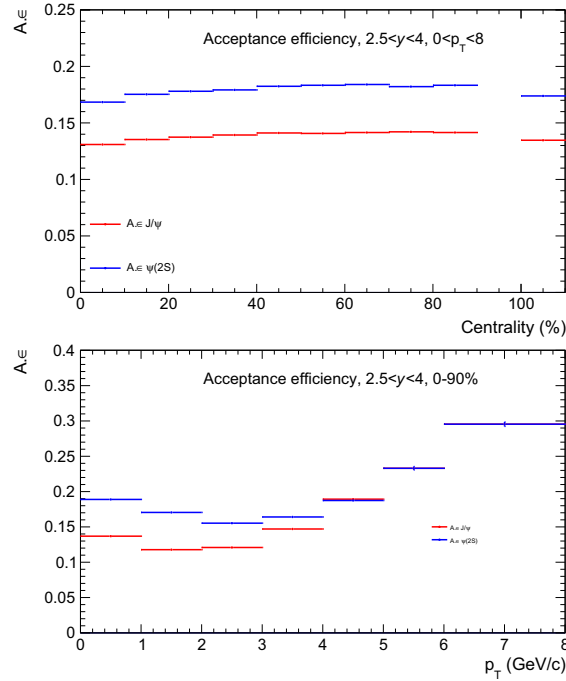


Figure 3.11: Top panel:  $p_T$ -integrated acceptance $\times$ efficiency of the  $\psi(2S)$  (blue) compared to the one of the  $J/\psi$  (red) versus centrality. Bottom panel: acceptance $\times$ efficiency of the  $\psi(2S)$  (blue) compared to the one of the  $J/\psi$  (red) in the centrality range 0-90% versus  $p_T$ .

### 3.4.2 Systematics uncertainties on the $A\varepsilon$

The sources of systematic uncertainties corresponding to the  $A\varepsilon$  correction are:

- Uncertainties on the  $p_T$  and  $y$  distributions used in input to the Monte Carlo simulation.
- Uncertainties on the tracking efficiencies.
- Uncertainties on the trigger efficiencies.
- Uncertainties on the efficiency of the matching of the tracks between the Muon Trigger and the Muon Tracker.

The systematic uncertainties on the tracking efficiency, trigger efficiency and matching efficiency, are the same for the  $J/\psi$  and the  $\psi(2S)$ .

The uncertainties on the tracking efficiency are estimated by comparing the efficiency on the single muon detection calculated with the data to the one obtained with simulations. This comparison is possible because the tracking algorithm used to reconstruct the muon tracks doesn't require all the chambers to be fired to be able to reconstruct a given track. As a consequence, there is an internal redundancy in the hits that belong to a given track. This redundancy of the chambers is used to measure their individual efficiency. In this instance the efficiency does not refer to the efficiency on  $\psi(2S)$  reconstruction, but the efficiency of a given chamber to detect a particle passing through it. Since these chamber efficiencies are independent from each other, one can estimate the overall tracking efficiency, which is the efficiency on the reconstruction of a single muon track, by combining the individual efficiencies.

However, this measurement is not precise enough to be used to correct directly the data, because only the mean efficiency per chamber can be computed with the statistics available in each run. Moreover, chamber inefficiencies occurring in overlapping region of space can remain undetected by the method. By comparing the result obtained from data with the same measurement performed in simulation, it is possible to estimate the accuracy of the simulations and the corresponding systematic uncertainty related to the tracking efficiency on the  $A\varepsilon$  corrections. This is done assuming that the same biases are present in the data and the MC. In order to go from the uncertainty on the single muon to the one on the dimuon, a factor 2 is applied, which is conservative. Taking all this into account, a 4% uncertainty is obtained. It is fully correlated as a function of centrality.

The systematic uncertainties on the trigger efficiency has two different contributions: the uncertainty on the shape of the trigger response and the uncertainty on the intrinsic chamber efficiency. The first contribution, which is the efficiency of the trigger on the single muon as a function of  $p_T$ , is obtained by comparing the influence of two different trigger response: one obtained from the data and the other from MC simulations, on the acceptance $\times$ efficiency. The uncertainty on the intrinsic chamber efficiency is estimated by varying the efficiency of each chamber of the trigger in the simulations. This two contributions are added in quadrature to obtain the final uncertainty on the trigger efficiency, which amounts to 3.6%. The uncertainty on the trigger efficiency is correlated as a function of centrality.

The uncertainty on the  $p_T$  and rapidity distributions used in input to the simulations accounts for the possible correlations between the  $p_T$  and  $y$

distributions in the MC simulation and the accuracy by which these distributions could be determined from the data. It is evaluated for the  $J/\psi$  by calculating the  $A\varepsilon$  in a fashion similar to that was explained previously, but instead of considering the number of  $J/\psi$  in  $p_T$  and centrality bins, this time rapidity bins are also taken into account. The result is compared to what was calculated with Equation 3.18 and the difference gives the systematic uncertainty on the MC inputs. The resulting value amounts to 2%, which is also correlated as a function of centrality.

For the  $\psi(2S)$ , a similar study was done to estimate the uncertainties on the  $\psi(2S)/J/\psi$  ratio for the data at  $\sqrt{s_{NN}} = 2.76$  TeV. The same value for the ratio is considered in this analysis: the 2% on the  $\psi(2S)$ -to- $J/\psi$  ratio calculated in 2011 is summed quadratically to the one on the  $J/\psi$  MC input to estimate the uncertainty on the MC inputs for the  $\psi(2S)$ , which amounts to 3%.

### 3.5 Number of equivalent minimum bias events

In order to compute yields from the number of charmonium, one must evaluate the number of minimum bias event equivalent to the number of triggered unlike-sign muons events used in the analysis, using the following formula:

$$N_{MB}^{eq} = \sum_{run=i} F_{norm}^i \times N_{MUL}^i \quad (3.21)$$

where  $N_{MUL}^i$  is the number of triggered unlike-sign muons events after the Physics Selection (see Section 3.2.2) in order to eliminate the events that do not correspond to nucleus-nucleus collisions and  $F_{norm}^i$  is the normalization factor computed run-by-run.

#### 3.5.1 The $F_{norm}$ calculation methods

There are several methods to calculate the normalization factor. The first method is based on the number of recorded events for a given trigger. For each run  $i$  we compute  $F_{norm}^{off1}$  with the following formula :

$$F_{norm}^{off1,i} = PU^i \times \frac{MB^i}{MB\&0MUL^i} \quad (3.22)$$

where:

- MB is the number of physics selected (PS) minimum bias (MB) events.
- MB&0MUL is the subsample of MB event that also satisfy the dimuon trigger requirement.
- PU is the pile-up correction factor associated to the MB trigger described in Section 3.5.2.

A second method, also based on recorded events, uses an intermediate trigger with higher statistics (like the single muon trigger MSL for example) to compute the normalization factor :

$$F_{norm}^{off2,i} = PU^i \times \frac{MSL^i}{MSL\&0MUL^i} \times \frac{MB^i}{MB\&0MSL^i} \quad (3.23)$$

where:

- MSL is the number of physics selected MSL events.
- MSL&0MUL is the subsample of MSL events also satisfying the dimuon trigger requirement.
- MB&0MSL is the subsample of MB events also satisfying the single muon trigger requirement.

The idea behind the introduction of this intermediate trigger class is to minimize the impact of the downscale factor applied to the different triggers: for some triggers, not all events are recorded online but only a fraction, because the acquisition system is busy and cannot record all events. For instance, for the Minimum Bias trigger, only one out of 10 events is recorded. The fraction of MSL events in the MB trigger is larger than the fraction of MUL events in the MB trigger. This allows to reduce the statistical uncertainty on the resulting ratio. This method is particularly useful when the number of recorded minimum bias events is small.

The last method uses the L0b (see Section 2.5.1 for the L0 definition, "b" means that it corresponds to the events before the CTP selection) trigger scalars:

$$F_{norm}^{scal,i} = PU^i \times \frac{F_{purity}^{MB} L0b_{MB}^i}{F_{purity}^{MUL} L0b_{MUL}^i} \quad (3.24)$$

where  $F_{purity}^{MB}$  and  $F_{purity}^{MUL}$  are the purity factor associated to the minimum bias trigger (MB) and dimuon trigger (MUL), respectively. The purity factor accounts for the number of recorded events that correspond to an actual

nucleus-nucleus collision, instead of background collisions. The purity is evaluated with the V0 and ZDC detectors (see Section 3.2.2).

The advantage of this method is that the scalers are considered before any downscale or acquisition time out and have a larger statistic than the triggers considered in the first two methods. However, at the level L0 the detectors are subject to the background and therefore the purity associated to each trigger has to be computed.

### 3.5.2 Pile-Up factor

As seen in the previous section, the pile-up factor PU appears in the evaluation of the normalization factor. The pile-up factor estimates the fraction of minimum bias events in which more than one collision happened. The triggers are designed so that there is at most one trigger per bunch crossing. However, during a bunch crossing, it is possible to have more than one collision, and then it is possible that more than one collision sets the trigger. When this happens, the collisions are registered in the same event by the trigger, which constitutes pile-up. The pile-up factor is computed run-by-run and is defined as:

$$PU^i = \frac{\mu^i}{1 - e^{-\mu^i}} \quad (3.25)$$

with  $i$  the run number and  $\mu^i$  is defined as:

$$\mu^i = -\ln \left( 1 - \frac{F_{purity}^{MB,i} \times L0b_{MB}^{rate,i}}{N_{colliding}^i \times f_{LHC}} \right) \quad (3.26)$$

where:

- $N_{colliding}^i$  is the number of colliding bunches
- $f_{LHC}$  is the frequency (rotation rate) of the LHC. It is equal to the speed of light  $c$  divided by the circumference of the LHC.
- $L0b_{MB}^{rate,i}$  is the rate of the Minimum Bias trigger at the level L0b (see Section 2.5).
- $F_{purity}^{MB}$  is the purity factor associated to MB events, meaning the fraction of the minimum bias events that pass the physics selection.

The pile-up factor for the Pb – Pb collisions at  $\sqrt{s_{NN}} = 5.02$  TeV is around 1.001.

### 3.5.3 Results

The evolution of  $F_{norm}^i$  as a function of the run number for the Minimum Bias trigger (which is the CINT7 trigger for our analysis, see Section 2.5) is shown in Figure 3.12. For the method using the L0 scalers, the CINT7 trigger could not be used directly, because of problems with the V0. Therefore an other trigger called COV0M is used, which doesn't cover the same centrality range but is equivalent to the Minimum Bias trigger after the appropriate correction [157].

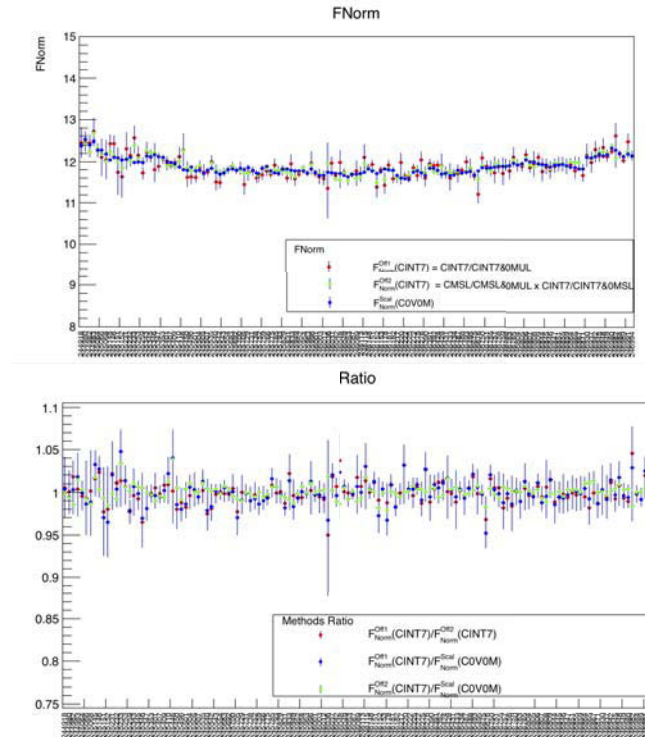


Figure 3.12: Evolution of  $F_{norm}(CINT7)$  for the three methods versus run number. For the scaler method (in blue), the CINT7 trigger could not be used directly, therefore the COV0M trigger is used instead, with the appropriate normalization factor to make it equivalent to the CINT7. All the methods are in good agreement within statistical uncertainties.

All the  $F_{norm}^i$  evaluations are consistent and in good agreement within statistical uncertainties. Using Equation 3.21, we can evaluate the number of equivalent minimum bias events per run. The final number we need,

$F_{norm}$  is the one to go from the total number of CMUL events analyzed to the equivalent number of MB events:

$$F_{norm} = \frac{\sum_{run=i} N_{MB,i}^{eq}}{\sum_{run=i} N_{MUL}^i} = \frac{\sum_{run=i} F_{norm}^i \times N_{MUL}^i}{\sum_{run=i} N_{MUL}^i} \quad (3.27)$$

$$F_{norm} = \sum_{run=i} F_{norm}^i \frac{N_{MUL}^i}{\sum_{run=i} N_{MUL}^i} \quad (3.28)$$

Results using the three methods are given in table 3.3. The final value is

Method	$F_{norm}$	statistical error
$F_{norm}^{off1} (CINT7)$	11.845	0.10%
$F_{norm}^{off2} (CINT7)$	11.850	0.07%
$F_{norm}^{scal} (COV0M)$	11.841	0.01%

Table 3.3: Average value of  $F_{norm}$  obtained with three different approaches.

given by the scaler method, because it has the smallest uncertainty. A systematic uncertainty is added to take into account the difference between the methods [157], in a similar fashion than what was done in p – Pb analysis in ALICE [213]. The final result is  $F = 11.84 \pm 0.06$ , where the uncertainty is dominated by the systematic uncertainty. As a function of centrality, the corresponding factor  $F_i$  is given by  $F_i = F \cdot \Delta_i$ , where  $\Delta_i$  is the fraction of the inelastic cross section of a given centrality class with respect to the 0-90% centrality range (0.1/0.9 for 0-10% centrality and so on).

### 3.6 $\psi(2S)$ cross-section in pp collisions

As shown in Equation 3.6, in order to compute the  $\psi(2S)$   $R_{AA}$  one also needs the  $\psi(2S)$  cross-section measured in pp collisions at the same energy. This cross-section is written:

$$\sigma_{\psi(2S)}^{pp} = \frac{1}{L_{int}} \frac{N_{\psi(2S)}}{\text{BR}_{\psi(2S) \rightarrow \mu^+ \mu^-} \cdot A\varepsilon}, \quad (3.29)$$

where  $\text{BR}_{\psi(2S) \rightarrow \mu^+ \mu^-}$  is the branching ratio of the  $\psi(2S)$  into a pair of muons [34],  $N_{\psi(2S)}$  is the number of  $\psi(2S)$  measured in this interval,  $A\varepsilon$

the corresponding acceptance and efficiency corrections and  $L_{int}$  the integrated luminosity of the data sample.

The pp data were collected during three days before the Pb – Pb collisions, for a total integrated luminosity of  $106.28 \pm 0.09 \pm 2.23 \text{ nb}^{-1}$ . The luminosity is evaluated using the formula:

$$L_{int} = \frac{N_{MUL} \cdot F_{norm}}{\sigma_{VDM}} \quad (3.30)$$

where :

- $N_{MUL}$  is the total number of events fulfilling the dimuon trigger condition
- $F_{norm}$  is a normalization factor calculated for a reference Minimum Bias Trigger. It is evaluated in a similar fashion as what was presented in Section 3.5.1.
- $\sigma_{VDM}$  is the cross section for that reference trigger evaluated using a Van der Meer scan procedure.

The procedure for the evaluation of the luminosity is described in Section 2.1.1.

The values of the number of extracted  $\psi(2S)$  and the  $A\varepsilon$  are evaluated in a similar fashion to what is done in Pb – Pb. After the QA and physics selection, a total of 25 runs remains. The track and event selection is the same as in Pb – Pb collisions, described in Section 3.2.

### 3.6.1 Signal extraction

As in Pb – Pb collisions,  $J/\psi$  and  $\psi(2S)$  yields are extracted using fits to the dimuon invariant mass distribution. The functions used for the fit are the same as the ones presented in Section 3.3. An example of fit is shown in figure 3.13.

The different tests performed to evaluate the systematic uncertainty on the signal extraction are the same as the ones performed in the case of Pb – Pb collisions and described in Section 3.3.5. However, event mixing is not performed in pp collisions, because the combinatorial background is much smaller than in Pb – Pb collisions. In total a number of 32 tests are performed.

The number of  $\psi(2S)$  obtained for all the tests are presented in Figure 3.14. The number of  $\psi(2S)$  and the corresponding statistical uncertainty

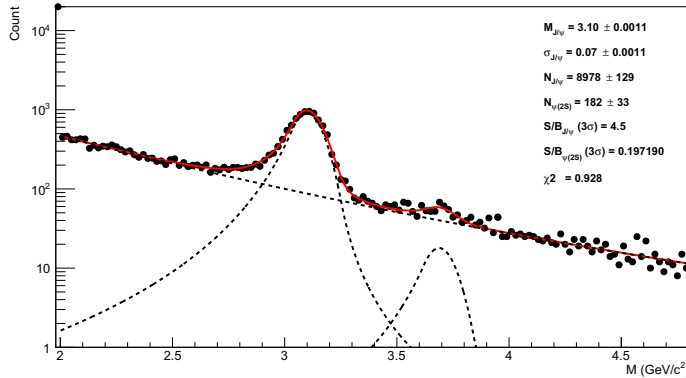


Figure 3.13: Example of fit to the  $p_T$ - and  $y$ -integrated dimuon invariant mass distribution in pp at  $\sqrt{s} = 5$  TeV. Dotted lines correspond to either signal or background functions, whereas the solid line corresponds to the sum of the signal and background functions.

are taken as the mean of the values and uncertainties obtained from all the fits, whereas the RMS of these values is used as a systematic uncertainty. The result is  $N_{\psi(2S)} = 158 \pm 34 \pm 15$ . The average signal-to-noise ratio for the  $\psi(2S)$  is  $(S/B)_{\psi(2S)}^{\text{PP}} = 0.16$ . For the  $J/\psi$  it is  $(S/B)_{J/\psi}^{\text{PP}} = 4.5$ .

Because the pp collisions at  $\sqrt{s} = 5$  TeV were collected during a short period of time, only a few number of  $\psi(2S)$  could be extracted, which results in an significant statistical uncertainty ( $\approx 23\%$ ).

### 3.6.2 Acceptance and efficiency correction

As for the Pb – Pb collisions, acceptance and efficiency corrections  $A\varepsilon$  are obtained with MC simulations. However, contrary to the Pb – Pb case, there is no need to use the embedding technique, because the background in pp collisions is small enough to not have any impact on the reconstruction efficiency. The generation procedure is the same as described in Section 3.4.1. Since there are no centrality classes in pp collision, the only weight to consider to calculate an average  $A\varepsilon$  is the one on the run statistics.

The average is:  $A\varepsilon = 0.2579 \pm 0.0003$ , with the uncertainty being due to the finite statistics used in the simulations.

Figure 3.15, left, shows the  $\psi(2S)$   $A\varepsilon$  corrections obtained as a function

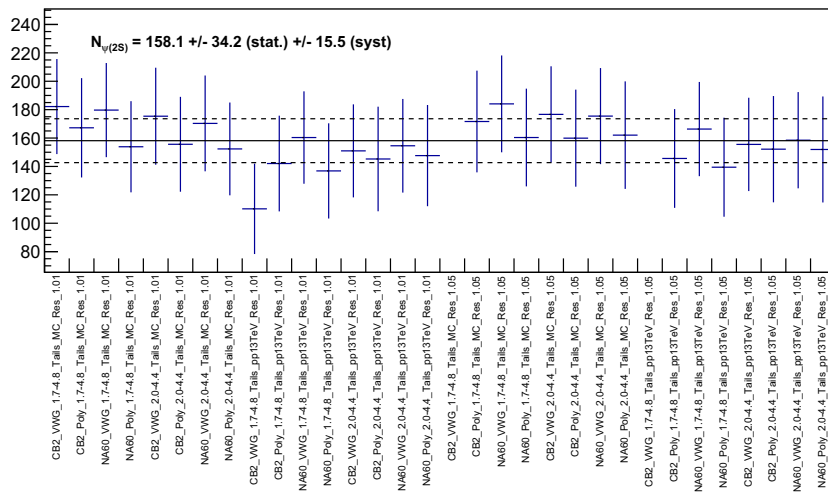


Figure 3.14: Different signal extraction tests, for the rapidity and  $p_T$ -integrated invariant mass distribution.

of the run number, using the  $p_T$  and  $y$  input distributions obtained from the  $J/\psi$  measurement at  $\sqrt{s} = 5$  TeV. Very little variations are seen from one run to the other due to the overall stability of the detector conditions during data taking. Figure 3.15, right, also shows the  $p_T$  dependence of the  $A\epsilon$ .

The systematic uncertainty on  $A\epsilon$  corrections has the following contributions and are evaluated in the same way as described in Section 3.4:

- The parametrization of the input  $p_T$  and  $y$  distributions.
- The uncertainty on the tracking efficiency in the Muon Tracker.
- The uncertainty on the Muon Trigger efficiency.
- The matching between tracks reconstructed in the Muon Trigger and tracks in the Muon Tracker.

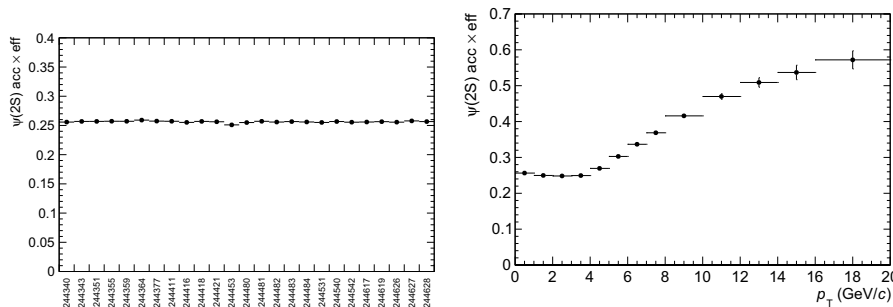


Figure 3.15:  $p_T$ - and  $y$ -integrated  $\psi(2S)$  acceptance $\times$ efficiency as a function of run number (left) and acceptance $\times$ efficiency as a function of  $p_T$  (right) using  $p_T$  and  $y$  input distributions from the  $J/\psi$  measurement at  $\sqrt{s} = 5$  TeV.

### 3.6.3 Result

Once all the terms of Equation 3.29 are evaluated, we can calculate the cross section that is used as a pp reference. The  $p_T$ - and  $y$ -integrated inclusive  $\psi(2S)$  cross section in pp collisions at  $\sqrt{s} = 5$  TeV is:

$$\sigma_{\psi(2S)}(2.5 < y < 4) = 0.72 \pm 0.16 \pm 0.06 \mu\text{b},$$

not including the uncertainty on the branching ratio (11%).

In the left panel of Figure 3.16, this cross section is compared to the ones measured at  $\sqrt{s} = 7$  [206], 8 [207] and 13 TeV [147]. In the right panel, the  $\psi(2S)$ -to- $J/\psi$  cross section ratio at  $\sqrt{s} = 5$  TeV is compared to those measured at the same three energies. In both figures, the vertical bars correspond to the quadratic sum of the statistical and systematic uncertainties.

### 3.6.4 Energy-extrapolated Cross Section

As mentioned in the previous section, the pp collisions at  $\sqrt{s} = 5$  TeV were collected in a very short period of time, resulting in a relatively small integrated luminosity ( $L_{int} = 106.28 \pm 0.09 \pm 2.23 \text{ nb}^{-1}$ ) recorded for this dataset, with respect to, for instance, the pp data collected at  $\sqrt{s} = 13$  TeV ( $L_{int} = 3.19 \pm 0.11 \text{ pb}^{-1}$ ) [147]. Therefore only a very small number of  $\psi(2S)$  could be extracted from the data. The resulting cross-section has a large

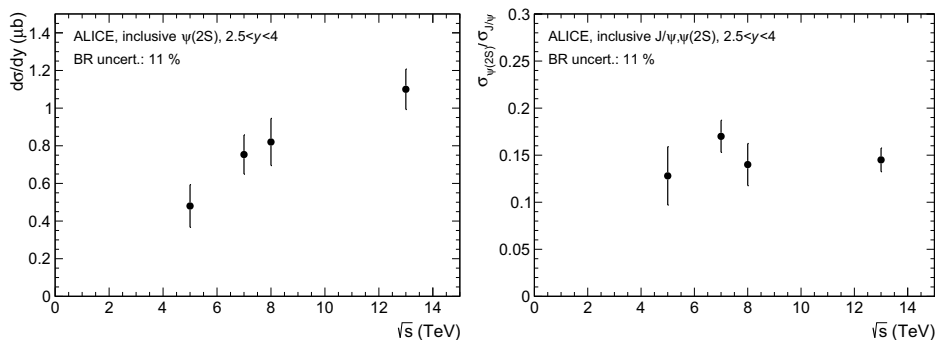


Figure 3.16:  $p_T$ - and  $y$ -integrated inclusive  $\psi(2S)$  cross section (left) and  $\psi(2S)$ -to- $J/\psi$  cross section ratio (right) as a function of  $\sqrt{s}$  in pp collisions.

uncertainty, around 23% for the statistical and 8% for the systematical uncertainty, as seen in the previous section. These large uncertainties may lead to a difficult interpretation of the results on the  $\psi(2S)$  nuclear modification factor, which is why one might prefer using an extrapolated cross-section for the  $\psi(2S)$  pp reference.

The data taken by ALICE in pp collisions at  $\sqrt{s} = 5, 7, 8,$  and  $13$  TeV indicate that the ratio of the  $\psi(2S)$  and  $J/\psi$  cross-section is constant within uncertainties as a function of energy, as seen in Figure 3.16 right. Since much more statistics were collected at 7, 8 and 13 TeV, we can use these measurements to extrapolate a value of the cross-section ratio at 5 TeV by doing a weighted average of all the available values:

$$\left. \frac{\sigma_{\psi(2S)}}{\sigma_{J/\psi}} \right|_{fit} = \frac{1}{\sum_i w_i} \sum_i w_i \frac{\sigma_{\psi(2S)}^i}{\sigma_{J/\psi}^i} \quad (3.31)$$

where  $w_i$  are the inverse square of the uncertainties on the ratio  $w_i = \frac{1}{\sigma_i^2}$ .

By doing this average over all the energies, we obtain a value for the ratio of cross section:  $\sigma_{\psi(2S)}/\sigma_{J/\psi}|_{fit} = 0.150 \pm 0.009$ .

And given the value of the cross section of the  $J/\psi$  at 5 TeV [157], we obtain an extrapolated value of the cross-section for the  $\psi(2S)$  at  $\sqrt{s} = 5$  TeV of:  $\sigma_{\psi(2S)}^{pp}|_{fit} = 0.84 \pm 0.07$ .

We see that comparatively to the values calculated in Section 3.6.3, the uncertainties have been reduced by a factor 3.

However the decision was made to continue with the value of the cross section calculated with the pp data at  $\sqrt{s} = 5$  TeV, since using the ex-

trapolation changes the definition of the  $R_{AA}$  and introduced additional correlation between the  $J/\psi$  and  $\psi(2S)$  measurements.

### 3.7 Summary of the systematics uncertainties

Table 3.4 summarizes all the sources of systematic uncertainties that enter the measurement of the  $R_{AA}$ .

Source	vs Centrality (%)	in the range 0-90% (%)
Signal extraction	9.4-34.9	36.6
MC input	3*	3
Tracking efficiency	3*	3
Trigger efficiency	3.6*	3.6
Matching efficiency	1*	1
$F_{norm}$	0.5*	0.5
$T_{AA}$	3.1-7.6	3.2
Centrality determination	0-6.6	0
pp reference	24*(8*)	24(8)

Table 3.4: Summary of the sources of systematic uncertainties. Values marked with an asterisk are correlated versus centrality and contribute to the global uncertainty. Only the signal extraction, MC input and pp reference are specific to the  $\psi(2S)$ , the others are common to the  $J/\psi$  and  $\psi(2S)$  and therefore cancel when doing a ratio.

The description of how each of these uncertainties is evaluated can be found in the dedicated section, however a quick summary is presented here.

The uncertainty on the signal extraction is evaluated by measuring the standard deviation of all the tests performed in a given centrality bin, by independently changing the fit range, fit function, etc. The resulting uncertainty is considered uncorrelated versus centrality. The values quoted in the table correspond to the two bins where the signal could be extracted, which is why the value in the 0-90% range is larger. It is the main contribution to the systematic uncertainty.

The uncertainty on the MC inputs is evaluated by changing the shape of the  $p_T$  and  $y$  input distribution in the MC simulation used to calculate the  $A\varepsilon$ . It is correlated versus centrality.

The uncertainty on the tracking efficiency also contributes to the total systematic uncertainty on the  $A\varepsilon$ . It is evaluated by comparing realistic simulations to measurements of the data. It is correlated versus centrality and is the same for the  $J/\psi$  and  $\psi(2S)$ .

The uncertainty on the trigger also comes into play in the  $A\varepsilon$ . It has two main contributions: the intrinsic trigger efficiency, evaluated with simulations and the uncertainty on the trigger response, which is evaluated by changing the  $p_T$  dependence of the trigger response. It is correlated versus centrality and is the same for the  $J/\psi$  and  $\psi(2S)$ .

The uncertainty on the matching efficiency corresponds to the efficiency of the reconstruction to match tracks in the trigger with the corresponding tracks in the tracker. It is evaluated by changing the value on the  $\chi^2$  cut used to decide if two tracks match or not. It is correlated versus centrality and is the same for the  $J/\psi$  and  $\psi(2S)$ .

The uncertainty on  $F_{norm}$  enters the evaluation in the evaluation of the number of equivalent minimum bias events and accounts for the differences obtained with the methods of evaluation. It is correlated versus centrality and is the same for the  $J/\psi$  and  $\psi(2S)$ .

The uncertainty on the nuclear overlap function  $T_{AA}$  is evaluated by changing the parameters of the Glauber model [176]. It is uncorrelated versus centrality and is the same for the  $J/\psi$  and  $\psi(2S)$ .

The determination of the centrality leads to an uncertainty that depends on the considered centrality class. It is related to the multiplicity value associated to the most peripheral collision that one is able to measure. The more central the class is, the smaller the uncertainty. It is uncorrelated versus centrality and is the same for the  $J/\psi$  and  $\psi(2S)$ .

Finally the pp reference has several sources of systematic uncertainty, such as the luminosity, the  $A\varepsilon$  in pp collisions and the signal extraction in pp collisions. It is correlated as a function of centrality and is the main component of the global systematic uncertainty.

### 3.8 Evaluation of Confidence limits with the CLs method

The CLs method is one of the method recommended by the PDG [34] in order to calculate confidence intervals. It is based on a frequentist approach of the statistics in which a probability is interpreted as the frequency of a possible result among all the experiments and is calculated by doing *pseudo-experiments* [214, 215, 216]. In the CLs method, it is assumed that the background is known and an hypothesis is made on the signal. Given this background and signal, pseudo-experiments are sorted in order to calculate the Confidence Level of that signal hypothesis. In order to do so, one needs to define a test-statistic of the known background and hypothesized signal which ranks the pseudo-experiments from the least to the most consistent with the measurement. Having defined that test statistic  $X$ , the probability distribution function (pdf) of  $X$  is constructed by tossing pseudo-experiments under the *signal+background* hypothesis.

The confidence limit on the *signal+background* hypothesis is defined as the probability given the *signal+background* hypothesis that the test statistic is less or equal to its value obtained for the measured data:

$$CL_{s+b} = P(X \leq X_{obs} | s + b) = P_{s+b}(X \leq X_{obs}) \quad (3.32)$$

The signal hypothesis is said to be excluded at a 95% confidence limit if  $CL_{s+b} \leq 0.05$ .

In addition, we can also define the confidence limit for the *background only* hypothesis in a similar way:

$$CL_b = P(X \leq X_{obs} | b) = P_b(X \leq X_{obs}) \quad (3.33)$$

by tossing pseudo-experiments under the *background only* hypothesis.

The CLs is then defined as the ratio of these two confidence limits:

$$CL_s = \frac{CL_{s+b}}{CL_b} \quad (3.34)$$

Even if it is not truly a confidence limit, but a ratio of confidence limits, with this method the signal hypothesis will be said to be excluded at a 95% Confidence Limit if  $CL_s \leq 0.05$ .

Dividing by the *background only* confidence limit allows to avoid the case where there is a downward fluctuation of the background with respect to the expected value, leading to a false exclusion of the 0 value of the signal: for instance, if the model predicts that there is  $N$  background counts, but in

the real experiment, there is  $N - 100$  background counts (because of statistical fluctuation) and 50 signal counts, then by using only  $CL_{s+b}$ , the value  $s = 0$  might be rejected, since the total number of observed events  $N_{obs} = N - 50$  is less than the expected background. The CLs method is by construction more conservative than the "true" value of the confidence limit.

### 3.8.1 Test Statistic

For the CLs method, we need to choose a test-statistic that will rank the pseudo-experiments. By the Neyman-Pearson lemma [217], the ratio of likelihoods  $Q$  is the better choice:

$$Q = \frac{L(data|s+b)}{L(data|b)} \quad (3.35)$$

Since the probabilities are described by a Poissonian law, if  $n$  is the number of observed events, whether it comes from the data or the pseudo-experiment, we have:

$$L(n|b) = \frac{e^{-b} \cdot b^n}{n!} \quad (3.36)$$

$$L(n|s+b) = \frac{e^{-(s+b)} \cdot (s+b)^n}{n!} \quad (3.37)$$

and

$$Q = e^{-s} \left(1 + \frac{s}{b}\right)^n \quad (3.38)$$

For convenience reasons, namely the divergence of the power function, we actually look at the log-likelihood ratio  $q = -2 \ln(Q)$ :

$$q = -2 \ln(Q) = 2 \left( s - n \cdot \ln \left( 1 + \frac{s}{b} \right) \right) \quad (3.39)$$

It can be thought as a generalization of the change in  $\chi^2$  for a fit to a distribution including *signal + background* relative to a fit to a pure background distribution. In the high-statistics limit, the distribution of  $-2 \ln(Q)$  is expected to converge to distribution of  $\Delta\chi^2$  [214].

Using Equation 3.39, one obtains the following three expressions for the test-statistic of the observed value, the *signal+background* hypothesis and

the *background only* hypothesis:

$$q_{obs} = 2 \left( s - n_{obs} \cdot \ln \left( 1 + \frac{s}{b} \right) \right) \quad (3.40)$$

$$q_{s+b} = 2 \left( s - n_{s+b} \cdot \ln \left( 1 + \frac{s}{b} \right) \right) \quad (3.41)$$

$$q_b = 2 \left( s - n_b \cdot \ln \left( 1 + \frac{s}{b} \right) \right) \quad (3.42)$$

where  $n_{obs}$  is the actual number of observed events,  $n_{s+b}$  is the number of observed events in a pseudo-experiment under the *signal+background* hypothesis and  $n_b$  is the number of observed events in a pseudo-experiment under the *background only* hypothesis. For each pseudo-experiment,  $n_{s+b}$  and  $n_b$  are chosen randomly, using a poissonian distribution of mean value corresponding to the  $s + b$  (or  $b$ ) hypothesis.

### 3.8.2 Application to a simple example

In order to illustrate the principle of the CLs method, a simple example is presented in the following. Let us assume we have a detector counting particles and an experiment is conducted in search for a phenomenon that will cause a slight excess in the number of measured particles in comparison to the expected background. For a numerical example, let us assume the models predict that in the complete absence of signal, the detector will measure 500 counts. After the experiment, the detector gives  $n_{data} = 510$  counts.

The question is then to evaluate what are the values of the signal compatible with the data at a 95% confidence. Given the known background  $b = 500$ , the procedure is to calculate the value of CLs for different signal hypotheses until finding the limit value  $CLs < 0.05$ . For instance, let's calculate the value of the Confidence Limit for a hypothesized value of the signal  $s = 50$ . The log-likelihood ratio under the *signal + background* hypothesis is then:

$$q_{s+b} = 2 \left( 50 - n_{s+b} \cdot \ln \left( 1 + \frac{50}{500} \right) \right) \quad (3.43)$$

The values of  $n_{s+b}$  are obtained by doing pseudo-experiments, in each of which the value of  $n_{s+b}$  is obtained by drawing values from a poissonian law of mean  $s + b$ , therefore in the example  $n_{s+b} = Poiss(550)$ . By doing several pseudo-experiment, a distribution of the log-likelihood function for the *signal + background* hypothesis is obtained.

In a similar fashion a distribution of the log-likelihood ratio under the *background only* hypothesis is obtained:

$$q_b = 2 \left( 50 \quad n_b \cdot \ln \left( 1 + \frac{50}{500} \right) \right) = 2 \left( 50 \quad \text{Poiiss}(500) \cdot \ln \left( 1 + \frac{50}{500} \right) \right) \quad (3.44)$$

These two distributions are compared to the value of the log-likelihood ratio obtained from the data :

$$q_{obs} = 2 \left( 50 \quad n_{obs} \cdot \ln \left( 1 + \frac{50}{500} \right) \right) = 2 \left( 50 \quad 510 \cdot \ln \left( 1 + \frac{50}{500} \right) \right) \quad (3.45)$$

The corresponding log-likelihood distributions are presented in Figure 3.17. The closer one of the hypothesis will be to the observed data, the more the center of its distribution is close to the value of  $q_{obs}$ . The values of  $CL_{s+b}$  and  $CL_b$  are calculated by doing the integral of the distribution from  $q_{obs}$  to infinity, normalized by the total integral of the distribution. This represents the fraction of pseudo-experiments that are more likely to be compatible with the hypothesis *signal + background* (or *background only*) than the observed experiment.

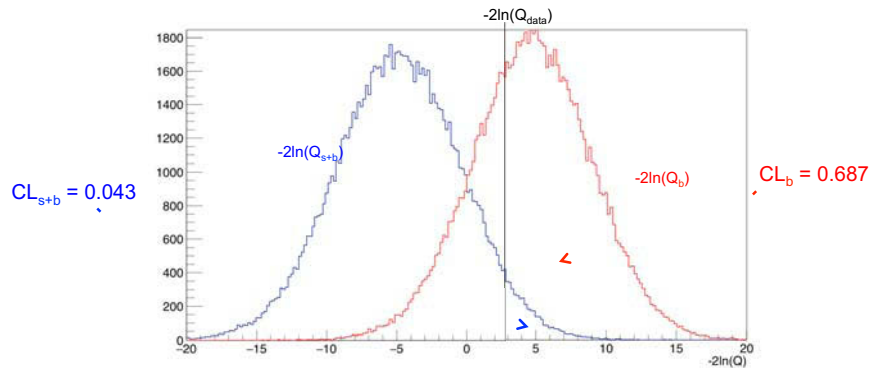


Figure 3.17: Example of log-likelihood distributions for the *signal+background* hypothesis (blue) and the *background only* hypothesis (red). In this example,  $s = 50$ ,  $b = 500$  and the actual number of observed events is  $n_{data} = 510$ . The corresponding value is  $CL_s = 0.063$ , meaning that the value of the signal  $s = 50$  is not excluded at a 95% confidence level.

The values of  $CL_{s+b}$  and  $CL_b$  are shown in the Figure. The corresponding CLs in then  $CLs = \frac{CL_{s+b}}{CL_b} = 0.063$ . Therefore the value of the signal  $s = 50$  is *not* excluded at a 95% confidence level.

In order to find the 95% confidence upper limit, the process is repeated for different values of the signal hypothesis until finding the value such as  $CL_s \leq 0.05$ , as shown in Figure 3.18.

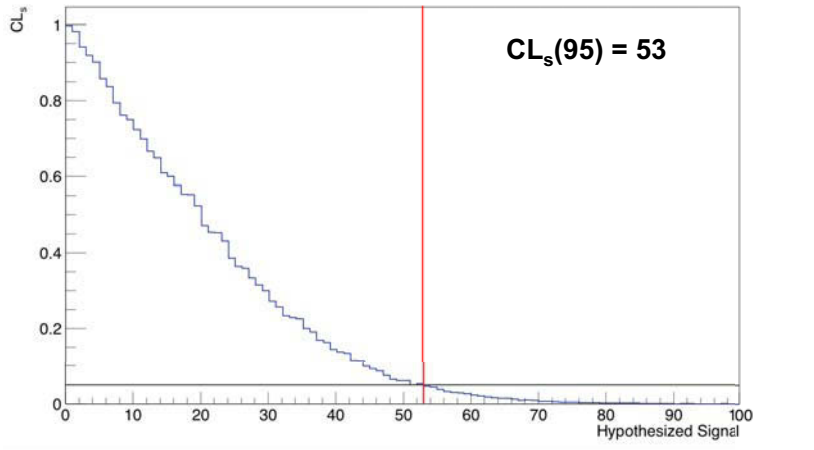


Figure 3.18: Example search for the signal value such as  $CL_s \leq 0.05$ . In this example,  $b = 500$ , the actual number of observed events is  $n_{data} = 510$  and values of  $s$  are tested from 0 to 100. The upper limit is found when  $CL_s = 0.05$ . It can be noted that by construction,  $CL_s = 1$  for a hypothesis  $s = 0$ , since it corresponds to the *background only* hypothesis.

The limit is found for a value of a hypothesized signal  $s = 53$ .

### 3.8.3 Inclusion of the systematic uncertainties

The signal and background are subject to several systematic uncertainties and since a confidence limit is already an expression of uncertainty, one doesn't want to quote these uncertainties separately but instead include them in the CL calculation. A simple way to take account for the effect of the systematic uncertainties is the hybrid bayesian-frequentist method [218] which consists in:

- Introducing a nuisance parameter  $\theta$ .
- Making the signal and background expectations function of that nui-

sance parameter:

$$\begin{aligned} s(\theta) &= \bar{s} + \sigma_s \cdot \theta \\ b(\theta) &= \bar{b} + \sigma_b \cdot \theta \end{aligned} \quad (3.46)$$

where  $\bar{s}$  and  $\bar{b}$  are the nominal values of  $s(\theta)$  and  $b(\theta)$  and  $\sigma_s$  and  $\sigma_b$  are the  $1\sigma$  systematic uncertainty that one wants to account for, for the signal and background estimations respectively.

When computing confidence limit that accounts for  $\sigma_s$  and  $\sigma_b$ , one would then:

- Keep the test statistic using the values  $\bar{s}$  and  $\bar{b}$ .
- Modify  $s$  and  $b$  before each pseudo-experiment by drawing random numbers from the *pdf* of  $\theta$ .

Other methods of inclusion of the systematic uncertainties are available and some examples can be found in [216], but the bayesian-frequentist is the easiest one to implement.

### 3.8.4 Application to the $\psi(2S)$ signal extraction

In the case of the  $\psi(2S)$ , there are multiple bins in the invariant mass histogram contributing to the values of the signal and the background. In case of multiple bins, the log-likelihood ratio can be simply extended as the sum of the log-likelihood ratios in each bin:

$$q = \sum_{i=0}^{n_{bins}} 2 \left( s_i - n_i \cdot \ln \left( 1 + \frac{s_i}{b_i} \right) \right) \quad (3.47)$$

where  $b_i$  is to the known background in bin  $i$ ,  $s_i$  the hypothesized signal in bin  $i$  and  $n_i$  the number of counts in that bin.

The  $\psi(2S)$  background contains both the *normal* background (combinatorial and continuum) and the  $J/\psi$  peak.  $b_i$  is written:

$$b_i = N_{BG} \times F_{BG}(x_i) + N_{J/\psi} \times F_{J/\psi}(x_i) \quad (3.48)$$

with  $N_{BG}$  the total number of normal background counts,  $F_{BG}(x_i)$  its shape normalized to unity,  $N_{J/\psi}$  the total number of  $J/\psi$  and  $F_{J/\psi}(x_i)$  its shape.

The signal  $s_i$  is written:

$$s_i = N_{\psi(2S)}^{\text{hyp}} \times F_{\psi(2S)}(x_i) \quad (3.49)$$

with  $N_{\psi(2S)}^{\text{hyp}}$  the number of hypothesized  $\psi(2S)$  and  $F_{\psi(2S)}(x_i)$  the shape of the  $\psi(2S)$  signal, fixed with respect to the one of the  $J/\psi$ .

In order to include the systematic uncertainty from the signal extraction, a similar method to the one described in the previous section is adopted: the mean shapes of the background,  $J/\psi$  and  $\psi(2S)$  are obtained by doing the mean of all the tests described in Sec 3.3.5 and used to calculate  $\bar{s}_i$  and  $\bar{b}_i$ . Before each pseudo-experiment, a random combination of background function, signal function, tail parameters and fit ranges from the tests is then drawn and the corresponding  $s_i$  and  $b_i$  are used as parameter to the poissonian drawing of  $n_{i,s+b}$  and  $n_{i,b}$ .

Since we do not know our background exactly, another uncertainty is added in a similar fashion as what is described previously. It is estimated by calculating the error of the integral on the fit function  $\sigma_{Fit}$  and is applied to the total number of background counts:

$$N_{BG} = N_{BG}^{\text{mean}} \times (1 + \sigma_{Fit} \cdot \theta) \quad (3.50)$$

In the cases where the signal extraction is done after performing the event mixing, the confidence limits cannot be calculated directly, because in that case the *pdf* of the number of counts in each bin is no longer poissonian. In order to account for the event mixing cases in the systematics, the background shape for those cases was defined as the sum of the background function from the fit and the normalized mixed event histogram:

$$F_{BG}(x) = F_{BG}^{\text{AfterMixing}}(x) + h^{\text{MixedEvents}}(x) \quad (3.51)$$

This is done in order to keep the *pdf* of the data poissonian. Finally, the value of CLs is calculated.

Results are presented in Figure 3.19 and Table 3.5, compared to the values obtained with the standard procedure of signal extraction.

For the 60-90% centrality bin, where the signal can be properly extracted, we can compare the value of the limit calculated with the CLs with the 95% confidence limit calculated with the uncertainty of the fit. Assuming that the signal has a gaussian distribution, the  $2\sigma$  law gives  $P(X_{\text{mean}} - 2\sigma < X < X_{\text{mean}} + 2\sigma) = 95\%$ . By definition of the confidence limit, we have  $P(X < CLs(95)) = 95\%$ , which is not exactly the same probability as the probability defined for the  $2\sigma$  law. In a gaussian distribution, the limit that verifies the same probability than  $CLs(95)$  is  $P(X < X_{\text{mean}} + 1.64\sigma) = 95\%$ . Therefore we expect:

$$\frac{CLs - X_{\text{mean}}}{2\sigma} = 0.82 \quad (3.52)$$

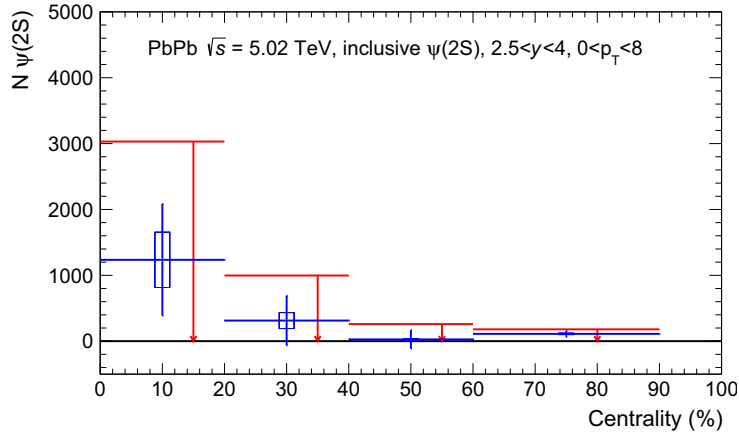


Figure 3.19: Confidence Levels calculated on the  $\psi(2S)$  signal as a function of centrality, compared to the values extracted from fits to the invariant mass distribution

In this case  $\sigma$  is the quadratic sum of the statistic and systematic uncertainty. The expected value for the CLs is then  $CL_s^{expected} = 186$ , which is a 3% difference with the obtained value. This difference can be imputed to the fact that the uncertainties are not exactly gaussian, but it validates the method. Similar tests were performed on the simple example of Section 3.8.2 and on the  $J/\psi$  signal extraction in order to validate the CLs method. Results for the  $J/\psi$  can be found in Annex A.

In addition to the confidence limit, we can also calculate the value  $1 - CL_b$ , which gives the probability of the *background only* hypothesis to be correct. This corresponds to the case of a complete suppression of the  $\psi(2S)$ . The results are presented in Table 3.5. In the 0-20% and 60-90% centrality bins, the *background only* hypothesis is very unlikely. However in the mid-central bins, the *background only* hypothesis has a non-negligible probability. In particular in the 40-60% bin, the probability of the  $\psi(2S)$  to be completely suppressed is close to 40%.

### 3.8.5 Application to the $R_{AA}$

In order to calculate the upper values of the confidence limit on the  $R_{AA}$ , the hypothesized signal value  $N_{\psi(2S)}^{hyp}$  is taken as a function of the nuclear

### 3.9. MEASUREMENT OF THE $\psi(2S)$ NUCLEAR MODIFICATION FACTOR

Centrality (%)	$N_{\psi(2S)} \pm (\text{stat}) \pm (\text{sys})$	$\text{CL}_s(95)$	$1 - \text{CL}_b$
0-20	$1553 \pm 905 \pm 543$	3097	0.069
20-40	$381 \pm 415 \pm 159$	1024	0.144
40-60	$28 \pm 144 \pm 12$	261	0.375
60-90	$111 \pm 45 \pm 11$	180	0.002

Table 3.5: Average  $\psi(2S)$  yield with statistical and systematic uncertainties in each centrality bin, integrated in  $p_T$  and rapidity.

modification factor and the hypothesis will be on the value of the  $R_{AA}$ :

$$N_{\psi(2S)}^{\text{hyp}} = \text{BR}_{\psi(2S) \rightarrow \mu^+ \mu^-} \times (A\varepsilon) \times N_{\text{MB}} \times T_{AA} \times \sigma_{\psi(2S)}^{pp} \times R_{AA}^{\text{hyp}} \quad (3.53)$$

Each contribution to the systematic uncertainties is included when calculating the CLs values by drawing a random value of the corresponding terms in Equation 3.53 before each pseudo-experiment as described in Section 3.8.3.

### 3.9 Measurement of the $\psi(2S)$ Nuclear Modification factor

As described in the introduction, the effects of the QGP on the  $\psi(2S)$  production is evaluated thanks to the nuclear modification factor  $R_{AA}$ . Now that all the ingredients entering in equation 3.6 and the corresponding systematic uncertainties have been evaluated, we can calculate the  $\psi(2S)$  nuclear modification factor in a given centrality class  $i$ :

$$R_{AA}^i = \frac{N_{\psi(2S)}^i}{\text{BR}_{\psi(2S) \rightarrow \mu^+ \mu^-} \times (A\varepsilon)^i \times N_{\text{MB}}^i \times T_{AA}^i \times \sigma_{\psi(2S)}^{pp}} \quad (3.54)$$

The integrated  $\psi(2S)$   $R_{AA}$  in the centrality range 0-90% is:

$$R_{AA\psi(2S)}^{0-90\%} = 0.2187 \pm 0.1123 (\text{stat}) \pm 0.0963 (\text{syst}) \quad (3.55)$$

All results are for inclusive  $\psi(2S)$ , which includes both prompt (direct  $\psi(2S)$ ) and non-prompt  $\psi(2S)$  (from  $b$ -hadron decay). When looking at the

evolution of the  $R_{AA}$  as a function of centrality, we face the problem of the bins for which the signal is compatible with zero. For those bins a 95% confidence limit is evaluated using the CLs method described in Section 3.8.

### 3.9.1 Nuclear Modification Factor

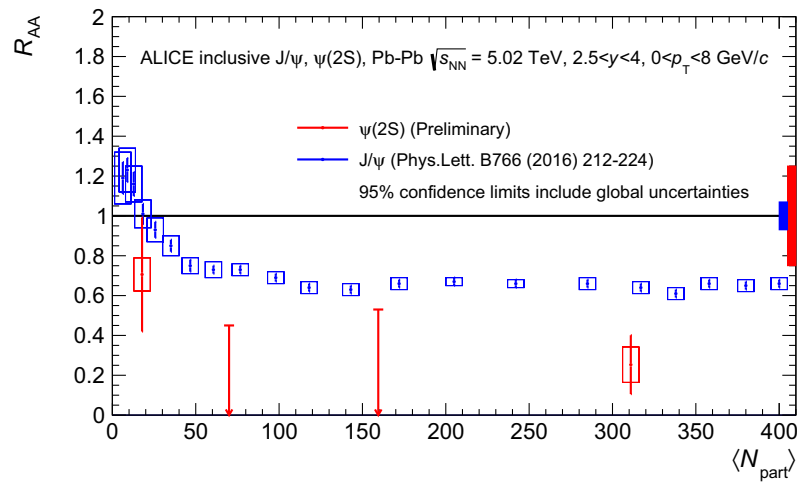


Figure 3.20: Nuclear modification factor of the  $\psi(2S)$  (red) compared to the one of the  $J/\psi$  (blue) as a function of  $N_{part}$ . For the centrality bins where the signal could not be extracted, only the 95% confidence limit is shown. The global systematic uncertainty is drawn in the box around unity. The global uncertainties are already included in the confidence limit calculation.

The  $R_{AA}$  of the  $\psi(2S)$  as a function of  $N_{part}$  measured in Pb – Pb collisions at an energy  $\sqrt{s_{NN}} = 5.02$  TeV is shown in Table 3.6 and in Figure 3.20. It is compared to the  $R_{AA}$  of the  $J/\psi$  at the same energy [157]. The four centrality bins considered are 0-20%, 20-40%, 40-60% and 60-90%. In the 0-20% and 60-90% bins, the bars represent the statistical uncertainties and the boxes around the points are the uncorrelated systematic uncertainty. In the 20-40% and 40-60% bins, for which the signal could not be extracted, the 95% confidence limit calculated with the CLs method is drawn instead. The box around unity represent the correlated systematic uncertainty and only applies to the 0-20% and 60-90% points. For the other two bins, it is included in the confidence limit calculation. As explained in Section 3.7,

part of the global systematic uncertainty is correlated between the  $J/\psi$  and  $\psi(2S)$ .

Centrality (%)	$CL_s(95)$	$R_{AA}^{\psi(2S)}$ (stat.) (syst.)
0-20	0.607	$0.253 \pm 0.147 \pm 0.088$
20-40	0.530	-
40-60	0.450	-
60-90	1.473	$0.705 \pm 0.286 \pm 0.083$

Table 3.6: Nuclear modification factor of the  $\psi(2S)$  in the different centrality bins in the ranges  $0 < p_T < 8$  GeV/ $c$  and  $2.5 < y < 4.0$ .

In the most peripheral bin, the  $\psi(2S)$   $R_{AA}$  is compatible with the  $J/\psi$  one. In all the other bins, the  $\psi(2S)$   $R_{AA}$  is smaller than the  $J/\psi$  one indicating that the  $\psi(2S)$  is more suppressed than the  $J/\psi$  for  $N_{\text{part}} > 50$ . However this statement would be better quantified by looking at either single ratios (namely  $Y_{\psi(2S)}/Y_{J/\psi}$ ) or double ratios, (namely  $R_{AA}^{\psi(2S)}/R_{AA}^{J/\psi}$ ), which properly account for correlations between the errors on the  $J/\psi$  and  $\psi(2S)$  yields in both pp and Pb – Pb collisions.

The effect of the non-prompt  $\psi(2S)$  can also be evaluated. LHCb is able to differentiate between the prompt and non-prompt  $\psi(2S)$  at forward rapidity and has measured in pp collisions at  $\sqrt{s} = 7$  TeV a fraction of non-prompt  $\psi(2S)$  to prompt  $\psi(2S)$   $f_B = (17.4 \pm 2.1)\%$  [77]. For the  $J/\psi$ , a reducing factor of 1.09 in  $f_B$  going from 7 TeV to 5.02 TeV was estimated [157], which amounts for the  $\psi(2S)$  to a non-prompt fraction of  $f_B = (15.9 \pm 1.9)\%$ .

The relation between the  $R_{AA}$  of the prompt, non-prompt and inclusive  $\psi(2S)$  is:

$$R_{AA}^{\text{prompt}} = (1 + f_B) \cdot R_{AA}^{\text{inclusive}} - f_B \cdot R_{AA}^{\text{non-prompt}} \quad (3.56)$$

It is difficult to estimate precisely  $R_{AA}^{\text{non-prompt}}$ , however making some extreme assumptions can be done.

If  $R_{AA}^{\text{non-prompt}} = 0$ , which means the non-prompt  $\psi(2S)$  are completely suppressed, then the  $R_{AA}$  of the prompt  $\psi(2S)$  would be 16% higher than the inclusive  $R_{AA}$ .

If  $R_{AA}^{\text{non-prompt}} = 1$ , which means the non-prompt  $\psi(2S)$  are not suppressed, then the  $R_{AA}$  of the prompt  $\psi(2S)$  would be from 7% lower than the inclusive  $R_{AA}$  in the most peripheral bin to 47% lower in the most central bin.

### 3.9.2 Single Ratio

In order to compare the results with the analysis at  $\sqrt{s_{NN}} = 2.76$  TeV [156], the  $\psi(2S)$ -to- $J/\psi$  yield ratio is considered:

$$\frac{Y_{\psi(2S)}}{Y_{J/\psi}} = \frac{N_{\psi(2S)}}{N_{J/\psi}} \times \frac{(A\varepsilon)_{J/\psi}}{(A\varepsilon)_{\psi(2S)}} \quad (3.57)$$

This equation comes from the definition of the yields given in Eq. 3.2. This yields are not corrected by the value of the branching ratio, as this is how the single ratio was defined in 2011 for the Pb – Pb collisions at  $\sqrt{s_{NN}} = 2.76$  TeV.

A 95% CL is calculated on the ratio by making the number of  $\psi(2S)$  a function of that ratio :

$$N_{\psi(2S)}^{\text{hyp}} = \frac{(A\varepsilon)_{\psi(2S)} \times N_{J/\psi}}{(A\varepsilon)_{J/\psi}} \times \left( \frac{Y_{\psi(2S)}}{Y_{J/\psi}} \right)^{\text{hyp}} \quad (3.58)$$

The value, integrated in  $p_T$ , in the centrality range 0-90% is :

$$\left. \frac{\psi(2S)}{J/\psi} \right|_{0-90\%} = 0.0057 \pm 0.0029 \pm 0.0021 \quad (3.59)$$

The values as a function of centrality integrated in  $p_T$  are presented in Table 3.7 and in Figure 3.21.

In order to compare with the results of 2011 at an energy of  $\sqrt{s_{NN}} = 2.76$  TeV, two  $p_T$  ranges are considered:  $0 < p_T < 3$  GeV/ $c$  and  $3 < p_T < 8$  GeV/ $c$ . Results are shown in Figure 3.22 and the corresponding values in Table 3.7. In the centrality bins for which the signal can be extracted and used to calculate the single ratio, the corresponding 95% confidence limit is also quoted for information. For the simple ratio, the systematic uncertainties that are correlated between  $J/\psi$  and  $\psi(2S)$  cancel out. More explicitly, the uncertainties on tracking efficiency, trigger efficiency, matching efficiency are cancelled and only the MC inputs contribute to the systematic uncertainties.

The new values at  $\sqrt{s_{NN}} = 5.02$  TeV are in agreement with the old ones, which were at a lower energy and with much smaller statistics.

When comparing this value to the ratios obtained in pp collisions presented in Figure 3.16, which average<sup>3</sup> at  $\left. \frac{\psi(2S)}{J/\psi} \right|_{pp} = 0.0200 \pm 0.0012$ , we can

<sup>3</sup>This value corresponds to the cross-section ratio shown in Figure 3.16 multiplied by the branching ratios, in order to obtain a ratio of yields.

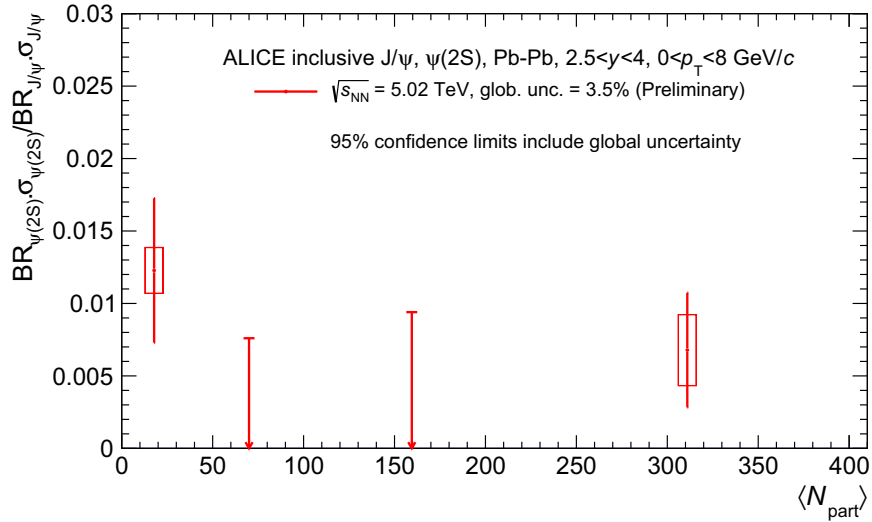


Figure 3.21: Single  $\psi(2S)$ -to- $J/\psi$  ratio as a function of  $N_{\text{part}}$ . For the centrality bins where the signal could not be extracted, only the 95% confidence limit is shown. The global systematic uncertainty is drawn in the box around unity. The global uncertainties are already included in the confidence limit calculation.

see that the production of  $\psi(2S)$  relative to the one of the  $J/\psi$  is less important in Pb – Pb collisions than in  $pp$ , supporting a picture where the  $\psi(2S)$  is more suppressed than the  $J/\psi$ , which confirms the statement made in the previous section.

Centrality (%)	$CL_s(95)$	$\psi(2S)$ -to- $J/\psi$ ratio
$2.5 < y < 4.0, 0 < p_T < 8 \text{ GeV}/c$		
0-20	0.0136	$0.0068 \pm 0.0039 \pm 0.0024$
20-40	0.0094	-
40-60	0.0076	-
60-90	0.0165	$0.0122 \pm 0.0050 \pm 0.0016$
$2.5 < y < 4.0, 0 < p_T < 3 \text{ GeV}/c$		
0-20	0.0159	$0.0063 \pm 0.0043 \pm 0.0039$
20-40	0.0122	-
40-60	0.0112	-
60-90	0.0221	$0.0127 \pm 0.0056 \pm 0.0018$
$2.5 < y < 4.0, 3 < p_T < 8 \text{ GeV}/c$		
0-20	0.0241	$0.0118 \pm 0.0076 \pm 0.0036$
20-60	0.0131	-
60-90	0.0306	-

Table 3.7:  $\psi(2S)$ -to- $J/\psi$  ratio in the different centrality bins for the  $p_T$  ranges  $0 < p_T < 3 \text{ GeV}/c$ ,  $3 < p_T < 8 \text{ GeV}/c$  and  $0 < p_T < 8 \text{ GeV}/c$ .

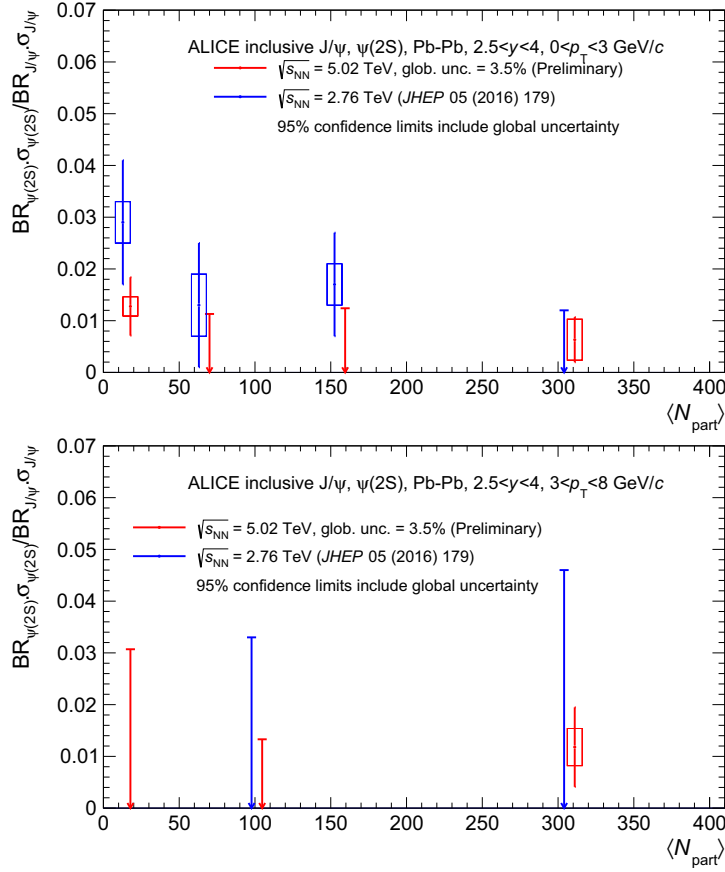


Figure 3.22:  $\psi(2S)$ -to- $J/\psi$  ratio as a function of  $N_{part}$  (red) compared to the values at  $\sqrt{s} = 2.76$  TeV (blue). The left (right) figure corresponds to the  $p_T$  range  $0 < p_T < 3$  GeV/ $c$  ( $3 < p_T < 8$  GeV/ $c$ ). For the centrality bins where the signal could not be extracted, only the 95% CL are shown.

### 3.9.3 Double Ratio

Finally, we can compare the relative abundances of the  $\psi(2S)$  and the  $J/\psi$  by looking at the  $\psi(2S)$ -to- $J/\psi$  nuclear modification factors ratio (also called double-ratio). A 95% CL is calculated on this quantity by making the number of  $\psi(2S)$  a function of the double-ratio:

$$N_{\psi(2S)}^{\text{hyp}} = \frac{\text{BR}_{\psi(2S) \rightarrow \mu^+ \mu^-} \times (A\varepsilon)_{\psi(2S)} \times N_{J/\psi} \times \sigma_{\psi(2S)}^{pp}}{\text{BR}_{J/\psi \rightarrow \mu^+ \mu^-} \times (A\varepsilon)_{J/\psi} \times \sigma_{J/\psi}^{pp}} \times \frac{R_{AA}^{\psi(2S)\text{hyp}}}{R_{AA}^{J/\psi}} \quad (3.60)$$

The integrated value over  $p_T$  in the centrality range 0-90% is:

$$\left. \frac{R_{AA}^{\psi(2S)}}{R_{AA}^{J/\psi}} \right|_{0-90\%} = 0.333 \pm 0.172 \pm 0.123 \quad (3.61)$$

The  $p_T$ -integrated values as a function of centrality are shown in Figure 3.23.

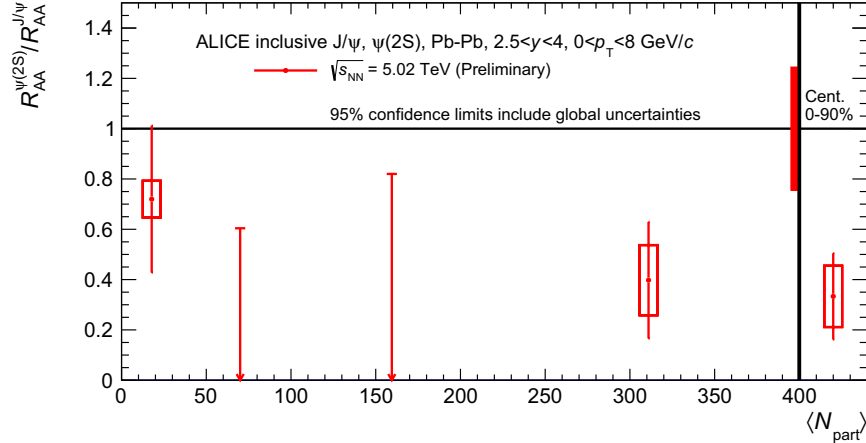


Figure 3.23: Double-ratio  $R_{AA}^{\psi(2S)}/R_{AA}^{J/\psi}$  as a function of  $N_{\text{part}}$  for  $0 < p_T < 8$  GeV/c. For the centrality bins where the signal could not be extracted, only the 95% confidence limit is shown. The global systematic uncertainty is drawn in the box around unity. The global uncertainties are already included in the confidence limit calculation. The value quoted for  $N_{\text{part}} > 400$  corresponds to the centrality-integrated value (0-90%).

As previously in order to compare with the 2011 results, two  $p_T$  ranges are considered. Results are shown in Figure 3.24 and the corresponding

values in Table 3.8. For the double ratio, uncertainties on tracking efficiency, trigger efficiency, matching efficiency and  $T_{AA}$  are cancelled out. The MC inputs and the pp references contribute to the uncertainty.

Centrality (%)	$CL_s(95)$	Double-ratio $R_{AA}^{\psi(2S)}/R_{AA}^{J/\psi}$
$2.5 < y < 4.0, 0 < p_T < 8 \text{ GeV}/c$		
0-20	0.920	$0.402 \pm 0.235 \pm 0.141$
20-40	0.820	-
40-60	0.604	-
60-90	1.580	$0.729 \pm 0.296 \pm 0.074$
0-90	-	$0.435 \pm 0.224 \pm 0.192$
$2.5 < y < 4.0, 0 < p_T < 3 \text{ GeV}/c$		
0-20	1.35	$0.524 \pm 0.378 \pm 0.397$
20-40	0.98	-
40-60	0.91	-
60-90	1.81	$1.056 \pm 0.966 \pm 0.483$
0-90	-	$0.388 \pm 0.275 \pm 0.489$
$2.5 < y < 4.0, 3 < p_T < 8 \text{ GeV}/c$		
0-20	0.88	$0.421 \pm 0.289 \pm 0.169$
20-60	0.45	-
60-90	1.10	-
0-90	-	$0.282 \pm 0.170 \pm 0.278$

Table 3.8: Double-ratio  $R_{AA}^{\psi(2S)}/R_{AA}^{J/\psi}$  in the different centrality bins for the  $p_T$  ranges  $0 < p_T < 3 \text{ GeV}/c$ ,  $3 < p_T < 8 \text{ GeV}/c$  and  $0 < p_T < 8 \text{ GeV}/c$ .

These results also support a picture where the  $\psi(2S)$  is more suppressed than the  $J/\psi$ .

We can also compare the double ratio in the  $p_T$  range  $3 < p_T < 8 \text{ GeV}/c$  with the results of CMS [219] in their forward rapidity region. Results are shown in Figure 3.25. CMS results are for prompt  $\psi(2S)$  and for an adjacent rapidity range, but both measurement are in very good agreement.

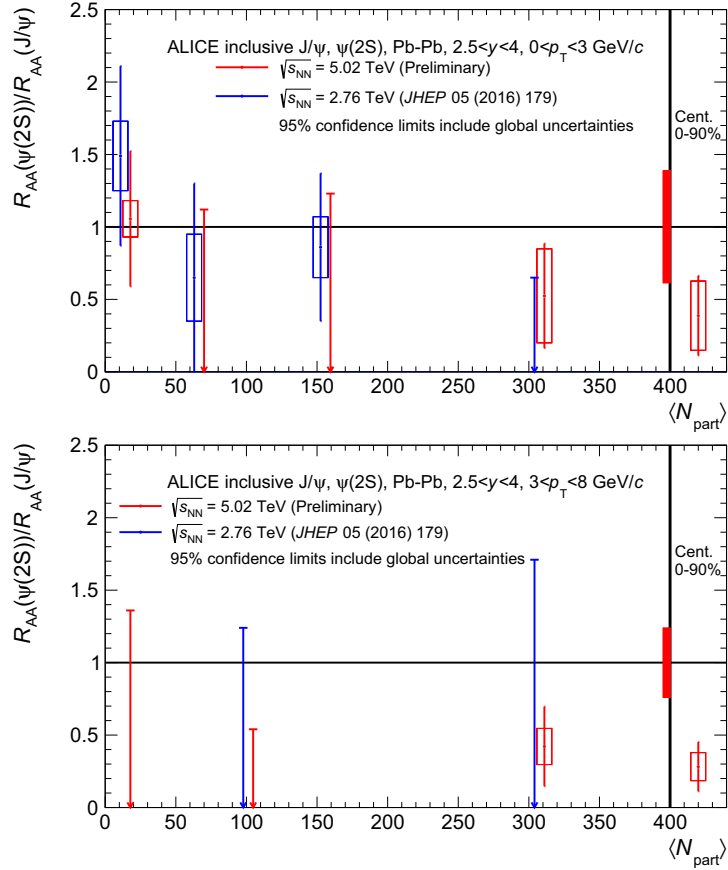


Figure 3.24: Double-ratio  $R_{AA}^{\psi(2S)}/R_{AA}^{J/\psi}$  as a function of  $N_{part}$  (red) compared to the values at  $\sqrt{s_{NN}} = 2.76 \text{ TeV}$  (blue). The left (right) figure corresponds to the  $p_T$  range  $0 < p_T < 3 \text{ GeV}/c$  ( $3 < p_T < 8 \text{ GeV}/c$ ). For the centrality bins where the signal could not be extracted, only the 95% confidence limit is shown. The global systematic uncertainty is drawn in the box around unity. The global uncertainties are already included in the confidence limit calculation. The value quoted for  $N_{part} > 400$  corresponds to the centrality-integrated value (0-90%).

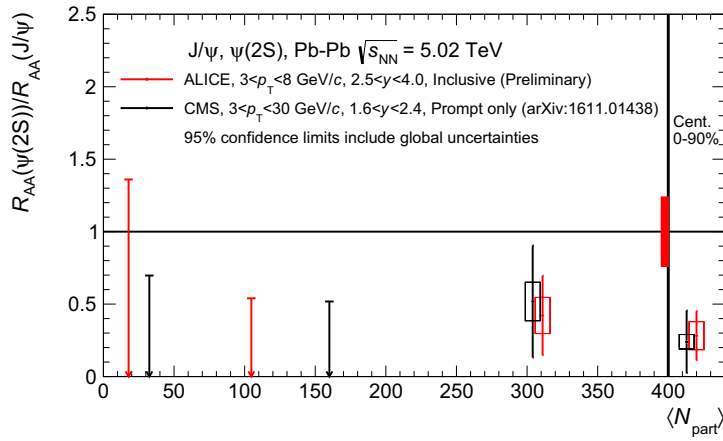


Figure 3.25: Double-ratio  $R_{AA}^{\psi(2S)}/R_{AA}^{J/\psi}$  as a function of  $N_{\text{part}}$  (red) compared to the values of CMS (black) for  $p_T > 3$  GeV/ $c$ . For the centrality bins where the signal could not be extracted, only the 95% confidence limit is shown. The global systematic uncertainty is drawn in the box around unity. The global uncertainties are already included in the confidence limit calculation. The value quoted for  $N_{\text{part}} > 400$  corresponds to the centrality-integrated value (0-90%).

### 3.9.4 Comparison to models

The first model to which our measurement are compared is the Comover Interaction Model [131], presented in Section 1.5.4. In this model, the  $R_{AA}$  is function of a product of  $S^{abs}$ , that accounts for the nuclear absorption,  $S^{sh}$  that accounts for the gluon shadowing and  $S^{co}$ , that accounts for the suppression and recombination in the plasma due to interaction with the comovers in the medium.

In the energy collisions of the LHC ( $\sqrt{s_{NN}} = 2.76$  and  $5.02$  TeV), the nuclear absorption is negligible (see Section 1.5.2) and therefore  $S^{abs} = 1$ . The shadowing is calculated with EPS09 parametrization [113] at leading order.

As detailed in 1.5.4, the term corresponding to the dissociation and recombination by comover interaction is given by:

$$S^{co}(b, s, y) = \exp \left[ -\sigma_{co} \left( N^{co}(b, s, y) - \frac{(d\sigma_{p\bar{c}}/dy)^2}{\sigma_{pp} d\sigma_{pp}^\psi/dy} N_{coll}(b, s) S_{HQ}^{sh} \right) \ln \left( \frac{N^{co}(b, s, y)}{N_{pp}(0)} \right) \right] \quad (3.62)$$

The value of  $\sigma_{co}$  for the  $\psi(2S)$  is  $\sigma_{co}(\psi(2S)) = 6$  mb, which is about ten times higher than for the  $J/\psi$  ( $\sigma_{co}(J/\psi) = 0.65$  mb).

It is possible to take  $\sigma_{pp}^{\psi(2S)}$  from the data or from a model extrapolation of experimental results (see Section 3.6).

The choice of  $\sigma_{c\bar{c}}$  is the main source of uncertainty of the model. Naturally, the same value for  $\sigma_{c\bar{c}}$  is used for the  $J/\psi$  and the  $\psi(2S)$ . It is chosen in the range  $0.45 < \sigma_{c\bar{c}} < 0.7$  mb. The corresponding results are presented in Figure 3.26.

The model is in agreement with the measurements and for the  $\psi(2S)$  a better agreement is found with the lower limits of the model, as opposed to the  $J/\psi$  where a better agreement is found with the upper limits. However, because of the large uncertainties on the  $\psi(2S)$ , no stronger conclusion can be drawn. A comparison of the model predictions for both particles is presented in Annex B.2.

The second model is the Transport Model [129, 220], presented in Section 1.5.4. In this model the time evolution of the number of charmonium in the medium is described by a rate equation:

$$\frac{dN_{\psi(2S)}}{d\tau} = -\Gamma_{\psi(2S)}^{diss}(T) \left[ N_{\psi(2S)} - N_{\psi(2S)}^{eq}(T) \right] \quad (3.63)$$

where  $\Gamma_{\psi(2S)}^{diss}$  is the dissociation rate and  $N_{\psi(2S)}^{eq}(T)$  is the number of  $\psi(2S)$  at the equilibrium of the medium.

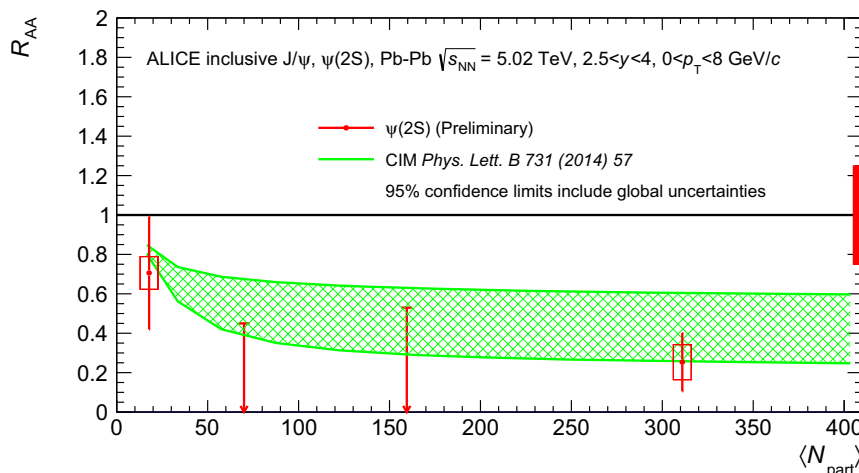


Figure 3.26: Nuclear modification factor  $R_{AA}$  versus  $N_{\text{part}}$  compared to the CIM. For the centrality bins where the signal could not be extracted, only the 95% confidence limit is shown. The global systematic uncertainty is drawn in the box around unity. The global uncertainties are already included in the confidence limit calculation. Uncertainties on the model correspond to different values of the  $c - \bar{c}$  pairs production cross section,  $\sigma_{c\bar{c}} = 0.70$  mb for the upper limit and  $\sigma_{c\bar{c}} = 0.45$  mb for the lower limit.

The production cross section of the  $J/\psi$  is set to  $d\sigma_{\text{pp}}^{J/\psi}/dy = 3.35$  mb in the range  $2.5 < y < 4.0$  and the  $\psi(2S)$  cross section was taken about 14% of the  $J/\psi$  inclusive cross section, with a harder  $p_T$  spectrum according to previous ALICE measurements [221].

The production cross-section of open charm is  $d\sigma_{c\bar{c}}/dy = 0.57$  mb at 5.02 TeV in the range  $2.5 < y < 4.0$ .

The uncertainty band due to gluon shadowing is evaluated with the EPS09 parametrizations [113] and p – Pb data [213]. The upper limit corresponds to 0% of shadowing and the lower limit corresponds to a shadowing up to 20% for the most central collisions. Additional uncertainties include uncertainties on the Cronin effect and the dissociation rate.

The range of dissociation temperatures for the  $\psi(2S)$  is  $T_{\text{diss}} = 170 - 180$  MeV which corresponds to the end of the mixed phase (see Section 1.3.1).

The corresponding results are presented in Figure 3.27. The model is in agreement with the measurements, but as was the case with the CIM model, because of the large uncertainties on the  $\psi(2S)$ , no stronger conclusion can

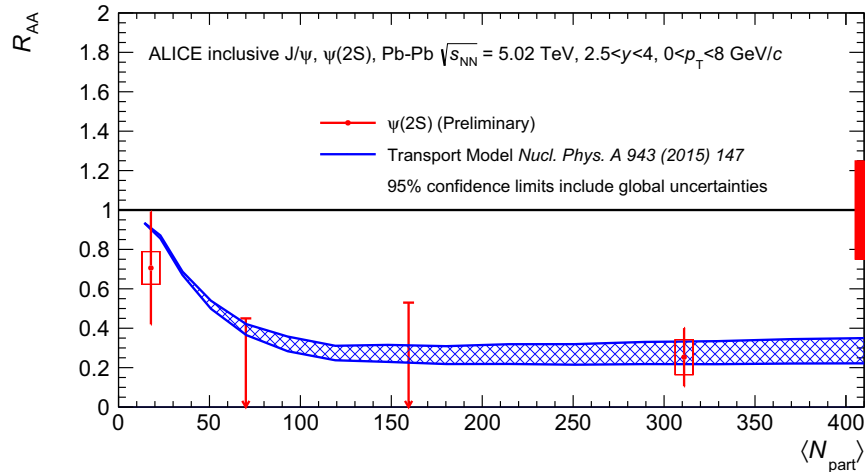


Figure 3.27: Nuclear modification factor  $R_{AA}$  as a function of  $N_{\text{part}}$  compared to the Transport Model. For the centrality bins where the signal could not be extracted, only the 95% confidence limit is shown. The global systematic uncertainty is drawn in the box around unity. The global uncertainties are already included in the confidence limit calculation. Uncertainties in the model correspond to different hypothesis in the magnitude of the shadowing: the upper limit corresponds to 0% of shadowing and the lower limit corresponds to a shadowing of up to 20% for the most central collisions.

be drawn. A comparison of the model predictions for the J/ψ and ψ(2S) is presented in Annex B.3. A comparison between the predictions of the Comover Interaction Model and the Transport Model can be found in Annex B.1. It can be noted that the differences in the uncertainties between the two models come from the way uncertainties on the shadowing and on the open-charm cross section.

The Transport Model also provides predictions for the Double Ratio in the range  $3 < p_T < 8$  GeV/c and the result is presented in Figure 3.28. The same conclusions as for the  $R_{AA}$  apply.

Finally, the Statistical Hadronization Model, described in Section 1.5.4 proposes a prediction for the ψ(2S)-to-J/ψ single ratio. In the SHM, charm and anti-charm quarks are produced in the collision and their number stays constant until hadronization, at which time the pairs may bound into charmonium states.

Inputs to the model calculation are the number of charm quarks initially

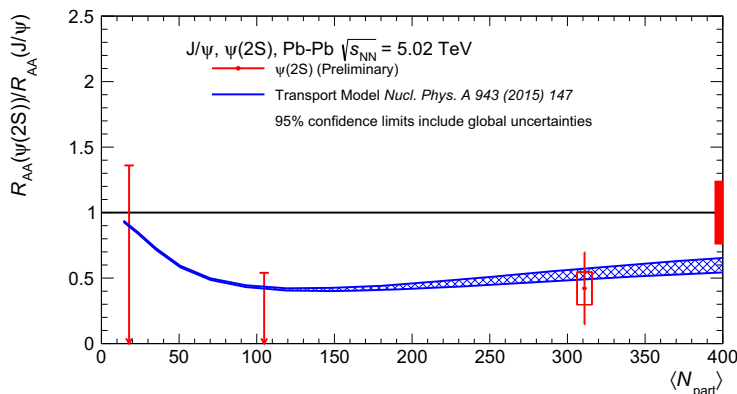


Figure 3.28: Double Ratio  $R_{AA}^{\psi(2S)}/R_{AA}^{J/\psi}$  as a function of  $N_{\text{part}}$  compared to the Transport Model. For the centrality bins where the signal could not be extracted, only the 95% confidence limit is shown. The global systematic uncertainty is drawn in the box around unity. The global uncertainties are already included in the confidence limit calculation. Uncertainties in the model correspond to different importances in the shadowing: the upper limit corresponds to 0% of shadowing and the lower limit corresponds to a shadowing of up to 20% for the most central collisions.

produced  $N_c$ , the critical temperature  $T_c$ , the baryon chemical potential  $\mu_B$  and the Volume of the fireball.

The number  $N_c$  is determined by measuring the charm production cross section in pp collisions and extrapolating it to nucleus-nucleus collisions assuming scaling with the number of hard scatterings. The gluon shadowing is incorporated using the EPS09 parametrization. The value used for the calculation is  $\sigma_{cc}^{pp} = 0.45$  mb.

The values of  $T_c$  and  $\mu_B$  obtained from fits to SPS and RHIC data [222, 223] can be parametrized as a function of  $\sqrt{s_{NN}}$ . In this calculation, they are  $T_c = 156$  MeV and  $\mu_B(\text{MeV}) = 1303/[1 + 0.286\sqrt{s_{NN}}(\text{GeV})]$ .

To account for the corona effect, the core is treated as QGP using the SHM and the corona as superposition of independent nucleon-nucleon collisions.

In the QGP, a ratio of cross-sections of  $\sigma_{J/\psi}/\sigma_{\psi(2S)} = 0.0278$  is predicted by the SHM model and in the corona the value is the ratio of production cross-section in pp collisions  $\sigma_{J/\psi}^{pp}/\sigma_{\psi(2S)}^{pp} = 0.148 \pm 0.005$ , taken from an extrapolation of ratios in pp collisions from multiple energies (see Sec-

tion 3.6.4). In order to evaluate the evolution of the ratio of cross-sections as a function of centrality, the contribution of the corona and the fireball have to be taken into account.

The corresponding result is presented in Figure 3.29. The uncertainty on the model corresponds to different values of the nucleus density below which nucleons are considered as part of the corona:  $\rho < 0.1\rho_0$  in the upper band and for  $\rho < 0.15\rho_0$  in the lower band (The nuclear density are defined within the Woods-Saxon model, as shown in Equation 3.8). The uncertainty on the temperature, about 3 MeV, is not included. It would change the ratio by  $\pm 7\%$ , which added in quadrature to the corona uncertainty would be almost negligible.

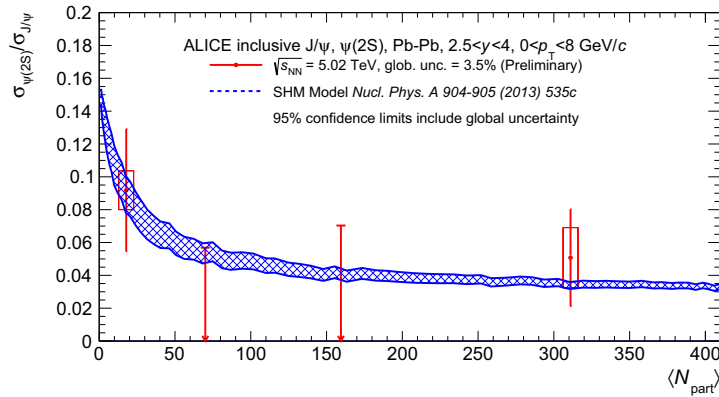


Figure 3.29:  $\psi(2S)$ -to- $J/\psi$  ratio versus  $N_{\text{part}}$  compared to the Statistical Hadronization Model. For the centrality bins where the signal could not be extracted, only the 95% CL is shown. The red box around unity corresponds to the global uncertainty which are included in the confidence limits calculation and therefore do not apply to the CL. Uncertainties in the model correspond to different values of the nucleus density below which nucleons are considered as part of the corona:  $\rho < 0.1\rho_0$  in the upper limit and for  $\rho < 0.15\rho_0$  in the lower limit.

As was the case with the other two models, the SHM is compatible with the data, but the uncertainties on the values prevent from drawing any stronger conclusion.

As we have seen in this chapter, the increase in the collision energy at the LHC allowed to perform the first measurement of the  $\psi(2S)$   $R_{AA}$  down

to  $p_T = 0$  in the rapidity range  $2.5 < y < 4.0$ . Results are in good agreement with the measurements from CMS for prompt charmonium in the rapidity range  $1.6 < y < 2.4$ . Theoretical models also show a good agreement with the data. However, the uncertainties in the  $\psi(2S)$  measurements prevent from drawing any stronger conclusion and a more precise measurement will be needed to sort out the underlying physics of quarkonium production.

In order to eventually discriminate between the models, it would be helpful to have a more precise measurement of the  $\psi(2S)$  signal. This could be achieved by an increase of the integrated luminosity of the data taking, both in Pb – Pb and in pp collisions, and by improving the signal-to-noise ratio for the  $\psi(2S)$ . To achieve this (and improve other measurements), several upgrades are planned in ALICE, which is the topic of the next chapter.



## Chapter 4

# Upgrades of the ALICE detector : the Muon Identifier (MID) - Estimation of the data flow

The ALICE collaboration, as the other LHC experiments, will implement a major upgrade of the detector during the Long Shutdown 2, planned in the years 2019-2020. The current detector will be improved by enhancing its low momentum vertexing and tracking capability and allowing it to take data at higher interaction rates. The upgrades are conducted under the assumption that after the LS2, the LHC will increase its luminosity in Pb – Pb collisions to reach an interaction rate of 50 kHz. The ALICE detector will be modified in order to be able to record all interactions, which would allow ALICE to reach an integrated luminosity in Pb – Pb collisions of  $L_{int} = 10 \text{ nb}^{-1}$ , corresponding to  $10^{11}$  interactions. In the 2015 Pb – Pb collisions, a luminosity of  $L_{int} = 225 \mu\text{b}^{-1}$  was recorded, corresponding to  $1.7 \times 10^9$  interactions at a collision rate up to 9.5 kHz. The expected increase in the statistics is of a factor 100 over what is reachable at the moment.

In this section, a brief summary of the motivations for the upgrades in terms of quarkonium studies is presented, followed by a short description of the upgrades planned for the different detectors. The MID, which is the focus of this study, is then described and finally the question of the data flow implied by the upgraded detector at the higher rates is studied.

## 4.1 Physics motivations

With the increase in statistics expected for ALICE after the LS2, a more precise measurement of the physics observables is expected and also some new measurements should be possible. The detailed description of the physics motivation for the upgrade is described in the ALICE upgrades Letter Of Intent [224]. The ALICE physics program after LS2 will focus on rare probes and will aim mainly at performing measurements of heavy-flavour transport parameters, quarkonia down to zero  $p_T$  and low-mass dileptons. Additional physics topic will of course benefit from the ALICE upgrades, such as jet measurements and the search for exotic heavy nuclear states, such as light multi- $\Lambda$  hyper-nuclei.

Since we are interested in the  $\psi(2S)$ , we will describe in more details what the upgrades could bring in the charmonium study. As we have seen in chapter 1 of this thesis, the study of charmonium production is a prominent probe of the QGP. However, a more precise measurement is necessary to fully understand the underlying physics occurring in the plasma. The upgrades program is expected to provide such a comprehension by improving the

measurement of several observables:

- The  $J/\psi$  yields and  $R_{AA}$ : although a good measurement is possible right now, as illustrated by Figure 1.25, where the  $R_{AA}$  could be measured in more than 20 different centrality bins, with the increase in the Luminosity expected after LS2, an even more precise measurement will be possible as a function on  $p_T$ ,  $y$  and centrality. Moreover the addition of a new detector, the Muon Forward Tracker (MFT), is planned. The MFT will help separate the prompt from the non-prompt  $J/\psi$  in the forward direction.
- The  $J/\psi$  elliptic flow (see Section 1.6.3): with the luminosity increase, the measurement of the  $J/\psi$  elliptic flow will also be more precise, as illustrated in Figure 4.1 which presents the absolute statistical uncertainty on the  $J/\psi$  elliptic flow for two different rapidity ranges. The recent measurement of the  $J/\psi$   $v_2$  in Pb – Pb collisions at  $\sqrt{s_{NN}} = 5.02$  TeV with a luminosity  $L_{int} = 225 \mu\text{b}^{-1}$  exhibits an absolute error on the rapidity integrated  $v_2$  that varies from 0.012 to 0.031 versus  $p_T$ , as seen in Figure 1.24. With the anticipated  $10 \text{ nb}^{-1}$  luminosity, one can see that even in the rapidity range  $3.7 < y < 4.0$ , where the detector acceptance and the production cross-section are the lowest, the  $J/\psi$  elliptic flow could be measured with a similar precision.
- The  $J/\psi$  polarization (see Section 1.5.1): a measurement of the  $J/\psi$  polarization at low- $p_T$  in Pb – Pb collisions is expected to be possible with the anticipated luminosity of  $10 \text{ nb}^{-1}$ . Theoretical models predict that the  $J/\psi$  escaping the QGP should possess a polarization [225], which has not been observed yet. As illustrated in Figure 4.2, it is expected that the statistical errors on  $\lambda_\theta$  will be about 0.02 with the Muon Spectrometer data at the expected luminosity.
- The photo-produced  $J/\psi$ : the electromagnetic  $J/\psi$  production (see Section 1.5.1) could be measured with a higher precision and the relative uncertainty is expected to be reduced by a factor five compared to the first measurement at  $\sqrt{s_{NN}} = 2.76$  TeV [106].
- The  $\psi(2S)$  yields:  $\psi(2S)$  measurement should be greatly improved by the implementation of the upgrades and the increase of luminosity. Figure 4.3 shows the estimated relative error on the number of  $\psi(2S)$  as a function of centrality for the anticipated luminosity using the Statistical Hadronization model. When comparing to the relative error

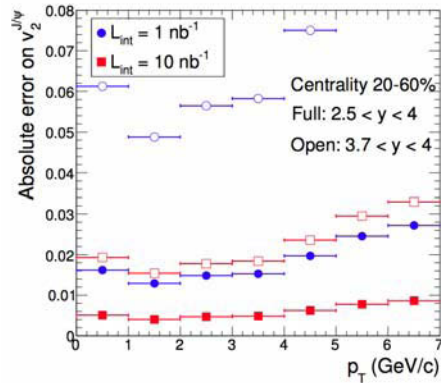


Figure 4.1: Expected absolute statistical uncertainty of the  $J/\psi$  elliptic flow as a function of the transverse momentum measured with the new Muon Spectrometer (with the MFT), estimated for integrated luminosities  $L_{int} = 1 \text{ nb}^{-1}$  (blue) and  $L_{int} = 10 \text{ nb}^{-1}$  (red) in Pb–Pb collisions at  $\sqrt{s_{NN}} = 5.5 \text{ TeV}$  [224].

measured at  $\sqrt{s_{NN}} = 5.02 \text{ TeV}$  for an integrated luminosity of  $L_{int} = 225 \mu\text{b}^{-1}$ , where the relative uncertainty on the  $\psi(2S)$  in the centrality range 60-90% is around 0.40 (see Section 3.3.6), we see that it would be a considerable improvement.

- Additionally, with an integrated luminosity of  $10 \text{ nb}^{-1}$ , the photo-produced  $\psi(2S)$  could be measured for the first time in heavy ion collisions.
- The separation between the prompt and non-prompt charmonium will allow to remove the ambiguities on the interpretation of the inclusive  $R_{AA}$  in terms of a prompt  $J/\psi$  measurements, since the  $R_{AA}$  of prompt  $J/\psi$  varies by up to 10% with respect to the  $R_{AA}$  of inclusive  $J/\psi$ , depending on the hypothesis on the non-prompt charmonium. Moreover it will allow a direct measurement of open beauty at forward rapidity, by the measurement of non-prompt  $J/\psi$  that come from B hadron decay.

These are the main points that are expected to be improved after LS2 for the charmonium study. Besides this improvements, measurements of new observables might also become possible such as the observation of the  $\chi_c$  through photon reconstruction in the central barrel. However, the detector

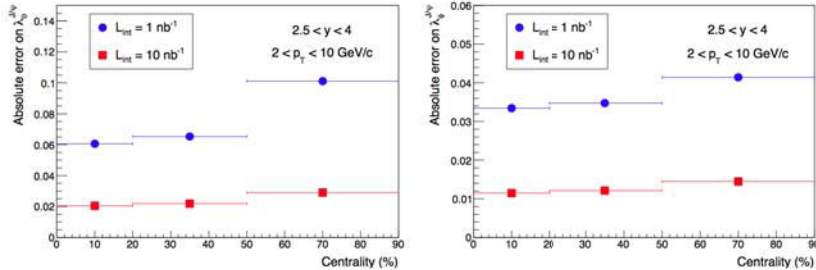


Figure 4.2: Absolute statistical uncertainty on the  $J/\psi$  polarization parameters  $\lambda_\theta$  (left panel) and  $\lambda_\phi$  (right panel) as a function of collision centrality measured with the Muon Spectrometer, estimated for integrated luminosities  $L_{int} = 1 \text{ nb}^{-1}$  (blue) and  $L_{int} = 10 \text{ nb}^{-1}$  (red) in Pb–Pb collisions at  $\sqrt{s_{NN}} = 5.5 \text{ TeV}$  [224].

has to be upgraded to be able to perform these measurements and cope with the anticipated luminosity and collision rates. The next section describes briefly the upgrades that will be implemented in ALICE.

## 4.2 ALICE Upgrades

The nominal performances of the upgrades are based on expected Pb–Pb collisions with a rate of 50 kHz, with a luminosity up to  $\mathcal{L} = 6 \times 10^{27} \text{ cm}^{-2} \text{ s}^{-1}$ , in addition to pp and p–Pb collisions at a collision rate of 200 kHz. Each collision will be recorded by the online systems, either using a Minimum Bias trigger or in a continuous triggerless fashion. Where feasible, a safety margin of 2 is applied in the system design. Below is the list of detectors that will be replaced, added or upgraded.

The central trigger processor (CTP, see Section 2.5.1) will be upgraded to be able to process data with the higher interaction rate [226]. As seen in the section 2.5.1, the current trigger strategy is to combine a Minimum Bias sample with a sample selected according to thresholds in high  $p_T$  or high multiplicity and the trigger is successful only if every detector in a list of read-out detectors (a trigger cluster) is available to read out the data. The association between the group of detectors and trigger condition defines a trigger class.

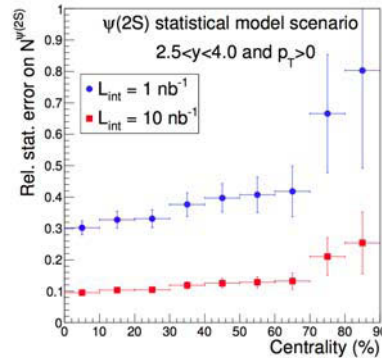


Figure 4.3: Estimated relative statistical uncertainty on the  $\psi(2S)$  measurement in the Muon Spectrometer as a function of collision centrality using statistical model predictions for integrated luminosities  $L_{int} = 1 \text{ nb}^{-1}$  (blue) and  $L_{int} = 10 \text{ nb}^{-1}$  (red) in Pb–Pb collisions at  $\sqrt{s_{NN}} = 5.5 \text{ TeV}$  [224].

For the upgrade, the strategy is to select and read out all interactions and apply an online data reduction in the online computing system. This will be done by using a combination of triggerless read-out and minimum bias trigger. If a trigger condition is satisfied, the event is read out with the continuous read-out detectors and all available detectors, treating each detector as a separate cluster. However, the trigger will also allow to define further clusters consisting of group of detectors as it is the case at present.

The Inner Tracking System (ITS, see Section 2.2.1) will be replaced by a new ITS composed of seven layers of monolithic silicon pixel detectors [227]. The first detection layer will be placed closer to the beam line, allowing to improve the measurement of the impact parameter. The material budget of these first detection layers will also be reduced in comparison to what is currently implemented in order to improve the tracking performance and the momentum resolution. This will be achieved by using Monolithic Active Pixel Sensors (MAPS). The pixel density will also be increased by a factor 50 thanks to an optimization of the read-out architecture.

The seven layers will be located at radii ranging from 22 mm to 430 mm from the beam line. A layout of the new ITS is presented in Figure 4.4. The three inner most layer constitute the inner barrel, while the four outermost are the outer barrel. The ITS layers are segmented into units called Staves. The new ITS will not measure the ionization in the silicon layers, but will rather have a binary read-out without the information on the charge signal

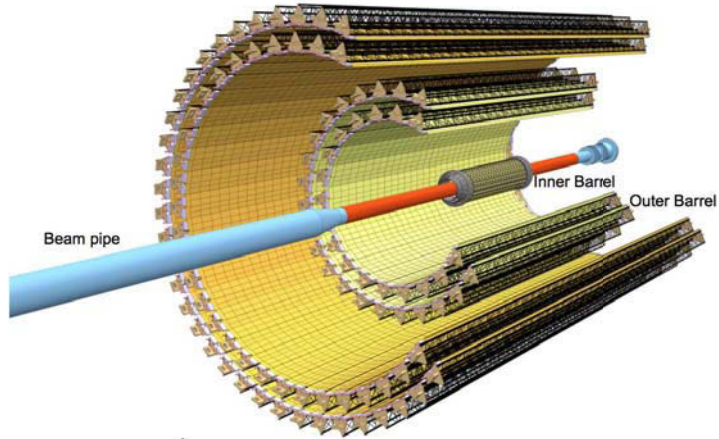


Figure 4.4: Layout of the new ITS detector [227].

amplitude. With the upgrade, the ITS will be able to provide read-out at rates of 100 kHz for Pb–Pb collisions and 400 kHz for pp collisions.

The ITS is primarily aimed at heavy-flavor measurements and with the upgrade and  $10 \text{ nb}^{-1}$  of luminosity, at measurements such as D meson  $R_{AA}$  down to zero  $p_T$  and B meson  $R_{AA}$  down to  $1 \text{ GeV}/c$ . It will also allow to measure the secondary vertices from the B to D meson decay. In addition the ITS will also contribute to the measurement of low-mass dielectrons. Measurement such as thermal radiation from de QGP via real and virtual photons detected as dielectrons should be possible [227].

The Muon Forward Tracker (MFT) will be added in the forward region between the ITS and the front absorber [228]. The main goal of the MFT is to measure charged particles with high spatial resolution in front of the Muon Spectrometer and within its acceptance. The acceptance of the MFT will however be smaller than the Muon Spectrometer one.

The MFT will be composed of two half-MFT cones, each half-cone being composed of 5 half-disks positioned along the beam axis. Each half disk is composed of a half disk spacer and support, two printed circuit boards and the sensor ladders. The sensor ladders are composed of silicon pixel sensors, using the same technology as the upgraded ITS. A layout of the MFT is presented in Figure 4.5. Combined with the Muon Spectrometer, the MFT will improve the charmonium measurement by allowing to distinguish between the prompt and non-prompt  $J/\psi$ , thanks to its high precision

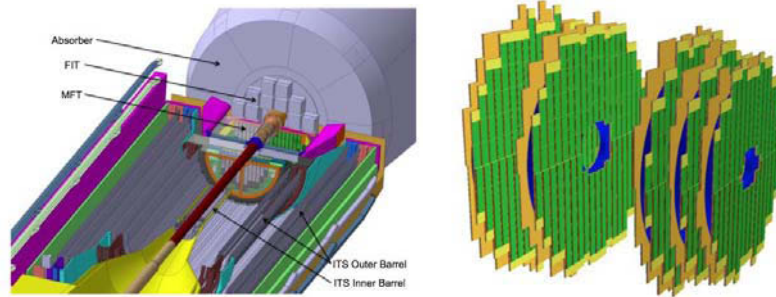


Figure 4.5: Layout of the MFT in ALICE (left) and layout of the active area of the MFT (right), showing the positioning of the half-disks and MFT ladders [228].

vertexing capabilities. It will also reduce the background below the  $J/\psi$  and  $\psi(2S)$  by tagging some of the muons coming from pion and kaon decay on an event by event basis.

The Time Projection Chamber (TPC, see Section 2.2.2) is presently based on a gated read-out with wire chambers. The read-out rate is limited to 3.5 kHz by the electron drift time from the central electrode to the read-out chambers, together with the ion drift time from the sense wires to the gating grid. These wire chambers will therefore be replaced by Gas Electron Multiplier (GEM) detectors, that allow continuous operation to read-out the foreseen 50 kHz Pb–Pb collisions [229]. With the upgraded TPC, the read-out rate should be increased by two orders of magnitude. The overall dimension of the TPC will remain unchanged, as well as the segmentation of the read-out planes. However the powering scheme of the field cage will have to be adapted to match the voltages of the GEM system. The electronics of the TPC will send the TPC data to the online system in a triggerless mode. These changes will not affect the performances of the TPC and the tracking and PID capabilities of the current TPC will be maintained.

The Muon Chambers (MCH, see Section 2.4.2) will have their read-out electronics replaced to digitize the detector signal [226]. The new ASIC (Application Specific Integrated Circuit) that will be used for the front-end read-out, called SAMPAs, supports both triggered and continuous read-out. A Common Read-out Unit (CRU) will replace the current read-out system to concentrate the data before transmitting them to the online and offline computing system.

The Muon Trigger (MTR, see Section 2.4.3) will no longer serve the

purpose of a muon trigger: all events will be read upon the interaction trigger and the data are used offline for the hadron rejection. Therefore, the detector will be called the Muon Identifier (MID). It is described in more details in Section 4.3.

The V0, T0 and Forward Multiplicity Detector (FMD, see Section 2.3) will be replaced by a single detector system: the Fast Interaction Trigger (FIT). The FIT will provide the same functionalities as the V0, T0 and FMD, namely a Minimum Bias trigger, a multiplicity trigger, beam-gas event rejection and measurement of the collision time, needed for the TOF detector.

The FIT will be composed of two sub-detectors, T0-plus and V0-plus, that can be seen as improvements of the current V0 and T0 detectors. This choice was made to keep some of the redundancy that exists between the T0 and V0. The T0-plus will be composed of 20 modules of quartz radi-

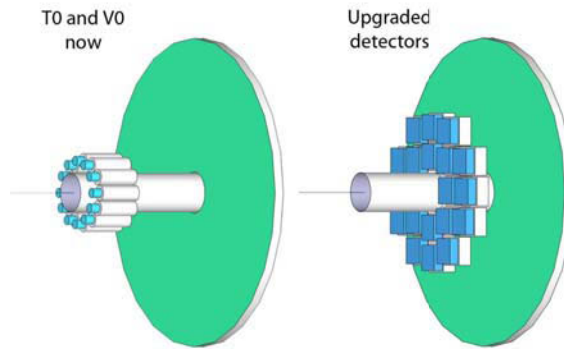


Figure 4.6: Conceptual drawing of the trigger detectors on the C-side (forward direction) as they are now (left) and after the upgrade (right) [226].

ators directly coupled to light sensors based on Micro Channel Plate and PhotoMultipliers Tubes (MCP-PMT). The V0-plus will be an improved V0, using a plastic scintillator based system, but with the front end electronics integrated with the T0-plus. A sketch of the new detectors is shown in Figure 4.6. The read-out electronics will be the same for both T0-plus and V0-plus and will be based on the present T0 detector.

The Transition Radiation Detector (TRD, see Section 2.2.3) will be upgraded by changing the data throughput of the electronics that are off the detector, in order to sustain a 100 kHz interaction rate for Pb–Pb and pp

collisions. The electronics on the detector will not be changed, as it requires a removal and disassembly of all TRD modules.

The Time-Of-Flight detector (TOF, see Section 2.2.4) and the Zero Degree Calorimeter (ZDC, see Section 2.3.1) will also have their read-out electronics changed in order to run into high trigger rate conditions.

The other detectors will not be modified (namely the EMCal, Section 2.2.7, the PHOS, Section 2.2.6, the HMPID, Section 2.2.5 and the ACORDE, Section 2.2.8) but will have to be implemented in the upgrade read-out architecture.

### 4.3 The Muon Identifier (MID)

During the considerations for the upgrade, it appeared that it would be better to record all minimum bias collisions with the muon detector, in order to benefit the most from the potential of the detector for muon physics. Therefore some changes have to be brought to the read-out architecture [226].

The current MTR is composed of four planes of RPC detectors, arranged in two stations. It is described in more details in Section 2.4.3.

The read-out process in the MTR goes as described in Figure 4.7: the RPC signals are collected by the strips placed on the RPCs and the Front-End (FE) electronics, also placed on the RPCs. The signals from the 21 000 FE electronic channels is then propagated to 234 local cards that act as the read-out interface. The signal is then propagated to 16 regional cards. The read-out is performed by two Dimuon trigger ALICE Read-out Controller (DARC) cards, interfaced to the regional cards.

For the upgrade, the strategy is to remove the trigger decision functionalities. However, since the detector is separated from the MCH by an iron wall, the contamination of the Muon Tracker by reconstructed tracks in the Muon Spectrometer that are either low momentum muons or hadrons either traveling through the absorber or produced in it, also called hadron contamination, is greatly reduced when matching the tracks of the MCH with the ones in the MTR. Therefore the upgraded MTR will still be used as a muon identifier, hence the change of the name to MID. Finally, the rejection of the remaining hadron contamination will be done offline.

A consequence of the passage from a Muon Trigger to a Muon Identifier is that the MTR read-out electronics will have to be replaced in order to

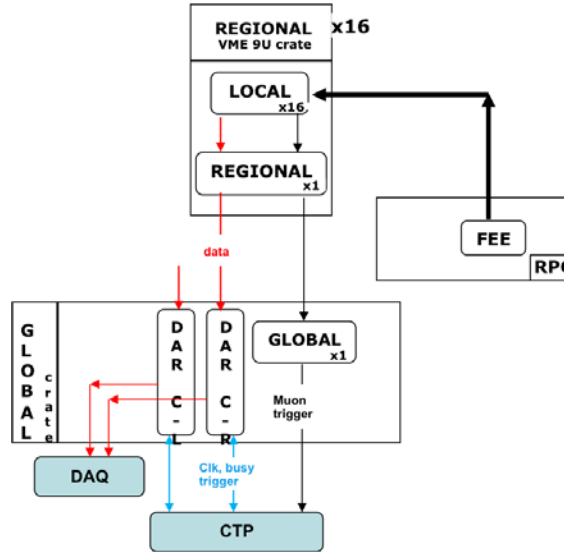


Figure 4.7: Schematic of the MTR readout electronics architecture.

stand the new trigger rates. The local, regional and DARC boards will be replaced. In the new architecture, the local cards receives the binary signals via Low Voltage Differential Signaling (LVDS) cables indicating whether the corresponding channel has been hit. Events are stored in the local card multi-event buffer at each trigger. This buffer, which is First-In First-Out (FIFO) buffer, is designed to be larger than the size of one event in a local board. The constraints on the size of the buffer are discussed in Section 4.4. Then the regional cards receive the information via 16 electrical serial links (e-links). The regional cards then send the data via a GigaBit Transceiver (GBT) to the CRU, which will forward the data to the online calculation system. A scheme of the read-out electronics architecture for the MID is presented in Figure 4.8.

The summary of the MID number of cards and links is presented in Table 4.1. Prototypes of these cards have been developed at the Subatech Institute in Nantes.

In addition to the read-out architecture, the FE electronic will also be changed. In the current operating mode of the RPCs and without any amplification in the FE electronics, the mean charge is around 100 pC per hit. According to the tests carried out on the RPCs [230], this sets a instantaneous counting rate limitation below 50 hits/s/cm<sup>2</sup>, including safety

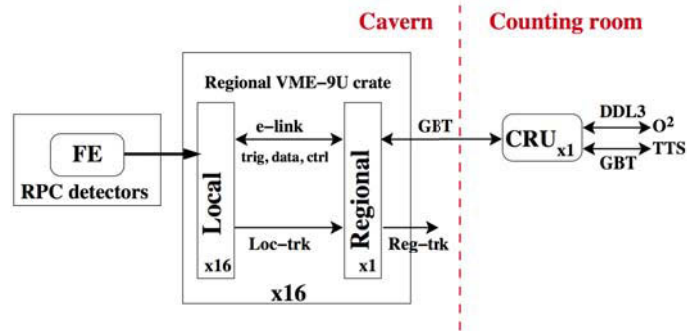


Figure 4.8: Schematic of the MID readout electronics architecture [226].

margins. However, the expected counting rate in the RPCs for 100 kHz Pb–Pb collisions could exceed  $120 \text{ hits/s/cm}^2$ , according to extrapolation from previous measurements [231].

Considerations on the ageing of the RPCs also constitute a motivation for the replacement of the FE electronics. The R&D on the RPCs shows that the detector cannot be operated safely for a cumulated dose larger than  $50 \text{ mC/cm}^2$  [230]. The planned physics program for after LS2 would result in a charge deposit of more than  $100 \text{ mC/cm}^2$  for the most exposed RPCs in the current operation mode, to which one must also add the dose received before LS2. It was therefore decided to change the operation mode from "saturated avalanche" mode (see Section 2.4.3) to "genuine avalanche", in order to limit the charge production in the gas. This will allow to reduce the ageing effects.

The change of operating mode requires an amplification stage in the FE electronics, which the current design doesn't provide. Therefore the current FE chip will be replaced by a new chip called FEERIC (Front End Electronics Rapid Integrated Circuit), that has been developed by the LPC at Clermont-Ferrand.

The FEERIC ASIC is composed of a transpedance amplifier, a zero-crossing discriminator, one-shot which prevents re-triggering during 100 ns and the LVDS drivers. A diagram of the FEERIC ASIC is presented in Figure 4.9. The first prototype of FEERIC ASIC was delivered in 2013 and developed through prototypes and tests in the ALICE Muon trigger. The production was validated in June 2016. The number of new FE cards to be installed is also quoted in Table 4.1.

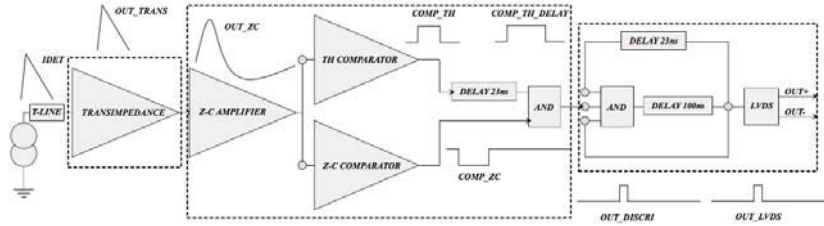


Figure 4.9: Block diagram of the FEERIC[227].

Component	Number
FE Cards	2384
Local Cards	234
Regional Cards	16
CRU Cards	1
e-links	234
GBT links	32

Table 4.1: Summary of the number of MID cards and links [227].

## 4.4 Estimation of the Data Flow

One of the problems raised by the change of the architecture is the estimation of the data flow from a local board to a regional board and the total data flow for the detector. This will allow to know the size of the buffers that will have to be implemented before evacuating the data from the local to regional boards and from the regional board to the CRU. Even if the requirement is set for  $P_b - P_b$  collisions at 50 kHz, for the MID the safety factor of 2 is applied and the calculation will be performed assuming  $P_b - P_b$  collisions at 100 kHz.

#### 4.4.1 Event Format

The first step consists in evaluating the size of an event. When a particle goes through the MID, the generated data going from the local board to the regional board are organized as follows:

- First there is a header containing several information such as the type of card. The header has a size of 16 bits.
- Then there are 16 bits dedicated to the local bunch counter.
- The next 4 bits indicate the local board position: 16 local boards are linked to one regional board, so the number of the local board (0-15) is indicated by these bits. For instance if the local board n°11 has been hit, the four bits will read: 1011.
- The next 4 bits indicate which of the four planes of the MID have been hit. For instance, if the two planes of the first station and only the first plane of the second station have been hit, these bits will read: 1110.
- Finally the remaining bits indicate the non-zero strip patterns. For all the planes that have been hit, it gives the strips hit in the  $(X_i, Y_i)$  plane. For each plane the output size is 32 bits, therefore the size of the data for the non-zero strips patterns is  $32 \times i$ , with  $i$  varying from 1 to 4 depending on the number of planes that were hit.

Therefore, per local board, the total number of bits corresponding to a hit in the MID goes from 72 to 168 depending on the number of planes hit. Given that the e-links from local to regional boards have a throughput of 320 Mbits/s with a clock of 40 MHz, the number of clock cycles needed to send the data from local to regional goes from 9 to 21.

When going from the regional board to the CRU, another information corresponding to the local board is added. It is organized as follows:

- First there is also a header with a size of 16 bits.
- Then there are the 16 bits dedicated to the local bunch counter.
- The next 4 bits indicate which regional board has been hit. Since there are 16 regional boards in the MID, the number of the regional board hit is indicated by these bits.

- The next 4 bits are information on the non-zero tracklets inputs. Since there is one tracklet per local board and 16 local boards, the number of non-zero tracklets is indicated by these bits.

In total there are 40 bits that correspond to the Regional Board information. These bits will be added to the ones corresponding to the Local Board information and will be sent to the CRU through the GBT links, which have a throughput of 3.2 GBits/s. The event formats for the local and regional information is summarized in Table 4.2.

#### 4.4.2 Data flow from scalers

In order to evaluate the data flow in the MID, we use the data in Pb – Pb collisions at  $\sqrt{s_{NN}} = 5.02$  TeV and in pp collisions at  $\sqrt{s} = 13$  TeV. The estimation are based on the scalers: for each trigger class the number of counts received by the electronics are counted. Scalers are read at regular intervals, every 600 seconds. So the number of hits, per local board, plane and cathode in a period of 600 seconds, are stored regularly in the offline data base.

This can be used to estimate the data flow, however some hypothesis have to be made. The scalers do not provide information on the time distribution of the hits during this 600 seconds lapse. A first reasonable assumption is that the hits are uniformly distributed in time. The other information missing is that there is no way to know if some of the hits in the different planes are correlated, corresponding to one track going through multiple planes. To account for this we will do the conservative assumption that all the hits are independent and the contribution to the data flow of each hit will be counted individually. This is equivalent to considering that all the hits in the MID correspond to noise rather than actual tracks. With a 100% efficient MID, a track would generate a least 4 hits (more if more than one card is hit), which would reduce the data size.

#### Estimation of the data flow in Pb – Pb at 100 kHz

To evaluate the data flow in the conditions of the data taking anticipated after LS2, we look at the minimum bias trigger rate for the Pb – Pb data taken at  $\sqrt{s_{NN}} = 5.02$  TeV. The trigger rate as a function of the run number is presented in Figure 4.10. In this figure the sudden increases in the trigger rate correspond to new fills in the accelerator while the following steady decreases corresponds to a decrease of the quality of the bunches (and the number of ions that they contain), until a new fill. An overall increasing

<i>Coding of self triggered physics event in LOCAL</i>	Number of bits
START BIT (always '1')	1
CARD TYPE (always '1'=LOCAL)	1
LOCAL BUSY ('0'=OK; '1'=FIFO full)	1
LOCAL DECISION (tracklet)	1
ACTIVE (always '1'=ON)	1
REJECTING (always '0'=OFF)	1
MASKED ('0'=OFF; '1'=ON)	1
OVERWRITEN ('0'=OFF; '1'=ON)	1
Always '0'	8
LOCAL Internal bunch counter	16
LOCAL board position in crate (0-15)	4
Data: Non zero detector plane(s) (1 bit/word)	4
Data: Only non zero, masked strip pattern(s) [(X <sub>4</sub> , Y <sub>4</sub> ), (X <sub>3</sub> , Y <sub>3</sub> ), (X <sub>2</sub> , Y <sub>2</sub> ), (X <sub>1</sub> , Y <sub>1</sub> )]	32×i (i=1 to 4)
Total Number of hits	40+32×i (i=1 to 4)
Bunches needed to send	9 to 21

<i>Coding of self triggered physics event in REGIONAL</i>	Number of bits
START BIT (always '1')	1
CARD TYPE (always '0'=REGIONAL)	1
REGIONAL BUSY ('0'=OK; '1'=FIFO full)	1
REGIONAL DECISION (tracklet)	1
ACTIVE (always '1'=ON)	1
REJECTING (always '0'=OFF)	1
MASKED ('0'=OFF; '1'=ON)	1
OVERWRITEN ('0'=OFF; '1'=ON)	1
Always '0'	8
REGIONAL Internal bunch counter	16
REGIONAL crate number (0-15)	4
Data: All tracklets inputs (Masked)	4
Total Number of hits	40
Bunches needed to send	5

Table 4.2: Event Format for the Local Boards (top) and Regional Boards (bottom).

trend is observed as more ions were injected in the accelerator during the data taking period. To illustrate how the data flow is evaluated, the run with the maximum trigger rate will be taken as example: Run 246036 with a trigger rate of 9.54 kHz. For this run, the data flow is estimated in each local board. The calculation is based on the counts on the strips on the

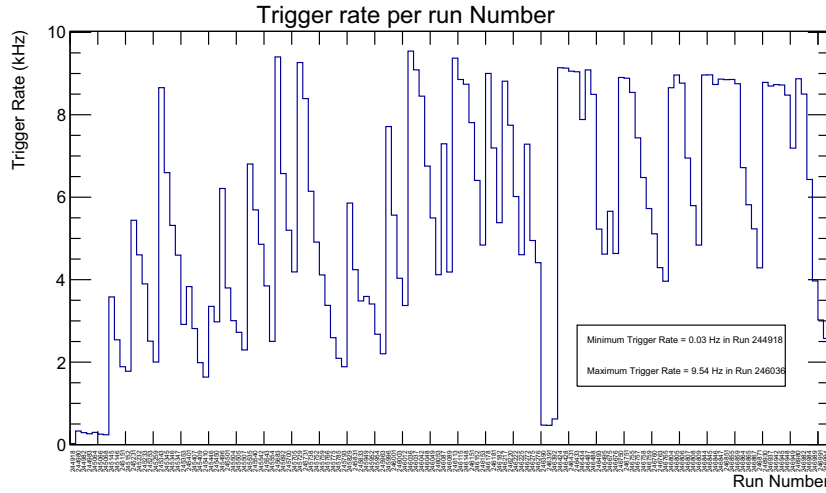


Figure 4.10: Minimum Bias trigger rate in Pb – Pb collisions at  $\sqrt{s_{NN}} = 5.02$  TeV as a function of the run number.

$X$  cathode, which is segmented with horizontal strips and measures the position in the bending plane, but an equivalent result would be found basing the calculation on the counts on the  $Y$  cathode, corresponding to the non-bending plane. Indeed, the information transmitted indicates which strips are hit in the  $(X, Y)$  plane in one local board, but the number of strips hit does not change the size of the data, as described above. Counting only the hits on the bending plane is therefore sufficient. The data flow in the local board  $i$  is then:

$$DF^i = \frac{(x_1^i + x_2^i + x_3^i + x_4^i) \times 72}{\Delta t} \text{ Bits/s} \quad (4.1)$$

where  $DF^i$  is the data flow in the local board  $i$ ,  $x_j^i$  is the number of scaler counts for the local board  $i$  in the plane  $X_j$  and  $\Delta t$  is the time lapse during which the scalers were collected; it is approximately 600 seconds as mentioned before.

The Data Flow per local board is presented in Figure 4.11. We can identify the local board with the maximum data flow: the local board 231 with a data flow of 1.97 MBits/s.

The process is repeated for all the Pb – Pb runs: in order to be conservative, the local board with the maximum data flow is identified, in order

to see the evolution of the maximum data flow as a function of the trigger rate. The results are presented in Figure 4.12. The data flow follows a linear trend as a function of trigger rate and this linear trend is used to extrapolate the value that corresponds to a trigger rate of 100 kHz. We obtain an extrapolated Data Flow at 100 kHz of 20.3 MBits/s. Given that the links between local and regional transfer data at 320 MBits/s, the bandwidth is sufficient and with large safety margins given the conservative assumptions that have been made.

The next step is to evaluate the total data flow going to the CRU. The idea is the same, to be conservative, each hit is counted individually, but this time the size of the data corresponding to a hit is (72+40), since the information from the regional board are added to the one from the local board. And the contribution from all the local boards has to be taken into account:

$$DF^{\text{CRU}} = \sum_{i=1}^{234} \frac{(x_1^i + x_2^i + x_3^i + x_4^i) \times (72 + 40)}{\Delta t} \text{ Bits/s} \quad (4.2)$$

This hypothesis is again very conservative, as the regional boards receive inputs from 16 local boards. However, as already mentioned, the scalers do not give any information regarding the correlation between the tracks, therefore we consider them to be completely uncorrelated. In the case where the 16 local boards of a regional board where hit in the same event, the corresponding data size to go from the Regional Board to the CRU would be  $72 \times 16 + 40$ . This would reduce the volume of data by 35%.

The data flow at the CRU as a function of the trigger rate is presented in Figure 4.13. The values follow again a linear trend and when extrapolated to 100 kHz, the total data flow from the regional boards to the CRU is found to be 3.6 GBits/s. Given that there are 2 GBT links per regional board to the CRU and 16 regional boards, the bandwidth available to CRU is over 100 GBits/s. As was the case for the per-local board data flow, the links between the boards have enough bandwidth to stand the data flow with large safety margins.

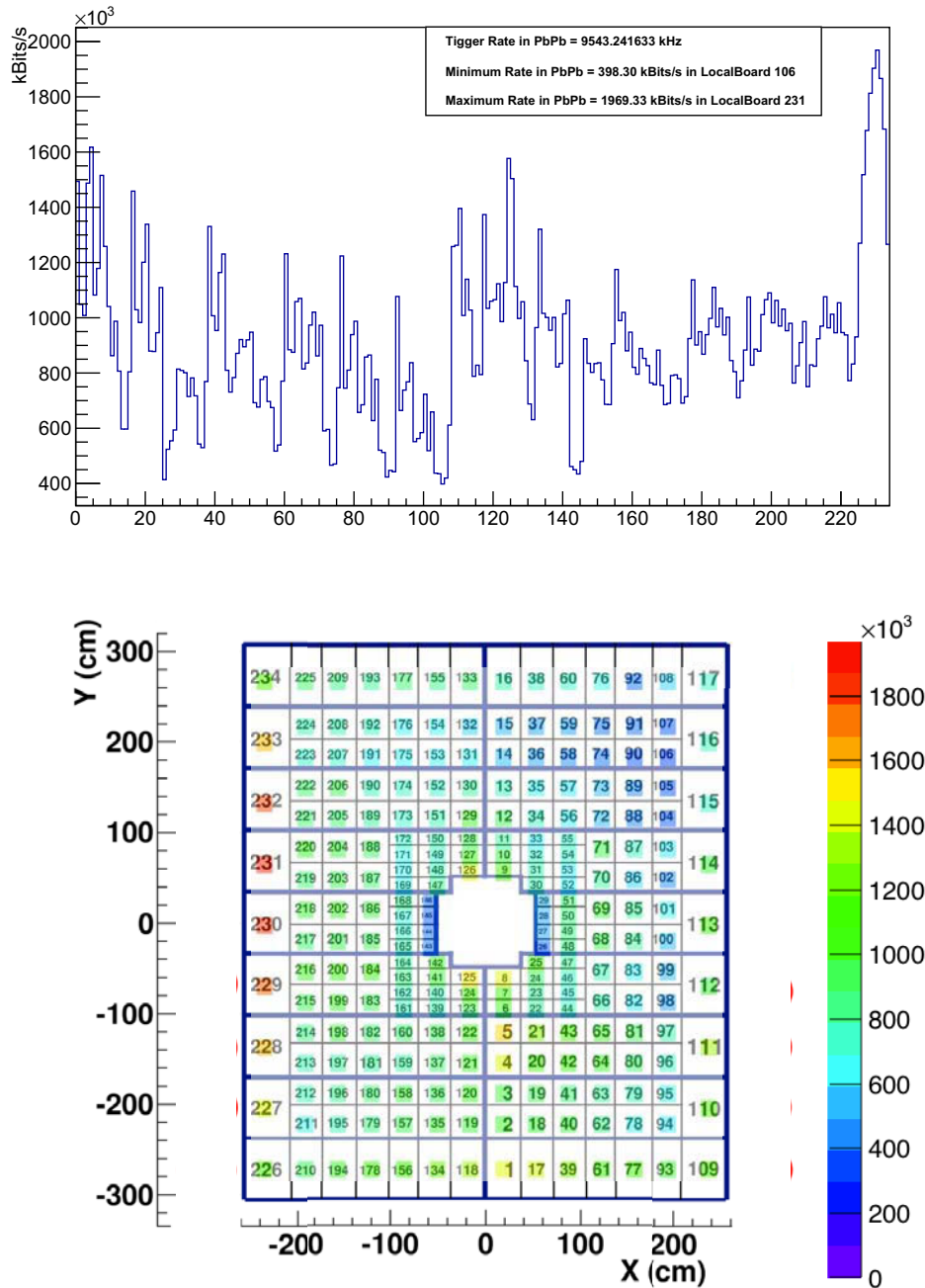


Figure 4.11: Data flow per local board for the Pb-Pb run 246036 (top). 2D-view of the data flow per local board (bottom).

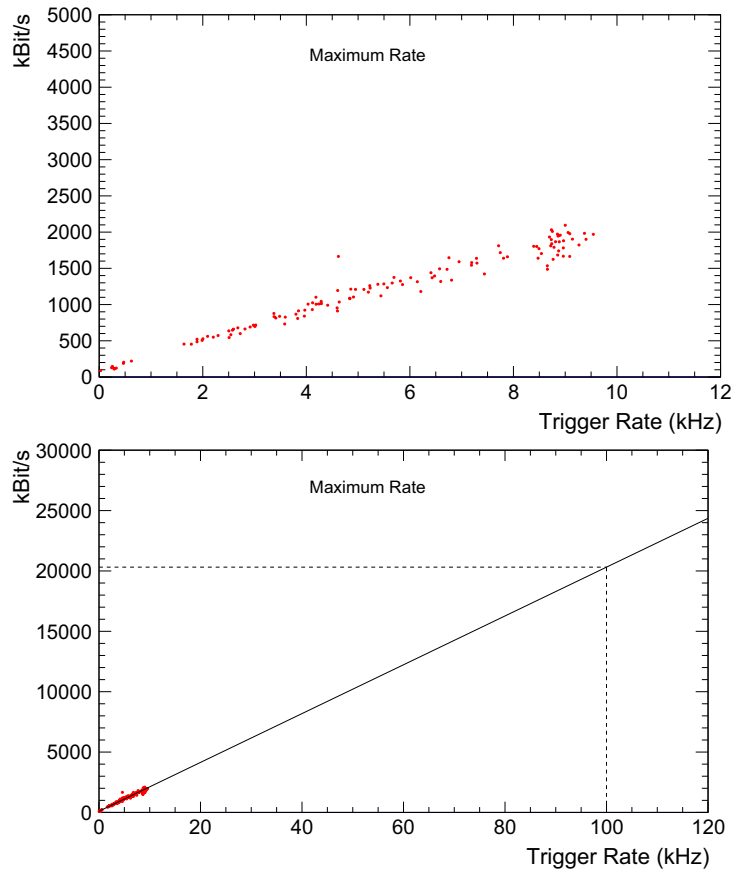


Figure 4.12: Maximum data flow as a function of the trigger rate for all the Pb – Pb runs. The values are extrapolated to a 100 kHz rate with a linear function (right panel).

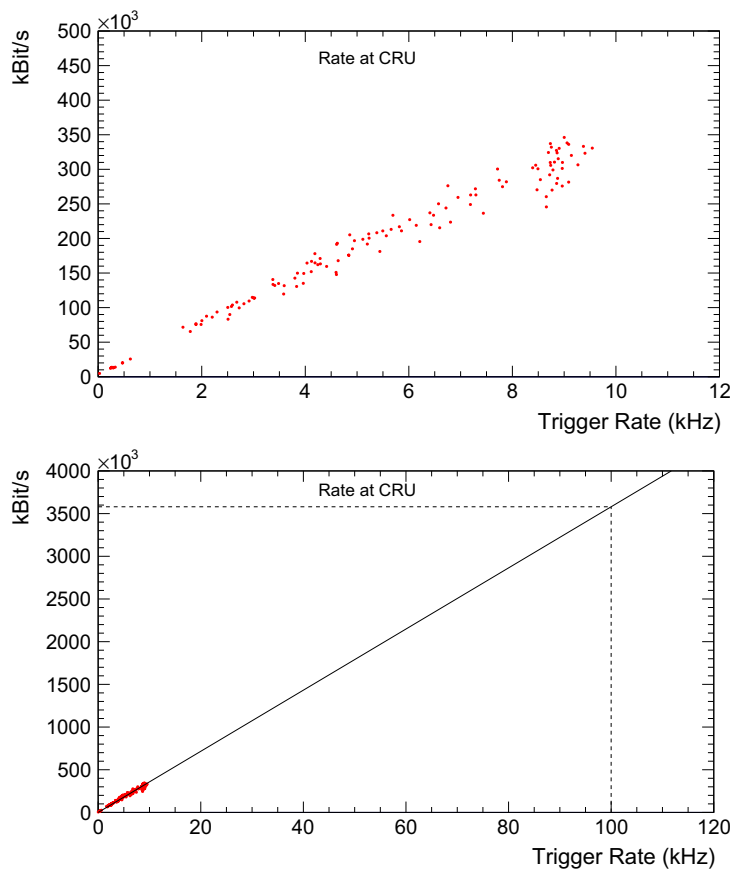


Figure 4.13: Data Flow to the CRU as a function of the trigger rate for all the Pb – Pb runs. The values are extrapolated to a 100 kHz rate with a linear function (right panel).

### Estimation of the data flow in pp at 200 kHz

The same estimation can be done for pp collisions, given the anticipated rate of 200 kHz. The calculation are this time based on the pp data taken at  $\sqrt{s} = 13$  TeV. The evolution on the Minimum Bias trigger rate as a function of the run number is presented in Figure 4.14.

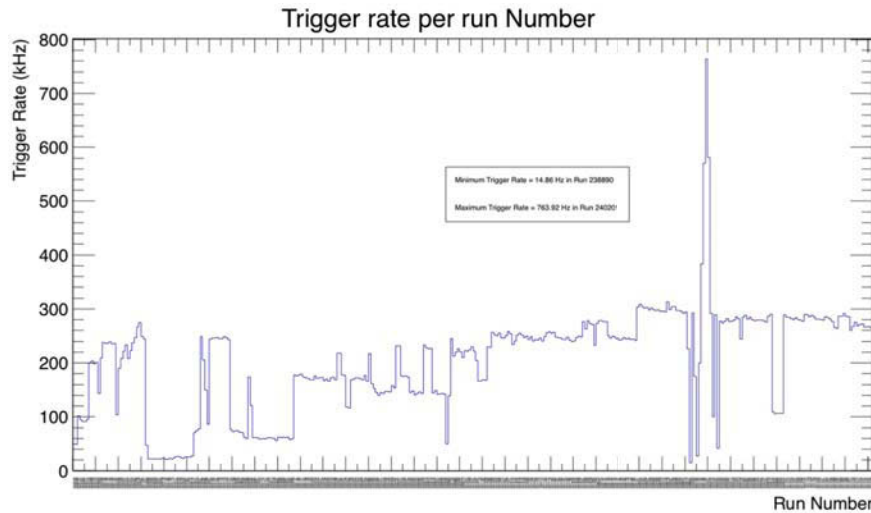


Figure 4.14: Value of the Minimum Bias trigger rate in pp collisions at  $\sqrt{s} = 13$  TeV as a function of the run number.

The data flow is evaluated with the same hypothesis, counting each hit individually and assuming an uniform distribution of the hits in the time. For each run, the data flow from the local boards to the regional boards is evaluated using Equation 4.1 and then the maximum value is plotted as a function of the trigger rate in Figure 4.15. The points are more scattered than in Pb-Pb collisions, due to larger fluctuations in beam conditions (since the data taking period in pp at 13 TeV was longer than the Pb-Pb at 5.02 TeV one) resulting in stronger variations of the background in the Muon Trigger for a given trigger rate. However, a linear increase with the increasing rate is still observed. This allows to evaluate the Data Flow from local to regional at 200 kHz: 1.9 MBits/s.

It can be noted that the trigger rate observed in pp collisions at 13 TeV is higher than what is expected for the upgrade. Indeed, the requirements for the upgrade are defined in order to have a statistics in pp collisions equivalent

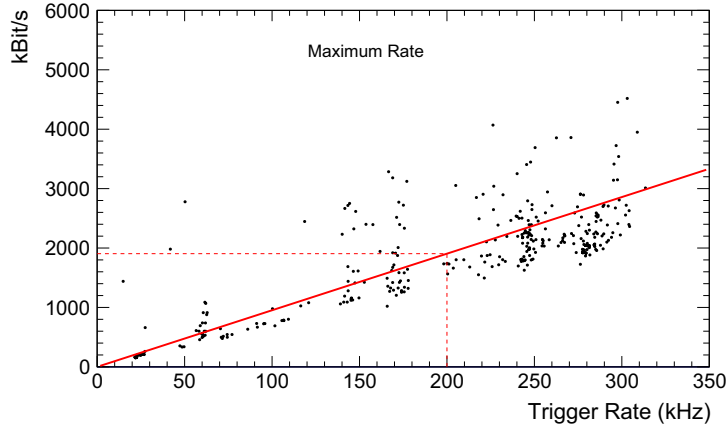


Figure 4.15: Maximum data flow as a function of the trigger rate for all the pp runs. The values are fitted with a linear function to evaluate the value at 200kHz.

to the  $10 \text{ nb}^{-1}$  expected in Pb – Pb collisions, in order to have a good pp reference for the analyses. This would require  $6 \text{ pb}^{-1}$  in pp collisions, which corresponds to 6 months of data taking at 200 kHz. On the other hand, the data taking at 13 TeV is not used for reference and therefore the detector was functioning at its maximum capacities.

As for the Pb – Pb data, we then evaluate the total data flow sent to the CRU with Equation 4.2 and the result is presented in Figure 4.16. The corresponding value at 200 kHz is 0.25 GBits/s. Again the available bandwidth is largely sufficient.

Figure 4.17 compares the evolution of the total Data Flow to the CRU as a function of the trigger rate for Pb – Pb collisions at  $\sqrt{s_{\text{NN}}} = 5.02 \text{ TeV}$  and pp collisions at  $\sqrt{s} = 13 \text{ TeV}$ . Unsurprisingly, pp collisions produce a much smaller volume of data than Pb – Pb collisions for an equivalent trigger rate. The estimations of the data flow are summarized in Table 4.3

In conclusion, despite the increase in the interaction rate, the technology implemented to process the data provides sufficient bandwidth to transfer the data from the local boards to the regional boards and from the local board to the CRU.

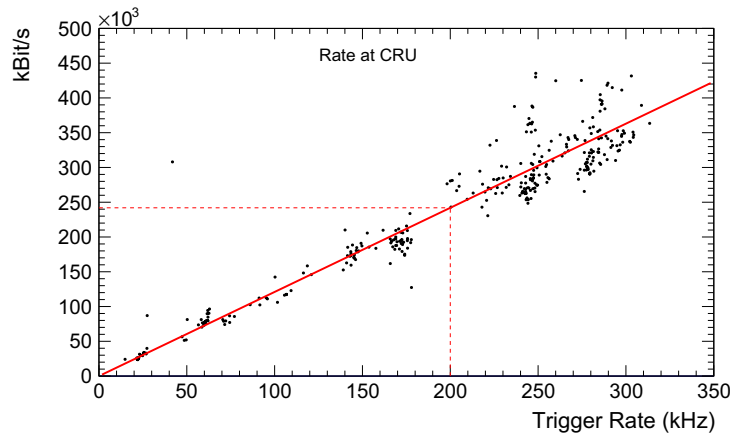


Figure 4.16: Data Flow to the CRU as a function of the trigger rate for all the pp runs. The values are fitted with a linear function to evaluate the value at 200kHz.

<b>Pb - Pb, <math>\sqrt{s_{NN}} = 5.02</math> TeV, 100 kHz</b>	
Maximum data flow per Local-Regional link	Total data flow to CRU
20.3 MBits/s (320 MBits/s available)	3.6 GBits/s (100 GBits/s available)
<b>pp, <math>\sqrt{s} = 13</math> TeV, 200 kHz</b>	
Maximum data flow per Local-Regional link	Total data flow to CRU
1.9 MBits/s	0.25 GBits/s

Table 4.3: Summary of the estimated data flows in Pb – Pb at an interaction rate of 100 kHz and in pp collisions at an interaction rate of 200 kHz.

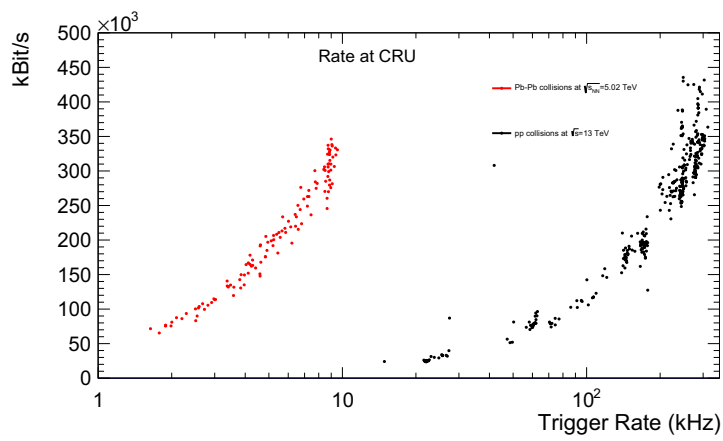


Figure 4.17: Data Flow to the CRU as a function of the trigger rate for the Pb – Pb data at  $\sqrt{s_{NN}} = 5.02$  TeV and pp data at  $\sqrt{s} = 13$  TeV.



# Conclusion

In this thesis, the inclusive production of  $\psi(2S)$  in Pb – Pb collisions at a center-of-mass energy  $\sqrt{s_{NN}} = 5.02$  TeV with the ALICE Muon Spectrometer has been measured. Data have been taken in December 2015 and correspond to a integrated luminosity of  $L_{int} = 225 \mu\text{b}^{-1}$ .  $\psi(2S)$  have measured in the dimuon decay channel in the rapidity range  $2.5 < y < 4.0$  and in the  $p_T$  range  $0 < p_T < 8$  GeV/ $c$ . The upper limit in the  $p_T$  range is limited by the low number of  $\psi(2S)$  produced.

The effects of the QGP were studied through the nuclear modification factor as a function of centrality. Also because of the lack of abundance of  $\psi(2S)$ , only four centrality bins could be considered: 0-20%, 20-40%, 40-60%, 60-90%. In particular in some of these bins, clear value of the  $\psi(2S)$  signal could not be extracted and when it happened a 95% confidence limit is quoted. The value of the  $R_{AA}$  in the centrality range 0-90% was found to be:  $R_{AA}^{\psi(2S)} = 0.2187 \pm 0.1123$  (stat)  $\pm 0.0963$  (syst). Compared to the  $R_{AA}$  of the  $J/\psi$  at the same collision energy, it shows that the  $\psi(2S)$  is more suppressed than the  $J/\psi$ , which is expected taking into account its lower binding energy. This effect is also observed as a function of centrality, where the  $\psi(2S)$  appeared to be more suppressed than the  $J/\psi$  for mid-central and central collisions ( $N_{part} > 70$ ).

In order to evaluate the difference between the  $J/\psi$  and  $\psi(2S)$ , the ratio of production cross-section as well as the ratio of  $R_{AA}$  was evaluated. In the 0-90% centrality range, it was found to be  $R_{AA}^{\psi(2S)}/R_{AA}^{J/\psi} = 0.388 \pm 0.275 \pm 0.489$ , indicating again that the  $\psi(2S)$  is more suppressed than the  $J/\psi$ .

The results were then compared to several theoretical models. A good agreement between models and data has been found, however because of the large systematic and statistical uncertainties, no stronger conclusion would

be drawn.

Finally, the upgrades of the ALICE detector were presented, which aim to be able to perform more precise measurement, in particular to provide the ability to extract a clear  $\psi(2S)$  signal, which was not always the case in this thesis. The future detectors will allow to perform collisions at a higher trigger rate and to improve the statistics by a factor 100 as well as to improve the signal-to-background ratio. The expected data flow for the future Muon Identifier was evaluated with very strong safety parameters, in order to determine if the implemented links in the Muon Identifier will sustain the data flow. It was found that the maximum volume of data would be 20.3 MBits/s in the Local boards and 3.6 GBits/s in the Regional Boards, when the expected available bandwidth is 320 MBits/s and 100 GBits/s respectively.

## Appendix A

# Confidence Limit on the $J/\psi$ signal

In order to assess the validity of the method, the Confidence Limits are calculated for the  $J/\psi$ . Multiple bins in the invariant mass histogram are contributing to the values of the signal and the background. In case of multiple bins, the log-likelihood ratio can be simply extended as the sum of the log-likelihood ratios in each bin:

$$q = \sum_{i=0}^{n_{bins}} 2(s_i - n_i \cdot \ln(1 + \frac{s_i}{b_i})) \quad (\text{A.1})$$

where  $b_i$  is to the known background for the  $\psi(2S)$  in bin  $i$ ,  $s_i$  the hypothesized signal in bin  $i$  and  $n_i$  the number of counts in that bin.

The background contains combinatorial background and continuum, taken from the  $J/\psi$  analysis.  $b_i$  is written:

$$b_i = N_{BG} \times F_{BG}(x_i) \quad (\text{A.2})$$

with  $N_{BG}$  the total number of background counts,  $F_{BG}(x_i)$  its shape,  $N_{J/\psi}$  the total number of  $J/\psi$  and  $F_{J/\psi}(x_i)$  its shape.

$s_i$  is written:

$$s_i = N_{J/\psi}^{\text{hyp}} \times F_{J/\psi}(x_i) \quad (\text{A.3})$$

with  $N_{J/\psi}^{\text{hyp}}$  the number of hypothesized  $J/\psi$  and  $F_{J/\psi}(x_i)$  the shape of the  $J/\psi$  signal.

In order to include the systematic uncertainty from the signal extraction, a method adapted from the one described in Sec 3.8.4 was adopted: the

mean shapes of the background and  $J/\psi$  are obtained by doing the mean of all the tests performed to evaluate the signal and used to calculate  $\bar{s}_i$  and  $\bar{b}_i$ . Before each pseudo-experiment, a random combination of background function, signal function, tail parameters and fit ranges from the tests is then drawn and the corresponding  $s_i$  and  $b_i$  are used as parameter to the poissonian drawing of  $n_{i,s+b}$  and  $n_{i,b}$ . In addition, a uncertainty is added on the background to represent how well the background is known. Indeed, the CLs method implies that the background is perfectly known, whereas in this case it is not true, since it comes from a fit which has a statistical uncertainty (due to the free parameters). In order to take into account this effect, the uncertainty on the background function from the fit  $\sigma_{Fit}$  is calculated. Then, in the same way the systematics are included, this uncertainty is added to the total number of background counts  $N_{BG}$  :

$$N_{BG}(\theta) = N_{BG}^{mean}(1 + \sigma_{Fit} \cdot \theta) \quad (\text{A.4})$$

where  $\theta$  is drawn from a gaussian of mean 0 and width 1.

Finally, the value of CLs is calculated. Results can be found in Tab. A.1, compared to the values obtained with the standard procedure of signal extraction. Because there is a significant signal, one expects the value of the  $\frac{CLs(95)-N}{2\sigma}$  to be close to 0.82. Indeed by definition the 95% confidence limit is the value CL that satisfies :

$$P(X < CL) = 95\% \quad (\text{A.5})$$

If we assume that X has a gaussian pdf of mean  $\bar{X}$  and width  $\sigma$  and define  $\alpha$  such as :

$$P(X < \bar{X} + 2\alpha\sigma) = 95\% \quad (\text{A.6})$$

we find  $\alpha = 0.82$ . In other word we expect  $\frac{CLs(95)-N}{2\sigma} = \alpha = 0.82$ .

In the example of the  $J/\psi$ , the differences between the expected and measured values are under 3.5%. Differences may be due to the non gaussianness of the uncertainties and the way systematic uncertainties are introduced, which for the signal extraction is not gaussian. However a good agreement is found, which validates the use of the CLs method.

Centrality (%)	$N_{J/\psi} \pm (stat) \pm (sys)$	Expected $CL_s$	Measured $CL_s(95)$	Difference (%)
0-10	$109882 \pm 1395 \pm 3583$	116187	116180	0.06
10-20	$70398 \pm 1152 \pm 1815$	73923	73650	0.37
20-30	$45324 \pm 758 \pm 1084$	47493	47210	0.60
30-40	$24857 \pm 484 \pm 593$	26112	25960	0.59
40-50	$15026 \pm 317 \pm 374$	15830	15750	0.51
50-60	$8005 \pm 191 \pm 192$	8449	8370	0.95
60-70	$4095 \pm 111 \pm 83$	4322	4320	0.05
70-80	$2082 \pm 72 \pm 52$	2227	2270	1.86
80-90	$946 \pm 41 \pm 34$	1070	1070	3.42

Table A.1: Average  $J/\psi$  yield with statistical and systematic uncertainties in each centrality bin in the  $p_T$  range 0-8 GeV/ $c$  and rapidity range  $2.5 < y < 4.0$ , compared to confidence limits calculated with the CLs method.



## Appendix B

# Comparison of the model prediction

### B.1 CoMover Interaction Model and Transport Model comparison

In Figure B.1, the predictions for the  $\psi(2S)$  with the CIM and the TM are presented. The differences in the uncertainties in the models come from the way uncertainties are treated. In the CIM, the shadowing is evaluated according to EPS09 LO parametrization and the values of the open-charm cross section  $d\sigma_{c\bar{c}}/dy$  are taken in a range from 0.45 to 0.7 mb, accounting for different hypothesis on the importance of the regeneration component. On the contrary, in the TM, the value of the open-charm cross-section is set at  $d\sigma_{c\bar{c}}/dy = 0.57$  mb in the considered rapidity range, in agreement with FONLL calculations, whereas the hypothesis on the importance of the shadowing effects are changed from no shadowing to the values obtained with EPS09 NLO parametrization.

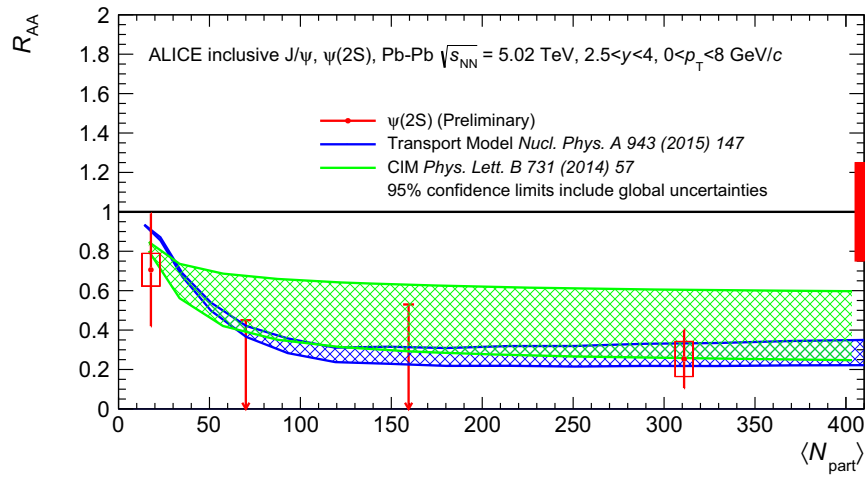


Figure B.1: Nuclear modification factor  $R_{AA}$  versus  $N_{\text{part}}$  compared to the Transport Model (in blue) and the Comover Interaction Model (in green). For the centrality bins where the signal could not be extracted, only the 95% confidence limit is shown. The global systematic uncertainty is drawn in the box around unity. The global uncertainties are already included in the confidence limit calculation.

## B.2 CoMover Interaction Model

In Figure B.2, the predictions for the  $\psi(2S)$  and  $J/\psi$  with the CIM are presented. For the  $J/\psi$ , a cut  $p_T > 0.3$  GeV/ $c$  is performed to suppress the photo-produced  $J/\psi$  [106]. The prediction are very similar for the  $J/\psi$  and the  $\psi(2S)$ . This is due to the fact that even though the co-mover interaction cross-section is ten times higher for the  $\psi(2S)$  than for the  $J/\psi$ , leading to a more important suppression for the  $\psi(2S)$ , it also causes the regeneration component to be more important for the  $\psi(2S)$ , as seen in Equation 3.62. And in this case, it leads to similar predictions for the  $\psi(2S)$  and the  $J/\psi$ .

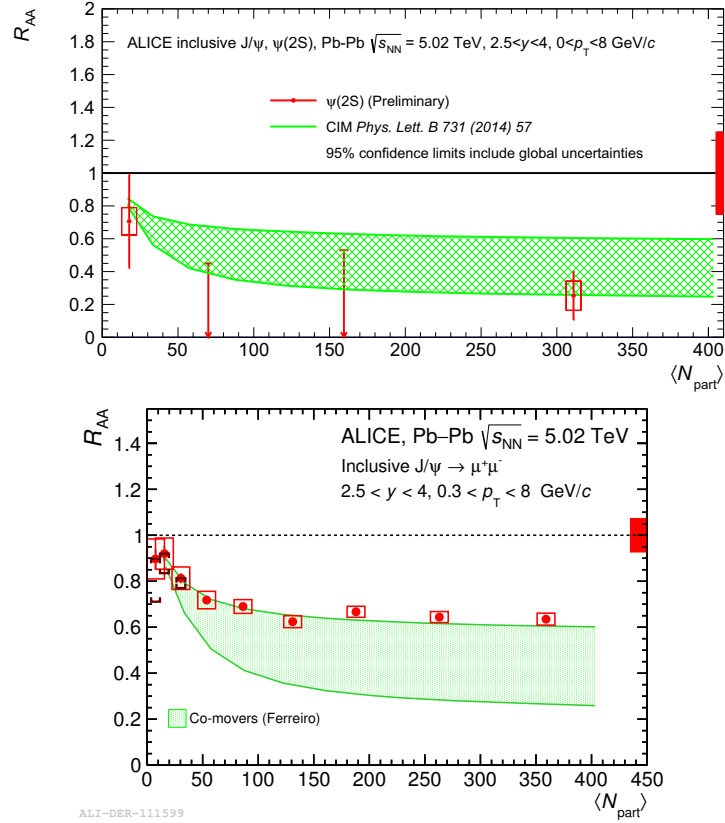


Figure B.2: Nuclear modification factor  $R_{AA}$  versus  $N_{part}$  compared to the CIM for the  $\psi(2S)$  (top) and the  $J/\psi$  (bottom). For the centrality bins where the signal could not be extracted, only the 95% CL is shown. The red box around unity corresponds to the global uncertainty which are included in the confidence limits calculation and therefore do not apply to the CL. Uncertainties in the model correspond to different values of the  $c - \bar{c}$  pairs production cross sections,  $\sigma_{c\bar{c}} = 0.70$  mb for the upper limit and  $\sigma_{c\bar{c}} = 0.45$  mb for the lower limit.

### B.3 Transport Model

In Figure B.3, the predictions for the  $\psi(2S)$  and  $J/\psi$  with the TM are presented. For the  $J/\psi$ , a cut  $p_T > 0.3$  GeV/ $c$  is performed to suppress the photo-produced  $J/\psi$ .

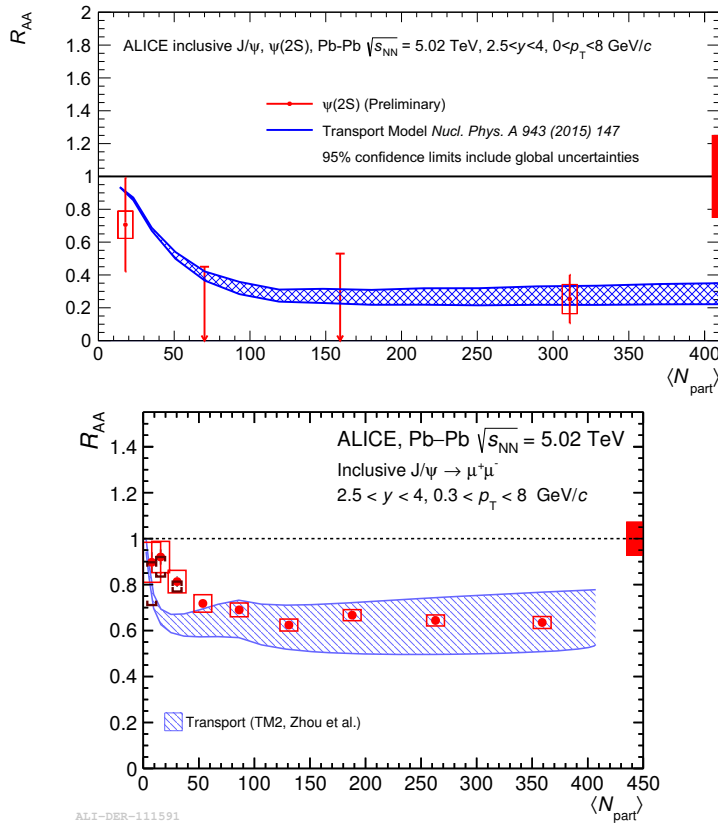


Figure B.3: Nuclear modification factor  $R_{AA}$  versus  $N_{part}$  compared to the TM for the  $\psi(2S)$  (left) and the  $J/\psi$  (right). For the centrality bins where the signal could not be extracted, only the 95% CL is shown. The red box around unity corresponds to the global uncertainty which are included in the confidence limits calculation and therefore do not apply to the CL. Uncertainties in the model correspond to different importances in the shadowing.



# List of Figures

1.1	Table of the different elementary particles of the Standard Model . . . . .	6
1.2	Feynman Diagram of the QCD vacuum polarization . . . . .	9
1.3	Summary of the measurements of $\alpha_s$ as function of the energy scale $Q$ . . . . .	10
1.4	Sketch of the QCD phase diagram as a function of temperature and the Baryon Chemical Potential . . . . .	12
1.5	Representation of a nucleus-nucleus collision using URQMD. . . . .	13
1.6	Illustration of the space-time evolution of the QGP as generated in a heavy ion collision at LHC energies . . . . .	15
1.7	Spectroscopic diagram of the Charmonium family . . . . .	20
1.8	Heavy Quark pair production Feynman diagrams at leading order . . . . .	21
1.9	Feynman diagram of the $J/\psi$ photo-production. . . . .	25
1.10	Parton distribution functions for the gluons and quarks . . . . .	26
1.11	The different regions of $R_i^A(x, Q^2)$ for a gluon . . . . .	27
1.12	$J/\psi$ nuclear absorption dependence with energy . . . . .	29
1.13	Illustration of the sequential suppression of different charmonium states by the color screening . . . . .	31
1.14	Compilation of medium dissociation temperatures relative to the critical temperature $T_c$ for different quarkonium states . . . . .	32
1.15	Illustration of the regeneration phenomenon . . . . .	33
1.16	Measurement of $J/\psi$ normalized to only Drell-Yann production and CNM performed by NA60 and NA50 in In – In and Pb – Pb collisions, respectively . . . . .	39

1.17	Left panel: Measured $J/\psi$ nuclear modification factors $R_{AA}$ vs $N_{\text{part}}$ . The lower panel shows the ratio of forward rapidity (circles, red) to mid-rapidity (squares, blue) for the points in the upper panel. Right panel: $R_{AA}$ corrected by the CNM effects as a function of the charged particle multiplicity for NA50, NA60 and PHENIX . . . . .	40
1.18	$J/\psi$ nuclear modification factor in the centrality range 0-100% as a function of rapidity in d – Au collisions measured by PHENIX . . . . .	41
1.19	$J/\psi$ production cross-section in pp collisions at $\sqrt{s}=2.76, 5, 7, 8,$ and $13$ TeV (left) and $\psi(2S)$ production cross-section in pp collisions at $\sqrt{s}=7, 8,$ and $13$ TeV (right) as a function of $p_T$ . . . . .	42
1.20	$J/\psi$ and $\psi(2S)$ production cross-sections in pp collisions at $\sqrt{s} = 13$ TeV compared to NLO NRQCD summed with FONLL calculations and LO NRQCD summed with FONLL calculation . . . . .	42
1.21	$\lambda_\theta$ and $\lambda_\phi$ parameters of the inclusive $J/\psi$ polarization as a function of $p_T$ , measured in the Helicity and Collins-Soper reference frames . . . . .	43
1.22	$J/\psi$ and $\psi(2S)$ $R_{pA}$ at $\sqrt{s_{NN}} = 5.02$ TeV as a function of $N_{\text{coll}}$ at forward and backward rapidities compared to models . . . . .	45
1.23	$J/\psi$ $R_{pA}$ at $\sqrt{s_{NN}} = 8.16$ TeV as a function of $y$ compared to models and with results at $\sqrt{s_{NN}} = 5.02$ TeV . . . . .	46
1.24	$J/\psi$ elliptic flow in the centrality range 20-40% as a function of rapidity at $\sqrt{s_{NN}} = 2.76$ TeV and $\sqrt{s_{NN}} = 5.02$ TeV . . . . .	47
1.25	Top: Inclusive $J/\psi$ $R_{AA}$ as of function of $N_{\text{part}}$ measured in Pb – Pb collisions at $\sqrt{s_{NN}} = 2.76$ TeV and $\sqrt{s_{NN}} = 5.02$ TeV compared to PHENIX measurement in Au – Au collisions at $\sqrt{s_{NN}} = 0.2$ TeV. Bottom: Inclusive $J/\psi$ $R_{AA}$ as of function of $N_{\text{part}}$ with a cut $p_T > 0.3$ GeV measured in Pb – Pb collisions at $\sqrt{s_{NN}} = 5.02$ TeV compared to models . . . . .	48
1.26	Inclusive $J/\psi$ $R_{AA}$ at $\sqrt{s_{NN}} = 5.02$ TeV as of function of $p_T$ measured in three different centrality bins, compared to Transport Model Calculations . . . . .	49

1.27	Inclusive $\psi(2S)$ -to- $J/\psi$ ratio measured as a function of centrality in Pb – Pb collisions at $\sqrt{s_{NN}} = 2.76$ TeV for two $p_T$ intervals, compared to NA50 results and to a theoretical calculation (left). Double ratio as a function of centrality, between the $\psi(2S)$ and $J/\psi$ measured in Pb – Pb collisions at $\sqrt{s_{NN}} = 2.76$ TeV and pp collisions at $\sqrt{s} = 7$ TeV, compared to theoretical calculations (right) . . . . .	50
2.1	Schematic of the CERN accelerator complex (left) and angular coverage of the different detectors for the four main LHC experiments (right) . . . . .	54
2.2	Schematic of the ALICE detector. . . . .	57
2.3	3D view of the TPC . . . . .	59
2.4	Transverse view of EMCAL (above mid-plane) and DCal (below mid-plane) . . . . .	62
2.5	Front view of V0A (left) and V0C (right) arrays . . . . .	64
2.6	Muon Spectrometer longitudinal section . . . . .	66
2.7	Layout of the front absorber . . . . .	67
2.8	Schematic of the CPC . . . . .	68
2.9	Pictures of the station 2 with a quadrant design (left) and of the stations 4 and 5 with a slat design (right) of the Tracking system . . . . .	68
2.10	Structure of the Trigger Detector (left) and schematic view of the RPC (right) . . . . .	69
2.11	Principle of the Muon Trigger represented in the bending plane (X,Z) . . . . .	70
3.1	Centrality estimation based on a NBD-Glauber fit (red line) fit to the distribution of the V0 amplitudes . . . . .	79
3.2	Dimuon invariant mass distributions in the centrality range 0-90% (left) and in the centrality range 70-90% (right) . . . . .	84
3.3	Direct Fit to the dimuon invariant mass distributions in the centrality range 0-20% (top) and 60-90% (bottom) . . . . .	88
3.4	Illustration of the principle of the event mixing. . . . .	89
3.5	Normalization factor $R$ as a function of the invariant mass obtained from events in the 0-10% centrality range. . . . .	90
3.6	Comparison between the event mixing distribution and the data as a function of invariant mass (left), $p_T$ (middle) and rapidity (right), for the $\mu^+\mu^-$ distribution (top), $\mu^+\mu^+$ distribution (middle) and $\mu^-\mu^-$ distribution (bottom) . . . . .	92

3.7	Fit to the dimuon invariant mass distribution after event mixing subtraction in the centrality range 0-20% (top) and 60-90% (bottom) . . . . .	93
3.8	Different signal extraction tests, for the rapidity and $p_T$ -integrated invariant mass distributions, in the centrality range 0-90%. . . . .	95
3.9	Distribution of the $\psi(2S)/J/\psi$ ratio as a function of the different signal extraction tests, for the rapidity and $p_T$ -integrated invariant mass distributions, in the centrality range 0-90%. . . . .	96
3.10	Simulated acceptance $\times$ efficiency corrected $J/\psi$ $p_T$ distributions in seven centrality bins. . . . .	100
3.11	Top panel: $p_T$ -integrated acceptance $\times$ efficiency of the $\psi(2S)$ (blue) compared to the one of the $J/\psi$ (red) versus centrality. Bottom panel: acceptance $\times$ efficiency of the $\psi(2S)$ (blue) compared to the one of the $J/\psi$ (red) in the centrality range 0-90% versus $p_T$ . . . . .	101
3.12	Evolution of $F_{norm}(CINT7)$ for the three methods versus run numbers . . . . .	106
3.13	Example of fit to the $p_T$ - and $y$ -integrated dimuon invariant mass distribution . . . . .	109
3.14	Different signal extraction tests, for the rapidity and $p_T$ -integrated invariant mass distribution. . . . .	110
3.15	$p_T$ - and $y$ -integrated $\psi(2S)$ acceptance $\times$ efficiency as a function of run number (left) and acceptance $\times$ efficiency as a function of $p_T$ (right) using $p_T$ and $y$ input distributions from the $J/\psi$ measurement at $\sqrt{s} = 5$ TeV. . . . .	111
3.16	$p_T$ - and $y$ -integrated inclusive $\psi(2S)$ cross section (left) and $\psi(2S)$ -to- $J/\psi$ cross section ratio (right) as a function of $\sqrt{s}$ in pp collisions. . . . .	112
3.17	Example of log-likelihood distributions . . . . .	118
3.18	Example search for the signal value such as $CL_s \leq 0.05$ . . . . .	119
3.19	Confidence Levels calculated on the $\psi(2S)$ signal as a function of centrality, compared to the values extracted from fits to the invariant mass distribution . . . . .	122
3.20	Nuclear modification factor of the $\psi(2S)$ compared to the one of the $J/\psi$ as a function of $N_{part}$ . . . . .	124
3.21	Single $\psi(2S)$ -to- $J/\psi$ ratio as a function of $N_{part}$ . . . . .	127
3.22	$\psi(2S)$ -to- $J/\psi$ ratio as a function of $N_{part}$ compared to the values at $\sqrt{s} = 2.76$ TeV . . . . .	129
3.23	Double-ratio $R_{AA}^{\psi(2S)}/R_{AA}^{J/\psi}$ as a function of $N_{part}$ for $0 < p_T < 8$ GeV/ $c$ . . . . .	130

3.24	Double-ratio $R_{AA}^{\psi(2S)}/R_{AA}^{J/\psi}$ as a function of $N_{\text{part}}$ compared to the values at $\sqrt{s_{\text{NN}}} = 2.76$ TeV . . . . .	132
3.25	Double-ratio $R_{AA}^{\psi(2S)}/R_{AA}^{J/\psi}$ as a function of $N_{\text{part}}$ compared to the values of CMS . . . . .	133
3.26	Nuclear modification factor $R_{AA}$ versus $N_{\text{part}}$ compared to the CIM . . . . .	135
3.27	Nuclear modification factor $R_{AA}$ as a function of $N_{\text{part}}$ compared to the Transport Model . . . . .	136
3.28	Double Ratio $R_{AA}^{\psi(2S)}/R_{AA}^{J/\psi}$ as a function of $N_{\text{part}}$ compared to the Transport Model . . . . .	137
3.29	$\psi(2S)$ -to- $J/\psi$ ratio versus $N_{\text{part}}$ compared to the Statistical Hadronization Model . . . . .	138
4.1	Expected absolute statistical uncertainty of the $J/\psi$ elliptic flow as a function of the transverse momentum measured with the new Muon Spectrometer (with the MFT), estimated for integrated luminosities $L_{\text{int}} = 1 \text{ nb}^{-1}$ and $L_{\text{int}} = 10 \text{ nb}^{-1}$ in Pb – Pb collisions at $\sqrt{s_{\text{NN}}} = 5.5$ TeV . . . . .	144
4.2	Absolute statistical uncertainty on the $J/\psi$ polarization parameters $\lambda_{\theta}$ (left panel) and $\lambda_{\phi}$ (right panel) as a function of collision centrality measured with the Muon Spectrometer, estimated for integrated luminosities $L_{\text{int}} = 1 \text{ nb}^{-1}$ and $L_{\text{int}} = 10 \text{ nb}^{-1}$ in Pb – Pb collisions at $\sqrt{s_{\text{NN}}} = 5.5$ TeV . . .	145
4.3	Estimated relative statistical uncertainty on the $\psi(2S)$ measurement in the Muon Spectrometer as a function of collision centrality using statistical model predictions for integrated luminosities $L_{\text{int}} = 1 \text{ nb}^{-1}$ and $L_{\text{int}} = 10 \text{ nb}^{-1}$ in Pb – Pb collisions at $\sqrt{s_{\text{NN}}} = 5.5$ TeV . . . . .	146
4.4	Layout of the new ITS detector . . . . .	147
4.5	Layout of the MFT in ALICE (left) and layout of the active area of the MFT (right), showing the positioning of the half-disks and MFT ladders . . . . .	148
4.6	Conceptual drawing of the trigger detectors on the C-side (forward direction) as they are now (left) and after the upgrade (right) . . . . .	149
4.7	Schematic of the MTR readout electronics architecture. . . . .	151
4.8	Schematic of the MID readout electronics architecture . . . . .	152
4.9	Block diagram of the FEERIC . . . . .	153
4.10	Minimum Bias trigger rate in Pb – Pb collisions at $\sqrt{s_{\text{NN}}} = 5.02$ TeV as a function of the run number. . . . .	157

4.11	Data flow per local board for the Pb – Pb run 246036 (top). 2D-view of the data flow per local board (bottom). . . . .	159
4.12	Maximum data flow as a function of the trigger rate for all the Pb – Pb runs. The values are extrapolated to a 100 kHz rate with a linear function (right panel). . . . .	160
4.13	Data Flow to the CRU as a function of the trigger rate for all the Pb – Pb runs. The values are extrapolated to a 100 kHz rate with a linear function (right panel). . . . .	161
4.14	Value of the Minimum Bias trigger rate in pp collisions at $\sqrt{s} = 13$ TeV as a function of the run number. . . . .	162
4.15	Maximum data flow as a function of the trigger rate for all the pp runs. The values are fitted with a linear function to evaluate the value at 200kHz. . . . .	163
4.16	Data Flow to the CRU as a function of the trigger rate for all the pp runs. The values are fitted with a linear function to evaluate the value at 200kHz. . . . .	164
4.17	Data Flow to the CRU as a function of the trigger rate for the Pb – Pb data at $\sqrt{s_{NN}} = 5.02$ TeV and pp data at $\sqrt{s} = 13$ TeV.	165
B.1	Nuclear modification factor $R_{AA}$ versus $N_{part}$ compared to the Transport Model and the Comover Interaction Model . .	174
B.2	Nuclear modification factor $R_{AA}$ versus $N_{part}$ compared to the CIM for the $\psi(2S)$ (top) and the $J/\psi$ (bottom) . . . . .	176
B.3	Nuclear modification factor $R_{AA}$ versus $N_{part}$ compared to the TM for the $\psi(2S)$ (left) and the $J/\psi$ (right) . . . . .	177

# List of Tables

1.1	Charmonium states and binding energies. . . . .	21
2.1	Summary of the collisions performed at the LHC. . . . .	53
3.1	Centrality classes considered in this analysis and corresponding values of $N_{\text{part}}$ , $N_{\text{coll}}$ , $b$ and $T_{AA}$ . . . . .	80
3.2	$\psi(2S)$ counts in four centrality bins and for three $p_T$ intervals	97
3.3	Average value of $F_{\text{norm}}$ obtained with three different approaches.	107
3.4	Summary of the sources of systematic uncertainties. . . . .	113
3.5	Average $\psi(2S)$ yield with statistical and systematic uncertainties in each centrality bin, integrated in $p_T$ and rapidity. .	123
3.6	Nuclear modification factor of the $\psi(2S)$ in the different centrality bins in the ranges $0 < p_T < 8 \text{ GeV}/c$ and $2.5 < y < 4.0$ . . . . .	125
3.7	$\psi(2S)$ -to- $J/\psi$ ratio in the different centrality bins for the $p_T$ ranges $0 < p_T < 3 \text{ GeV}/c$ , $3 < p_T < 8 \text{ GeV}/c$ and $0 < p_T < 8 \text{ GeV}/c$ . . . . .	128
3.8	Double-ratio $R_{AA}^{\psi(2S)}/R_{AA}^{J/\psi}$ in the different centrality bins for the $p_T$ ranges $0 < p_T < 3 \text{ GeV}/c$ , $3 < p_T < 8 \text{ GeV}/c$ and $0 < p_T < 8 \text{ GeV}/c$ . . . . .	131
4.1	Summary of the number of MID cards and links . . . . .	153
4.2	Event Format for the Local Boards (top) and Regional Boards (bottom). . . . .	156
4.3	Summary of the estimated data flows in Pb – Pb at an interaction rate of 100 kHz and in pp collisions at an interaction rate of 200 kHz. . . . .	164

A.1	Average $J/\psi$ yield with statistical and systematic uncertainties in each centrality bin in the $p_T$ range 0-8 GeV/ $c$ and rapidity range $2.5 < y < 4.0$ , compared to confidence limits calculated with the CLs method. . . . .	171
-----	--	-----

# Bibliography

- [1] Edward V. Shuryak. **Quantum chromodynamics and the theory of superdense matter.** *Physics Reports*, 61(2):71 – 158, 1980. (Cited on pages 4 and 11.)
- [2] Dominik J. Schwarz. **The first second of the universe.** *Annalen Phys.*, 12:220–270, 2003. (Cited on page 4.)
- [3] P. Rosnet. **Quark-Gluon Plasma: from accelerator experiments to early Universe.** In *11th Rencontres du Vietnam: Cosmology: 50 years after CMB discovery Quy Nhon, Vietnam, August 16-22, 2015*, 2015. (Cited on page 4.)
- [4] **New State of Matter created at CERN. Un nouvel état de la matière.** (PRESSCUT-2000-210. CERN-PR-2000-01-EN. CERN-PR-2000-01-FR):mult. p, 2000. Issued on 10 Feb 2000. (Cited on page 4.)
- [5] T. Roser. **RHIC performance.** *Nuclear Physics A*, 698(1):23 – 28, 2002. 15th Int. Conf. on Ultra-Relativistic Nucleus-Nucleus Collisions (Quark Matter 2001). (Cited on page 4.)
- [6] Lyndon Evans and Philip Bryant. **LHC Machine.** *JINST*, 3:S08001, 2008. (Cited on pages 4 and 52.)
- [7] J. J. Thomson M.A. F.R.S. **XL. Cathode Rays.** *Philosophical Magazine*, 44(269):293–316, 1897. (Cited on page 4.)
- [8] Professor E. Rutherford F.R.S. **LXXIX. The scattering of  $\alpha$  and  $\beta$  particles by matter and the structure of the atom.** *Philosophical Magazine*, 21(125):669–688, 1911. (Cited on page 4.)
- [9] Professor Sir E. Rutherford F.R.S. **LIV. Collision of  $\alpha$  particles with light atoms. IV. An anomalous effect in nitrogen.** *Philosophical Magazine*, 37(222):581–587, 1919. (Cited on page 4.)

- [10] J. Chadwick. **Possible Existence of a Neutron.** *Nature*, 129:312, February 1932. (Cited on page 4.)
- [11] Seth H. Neddermeyer and Carl D. Anderson. **Note on the Nature of Cosmic-Ray Particles.** *Phys. Rev.*, 51:884–886, May 1937. (Cited on page 4.)
- [12] M. Conversi, E. Pancini, and O. Piccioni. **On the Disintegration of Negative Mesons.** *Phys. Rev.*, 71:209–210, Feb 1947. (Cited on page 4.)
- [13] G. D. Rochester and C. C. Butler. **Evidence for the Existence of New Unstable Elementary Particles.** *Nature*, 160:855–857, December 1947. (Cited on page 4.)
- [14] M. Gell-Mann. *The Eightfold Way: a theory of strong interaction symmetry.* Mar 1961. (Cited on page 5.)
- [15] V. Barnes and others. **Observation of a Hyperon with Strangeness Minus Three.** *Phys. Rev. Lett.*, 12:204–206, Feb 1964. (Cited on page 5.)
- [16] M. Gell-Mann. **A schematic model of baryons and mesons.** *Physics Letters*, 8(3):214 – 215, 1964. (Cited on page 5.)
- [17] G Zweig. **An  $SU_3$  model for strong interaction symmetry and its breaking; Version 1.** Technical Report CERN-TH-401, CERN, Geneva, Jan 1964. (Cited on page 5.)
- [18] G. Arnison and others. **Experimental observation of isolated large transverse energy electrons with associated missing energy at  $\sqrt{s} = 540\text{GeV}$ .** *Phys. Lett. B*, 122(CERN-EP-83-13):103–116. 31 p, Jan 1983. (Cited on page 5.)
- [19] G. Arnison and others. **Experimental observation of lepton pairs of invariant mass around 95 GeV/c<sup>2</sup> at the CERN SPS collider.** *Physics Letters B*, 126(5):398 – 410, 1983. (Cited on page 5.)
- [20] Ariel Goobar, Steen Hannestad, Edvard Mörtsell, and Huitzu Tu. **The neutrino mass bound from WMAP 3 year data, the baryon acoustic peak, the SNLS supernovae and the Lyman- $\alpha$  forest.** *Journal of Cosmology and Astroparticle Physics*, 2006(06):019, 2006. (Cited on page 5.)

- [21] Richard A. Battye and Adam Moss. **Evidence for Massive Neutrinos from Cosmic Microwave Background and Lensing Observations.** *Phys. Rev. Lett.*, 112(5):051303, 2014. (Cited on page 5.)
- [22] F. Zwicky. **On the Masses of Nebulae and of Clusters of Nebulae.** *AstroPhysical Journal*, 86:217, October 1937. (Cited on page 5.)
- [23] P. J. E. Peebles and Bharat Ratra. **The Cosmological constant and dark energy.** *Rev. Mod. Phys.*, 75:559–606, 2003. (Cited on page 5.)
- [24] P. W. Higgs. **Broken Symmetries and the Masses of Gauge Bosons.** *Physical Review Letters*, 13:508–509, October 1964. (Cited on page 5.)
- [25] F. Englert and R. Brout. **Broken Symmetry and the Mass of Gauge Vector Mesons.** *Physical Review Letters*, 13:321–323, August 1964. (Cited on page 5.)
- [26] Georges Aad et al. **Observation of a new particle in the search for the Standard Model Higgs boson with the ATLAS detector at the LHC.** *Phys. Lett.*, B716:1–29, 2012. (Cited on page 5.)
- [27] Serguei Chatrchyan et al. **Observation of a new boson at a mass of 125 GeV with the CMS experiment at the LHC.** *Phys. Lett.*, B716:30–61, 2012. (Cited on page 5.)
- [28] Steven Weinberg. **Conceptual foundations of the unified theory of weak and electromagnetic interactions.** *Rev. Mod. Phys.*, 52:515–523, Jul 1980. (Cited on page 6.)
- [29] Roel Aaij et al. **Observation of  $J/\psi p$  Resonances Consistent with Pentaquark States in  $\Lambda_b^0 \rightarrow J/\psi K^- p$  Decays.** *Phys. Rev. Lett.*, 115:072001, 2015. (Cited on page 7.)
- [30] David J. Gross and Frank Wilczek. **Asymptotically Free Gauge Theories. I.** *Phys. Rev. D*, 8:3633–3652, Nov 1973. (Cited on page 7.)
- [31] David J. Gross and Frank Wilczek. **Asymptotically free gauge theories. II.** *Phys. Rev. D*, 9:980–993, Feb 1974. (Cited on page 7.)
- [32] David J. Gross and Frank Wilczek. **Ultraviolet Behavior of Non-Abelian Gauge Theories.** *Phys. Rev. Lett.*, 30:1343–1346, Jun 1973. (Cited on pages 8 and 9.)

- [33] H. David Politzer. **Reliable Perturbative Results for Strong Interactions?** *Phys. Rev. Lett.*, 30:1346–1349, Jun 1973. (Cited on pages 8 and 9.)
- [34] C. Patrignani et al. **Review of Particle Physics.** *Chin. Phys.*, C40(10):100001, 2016. (Cited on pages 10, 76, 86, 107, and 115.)
- [35] W. Weise. **Nuclear aspects of chiral symmetry.** *Nuclear Physics A*, 553:59 – 72, 1993. (Cited on page 10.)
- [36] Jeffrey Goldstone, Abdus Salam, and Steven Weinberg. **Broken Symmetries.** *Phys. Rev.*, 127:965–970, Aug 1962. (Cited on page 10.)
- [37] Berndt Müller. **Hadronic signals of deconfinement at RHIC.** *Nuclear Physics A*, 750(1):84 – 97, 2005. Quark-Gluon Plasma. New Discoveries at RHIC: Case for the Strongly Interacting Quark-Gluon Plasma. Contributions from the RBRC Workshop held May 14-15, 2004. (Cited on pages 10 and 11.)
- [38] N. Cabibbo and G. Parisi. **Exponential hadronic spectrum and quark liberation.** *Physics Letters B*, 59(1):67 – 69, 1975. (Cited on page 11.)
- [39] J. C. Collins and M. J. Perry. **Superdense Matter: Neutrons or Asymptotically Free Quarks?** *Phys. Rev. Lett.*, 34:1353–1356, May 1975. (Cited on page 11.)
- [40] Uwe-Jens Wiese. **An introduction to lattice field theory.** 2009. (Cited on page 11.)
- [41] A. Chodos, R. L. Jaffe, K. Johnson, C. B. Thorn, and V. F. Weisskopf. **New extended model of hadrons.** *Phys. Rev. D*, 9:3471–3495, Jun 1974. (Cited on page 11.)
- [42] Y. Nambu and G. Jona-Lasinio. **Dynamical Model of Elementary Particles Based on an Analogy with Superconductivity. I.** *Phys. Rev.*, 122:345–358, Apr 1961. (Cited on page 11.)
- [43] Y. Nambu and G. Jona-Lasinio. **Dynamical Model of Elementary Particles Based on an Analogy with Superconductivity. II.** *Phys. Rev.*, 124:246–254, Oct 1961. (Cited on page 11.)
- [44] A. Bazavov et al. **Equation of state in ( 2+1 )-flavor QCD.** *Phys. Rev.*, D90:094503, 2014. (Cited on page 11.)

- [45] Y. Aoki, Szabolcs Borsanyi, Stephan Durr, Zoltan Fodor, Sandor D. Katz, Stefan Krieg, and Kalman K. Szabo. **The QCD transition temperature: results with physical masses in the continuum limit II.** *JHEP*, 06:088, 2009. (Cited on page 11.)
- [46] C. R. Allton, M. Doring, S. Ejiri, S. J. Hands, O. Kaczmarek, F. Karsch, E. Laermann, and K. Redlich. **Thermodynamics of two flavor QCD to sixth order in quark chemical potential.** *Phys. Rev.*, D71:054508, 2005. (Cited on page 11.)
- [47] A. Bazavov et al. **The chiral and deconfinement aspects of the QCD transition.** *Phys. Rev.*, D85:054503, 2012. (Cited on page 11.)
- [48] Z. Fodor and S. D. Katz. **Critical point of QCD at finite T and mu, lattice results for physical quark masses.** *JHEP*, 04:050, 2004. (Cited on page 11.)
- [49] R. V. Gavai and Sourendu Gupta. **QCD at finite chemical potential with six time slices.** *Phys. Rev.*, D78:114503, 2008. (Cited on page 11.)
- [50] Helmut Satz. **The Thermodynamics of Quarks and Gluons.** *Lect. Notes Phys.*, 785:1–21, 2010. (Cited on page 11.)
- [51] Mark G. Alford, Andreas Schmitt, Krishna Rajagopal, and Thomas Schafer. **Color superconductivity in dense quark matter.** *Rev. Mod. Phys.*, 80:1455–1515, 2008. (Cited on page 12.)
- [52] Simon Hands. **The phase diagram of QCD.** *Contemporary Physics*, 42(4):209–225, 2001. (Cited on page 12.)
- [53] Ulrich Heinz et al. **Exploring the properties of the phases of QCD matter - research opportunities and priorities for the next decade.** 2015. (Cited on page 12.)
- [54] F. Karsch. **Lattice QCD at high temperature and density.** *Lect. Notes Phys.*, 583:209–249, 2002. (Cited on page 13.)
- [55] S. A. Bass et al. **Microscopic models for ultrarelativistic heavy ion collisions.** *Prog. Part. Nucl. Phys.*, 41:255–369, 1998. [Prog. Part. Nucl. Phys.41,225(1998)]. (Cited on page 13.)
- [56] M. Bleicher et al. **Relativistic hadron hadron collisions in the ultrarelativistic quantum molecular dynamics model.** *J. Phys.*, G25:1859–1896, 1999. (Cited on page 13.)

- [57] J. D. Bjorken. **Highly relativistic nucleus-nucleus collisions: The central rapidity region.** *Phys. Rev. D*, 27:140–151, Jan 1983. (Cited on page 14.)
- [58] Wong, C.-Y. **Lectures on the Near-Side Ridge, Landau Hydrodynamics, and Heavy Quarkonia in High Energy Heavy-Ion Collisions.** *EPJ Web of Conferences*, 7:01006, 2010. (Cited on page 14.)
- [59] B. B. Back et al. **Energy dependence of directed flow over a wide range of pseudorapidity in Au + Au collisions at RHIC.** *Phys. Rev. Lett.*, 97:012301, 2006. (Cited on page 14.)
- [60] Michael Strickland. **Anisotropic Hydrodynamics: Three lectures.** *Acta Phys. Polon.*, B45(12):2355–2394, 2014. (Cited on page 15.)
- [61] S. A. Bass, M. Gyulassy, Horst Stoecker, and W. Greiner. **Signatures of quark gluon plasma formation in high-energy heavy ion collisions: A Critical review.** *J. Phys.*, G25:R1–R57, 1999. (Cited on page 17.)
- [62] Johann Rafelski and Berndt Müller. **Strangeness Production in the Quark-Gluon Plasma.** *Phys. Rev. Lett.*, 48:1066–1069, Apr 1982. (Cited on page 17.)
- [63] P Koch, B Müller, and J Rafelski. **Strangeness in relativistic heavy ion collisions.** *Physics Reports*, 142(4):167 – 262, 1986. (Cited on page 17.)
- [64] Jean-Yves Ollitrault. **Anisotropy as a signature of transverse collective flow.** *Phys. Rev. D*, 46:229–245, Jul 1992. (Cited on page 18.)
- [65] S. Voloshin and Y. Zhang. **Flow study in relativistic nuclear collisions by Fourier expansion of azimuthal particle distributions.** *Zeitschrift für Physik C Particles and Fields*, 70(4):665–671, 1996. (Cited on page 18.)
- [66] Jaroslav Adam et al. **Direct photon production in Pb-Pb collisions at  $\sqrt{s_{NN}} = 2.76$  TeV.** *Phys. Lett.*, B754:235–248, 2016. (Cited on page 18.)

- [67] K. Aamodt et al. **Suppression of Charged Particle Production at Large Transverse Momentum in Central Pb-Pb Collisions at  $\sqrt{s_{NN}} = 2.76$  TeV.** *Phys. Lett.*, B696:30–39, 2011. (Cited on page 19.)
- [68] François Arleo, Rodion Kolevatov, Stéphane Peigné, and Maryam Rustamova. **Centrality and  $p_T$  dependence of  $J/\psi$  suppression in proton-nucleus collisions from parton energy loss.** *Journal of High Energy Physics*, 2013(5):155, 2013. (Cited on page 19.)
- [69] J. Aubert et al. **Experimental Observation of a Heavy Particle  $J$ .** *Phys. Rev. Lett.*, 33:1404–1406, Dec 1974. (Cited on page 19.)
- [70] J-E. Augustin and others. **Discovery of a Narrow Resonance in  $e^+e^-$  Annihilation.** *Phys. Rev. Lett.*, 33:1406–1408, Dec 1974. (Cited on page 19.)
- [71] L. Antoniazzi and others. **Production of  $J/\psi$  via  $\psi'$  and  $\chi$  decay in 300 GeV/c proton- and  $\pi^\pm$ -nucleon interactions.** *Phys. Rev. Lett.*, 70:383–386, Jan 1993. (Cited on page 19.)
- [72] L. Antoniazzi and others. **Measurement of  $J/\psi$  and  $\psi'$  production in 300-GeV/c proton, antiproton, and  $\pi^\pm$  interactions with nuclei.** *Phys. Rev. D*, 46:4828–4835, Dec 1992. (Cited on page 19.)
- [73] I. Abt and others.  **$J/\psi$  production via  $\chi c$  decays in 920 GeV pA interactions.** *Physics Letters B*, 561(1-2):61 – 72, 2003. (Cited on page 19.)
- [74] I. Abt and others. **A Measurement of the  $\psi$  to  $J/\psi$  production ratio in 920 GeV proton-nucleus interactions.** *The European Physical Journal C*, 49(2):545–558, Jan 2007. (Cited on page 19.)
- [75] R. Aaij et al. **Measurement of  $J/\psi$  production in pp collisions at  $\sqrt{s} = 7$  TeV.** *Eur. Phys. J.*, C71:1645, 2011. (Cited on page 20.)
- [76] R Aaij et al. **Measurement of  $J/\psi$  production in pp collisions at  $\sqrt{s} = 2.76$  TeV.** *JHEP*, 02:041, 2013. (Cited on page 20.)
- [77] R Aaij et al. **Measurement of  $\psi(2S)$  meson production in pp collisions at  $\sqrt{s}=7$  TeV.** *Eur. Phys. J.*, C72:2100, 2012. (Cited on pages 20 and 125.)

- [78] Kai Zhu. **Charmonium and Light Meson Spectroscopy**. In *Proceedings, 32nd International Symposium on Physics in Collision (PIC 2012): Strbske Pleso, Slovakia, September 12-15, 2012*, pages 229–238, 2012. (Cited on page 20.)
- [79] E. Eichten, K. Gottfried, T. Kinoshita, K. D. Lane, and Tung-Mow Yan. **Charmonium: The Model**. *Phys. Rev.*, D17:3090, 1978. [Erratum: *Phys. Rev.* D21,313(1980)]. (Cited on page 20.)
- [80] E. Eichten, K. Gottfried, T. Kinoshita, K. D. Lane, and T. M. Yan. **Charmonium: Comparison with experiment**. *Phys. Rev. D*, 21:203–233, Jan 1980. (Cited on page 20.)
- [81] Helmut Satz. **Colour deconfinement and quarkonium binding**. *J. Phys.*, G32:R25, 2006. (Cited on pages 21, 30, 31, and 33.)
- [82] B.L. Combridge. **Associated production of heavy flavour states in pp and  $\bar{p}p$  interactions: Some QCD estimates**. *Nuclear Physics B*, 151:429 – 456, 1979. (Cited on page 21.)
- [83] N. Brambilla et al. **Heavy quarkonium: progress, puzzles, and opportunities**. *Eur. Phys. J.*, C71:1534, 2011. (Cited on page 22.)
- [84] N. Brambilla et al. **Heavy quarkonium physics**. 2004. (Cited on page 22.)
- [85] A. Andronic et al. **Heavy-flavour and quarkonium production in the LHC era: from proton-proton to heavy-ion collisions**. *Eur. Phys. J.*, C76(3):107, 2016. (Cited on page 22.)
- [86] Edmond L. Berger and D. Jones. **Inelastic photoproduction of  $J/\psi$  and  $\Upsilon$  by gluons**. *Phys. Rev. D*, 23:1521–1530, Apr 1981. (Cited on page 22.)
- [87] R. Baier and R. Rückl. **Hadronic production of  $J/\psi$  and  $\gamma$ : Transverse momentum distributions**. *Physics Letters B*, 102(5):364 – 370, 1981. (Cited on page 22.)
- [88] M. B. Einhorn and S. D. Ellis. **Hadronic production of the new resonances: Probing gluon distributions**. *Phys. Rev. D*, 12:2007–2014, Oct 1975. (Cited on page 22.)
- [89] J. P. Lansberg. **Total  $J/\psi$  and Upsilon production cross section at the LHC: theory vs. experiment**. *PoS*, ICHEP2010:206, 2010. (Cited on page 22.)

- [90] M. Vanttinen, P. Hoyer, S. J. Brodsky, and W.-K. Tang. **Hadroproduction and polarization of charmonium.** *Phys. Rev. D*, 51:3332–3339, Apr 1995. (Cited on page 22.)
- [91] Daniel M. Kaplan. **Charmonium Production in Fermilab E789.** *International Journal of Modern Physics A*, 12(22):3827–3836, 1997. (Cited on page 22.)
- [92] F. Abe and others.  **$J/\psi$  and  $\psi(2S)$  production in  $p\bar{p}$  collisions at  $\sqrt{s} = 1.8$  TeV.** *Phys. Rev. Lett.*, 79:572–577, Jul 1997. (Cited on page 22.)
- [93] John M. Campbell, F. Maltoni, and F. Tramontano. **QCD corrections to  $J/\psi$  and Upsilon production at hadron colliders.** *Phys. Rev. Lett.*, 98:252002, 2007. (Cited on page 22.)
- [94] P. Artoisenet, J. P. Lansberg, and F. Maltoni. **Hadroproduction of  $J/\psi$  and  $v$  in association with a heavy-quark pair.** *Phys. Lett.*, B653:60–66, 2007. (Cited on page 22.)
- [95] Harald Fritzsch. **Producing heavy quark flavors in hadronic collisions - A test of quantum chromodynamics.** *Physics Letters B*, 67(2):217 – 221, 1977. (Cited on page 23.)
- [96] G. Peter Lepage, Lorenzo Magnea, Charles Nakhleh, Ulrika Magnea, and Kent Hornbostel. **Improved nonrelativistic QCD for heavy-quark physics.** *Phys. Rev. D*, 46:4052–4067, Nov 1992. (Cited on page 23.)
- [97] Geoffrey T. Bodwin, Eric Braaten, and G. Peter Lepage. **Rigorous QCD analysis of inclusive annihilation and production of heavy quarkonium.** *Phys. Rev. D*, 51:1125–1171, Feb 1995. (Cited on page 23.)
- [98] Eric Braaten and Sean Fleming. **Color-Octet Fragmentation and the  $\psi'$  Surplus at the Fermilab Tevatron.** *Phys. Rev. Lett.*, 74:3327–3330, Apr 1995. (Cited on page 23.)
- [99] Pietro Faccioli, Carlos Lourenço, João Seixas, and Hermine K. Wöhri. **Towards the experimental clarification of quarkonium polarization.** *The European Physical Journal C*, 69(3):657–673, Oct 2010. (Cited on page 24.)

- [100] J. P. Lansberg. **QCD corrections to  $J/\psi$  polarisation in pp collisions at RHIC.** *Phys. Lett.*, B695:149–156, 2011. (Cited on page 24.)
- [101] B. L. Ioffe and D. E. Kharzeev. **Quarkonium polarization in heavy ion collisions as a possible signature of the quark gluon plasma.** *Phys. Rev.*, C68:061902, 2003. (Cited on page 24.)
- [102] A.J. Baltz, G. Baur, D. d’Enterria, L. Frankfurt, F. Gelis, V. Guzey, K. Hencken, Yu. Kharlov, M. Klasen, S.R. Klein, V. Nikulin, J. Nystrand, I.A. Pshenichnov, S. Sadovsky, E. Scapparone, J. Seger, M. Strikman, M. Tverskoy, R. Vogt, S.N. White, U.A. Wiedemann, P. Yepes, and M. Zhalov. **The physics of ultraperipheral collisions at the LHC.** *Physics Reports*, 458(1):1 – 171, 2008. (Cited on page 24.)
- [103] Gerhard Baur, Kai Hencken, and Dirk Trautmann. **Photon-photon and photon - hadron interactions at relativistic heavy ion colliders.** *Prog. Part. Nucl. Phys.*, 42:357–366, 1999. (Cited on page 24.)
- [104] Betty Abelev et al. **Coherent  $J/\psi$  photoproduction in ultra-peripheral Pb-Pb collisions at  $\sqrt{s_{NN}} = 2.76$  TeV.** *Phys. Lett.*, B718:1273–1283, 2013. (Cited on page 25.)
- [105] Jaroslav Adam et al. **Coherent  $\psi(2S)$  photo-production in ultra-peripheral Pb Pb collisions at  $\sqrt{s_{NN}} = 2.76$  TeV.** *Phys. Lett.*, B751:358–370, 2015. (Cited on page 25.)
- [106] Jaroslav Adam et al. **Measurement of an excess in the yield of  $J/\psi$  at very low  $p_T$  in Pb-Pb collisions at  $\sqrt{s_{NN}} = 2.76$  TeV.** *Phys. Rev. Lett.*, 116(22):222301, 2016. (Cited on pages 25, 143, and 175.)
- [107] F. D. Aaron et al. **Inclusive Deep Inelastic Scattering at High  $Q^2$  with Longitudinally Polarised Lepton Beams at HERA.** *JHEP*, 09:061, 2012. (Cited on page 26.)
- [108] J.J. Aubert and others. **The ratio of the nucleon structure functions  $F_2N$  for iron and deuterium.** *Physics Letters B*, 123(3):275 – 278, 1983. (Cited on page 26.)
- [109] K. J. Eskola, V. J. Kolhinen, and C. A. Salgado. **The Scale dependent nuclear effects in parton distributions for practical applications.** *Eur. Phys. J.*, C9:61–68, 1999. (Cited on page 27.)

- [110] Kari J. Eskola, Vesa J. Kolhinen, Hannu Paukkunen, and Carlos A. Salgado. **A Global reanalysis of nuclear parton distribution functions.** *JHEP*, 05:002, 2007. (Cited on page 27.)
- [111] D. de Florian and R. Sassot. **Nuclear parton distributions at next-to-leading order.** *Phys. Rev.*, D69:074028, 2004. (Cited on page 27.)
- [112] M. Hirai, S. Kumano, and T. H. Nagai. **Determination of nuclear parton distribution functions and their uncertainties in next-to-leading order.** *Phys. Rev.*, C76:065207, 2007. (Cited on page 27.)
- [113] K. J. Eskola, H. Paukkunen, and C. A. Salgado. **EPS09: A New Generation of NLO and LO Nuclear Parton Distribution Functions.** *JHEP*, 04:065, 2009. (Cited on pages 27, 41, 134, and 135.)
- [114] Stefano Forte and Graeme Watt. **Progress in the Determination of the Partonic Structure of the Proton.** *Ann. Rev. Nucl. Part. Sci.*, 63:291–328, 2013. (Cited on page 27.)
- [115] R. Vogt. **Cold nuclear matter effects on  $J/\psi$  and  $\Upsilon$  production at energies available at the CERN Large Hadron Collider (LHC).** *Phys. Rev. C*, 81:044903, Apr 2010. (Cited on page 27.)
- [116] Edmond Iancu and Raju Venugopalan. **The Color glass condensate and high-energy scattering in QCD.** In *In \*Hwa, R.C. (ed.) et al.: Quark gluon plasma\* 249-3363*. 2003. (Cited on page 28.)
- [117] Heribert Weigert. **Evolution at small  $x_{bj}$ : The color glass condensate.** *Progress in Particle and Nuclear Physics*, 55(2):461 – 565, 2005. (Cited on page 28.)
- [118] C. Gerschel and J. Hüfner. **A contribution to the suppression of the  $J/\psi$  meson produced in high-energy nucleus-nucleus collisions.** *Physics Letters B*, 207(3):253 – 256, 1988. (Cited on page 28.)
- [119] Carlos Lourenço, Ramona Vogt, and Hermine K. öhri. **Energy dependence of  $J/\psi$  absorption in proton-nucleus collisions.** *Journal of High Energy Physics*, 2009(02):014, 2009. (Cited on pages 28 and 29.)

- [120] B. Alessandro et al. **J/psi and psi-prime production and their normal nuclear absorption in proton-nucleus collisions at 400-GeV.** *Eur. Phys. J.*, C48:329, 2006. (Cited on page 28.)
- [121] R. Baier, Yuri L. Dokshitzer, Alfred H. Mueller, S. Peigne, and D. Schiff. **Radiative energy loss of high-energy quarks and gluons in a finite volume quark - gluon plasma.** *Nucl. Phys.*, B483:291–320, 1997. (Cited on page 29.)
- [122] Francois Arleo and Stephane Peigne. **Heavy-quarkonium suppression in p-A collisions from parton energy loss in cold QCD matter.** *JHEP*, 03:122, 2013. (Cited on page 29.)
- [123] Yu.L Dokshitzer and D.E Kharzeev. **Heavy-quark colorimetry of QCD matter.** *Physics Letters B*, 519(3):199 – 206, 2001. (Cited on page 29.)
- [124] T. Matsui and H. Satz. **J/psi suppression by quark-gluon plasma formation.** *Physics Letters B*, 178(4):416 – 422, 1986. (Cited on page 30.)
- [125] A. Adare and others. **Measurement of  $\Upsilon(1S + 2S + 3S)$  production in p + p and Au + Au collisions at  $\sqrt{s_{NN}} = 200$  GeV.** *Phys. Rev. C*, 91:024913, Feb 2015. (Cited on page 32.)
- [126] P. Braun-Munzinger and J. Stachel. **(Non)thermal aspects of charmonium production and a new look at J/psi suppression.** *Phys. Lett.*, B490:196–202, 2000. (Cited on page 32.)
- [127] Robert L. Thews, Martin Schroedter, and Johann Rafelski. **Enhanced J/psi production in deconfined quark matter.** *Phys. Rev.*, C63:054905, 2001. (Cited on page 32.)
- [128] R.L. Thews. **Quarkonium formation at high energy.** *Nuclear Physics A*, 702(1):341 – 345, 2002. International Symposium on Statistical QCD. (Cited on page 33.)
- [129] Xiaojian Du and Ralf Rapp. **Sequential Regeneration of Charmonia in Heavy-Ion Collisions.** *Nucl. Phys.*, A943:147–158, 2015. (Cited on pages 33, 36, 43, 45, and 134.)
- [130] A. Capella, A. Kaidalov, A. Kouider Akil, and C. Gerschel. **J / psi and psi-prime suppression in heavy ion collisions.** *Phys. Lett.*, B393:431–436, 1997. (Cited on page 34.)

- [131] E. G. Ferreira. **Charmonium dissociation and recombination at LHC: Revisiting comovers.** *Phys. Lett.*, B731:57–63, 2014. (Cited on pages 34 and 134.)
- [132] A. Capella, L. Bravina, E. G. Ferreira, A. B. Kaidalov, K. Tywoniuk, and E. Zabrodin. **Charmonium dissociation and recombination at RHIC and LHC.** *The European Physical Journal C*, 58(3):437–444, 2008. (Cited on page 34.)
- [133] E. G. Ferreira. **Excited charmonium suppression in proton-nucleus collisions as a consequence of comovers.** *Phys. Lett.*, B749:98–103, 2015. (Cited on pages 35, 43, and 45.)
- [134] Robert L. Thews, Martin Schroedter, and Johann Rafelski. **Enhanced  $J/\psi$  production in deconfined quark matter.** *Phys. Rev. C*, 63:054905, Apr 2001. (Cited on page 36.)
- [135] Xingbo Zhao and Ralf Rapp. **Medium modifications and production of charmonia at LHC.** *Nuclear Physics A*, 859(1):114 – 125, 2011. (Cited on page 36.)
- [136] P. Braun-Munzinger, I. Heppe, and J. Stachel. **Chemical equilibration in Pb+Pb collisions at the SPS.** *Physics Letters B*, 465(1):15 – 20, 1999. (Cited on page 37.)
- [137] P. Braun-Munzinger and J. Stachel. **Charmonium from Statistical Hadronization of Heavy Quarks: A Probe for Deconfinement in the Quark-Gluon Plasma.** *Landolt-Bornstein*, 23:424, 2010. (Cited on page 37.)
- [138] A. Andronic, P. Braun-Munzinger, and J. Stachel. **The Horn, the hadron mass spectrum and the QCD phase diagram: The Statistical model of hadron production in central nucleus-nucleus collisions.** *Nucl. Phys.*, A834:237C–240C, 2010. (Cited on page 37.)
- [139] B. Alessandro and al.  **$J/\psi$  and  $\psi(2S)$  production and their normal nuclear absorption in proton-nucleus collisions at 400 GeV.** *The European Physical Journal C - Particles and Fields*, 48(2):329–341, Nov 2006. (Cited on page 38.)
- [140] Roberta Arnaldi.  **$J/\psi$  production in p-A and A-A collisions at fixed target experiments.** *Nuclear Physics A*, 830(1):345c – 352c, 2009. Quark Matter 2009. (Cited on page 39.)

- [141] K. Adcox et al. **PHENIX detector overview**. *Nucl. Instrum. Meth.*, A499:469–479, 2003. (Cited on page 39.)
- [142] A. Adare and others. **J/ $\psi$  suppression at forward rapidity in Au-Au collisions at  $\sqrt{s_{\text{NN}}} = 200$  GeV**. *Phys. Rev. C*, 84:054912, Nov 2011. (Cited on page 40.)
- [143] N. Brambilla and others. **Heavy quarkonium: progress, puzzles, and opportunities**. *The European Physical Journal C*, 71(2):1534, 2011. (Cited on page 40.)
- [144] A. Adare and others. **Cold Nuclear Matter Effects on J/ $\psi$  Yields as a Function of Rapidity and Nuclear Geometry in d + A Collisions at  $\sqrt{s_{\text{NN}}} = 200$  GeV**. *Phys. Rev. Lett.*, 107:142301, Sep 2011. (Cited on pages 40 and 41.)
- [145] Dmitri Kharzeev and Kirill Tuchin. **Open charm production in heavy ion collisions and the color glass condensate**. *Nuclear Physics A*, 735(1):248 – 266, 2004. (Cited on page 41.)
- [146] K. Aamodt et al. **Two-pion Bose-Einstein correlations in central Pb-Pb collisions at  $\sqrt{s_{\text{NN}}} = 2.76$  TeV**. *Phys. Lett.*, B696:328–337, 2011. (Cited on page 40.)
- [147] Shreyasi Acharya et al. **Energy dependence of forward-rapidity J/ $\psi$  and  $\psi(2\text{S})$  production in pp collisions at the LHC**. 2017. (Cited on pages 42, 86, 88, 94, and 111.)
- [148] Yan-Qing Ma and Raju Venugopalan. **Comprehensive Description of J/ $\psi$  Production in Proton-Proton Collisions at Collider Energies**. *Phys. Rev. Lett.*, 113(19):192301, 2014. (Cited on page 41.)
- [149] Matteo Cacciari, Stefano Frixione, Nicolas Houdeau, Michelangelo L. Mangano, Paolo Nason, and Giovanni Ridolfi. **Theoretical predictions for charm and bottom production at the LHC**. *JHEP*, 10:137, 2012. (Cited on page 41.)
- [150] Yan-Qing Ma, Kai Wang, and Kuang-Ta Chao. **J/ $\psi$ ( $\psi'$ ) production at the Tevatron and LHC at  $\mathcal{O}(\alpha_s^4 v^4)$  in nonrelativistic QCD**. *Phys. Rev. Lett.*, 106:042002, 2011. (Cited on page 41.)
- [151] Betty Abelev et al. **J/ $\psi$  polarization in pp collisions at  $\sqrt{s} = 7$  TeV**. *Phys. Rev. Lett.*, 108:082001, 2012. (Cited on pages 43 and 99.)

- [152] R. Vogt. **Shadowing effects on  $J/\psi$  and  $\Upsilon$  production at energies available at the CERN Large Hadron Collider.** *Phys. Rev.*, C92(3):034909, 2015. (Cited on pages 43 and 45.)
- [153] François Arleo, Rodion Kolevatov, Stéphane Peigné, and Maryam Rustamova. **Centrality and  $p_T$  dependence of  $J/\psi$  suppression in proton-nucleus collisions from parton energy loss.** *JHEP*, 05:155, 2013. (Cited on pages 43 and 45.)
- [154] Jaroslav Adam et al. **Centrality dependence of  $\psi(2S)$  suppression in p-Pb collisions at  $\sqrt{s_{NN}} = 5.02$  TeV.** *JHEP*, 06:050, 2016. (Cited on page 45.)
- [155] Enrico Scomparin. **Quarkonium production in AA (pA) collisions.** <https://indico.cern.ch/event/433345/contributions/2321620/>, Feb 2017. (Cited on pages 46 and 47.)
- [156] Jaroslav Adam et al. **Differential studies of inclusive  $J/\psi$  and  $\psi(2S)$  production at forward rapidity in Pb-Pb collisions at  $\sqrt{s_{NN}} = 2.76$  TeV.** *JHEP*, 05:179, 2016. (Cited on pages 48, 50, and 126.)
- [157] Jaroslav Adam et al.  **$J/\psi$  suppression at forward rapidity in Pb-Pb collisions at  $\sqrt{s_{NN}} = 5.02$  TeV.** *Phys. Lett.*, B766:212–224, 2017. (Cited on pages 48, 106, 107, 112, 124, and 125.)
- [158] Audrey Francisco. **Quarkonium production in Pb-Pb collisions at  $\sqrt{s_{NN}} = 5.02$  TeV with ALICE.** <https://indico.cern.ch/event/576735/contributions/2565845/>, July 2017. (Cited on page 49.)
- [159] B. Alessandro et al.  **$\psi'$  production in Pb-Pb collisions at 158-GeV/nucleon.** *Eur. Phys. J.*, C49:559–567, 2007. (Cited on page 50.)
- [160] A. Andronic, F. Beutler, P. Braun-Munzinger, K. Redlich, and J. Stachel. **Statistical hadronization of heavy flavor quarks in elementary collisions: Successes and failures.** *Phys. Lett.*, B678:350–354, 2009. (Cited on page 50.)
- [161] Baoyi Chen, Yunpeng Liu, Kai Zhou, and Pengfei Zhuang.  **$\psi'$  Production and B Decay in Heavy Ion Collisions at LHC.** *Phys. Lett.*, B726:725–728, 2013. (Cited on page 50.)

- [162] T. S. Pettersson and P. Lefèvre. **The Large Hadron Collider: conceptual design**. Technical Report CERN-AC-95-05-LHC, Oct 1995. (Cited on page 52.)
- [163] **LHC Guide**. <https://cds.cern.ch/record/2255762>, Mar 2017. (Cited on page 52.)
- [164] O. Brüning, P. Collier, P. Lebrun, S. Myers, R. Ostojic, J. Poole, and P. Proudlock. **LHC Design Report**. CERN Yellow Reports: Monographs. CERN, Geneva, 2004. (Cited on page 52.)
- [165] O. Brüning, P. Collier, P. Lebrun, S. Myers, R. Ostojic, J. Poole, and P. Proudlock. **LHC Design Report**. CERN Yellow Reports: Monographs. CERN, Geneva, 2004. (Cited on page 52.)
- [166] S. van der Meer. **Calibration of the effective beam height in the ISR**. Technical Report CERN-ISR-PO-68-31. ISR-PO-68-31, CERN, Geneva, 1968. (Cited on page 53.)
- [167] K. Oyama. **Reference cross section measurements with ALICE in pp and Pb-Pb collisions at LHC**. In *LHC Lumi Days 2012 Geneva, Switzerland, February 29-March 1, 2012*, 2013. (Cited on page 54.)
- [168] ALICE Collaboration. **ALICE luminosity determination for pp collisions at  $\sqrt{s} = 13$  TeV**. Jun 2016. <https://cds.cern.ch/record/2160174>. (Cited on page 54.)
- [169] A. Beuret and al. **The LHC Lead Injector Chain**. (LHC-Project-Report-776. CERN-LHC-Project-Report-776):4 p, Aug 2004. revised version submitted on 2004-09-23 14:33:06. (Cited on page 54.)
- [170] The ATLAS Collaboration. **The ATLAS Experiment at the CERN Large Hadron Collider**. *Journal of Instrumentation*, 3(08):S08003, 2008. (Cited on page 54.)
- [171] The CMS Collaboration. **The CMS experiment at the CERN LHC**. *Journal of Instrumentation*, 3(08):S08004, 2008. (Cited on page 55.)
- [172] The LHCb Collaboration. **The LHCb Detector at the LHC**. *Journal of Instrumentation*, 3(08):S08005, 2008. (Cited on page 55.)

- [173] The ALICE Collaboration. **The ALICE experiment at the CERN LHC.** *Journal of Instrumentation*, 3(08):S08002, 2008. (Cited on pages 55, 56, 66, and 68.)
- [174] K. Aamodt et al. **The ALICE experiment at the CERN LHC.** *JINST*, 3:S08002, 2008. (Cited on pages 55 and 64.)
- [175] B. Abelev et al. **Performance of the ALICE Experiment at the CERN LHC.** *Int. J. Mod. Phys.*, A29:1430044, 2014. (Cited on pages 55, 56, 73, and 81.)
- [176] J. Adam et al. **Centrality dependence of the charged-particle multiplicity density at midrapidity in Pb-Pb collisions at  $\sqrt{s_{\text{NN}}} = 5.02$  TeV.** *Phys. Rev. Lett.*, 116(22):222302, 2016. (Cited on pages 55, 78, 79, and 114.)
- [177] P. Cortese et al. **ALICE: Physics performance report, volume I.** *J. Phys.*, G30:1517–1763, 2004. (Cited on page 56.)
- [178] P. Cortese et al. **ALICE: Physics performance report, volume II.** *J. Phys.*, G32:1295–2040, 2006. (Cited on page 56.)
- [179] **ALICE Inner Tracking System (ITS): Technical Design Report.** Technical Design Report ALICE. CERN, Geneva, 1999. (Cited on page 57.)
- [180] J. Alme and al. **The ALICE TPC, a large 3-dimensional tracking device with fast readout for ultra-high multiplicity events.** *Nuclear Instruments and Methods in Physics Research Section A: Accelerators, Spectrometers, Detectors and Associated Equipment*, 622(1):316 – 367, 2010. (Cited on pages 58 and 59.)
- [181] G. Dellacasa et al. **ALICE time projection chamber: Technical Design Report.** Technical Design Report ALICE. CERN, Geneva, 2000. (Cited on page 58.)
- [182] W. Blum, W. Riegler, and L. Rolandi. **Particle Detection with Drift Chambers.** Particle Acceleration and Detection. Springer-Verlag Berlin Heidelberg, 2008. (Cited on page 58.)
- [183] Y. Belikov, M. Ivanov, K. Safarik, and J. Bracinik. **TPC tracking and particle identification in high density environment.** *eConf*, C0303241:TULT011, 2003. (Cited on page 58.)

- [184] M. Ivanov, I. Belikov, P. Hristov, and K. Safarik. **Track reconstruction in high density environment**. *Nuclear Instruments and Methods in Physics Research Section A: Accelerators, Spectrometers, Detectors and Associated Equipment*, 566(1):70 – 74, 2006. TIME 2005. (Cited on page 58.)
- [185] P. Cortese. **ALICE transition-radiation detector: Technical Design Report**. Technical Design Report ALICE. CERN, Geneva, 2001. (Cited on page 59.)
- [186] **ALICE Time-Of-Flight system (TOF): Technical Design Report**. Technical Design Report ALICE. CERN, Geneva, 2000. (Cited on page 60.)
- [187] F. Piuz, W. Klempt, L. Leistam, J. De Groot, and J. Schükraft. **ALICE high-momentum particle identification: Technical Design Report**. Technical Design Report ALICE. CERN, Geneva, 1998. (Cited on page 60.)
- [188] V. I. Man'ko, W. Klempt, L. Leistam, J. De Groot, and Jürgen Schükraft. **ALICE Photon Spectrometer (PHOS): Technical Design Report**. Technical Design Report ALICE. CERN, Geneva, 1999. (Cited on page 61.)
- [189] P. Cortese et al. **ALICE Electromagnetic Calorimeter Technical Design Report**. Technical Report CERN-LHCC-2008-014. ALICE-TDR-14, Aug 2008. (Cited on page 61.)
- [190] J. Allen et al. **ALICE DCal: An Addendum to the EMCAL Technical Design Report Di-Jet and Hadron-Jet correlation measurements in ALICE**. Technical Report CERN-LHCC-2010-011. ALICE-TDR-14-add-1, Jun 2010. (Cited on pages 61 and 62.)
- [191] M. Gallio, W. Klempt, L. Leistam, J. De Groot, and J. Schükraft. **ALICE Zero-Degree Calorimeter (ZDC): Technical Design Report**. Technical Design Report ALICE. CERN, Geneva, 1999. (Cited on page 62.)
- [192] **ALICE Photon Multiplicity Detector (PMD): Technical Design Report**. Technical Design Report ALICE. CERN, Geneva, 1999. (Cited on page 63.)

- [193] P. Cortese et al. ***ALICE forward detectors: FMD, TO and VO: Technical Design Report***. Technical Design Report ALICE. CERN, Geneva, 2004. Submitted on 10 Sep 2004. (Cited on pages 63 and 64.)
- [194] ***ALICE dimuon forward spectrometer: Technical Design Report***. Technical Design Report ALICE. CERN, Geneva, 1999. (Cited on pages 65, 67, 68, 69, and 70.)
- [195] P. Cortese et al. **ALICE: Addendum to the technical design report of the time of flight system (TOF)**. 2002. (Cited on page 65.)
- [196] A. Zinchenko and G. Chabratova. **A new approach to cluster finding and hit reconstruction in cathode pad chambers and its development for the forward muon spectrometer of ALICE**. *Nuclear Instruments and Methods in Physics Research Section A: Accelerators, Spectrometers, Detectors and Associated Equipment*, 502(2):778 – 780, 2003. Proceedings of the VIII International Workshop on Advanced Computing and Analysis Techniques in Physics Research. (Cited on page 71.)
- [197] E. Mathieson. **Cathode charge distributions in multiwire chambers: 4. Empirical formula for small anode-cathode separation**. *Nuclear Instruments and Methods in Physics Research Section A: Accelerators, Spectrometers, Detectors and Associated Equipment*, 270(2):602 – 603, 1988. (Cited on page 71.)
- [198] L. Aphetche et al. **Numerical Simulations and Offline Reconstruction of the Muon Spectrometer of ALICE**. (Cited on page 71.)
- [199] G. Chabratova et al. **Development of the Kalman filter for tracking in the forward muon spectrometer of ALICE**. (Cited on page 71.)
- [200] C. Fabjan, L. Jirdén, V. Lindstruth, L. Riccati, D. Rorich, P. Van de Vyvre, O. Villalobos Baillie, and H. de Groot. ***ALICE trigger data-acquisition high-level trigger and control system: Technical Design Report***. Technical Design Report ALICE. CERN, Geneva, 2004. (Cited on pages 72 and 73.)

- [201] T. Alt, G. Grastveit, H. Helstrup, V. Lindenstruth, C. Loizides, D. Röhrich, B. Skaali, T. Steinbeck, R. Stock, H. Tilsner, K. Ullaland, A. Vestbo, T. Vik, A. Wiebalck, and the ALICE Collaboration. **The ALICE high level trigger**. *Journal of Physics G: Nuclear and Particle Physics*, 30(8):S1097, 2004. (Cited on page 73.)
- [202] Michael L. Miller, Klaus Reygers, Stephen J. Sanders, and Peter Steinberg. **Glauber modeling in high energy nuclear collisions**. *Ann. Rev. Nucl. Part. Sci.*, 57:205–243, 2007. (Cited on page 78.)
- [203] S. Gavin, P. L. McGaughey, P. V. Ruuskanen, and R. Vogt. **Lepton production from charm decay in nuclear collisions at  $\sqrt{s} = 200$  GeV and 5.5 TeV per nucleon**. *Phys. Rev. C*, 54:2606–2623, Nov 1996. (Cited on page 83.)
- [204] John Erthal Gaiser. *Charmonium Spectroscopy From Radiative Decays of the  $J/\psi$  and  $\psi'$* . PhD thesis, SLAC, 1982. (Cited on page 85.)
- [205] **Quarkonium signal extraction in ALICE**. Oct 2015. <https://cds.cern.ch/record/2060096>. (Cited on page 85.)
- [206] Betty Bezverkhny Abelev et al. **Measurement of quarkonium production at forward rapidity in pp collisions at  $\sqrt{s} = 7$  TeV**. *Eur. Phys. J.*, C74(8):2974, 2014. (Cited on pages 88 and 111.)
- [207] Jaroslav Adam et al. **Inclusive quarkonium production at forward rapidity in pp collisions at  $\sqrt{s} = 8$  TeV**. *Eur. Phys. J.*, C76(4):184, 2016. (Cited on pages 88 and 111.)
- [208] D. J. Lange. **The EvtGen particle decay simulation package**. *Nucl. Instrum. Meth.*, A462:152–155, 2001. (Cited on page 98.)
- [209] Elisabetta Barberio, Bob van Eijk, and Zbigniew Was. **PHOTOS: A Universal Monte Carlo for QED radiative corrections in decays**. *Comput. Phys. Commun.*, 66:115–128, 1991. (Cited on page 98.)
- [210] R. Brun et al. *CERN Program Library Long Write-up W5013*, 1994. <http://wwwasd.web.cern.ch/wwwasd/geant/>. (Cited on page 98.)
- [211] R Aaij et al. **Measurement of  $J/\psi$  polarization in pp collisions at  $\sqrt{s} = 7$  TeV**. *Eur. Phys. J.*, C73(11):2631, 2013. (Cited on page 99.)

- [212] Roel Aaij et al. **Measurement of  $\psi(2S)$  polarisation in pp collisions at  $\sqrt{s} = 7$  TeV.** *Eur. Phys. J.*, C74(5):2872, 2014. (Cited on page 99.)
- [213] Betty Bezverkhny Abelev et al.  **$J/\psi$  production and nuclear effects in p-Pb collisions at  $\sqrt{S_{NN}} = 5.02$  TeV.** *JHEP*, 02:073, 2014. (Cited on pages 107 and 135.)
- [214] A L Read. **Modified frequentist analysis of search results (the  $CL_s$  method).** (CERN-OPEN-2000-205), 2000. (Cited on pages 115 and 116.)
- [215] Thomas Junk. **Confidence level computation for combining searches with small statistics.** *Nucl. Instrum. Meth.*, A434:435–443, 1999. (Cited on page 115.)
- [216] **Procedure for the LHC Higgs boson search combination in summer 2011.** Technical Report ATL-PHYS-PUB-2011-011, CERN, Geneva, Aug 2011. (Cited on pages 115 and 120.)
- [217] J. Neyman and E. S. Pearson. **On the Problem of the Most Efficient Tests of Statistical Hypotheses.** *Philosophical Transactions of the Royal Society of London A: Mathematical, Physical and Engineering Sciences*, 231(694-706):289–337, 1933. (Cited on page 116.)
- [218] Robert D. Cousins and Virgil L. Highland. **Incorporating systematic uncertainties into an upper limit.** *Nucl. Instrum. Meth.*, A320:331–335, 1992. (Cited on page 119.)
- [219] Albert M Sirunyan et al. **Relative Modification of Prompt  $\psi(2S)$  and  $J/\psi$  Yields from pp to PbPb Collisions at  $\sqrt{S_{NN}} = 5.02$  TeV.** *Phys. Rev. Lett.*, 118(16):162301, 2017. (Cited on page 131.)
- [220] Xingbo Zhao and Ralf Rapp. **Medium Modifications and Production of Charmonia at LHC.** *Nucl. Phys.*, A859:114–125, 2011. (Cited on page 134.)
- [221] Biswarup Paul. **Inclusive  $\psi(2S)$  production at forward rapidity in pp, p-Pb and Pb-Pb collisions with ALICE at the LHC.** In *7th International Conference on Physics and Astrophysics of Quark Gluon Plasma (ICPAQGP 2015) Kolkata, West Bengal, India, February 2-6, 2015*, 2016. (Cited on page 135.)

- [222] A. Andronic, P. Braun-Munzinger, and J. Stachel. **Hadron production in central nucleus-nucleus collisions at chemical freeze-out.** *Nucl. Phys.*, A772:167–199, 2006. (Cited on page 137.)
- [223] A. Andronic, P. Braun-Munzinger, and J. Stachel. **Thermal hadron production in relativistic nuclear collisions: The Hadron mass spectrum, the horn, and the QCD phase transition.** *Phys. Lett.*, B673:142–145, 2009. [Erratum: *Phys. Lett.*B678,516(2009)]. (Cited on page 137.)
- [224] B Abelev and al. **Upgrade of the ALICE Experiment: Letter of Intent.** Technical Report CERN-LHCC-2012-012. LHCC-I-022. ALICE-UG-002, CERN, Geneva, Aug 2012. (Cited on pages 142, 144, 145, and 146.)
- [225] B. L. Ioffe and D. E. Kharzeev. **Quarkonium polarization in heavy ion collisions as a possible signature of the quark-gluon plasma.** *Phys. Rev. C*, 68:061902, Dec 2003. (Cited on page 143.)
- [226] P Antonioli, A Kluge, and W Riegler. **Upgrade of the ALICE Readout and Trigger System.** Technical Report CERN-LHCC-2013-019. ALICE-TDR-015, Sep 2013. Presently we require a LHCC-TDR reference number and a later stage we will fill the required information. (Cited on pages 145, 148, 149, 150, and 152.)
- [227] B Abelev and al. **Technical Design Report for the Upgrade of the ALICE Inner Tracking System.** Technical Report CERN-LHCC-2013-024. ALICE-TDR-017, Nov 2013. (Cited on pages 146, 147, and 153.)
- [228] **Technical Design Report for the Muon Forward Tracker.** Technical Report CERN-LHCC-2015-001. ALICE-TDR-018, Jan 2015. (Cited on pages 147 and 148.)
- [229] **Upgrade of the ALICE Time Projection Chamber.** Technical Report CERN-LHCC-2013-020. ALICE-TDR-016, Oct 2013. (Cited on page 148.)
- [230] R. Arnaldi et al. **Beam and ageing tests with a highly-saturated avalanche gas mixture for the ALICE p-p data taking.** *Nucl. Phys. Proc. Suppl.*, 158:149–153, 2006. [,149(2006)]. (Cited on pages 151 and 152.)

- [231] ALICE Collaboration, F Bossu, M Gagliardi, and M Marchisone. **Performance of the RPC-based ALICE muon trigger system at the LHC.** *Journal of Instrumentation*, 7(12):T12002, 2012. (Cited on page 152.)

# Measurement of the $\psi(2S)$ production in presence of a Quark-Gluon Plasma.

## Mesure de la production de la particule $\psi(2S)$ en présence d'un Plasma de Quarks et de Gluons.

### Abstract

The nuclear matter, which constitutes the atomic nuclei, is composed of quarks and gluons and interactions between them are described by quantum chromodynamics (QCD). Under ordinary conditions, quarks and gluons cannot be observed isolated and are confined inside hadrons such as protons and neutrons. The Quark-Gluon Plasma (QGP) is a state of nuclear matter predicted by QCD where quarks and gluons are deconfined. Experimentally, a QGP can be created in ultra-relativistic heavy ion collisions such as the lead-lead collisions delivered at the LHC, corresponding to speeds close to the speed of light. It is possible to obtain information on the characteristics of the QGP by measuring a large number of observables. In particular, the production of charmonium states such as the  $J/\psi$  and the  $\psi(2S)$ , heavy particles composed of a charm and anti-charm pair ( $c\bar{c}$ ), is studied to investigate the plasma. Indeed, the presence of QGP is expected to modify the charmonium production yields, due to a balance between the mechanism of color screening of the charm quark potential and a mechanism called recombination. This balance depends on the collision energy, the temperature of the plasma and nature of the considered particle, in particular one expects the  $\psi(2S)$  to be more suppressed than the  $J/\psi$ .

In this thesis the inclusive production of  $\psi(2S)$  in Pb – Pb collisions at an energy per nucleon-nucleon collision in the center of mass frame of  $\sqrt{s_{NN}} = 5.02$  TeV is measured in the dimuon-decay channel, using the ALICE Muon Spectrometer. The analysis is based on the data collected in ALICE (A Large Ion Collider Experiment) at the LHC in 2015 with an integrated luminosity of  $225 \mu\text{b}^{-1}$ . The nuclear modification factor  $R_{AA}$  is studied as a function of centrality. The ratio of the  $\psi(2S)$  and  $J/\psi$   $R_{AA}$  is also evaluated and shows that the  $\psi(2S)$  is more suppressed than the  $J/\psi$  for mid-central and central events. Compared with theoretical predictions, the measurements are, within uncertainty, in agreement with theoretical model.

The upgrade of the Muon Trigger, the MID (Muon Identifier), is also studied, in particular the expected data flow at a collisions rate of 100 kHz. Based on the Pb – Pb data at a collision energy of  $\sqrt{s_{NN}} = 5.02$  TeV, the estimations predict that the technology that will be implemented in the MID provides a sufficient bandwidth to sustain the data flow.

**Keywords:** Quark Gluon Plasma, heavy ions, quarkonium,  $\psi(2S)$ , ALICE, LHC.

### Résumé

La matière nucléaire, constituant le noyau des atomes, est formée de quarks et de gluons, dont l'interaction est décrite par la théorie de la chromodynamique quantique (QCD). Dans des conditions normales, quarks et gluons ne peuvent être observés de façon isolée et sont confinés dans des hadrons tels que les protons et les neutrons. Le Plasma de Quarks et de Gluons (PQG) est un état de la matière nucléaire prédit par la QCD pour lequel ces quarks et gluons sont déconfinés. Expérimentalement, le PQG peut être créé dans des collisions d'ions lourds ultra-relativistes, telles que les collisions d'ions lourds effectuées au LHC, correspondant à des vitesses proche de celle de la lumière. Il est possible d'obtenir des informations sur le PQG en mesurant un large nombre d'observables. En particulier, la production de charmonium tels que le  $J/\psi$  et le  $\psi(2S)$ , particules lourdes constituées d'une paire de quarks charme et anti-charme ( $c\bar{c}$ ) est mesurée pour étudier le plasma. En effet, la présence d'un PQG est censée modifier les taux de production des charmonia, à cause d'un équilibre entre un mécanisme d'écrantage de couleur du potentiel des quarks charme et un mécanisme dit de recombinaison. La position de cet équilibre dépend de l'énergie de collision, la température du plasma, et la nature de la particule considérée, et plus spécifiquement, il est attendu que le  $\psi(2S)$  soit plus supprimé que le  $J/\psi$ .

Dans cette thèse, la production inclusive de  $\psi(2S)$  en collisions Pb – Pb à une énergie par collision nucléon-nucléon dans le référentiel du centre de masse de  $\sqrt{s_{NN}} = 5.02$  TeV est mesurée dans le canal de décroissance de dimuon avec le Spectromètre à Muons d'ALICE. L'analyse est basée sur les données collectées dans ALICE (A Large Ion Collider Experiment) au LHC en 2015 correspondant à une luminosité intégrée de  $225 \mu\text{b}^{-1}$ . Le facteur de modification nucléaire  $R_{AA}$  est étudié en fonction de la centralité des collisions, correspondant à la distance transverse entre les centres des noyaux de plomb. Le rapport des  $R_{AA}$  du  $\psi(2S)$  et du  $J/\psi$  est également mesuré et montre que le  $\psi(2S)$  est plus supprimé que le  $J/\psi$  pour des collisions mi-centrales et centrales. Comparées aux prédictions théoriques, les mesures sont compatibles avec les modèles dans la limite des incertitudes.

L'amélioration du Muon Trigger, le MID, est également étudié, en particulier le débit de données attendu pour des fréquences de collision de 100 kHz. Basée sur les données en collisions Pb – Pb à une énergie de  $\sqrt{s_{NN}} = 5.02$  TeV, les estimations prédisent que la technologie qui sera implémentée sur le MID possède une bande passante suffisante.

**Mots-clés:** Plasma de Quarks et Gluons, ions lourds, quarkonium,  $\psi(2S)$ , ALICE, LHC.